University of Warsaw

Faculty of Physics

Adam Wincukiewicz

Dimensionality and composition modifications for highly efficient and durable perovskite solar cells

Modyfikacje wymiarowości i składu dla wysokowydajnych i stabilnych ogniw perowskitowych

Advisors:
prof. dr hab. Maria Kamińska
dr Jacek Jasiński

Warsaw, 2023

Abstract

This thesis presents a comprehensive study aimed at enhancing the performance and stability of perovskite photovoltaic cells. Perovskite solar cells represent a promising area in solar technology, but they face challenges including repeatability of the fabrication process and cell degradation over time. In addressing these challenges, the research focused on modifications of both perovskite chemical composition and perovskite solar cell structure.

It was shown that the addition of camphorsulfonic acid (CSA) in the active layer of solar cells is an effective method for enhancing performance. This strategy resulted in significant improvements in material quality and grain sizes, boosting the efficiency by 20% compared to CSA-free reference.

The research also delves into the development of a unique hole transport layer (HTL) using chemically synthesized polyaniline protonated with CSA. While this approach led to slightly lower efficiency compared to conventional methods, it demonstrated potential for boosting the long-term stability of the cells.

A significant portion of this work investigates the degradation mechanisms in perovskites, with a particular focus on the influence of oxygen and water diffusion. The study presents insightful findings on the impact of environmental factors on perovskite stability and proposes potential mitigation strategies, including the fabrication of quasi-3D perovskites or a partial substitution of iodine with bromine. In addition to perovskite chemistry modifications, an Al_2O_3 protective layer was applied onto the perovskites using Atomic Layer Deposition (ALD), which effectively limited both oxygen and water diffusion, thereby enhancing the stability of the perovskite layers and solar cells.

A non-standard *in-situ* technique of solidification processes and hydration of perovskite materials was utilized, proved to be highly fruitful in understanding the impact of precursor composition on the rate of crystallization processes and the resulting material structure. Furthermore, this technique enabled the tracing hydration processes and the determination of conditions for reversible hydration of perovskites.

Systematic studies of the degradation of modified perovskites (quasi-3D), iodide, and those mixed with bromine were conducted over 120 days. While classic 3D perovskites completely degraded within this timeframe, the newly developed perovskite formulations (quasi-3D) retained a significant portion of their original structure, demonstrating the effectiveness of the applied approach.

The work conducted provides novel insight into understanding degradation processes, as along with new strategies to enhance repeatability, efficiency, and durability of perovskite-based solar cells. The author hopes that these findings will serve as a foundation for future research in this exciting field.

Streszczenie

W tej pracy przedstawiono kompleksowe badania mające na celu poprawę wydajności i stabilności perowskitowych ogniw fotowoltaicznych. Ta generacja ogniw słonecznych stanowi obiecujący obszar energii odnawialnych, ale wciąż mierzy się z problemami na drodze do komercjalizacji, takimi jak powtarzalność procesu produkcji i degradacja ogniw z czasem. W odpowiedzi na te wyzwania, przedstawione badania koncentrują się na modyfikacjach zarówno składu chemicznego perowskitów, jak i struktury ogniw słonecznych.

Wykazano, że dodatek kwasu kamforsulfonowego (CSA) w aktywnej warstwie ogniw słonecznych jest skutecznym sposobem na poprawę wydajności. Ta strategia zaowocowała znaczną poprawą jakości materiału i wielkości ziaren, zwiększając sprawność o 20% w porównaniu do urządzenia referencyjnego bez CSA.

Badania dotyczą również modyfikacji warstwy transportującej dziury. W tym celu po raz pierwszy zastosowano polianilinę protonowaną CSA. Chociaż to podejście prowadziło do nieco niższej efektywności w porównaniu do tradycyjnych metod, wykazało potencjał dla zwiększenia długoterminowej stabilności ogniw.

Znaczna część tej pracy koncentruje się na mechanizmach degradacji perowskitów, ze szczególnym naciskiem na wpływ dyfuzji tlenu i wody. Przedstawiono wyniki badań i wnioski na temat wpływu tych czynników środowiskowych na stabilność perowskitów, jak również zaproponowano potencjalne strategie poprawy stabilności, między innymi syntezę perowskitów *quasi-3D* lub częściową substytucję jodu bromem. Poza modyfikacjami składu chemicznego perowskitów, zastosowano warstwę ochronną Al_2O_3. Ta ostatnia metoda wykazała skuteczność w ograniczaniu dyfuzji zarówno tlenu, jak i wody, co znacznie zwiększa stabilność warstw perowskitu i ogniw słonecznych.

Wykorzystano niestandardową technikę badań *in-situ* procesów zestalania, jak również uwadniania materiałów perowskitowych. Okazała się ona bardzo owocna dla zrozumienia wpływu składu prekursorów na tempo procesów krystalizacji i wynikającą z tego strukturę materiału. Ponadto technika ta pozwoliła na prześledzenie procesów uwadniania i określenie warunków odwracalnego uwadniania perowskitów.

Systematyczne badania degradacji zmodyfikowanych perowskitów (quasi-3D), jodkowych oraz mieszanych z bromem przeprowadzono przez okres 120 dni. Podczas gdy klasyczne perowskity 3D całkowicie uległy degradacji po tym okresie, nowe formuły perowskitów (quasi-3D) opracowane w tej pracy zachowały znaczącą część swojej pierwotnej formy, dowodząc skuteczności zastosowanego podejścia.

Przeprowadzone prace dostarczają nowych informacji na temat zrozumienia procesów degradacji, a również nowych strategii poprawy powtarzalności, efektywności i trwałości ogniw słonecznych na bazie perowskitów. Autor pracy ma nadzieję, że będą podstawą do przyszłych badań w tym ekscytującym obszarze.

Serdecznie dziękuję:

Prof. dr hab. Marii Kamińskiej z Wydziału Fizyki UW, za pomoc i zaangażowaną opiekę promotora, cenne uwagi i wsparcie podczas tworzenia tej pracy doktorskiej. Jej mądrość, cierpliwość i oddanie sprawiły, że ten trudny proces stał się dla mnie inspirującym doświadczeniem naukowym. Dzięki Prof. dr hab. Marii Kamińskiej miałem możliwość spędzenia dziewięciu miesięcy w ośrodkach naukowych w Stanach Zjednoczonych, co w znacznym stopniu ukierunkowało moje badania. Jej otwartość i dostępność dodawały mi sił w momentach zwątpienia i zawsze będę pamiętał o ogromnym wkładzie, jaki wniosła w mój rozwój.

Dr. Jackowi Jasińskiemu z Uniwersytetu w Louisville, za wsparcie podczas mojego pobytu w Louisville i opiekę promotora. Dziękuję za możliwość spędzenia stypendium Fulbrighta w jego laboratorium oraz naukę obsługi dyfraktometru rentgenowskiego, rentgenowskiej spektroskopii fotoelektronów i skaningowego mikroskopu elektronowego. Dr Jasiński poświęcił niezliczone godziny na dyskusje i interpretacje naszych wyników. Jego wkład w moją pracę był niezwykle cenny, a jego determinacja i pasja do nauki były dla mnie źródłem inspiracji. Dziękuję za wszystkie dyskusje, nie tylko te o fizyce.

Prof. dr hab. Krzysztofowi Koronie z Wydziału Fizyki UW, za wskazówki techniczne przy wytwarzaniu ogniw, napylanie elektrody metalicznej oraz cenne spostrzeżenia i uwagi do wyników moich badań.

Prof. dr hab. Magdalenie Skompskiej z Wydziału Chemii UW, za nałożenie nanocząstek złota na warstwę odprowadzająca elektrony z ogniwa i dyskusje wyników.

Dr. Mateuszowi Tokarczykowi z Wydziału Fizyki UW, za wykonanie części pomiarów dyfrakcji rentgenowskiej i pomoc w ich analizie oraz za naukę obsługi skaningowego mikroskopu elektronowego.

Mgr Ewelinie Wierzyńskiej z Wydziału Chemii UW, za syntezę polianiliny domieszkowanej CSA.

Dr. Piotrowi Wróblowi z Wydziału Fizyki UW, za nałożenie nanocząstek plazmonicznych na warstwę TiO_2 *i dyskusje wyników.*

Prof. dr hab. Tomaszowi Szoplikowi z Wydziału Fizyki UW, za wartościowe obserwacje i komentarze dotyczące wyników moich badań.

Dr. Pawłowi Trautmanowi z Wydziału Fizyki UW, za instalację układu do badań wydajności ogniw słonecznych i pomoc w pomiarach oporu.

Dr Carolin Sutter-Fella z Lawerence Berkeley National Laboratory, za opiekę podczas stażu.

Dr Tim Kodalle z Berkeley National Laboratory, za pomoc w obsłudze układu do pomiarów luminenscencji in-situ.

Mgr. Maciejowi Krajewskiemu z Wydziału Fizyki UW, za nałożenie warstwy Al_2O_3 *na ogniwa słoneczne.*

Prof. dr hab. Markowi Godlewskiemu z Instytutu Fizyki PAN i jego grupie badawczej, za nałożenie warstwy Al_2O_3 *na próbki perowskitów.*

Rodzinie i przyjaciołom, za wsparcie, które było dla mnie fundamentem podczas tego długiego i skomplikowanego procesu.

Pracę dedykuję Rodzicom.

Table of contents

This thesis explores the field of perovskite solar cells, their development, and the challenges associated with their fabrication and long-term stability. The thesis is structured as follows:

In the Chapter 1, the physics of solar cells is introduced, providing an overview of solar energy, photovoltaic technology, semiconductor basics, solar cell operation, and characterization methods. The chapter also presents the evolution of solar cells through different generations, from the first-generation crystalline silicon cells to the cutting-edge third-generation devices.

Chapter 2 focuses on perovskite materials, discussing their multidimensional nature, optoelectronic properties, and the impact of halide and dimensionality on bandgap and exciton binding energy. Moreover, perovskite solar cell structure is presented.

Chapter 3 delves into the identification of problems and challenges related to perovskite solar cells. These include understanding the solidification process of the perovskite layer, recognizing the effect of oxygen and moisture, and exploring modifications in the perovskite solar cell structure particularly in the electron transport, hole transport, and active layers.

Chapter 4 explains the methodologies employed in the thesis, including chemical synthesis of perovskites and solar cell fabrication, atomic layer deposition, X-ray diffraction, electron microscopy, X-ray photoelectron spectroscopy, in-situ photoluminescence, and current-voltage (IV) characteristics.

Chapter 5 presents a comprehensive study of perovskite morphology and crystal structure, linking these properties to the dynamics of the solidification process of perovskites with different compositions, dimensionality and precursor additives.

Chapter 6 delves into the dynamics of perovskite formation using *in-situ* photoluminescence to study mixed-halide perovskites of different dimensionality and Lewis acid-doped perovskites.

Chapter 7 examines the influence of oxygen on the degradation dynamics of perovskite solar cells.

In Chapter 8, the reversible hydration dynamics of perovskites are studied using X-ray diffraction and *in-situ* photoluminescence.

Chapter 9 focuses on the long-term stability of perovskites, assessing their degradation over time.

Chapter 10 explores various modifications in perovskite solar cells, including the introduction of gold nanoparticles, polyaniline, camphorsulfonic acid doping, and Al_2O_3 coverage for encapsulation.

Finally, Chapter 11 provides a summary of the thesis, highlighting the key findings and contributions to the field of perovskite solar cells.

1 INTRODUCTION TO SOLAR CELLS AND THEIR EVOLUTION

1.1 Introduction

Semiconductors play an essential role in the contemporary world. They are a key component of electronic devices, enabling advances in communication, computing, military systems, transportation, and clean energy[1]. In this chapter, physics of semiconductors and solar cells will be discussed.

1.2 Solar Energy and photovoltaics

Earth is the only know place where life can exist and thrive. One reason for this is that our planet lies within the sun's so-called Habitable Zone, a range where the planetary surface can support liquid water given sufficient atmospheric pressure[2,3]. The sun provides enormous amounts of energy. According to estimates from the US Department of Energy, our star delivers 430 quintillion (4.3×10^{20}) joules of energy to Earth every hour[4]. To put that into context, this is more energy than all humans use in a year (4.1×10^{20}J)[4]. Clearly, we have a virtually unlimited source of energy; we just need to capture it more effectively to meet the demand. Currently, we utilize a fraction of this incoming energy in two ways: solar thermal energy for generating thermal energy to heat water or air, and solar photovoltaics to generate electricity. The latter is the focus of this thesis and will be further discussed.

Climate change is one of the greatest challenges humanity faces. To achieve a sustainable future, a global energy transition from fossil fuel-based to zero-carbon-emitting technologies is required. One of the solutions for clean energy is photovoltaics (PV). According to the International Renewable Energy Agency (IRENA)[5], by 2050, PV could generate 25% of total global electricity demand, becoming the second-largest power generation source. This type of renewable energy is particularly promising due to of the accessibility of solar radiation and the enormous amount of solar energy our planet receives, coupled with the relatively low cost of manufacturing PV cells. According to the

US Energy Information Administration[6], PV is already three times cheaper than coal-based power plants. Furthermore, IRENA predicts a gradual tenfold decrease in the price by 2050.

1.3 Basics of semiconductors

Semiconductors constitute the main active materials of solar cells. The potential energy of an electron in crystalline materials is periodic in space. As a consequence, the energy spectrum consists of allowed bands, which can be filled with electrons, and forbidden energy bands, where no quantum states exist. At 0K temperature, undoped semiconductors contain a certain number of low-energy allowed bands that are completely filled with electrons, while the higher bands are empty. In the majority of cases involving the application of semiconductors, only the upper filled band, termed the valence band (VB) and the first empty band, termed the conduction band (CB) are of interest. The valence and conduction bands are separated by a forbidden energy gap, E_g. When a photon with energy higher than the energy gap hits the material and transfers its energy to an electron from the valence band, the excitation of the electron into the conduction band is possible. Another way to transfer an electron to the conduction band is by providing thermal energy. Electrons in the conduction band contribute to the electrical conductivity of the material. Semiconductors behave as insulators at absolute zero temperature ($T = 0$), but with temperature increase, electrical conductivity grows because more electrons acquire enough energy to jump to the conduction band.

A perfect semiconductor with no defects or impurities is termed an intrinsic semiconductor. In such a material, electron-hole pairs are thermally generated across the bandgap, and the number of electrons (n) in the conduction band is equal to the number of holes (p) in the valence band. The values of n and p increase quickly with temperature, but their absolute values are typically small. For example, in silicon (Si, $E_g = 1.12$eV), $n = p = 10^{10}$ cm^{-3} at 300K[7], i.e., which is many orders of magnitude lower than what is typically observed in metals (~ $10^{22\text{-}23}$cm^{-3}).

Concentrations of electrons and holes in a semiconductor can be increased through the addition of different elements, which are called dopants. If atoms with one more electron in valance shell than the host atoms are introduced to a semiconductor lattice (for example a phosphorus atom in a silicon crystal), additional states in the forbidden band, close to the bottom of the conduction band, are created. At $T = 0$, electrons occupy these additional states, but at $T \neq 0$ they can be thermally excited to the conduction band, causing an increase in the concentration of free electrons, n. Therefore, n increases with the concentration of dopants and this process is known as n-type doping. On the other hand, p-type doping involves the introduction of atoms with fewer electrons in the valence shell than the parent atoms of a crystal. Such doping leads to additional states near the top of the valence band, which are empty at T = 0. However, at T ≠ 0, electrons can be excited to these states, resulting in free holes within the valence band, a process termed p-type doping.

Insulators are materials with a considerably larger band gap compared to semiconductors (typically above 4 eV) and with very low conductivity. On the other hand, metals have a continuum of quantum states without a bandgap, and the wavefunctions of electrons at about Fermi energy are delocalized, enabling efficient electronic transport characterized by high electrical conductivity. **Figure 1.1** summarizes the differences in electronic structure between metals, semiconductors, and insulators.

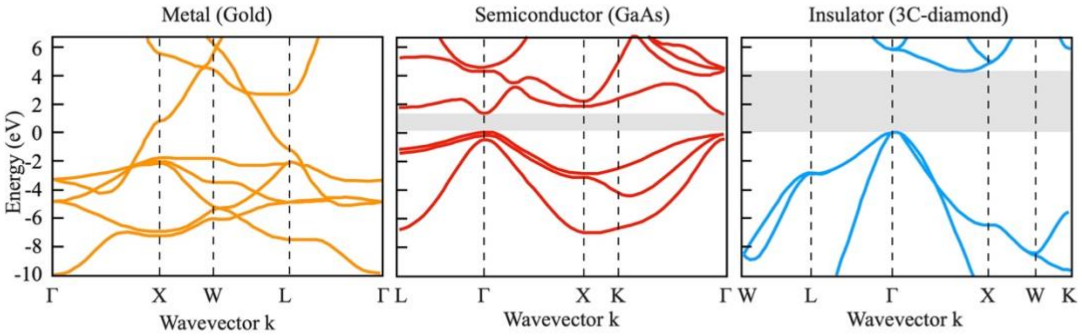

***Figure 1.1** DFT calculations of band structures of: metal, semiconductor and insulator. Data derived from Ref. [8–10], figure recreated by the author of this dissertation.*

Central to understanding the behavior of solar cells and quite a number of other semiconductor devices is the p-n junction, which is created when a p-type semiconductor is connected to an n-type semiconductor. By studying the p-n junction's behavior, one can derive the Shockley equation, which describes the current voltage (I-V) characteristics of solar cells[11].

Upon connecting a p-type semiconductor to an n-type semiconductor, due to the carrier concentration gradient, diffusion of majority carriers begins. Flow of charged carriers (electrons to p-type and holes to n-type material) creates an electric field, which further results in a drift of minority carriers in the opposite way to the diffusion current. When both currents (diffusion and drift) are equalized, a so called steady-state condition is reached, Fermi levels are equalized, and a space charge, also called depletion layer, is formed (**Figure 1.2**).

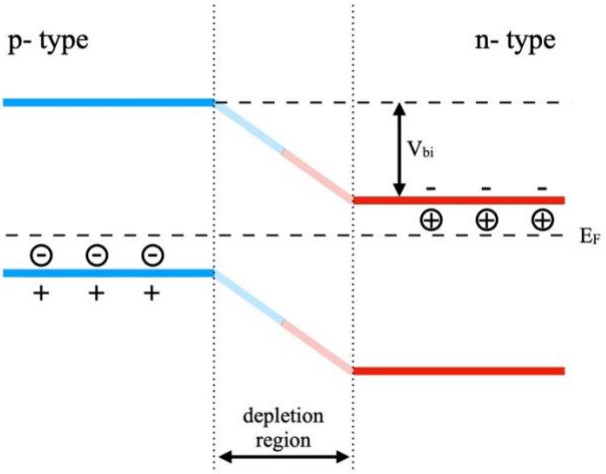

Figure 1.2 *Schematic diagram of p-n junction at a steady state.*

1.4 Solar cell operation

Solar cells directly convert sunlight energy into electricity using the photovoltaic effect. The operation of a photovoltaic cell involves several key steps: absorption of visible light, creation of electron-hole pairs (excitons) through the photoelectric effect, charge separation, and charge collection at electrodes. In effecient photovoltaic materials, these processes occur with minimal energy loss, recombination and trapping processes are negligible. When photons with energy equal to or higher than the bandgap (E_g) of a semiconductor used as the active layer interact with the electrons in the valence band, they can excite the electrons to the conduction band in both p-type and n-type region. This generates electron-hole pairs, known as excitons. In most photovoltaic materials, the binding energy of excitons is smaller than thermal energy (kT) at room temperature. As a result, excitons dissociate, leading to the formation of free electrons and holes. The electrons generated in the p-type region and the holes generated in the n-type region are minority carriers, which can diffuse to the junction and further, with the assistance of the built-in potential (drift current), reach the electrodes if their lifetime at the excited states is long enough. The schematic diagram of such a cell and its working principles are illustrated in **Figure 1.3**. In the steady state, the electric field generated in the depletion layer is characterized by the so-called built-in potential V_{bi}, as shown in **Figure 1.3**.

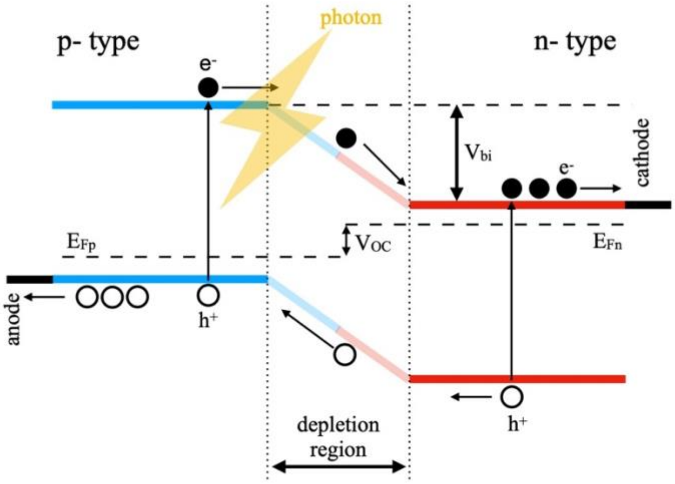

Figure 1.3 Solar cell under light illumination at zero current (open circuit condition).

When an incident light is absorbed, the increased concentration of carriers disrupts the thermal equilibrium, resulting in the splitting of the Fermi level into quasi-Fermi levels for electrons (E_{Fn}) and holes (E_{Fp}). The difference between these two Fermi levels corresponds to the open-circuit voltage ($V_{oc} = E_{Fn} - E_{Fp}$) of an ideal solar cell.

Conversly, the collection of photo-generated carriers under zero bias voltage gives rise to the short-circuit current of a solar cell.

The Shockley-Queisser limit refers to the maximum power-conversion efficiency of a solar cell when using a single semiconducting material (with a p-n junction) as an active layer. The optimal bandgap energies for absorbing material in solar cells fall within the range of $1.1eV < E_g < 1.4eV$, which leads to a maximum solar conversion efficiency of approximately $\eta = 34\%$[12]. In 1961, Shockley and Queisser calculated the efficiency of a solar cell using the generation, recombination, and transport equations[12].

Their results demonstrated that the maximum theoretical efficiency (34%) of a single junction solar cell can be achieved using a semiconductor with a bandgap of 1.34 eV (**Figure 1.4**). For wider bandgaps, the efficiency decreases due to absorption loss.

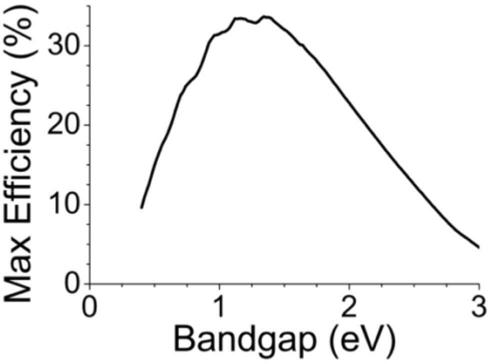

Figure 1.4 *Maximum efficiency vs. bandgap for single junction solar cell*[13].

Table 1.1 *Theoretical maximum current-density calculated from Eq. 1.1.*

Material	**Band gap, E_g (eV)**	**Maximum current density, J_{sc} (mA cm^{-2})**	**Maximum efficiency (%)**
Silicon (Si)	1.12[14]	43.79	32.23[15]
Perovskite	1.51[16]	27.24	31.64[15]

On one hand, to maximize generated current, minimizing E_g is required. Since photogenerated carriers thermalize to the conduction band and valence band edges, the generated energy per absorbed photon is related to E_g regardless of the initial photon energy E.

On the other hand, maximizing E_g maximizes the energy per absorbed photon. Therefore, an optimum bandgap exists between $E_g = 0$ (the number of electron-hole pairs has its maximum), and $E_g \rightarrow \infty$, (which maximizes the energy of a single electron-hole pair).

Standard solar radiation spectrum at the Earth's surface (denoted as AM1.5) is shown in **Figure 1.5**. AM0 (0 meaning "zero atmospheres") relates to the radiation spectrum of 5800K black- body, which is a good approximation for solar spectrum outside the Earth atmosphere, while AM1.5 includes both the presence of the atmosphere and a solar zenith angle of z=48.2° [17]. The simplest approximation of semiconductor's absorbance, A(E), is a step function, that is, $A(E) = 1$ (for $E > E_g$) and $A(E) = 0$ (for $E < E_g$). Therefore:

$$J_{sc,SQ} = q\int_0^\infty A(E)\phi_{ph}^{AM1.5}(E)dE = q\int_{E_g}^\infty \phi_{ph}^{AM1.5}(E)dE \qquad \text{Eq. 1.1}$$

where q denotes the elementary charge and $\phi_{ph}^{AM1.5}$ is the incoming photon flux density at a given wavelength.

$J_{sc,SQ}$ as a function of the band-gap energy of the solar absorber is plotted in **Figure 1.6**. The following short circuit-current density as a function of the band-gap energy is correct as long as we consider external quantum efficiency equals 100%, meaning lossless generation and collection of charges. Additionally, the theoretical maximum short-circuit ($J_{sc,SQ}$) for silicon and perovskite solar cells can be derived from Eq. 1.1 and **Figure 1.6**, see **Table 1.1**.

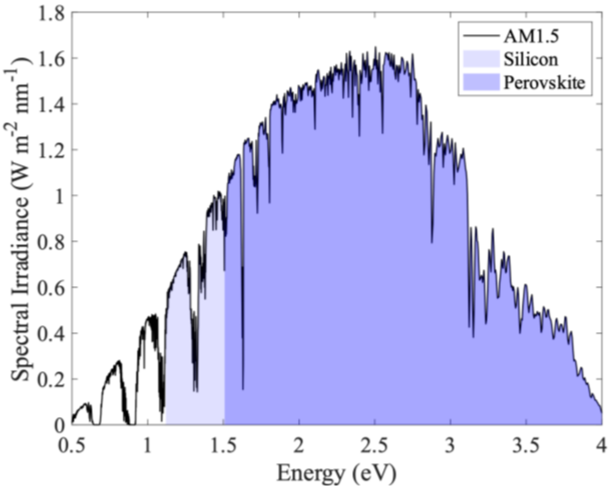

Figure 1.5 *Black line represents the spectral photon flux corresponding to the terrestrial AM1.5G norm spectrum. Shaded areas indicate absorption regions for silicon (bright and dark violet) and perovskite (dark violet).*

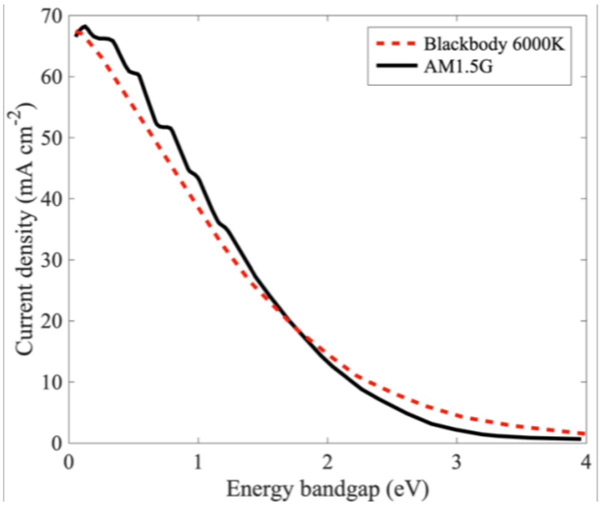

Figure 1.6 *The short-circuit current density $J_{sc,SQ}$ in the Shockley-Queisser limit as a function of the band gap E_g of the solar absorber, obtained using the AM1.5G spectrum and Eq. 1.1.*[18]

1.4.1 Current-Voltage (IV) Measurement

When a voltage is applied across the p-n junction, the behavior of the junction alters. The barrier height decreases in the forward direction, resulting in an increase in the diffusion current that grows exponentially with the applied voltage. In contrast, the barrier height increases in the reverse direction, limiting the diffusion current and causing the drift current to dominate. This drift current is constrained by the concentration of minority carriers and quickly saturates (**Figure 1.7**).

By considering the balance between the drift and diffusion currents under varying applied voltage conditions, one can derive the Shockley equation. This equation describes the current-voltage relationship for a diode in the dark:

$$J(V) = J_0\left[exp\left(\frac{qV}{kT}\right) - 1\right]$$

where J is the current density, J_0 is the saturation current, q is the elementary charge, V is the voltage across the junction, k is the Boltzmann constant, and T is the temperature.

Under illumination, excess carriers are generated within the solar cell due to the absorption of photons. This increase in carrier concentration leads to an increase in the drift current, which is proportional to the incident photon flux. Consequently, the IV curve of the solar cell shifts under illumination (**Figure 1.7**), with the photocurrent superimposed on the dark current described by the Shockley equation:

$$J(V) = J_0\left[exp\left(\frac{qV}{kT}\right) - 1\right] - J_{sc} \qquad \text{Eq. 1.2}$$

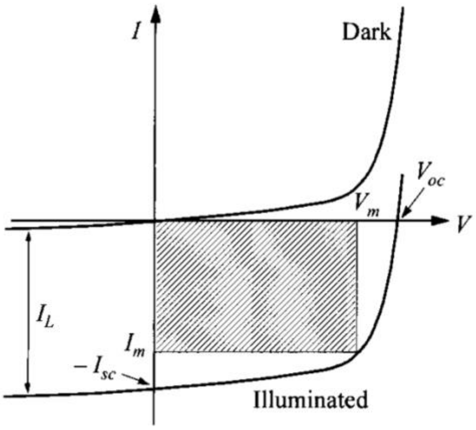

Figure 1.7 *I-V characteristics of solar cell under illumination*[19].

Finally, the *-1* term in Eq. 1.2 can usually be neglected under illumination:

(i) The exponential part is usually significantly bigger than 1 (except for relatively low voltages, <100 mV),

(ii) Further, at low voltages, the light generated current J_{sc} dominates J_0,

(iii) Moreover, the convention within the photovoltaic community is to flip the IV curve (multiplication of Eq. 1.2 by *-1*).

Additionally, the diode ideality factor n should be included in the equation. In the ideal case $n = 1$, but in real diodes it varies between 1-2[20]. Interestingly, for polymer-based solar cells, the ideality factor can be as high as 6 [21].

Regarding perovskite solar cells, it is worth mentioning that instead of relying on a p-n junction, they are commonly built as a heterojunction device, often with a structure similar to a dye-sensitized solar cell. In this type of structure, the perovskite material absorbs light and generates electron-hole pairs, and then a transport material is used to selectively transport either electrons or holes out of the device. That said, it is also possible to create a perovskite solar cell with a p-i-n or n-i-p structure, where the perovskite is the intrinsic (i) layer between p-type and n-type transport layers, and perovskite solar cells may be described using the Shockley equation.

Finally, the equation for the IV curve under illumination is as follows:

$$J(V) = J_{sc} - J_0 \left[exp\left(\frac{qV}{nkT}\right)\right] \qquad Eq.\ 1.3$$

Open-circuit voltage (V_{oc}) is a maximum value of voltage which can be generated by an illuminated solar cell (**Figure 1.9**), with no external load connected. V_{oc} can be found through evaluation of Eq. 1.3 under open-circuit conditions, that is, at $J(V) = 0$:

$$V_{oc} = \frac{nkT}{q} \ln\left(\frac{J_{sc}}{J_0}\right) \qquad Eq.\ 1.4$$

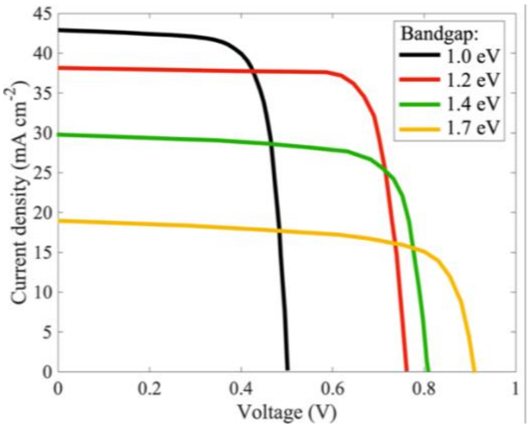

Figure 1.8 *J-V simulation of solar cells with various bandgaps (E_g) of semiconductors, from 1.0 eV to 1.7 eV* [22]*: the higher the band gap, the higher the open- circuit voltage V_{oc}. However, a higher bandgap also leads to decrease of short-circuit current density J_{sc} .*

Figure 1.8 shows J-V characteristics of solar cells based on semiconductors with different band gaps. Collection of photo-excited carriers generates J_{sc}. Therefore, as it was discussed above, to maximize J_{sc}, minimizing E_g is required (solar cells based on semiconductors with narrower E_g generate higher J_{sc} than materials with wider E_g, **Figure 1.8**). Since photogenerated carriers thermalize to the conduction band and valence band edges, the generated energy per absorbed photon is related to E_g regardless of the initial photon energy *E*. On the other hand, maximizing E_g maximizes the energy per absorbed photon, which affects V_{oc} (the wider the E_g, the higher the V_{oc}).

Parameters which can be extracted from the J-V curve are: J_{sc}, V_{oc}, fill factor (FF), and power conversion efficiency (η). FF and η are described by Eq. 1.5 and Eq. 1.6, respectively:

$$FF = \frac{J_{max}V_{max}}{J_{sc}V_{oc}} \qquad Eq.\ 1.5$$

$$\eta = \frac{P_{max}}{P_{inc}} = \frac{J_{sc}V_{oc}}{P_{inc}} \times FF \qquad Eq.\ 1.6$$

A solar cell, when an external load applied, reaches some maximum power point P_{max} with corresponding voltage V_{max} , and current J_{max} ($P_{max} = V_{max} \times J_{max}$), which is shown in **Figure 1.9**.

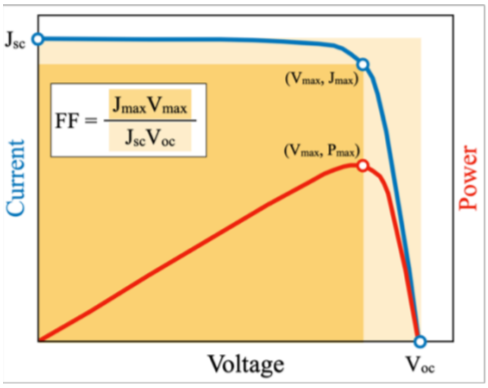

Figure 1.9 *Light IV characteristic and output power vs. voltage of a solar cell.*

1.4.2 Effect of parasitic resistances

J-V measurements are a powerful tool to analyze the resistance problem in solar cells. According to the Eq. 1.6, to obtain higher efficiency, one need to increase the product of J_{sc}, V_{oc}, and FF as high as possible.

The material properties and the device structure will affect J_{sc} and V_{oc}, whereas parasitic resistance (series and shunt resistance) will influence FF. **Figure 1.10** shows the equivalent circuit of a solar. J_{sc} is the generated photo-current; R_s and R_{sh} are the series and shunt resistance, respectively.

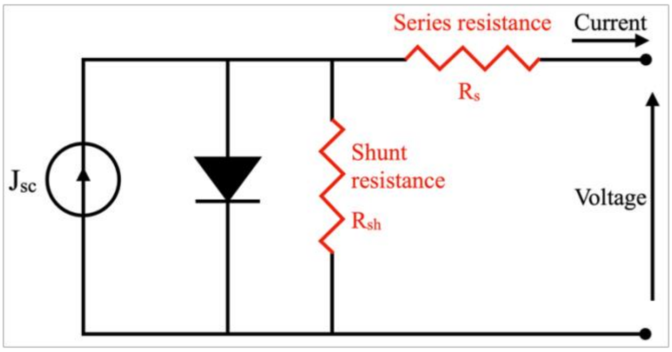

Figure 1.10 *Equivalent circuit of a solar cell under illumination.*

When series and shunt resistances are concerned, the J-V curve equation of the solar cell is given by:

$$J(V) = J_{sc} - J_0 exp\left[\frac{q(V+JR_s)}{nkT}\right] - \frac{V+JR_s}{R_{sh}} \qquad Eq.\ 1.7$$

The R_s and R_{sh} terms in Eq. 1.7 can be calculated as the slope of the JV curve at open-circuit point and short-circuit point, namely:

$$R_s = -\left.\frac{\partial V}{\partial J}\right|_{V=V_{oc}} \qquad Eq.\ 1.8$$

$$R_{sh} = -\frac{\partial V}{\partial J}\bigg|_{V=0} \qquad Eq.\ 1.9$$

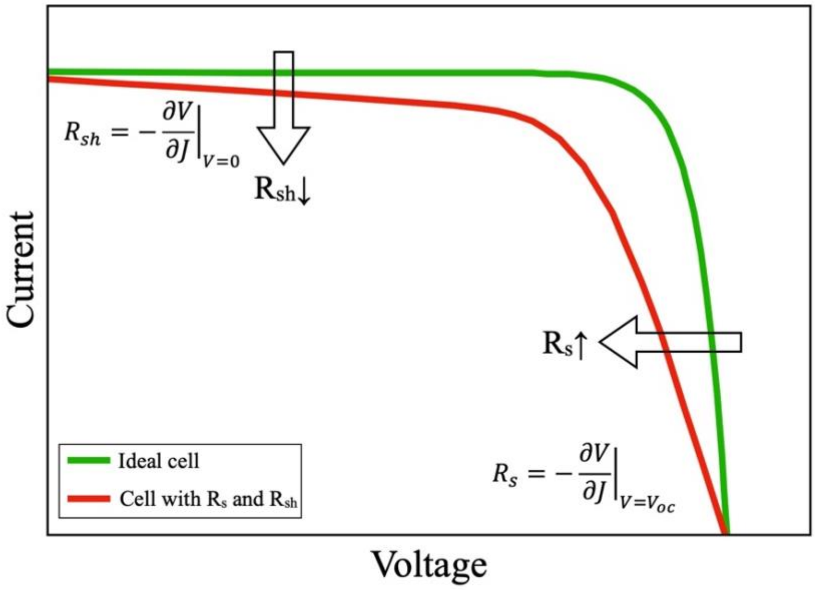

***Figure 1.11** Comparison between JV characteristics of an ideal solar cell (green curve) and a solar cell with parasitic resistances (red curve).*

In **Figure 1.11**, a difference between J-V curves of an ideal solar cell and a solar cell with parasitic resistances is shown. Fill factor of the red curve is considerably lower in comparison to an ideal JV curve (green one).

1.4.3 Origin of parasitic resistances

Series resistance

In perovskite solar cells, the efficiency is significantly influenced by the series resistance within different components of the cell. First, the current moving through the perovskite material can experience Ohm resistance. Secondly, the interface between the perovskite layer and electron (ETL) or hole transporting layer (HTL), and between ETL/HTL and the metal contacts can act as a resistor as well. Finally, the metal contacts will have their own resistances. Low series resistance indicates good conductivity of all the layers (perovskite, ETL, HTL, metal electrode) and good carrier transport at the interfaces. Therefore, the lower the series resistance the better for the efficiency of the solar cell.

Shunt resistance

A shunt is a macroscopic defect in the solar cell which provides alternative paths for the photogenerated carriers (example: a current path at the edge of the solar cell). Low shunt resistance means that a significant fraction of the photoexcited carriers prefers to travel through the shunt. Therefore, the higher the shunt resistance the better for the efficiency of the solar cell.

1.5 GENERATIONS OF SOLAR CELLS

1.5.1 Introduction

On April 25th, 1954, Bell Labs demonstrated the invention of the first practical silicon solar cell[23]. Since then, the solar cell industry has been growing rapidly. The New York Times has forecasted then that solar cells would eventually lead to a source of "limitless energy of the sun"[24]. The more widespread technology, the cheaper it becomes and due to this empirical rule exponential growth of solar cells' capacity is currently observed[25]. **Figure 1.12** reveals how efficiencies of each generation of solar cells have changed since 1976. Generations of solar cells can be divided into three types:

(i) 1st gen, also called conventional – mono- and polycrystalline silicon,

(ii) 2nd gen, thin film solar cells – GaAs, CdTe, CIGS, amorphous silicon,

(iii) 3rd gen, emerging photovoltaics – polymers and dyes, perovskites

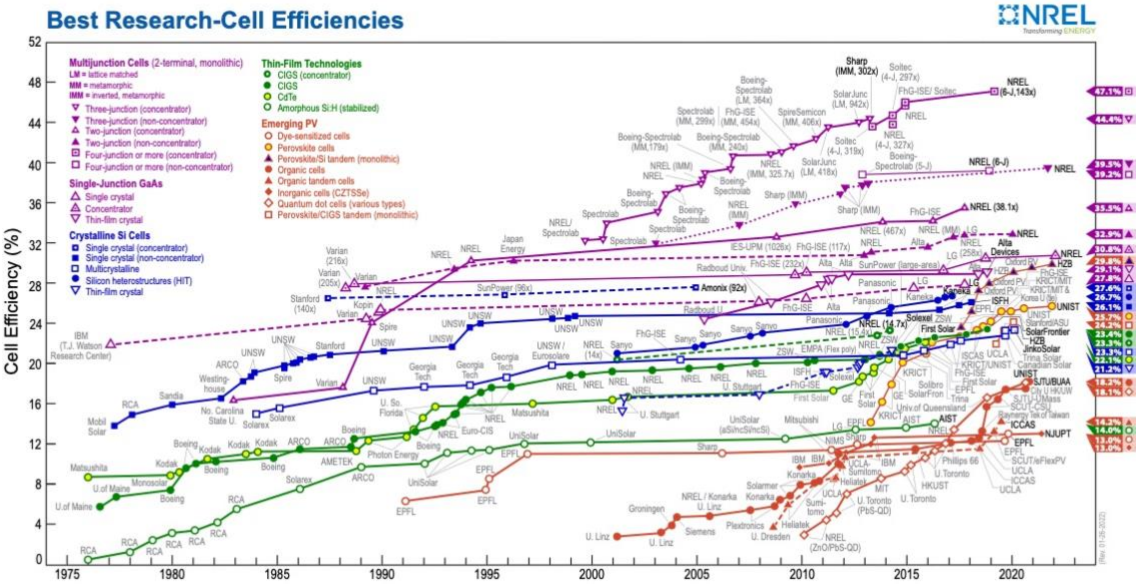

Figure 1.12 Best reached efficiencies of solar cells of the 1st (blue), 2nd (green and violet) and 3rd (red) generation[26].

1.5.2 First generation

Monocrystalline – solar cells based on monocrystalline silicon are manufactured from a single crystal. They are highly efficient and have a long lifetime (about 25 years warranties, but you can expect your system to last for up to 40 years or more). Due to the time-consuming production process, monocrystalline cells are relatively expensive compared to other photovoltaic technologies. They have a characteristic black color. As of 2022, the highest reported efficiency is 26.1%[27].

Polycrystalline – solar cells based on polycrystalline silicon are cheaper to produce and less efficient than monocrystalline cells. Unlike monocrystalline, they consist of many different silicon fragments instead of a single ingot. The highest achieved efficiency so far is 23.3%[26].

Comparison of mono- and polycrystalline silicon solar cells is shown in **Figure 1.13**.

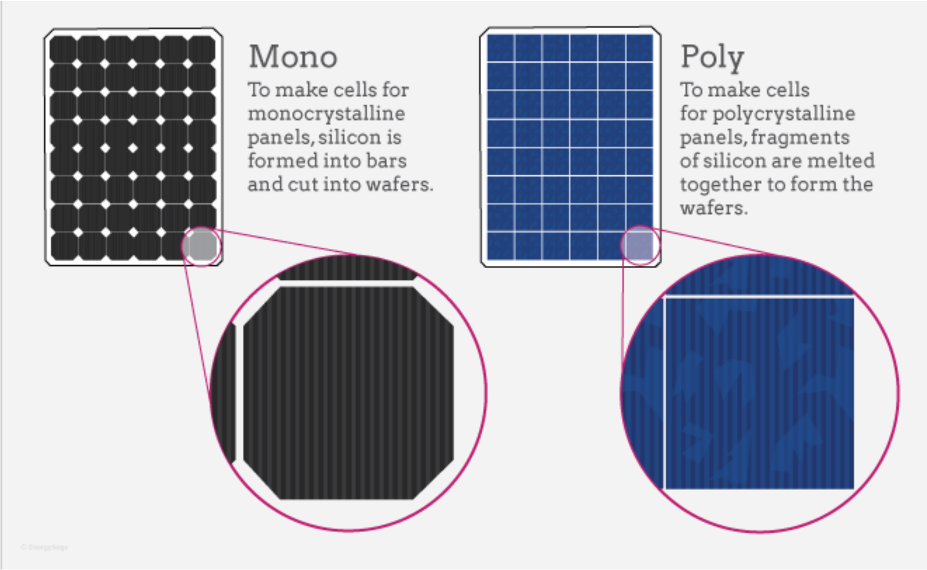

Figure 1.13 *Comparison of mono- and polycrystalline silicon solar cells*[28].

1.5.3 Second generation

The second generation of solar cells is a generation of thin-film cells. Its development was related to the need to reduce costs by using less semiconductor material. This also means that the thin-film active layer must be made of a semiconductor with a high absorption coefficient. Crystalline silicon is unsuitable for thin-film solar cells due to its relatively low absorption coefficient, which stems from its indirect bandgap. In contrast, materials with direct bandgaps and higher absorption coefficients, such as cadmium telluride (CdTe), copper indium gallium selenide (CIGS), and amorphous silicon (a-Si), are better suited for thin-film solar cell applications.

In the 1970s, it was possible to produce the first thin-film cells based on amorphous silicon, and then other materials[29]. Due to the very thin layer (from 0.001 to 0.08 mm), cells of this generation are much cheaper than cells made of crystalline silicon. The semiconductors in these cells are deposited using vapor deposition, sputtering, or epitaxy. The highest reported efficiency as of 2022 is 14% for cells based on amorphous silicon[26], or 23.35% for CIGS[27].

Multijunction cells should be distinguished within this generation. They are based on three or even four junctions such as: InGaP/GaAs/InGaAs, even in tandems with silicon. The highest reported efficiency of multijunction cells is 47.1%[26]. Said that, their applications are currently rather limited due to their relatively high price.

1.5.4 Third generation

Third-generation solar cells offer even more cost-effective. Similar to the second-generation devices, they are thin-film solar cells. The key concept behind these cells is selective charge transfer, where electrons flow towards one electrode and holes towards another. This arrangement is achieved by taking advantage of the energy benefits associated with carriers in different layers of the cell's structure. To facilitate this process, specific layers are incorporated to block one type of charge carriers while enabling the transport of the other type. These layers are known as the Hole Transport Layer (HTL) and the Electron Transport Layer (ETL). The energy band diagram of a third-generation solar cell is illustrated in **Figure 1.14**. The HTL restricts the movement of electrons while allowing holes to pass through, while the ETL facilities electron transport while impeding the passage of holes.

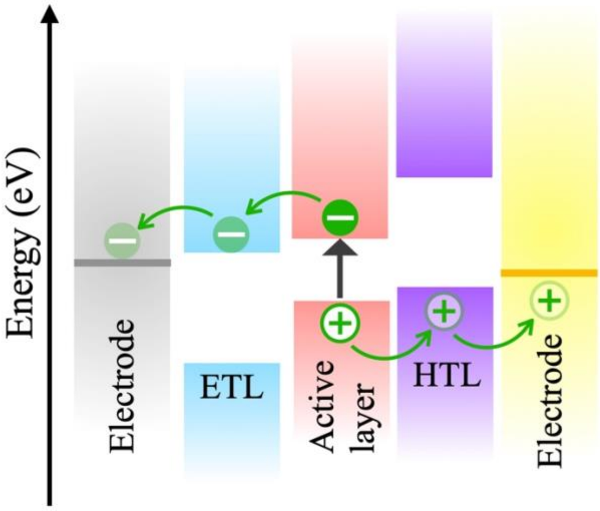

__Figure 1.14__ Schematic representation of energy band diagram of 3^{rd} generation solar cell.

The starting point for these cells was dye-sensitized solar cells, as dyes exhibit high absorption coefficients within the solar spectrum range. The generated charge carriers in the dyes were transferred to other layers, such as TiO_2 (electron transport layer or ETL) and hole transport layers (HTL). Currently, the dye cells exhibit a maximum power conversion efficiency (PCE) efficiency of 12.25%[27].

In recent years, organic – inorganic (hybrid) perovskites have gained tremendous attention as highly efficient absorber materials for next-generation solar cells[30–41]. Perovskite based solar cells have experienced exceptionally rapid advancements in power conversion efficiencies (PCE) in the last few years. Currently, such cells have reached a PCE of 25.7%[27]. They are suitable for large-scale technologies such as low-temperature inkjet printing[42] and roll-to-roll fabrication[43]. Additionally, they can be produced at relatively low environmental impact as compared to traditional semiconductor technologies[44].

A new emerging type of solar cells is based on silicon/perovskite tandems, reaching an efficiency of 29.8%[27].

Another branch of development involves polymer solar cells. In systems employing solar cell technologies with organic materials, the focus is not on the junction effect but rather on the energy gain during charge carrier transport within the cell structure.

Polymer solar cells represent a specific type of third-generation photovoltaic technology characterized by the use of organic polymers as the active layer. In an effort to improve their efficiency, the active layer is mixed with a Hole Transport Layer (HTL) to create what is known as a bulk heterojunction. This design optimizes the interface for charge separation and transport, leading to a significant improvement in the cell's performance. Traditionally, fullerene derivatives have been employed as the HTL due to their excellent electron-accepting properties. However, recent advancements have increasingly replaced them with non-fullerene organic molecules. The shift towards non-fullerene acceptors has shown promise in further enhancing the solar cells, resulting in a significant increase in the power conversion efficiency (PCE) of polymer solar cells from 5.15% in 2010[45], to 18.2% in 2022[46].

Finally, to address the degradation issues in organic materials, third-generation solar cells are also realized using inorganic materials such as quantum dots (e.g., realized in the Polish company ML System).

2 PEROVSKITE MATERIALS AND PEROVSKITE SOLAR CELLS

2.1 Introduction

The term *perovskite* refers to any material with ABX_3 formula that adopts the lattice structure of calcium titanate ($CaTiO_3$). It is a very broad class of materials, and perovskites are among the most abundant minerals on Earth, making up to 38% of the total mass of our planet, as reported by Science Magazine[47]. Cations A and B are typically inorganic in nature, but a significant breakthrough in optoelectronic applications occurred when one of these cations was replaced with an organic counterpart.

The majority of perovskites (ABX_3) used in solar cells consist of an organic component (cation A), such as methylammonium cation ($CH_3NH_3^+$, MA^+)) or formamidinium iodide ($CH(NH_2)_2^+$, FA^+). Furthermore, research on optimizing perovskite solar cells has led to the development of mixed A-site cations, such as the organic-inorganic hybrid $Cs_x(FA)_{1-x}$, which show promise in enhancing the efficiency and stability of the cells[48]. The inorganic component commonly chosen for perovskite solar cells is lead (Pb^{2+}) as the B-site cation, with iodine (I^-) as the X-site anion.

On the other hand, some of perovskites consist of large organic cation groups (LC), such as $C_{10}H_{21}NH_3^+$, $CH_3C_6H_4CH_2NH_3^+$, or a combination of both (SC, LC).

Perovskites that contain both organic and inorganic components are referred to as *hybrid perovskites*.

The classic material often used as a reference in the photovoltaic field is methylammonium lead iodide ($CH_3NH_3PbI_3$, referred to as *MAPI* in this dissertation). The lattice arrangement of this material, representing its cubic structure, is shown in **Figure 2.1**.

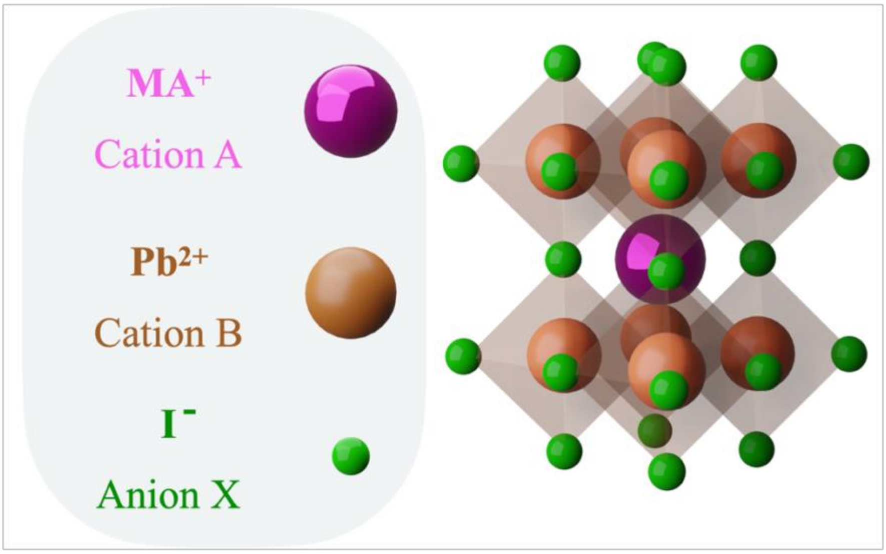

Figure 2.1 *Unit cell of perovskite structure of the* ABX_3 *formula, where A is organic cation* ($CH_3NH_3^+$)*, B is metal cation* (Pb^{2+}) *and X is halide anion (I).*

The perovskites discussed, in contrast to other groups that will be presented in the next chapter, are referred to as 3D perovskites. To determine whether it is possible to form a three-dimensional perovskite from given atoms, the Goldschmidt tolerance factor, t, has been proposed:

$$t = \frac{r_A + r_x}{\sqrt{2}(r_B + r_X)} \qquad \text{Eq. 2.1}$$

where r_A is the radius of A-cation, r_B is the radius of B-cation, and r_X is the radius of X anion.

A tolerance factor (t) value ranging between 0.8 and 1.0 is favorable for the perovskite structure, while larger values (>1) or smaller values (<0.8) usually lead to the formation of non-perovskite structures[49]. The tolerance factors of a few hybrid perovskites are shown in **Figure 2.2**.

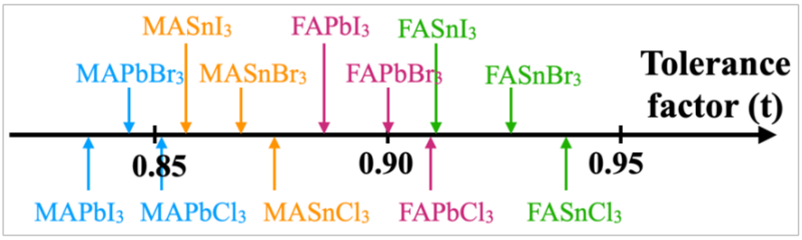

Figure 2.2 *Tolerance factors (t) of a series of halide perovskites. Figure recreated by the Author of this dissertation based on data in Ref.* [50]*.*

2.2 Multidimensional perovskites

Perovskite solar cells (PSCs) based on hybrid 3D halide perovskites (3D PVSKs) suffer from poor long-term stability due to hydrophilic nature of 3D PVSK[51–53]. In particular, they are highly sensitive to temperature and moisture. Therefore, numerous approaches have been used to improve the stability of 3D PVSKs, such as enhancing the perovskite grain sizes, passivating the perovskite surface with hydrophobic groups, and reducing perovskite dimensionality [54–62].

The introduction of 2D perovskites (2D PVSKs) may address, at least partially, the water and temperature sensitivity issues. These materials consist of long-chain organic cations, such as phenylethylammonium cation (PEA^+) or buthylammonium cation (BA^+), which intercalate between the lead halide octahedral slabs in the PVSK structure.

Due to the stronger van der Waals interactions between the organic spacers and the $[PbX_6]^{4-}$ units compared to 3D PVSK, as well as the high hydrophobicity of the organic molecules intercalated into the structure, 2D PVSK exhibit higher stability than their 3D counterparts[60,63,64]. However, the power conversion efficiency (PCE) of 2D PCSs lags far behind that of the state-of-the-art 3D PCSs[65]. Firstly, 2D PVSKs have a narrower absorption window due to their larger bandgaps compared to 3D PVSKs (2.1 eV[66] vs. 1.63eV[67]) resulting from the confinement effect. Secondly, the high exciton binding energy of 2D PVSKs (hundreds of meV as compared to tens of meV for 3D PVSKs[68]) makes the exciton dissociation more difficult. Finally, 2D PVSKs tend to crystallize parallel to the substrate[30], leading to a significant difference in charge mobility for in-plane and out-of-plane transport[66], which adversely affects the performance of planar heterojunction solar cells based on the charge transport perpendicular to the substrate plane.

To overcome the problems associated with 2D PVSKs and simultaneously utilize the advantages of 3D PVSKs, multidimensional perovskite (2D-3D PVSK) materials have recently been developed. These materials exhibit excellent moisture resistance due to the presence of large organic cations, while maintaining optimal physical properties derived from 3D PVSKs, such as narrower bandgap, low exciton binding energy, and optimal out-of-plane charge transfer. The general formula of 2D-3D PVSK is $(RNH_3)_2A_{n-1}B_nX_{3n+1}$ (Ruddlesden-Popper phase), where R represents a long-chain or bulky organic group like *phenylethylammonium* (PEA) or *butylammonium* (BA), A is a small organic cation found in 3D PVSKs (e.g., *methylammonium* – MA^+ or *formamidinium* – FA^+), B corresponds to the B-cation in the 3D PVSKs (i.e., Pb^{2+} and Sn^{2+}), X is a halide anion (I^-, Br^-, Cl^-), and n is the number of inorganic layers. By adjusting the stoichiometry, the average n number and the dimensionality of the material can be tuned from pure 2D (<n> = 1) to pure 3D (<n> = ∞) (**Figure 2.3**).

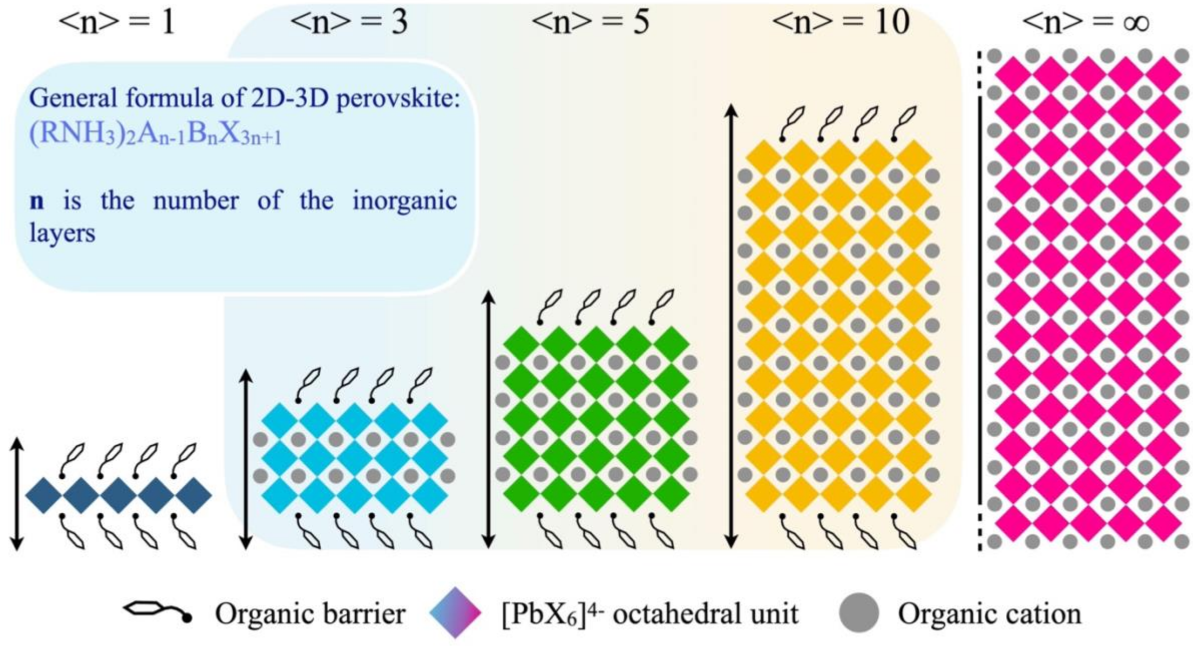

Figure 2.3 *Multidimensional perovskites with different <n> values, showing the evolution of dimensionality from 2D (n = 1) to 3D (n = ∞).*

2.3 Optoelectronic properties

2.3.1 Impact of halide on bandgap and exciton binding energy

Perovskite is a direct-bandgap semiconductor that can be spectrally tuned by modifying the composition of halides. The emission ranges from approximately 400 nm to 800 nm (**Figure 2.4**). While perovskites are primarily used in solar cells where absorption is critical, it is important to consider the Stokes shift, which causes absorption to occur at slightly higher energy than the emission shown in **Figure 2.4**. The greatest overlap between solar spectrum and the perovskite absorption, and thus the highest solar cell efficiency, has been observed for iodine-based perovskites (with small addition of bromine or chlorine)[69,70].

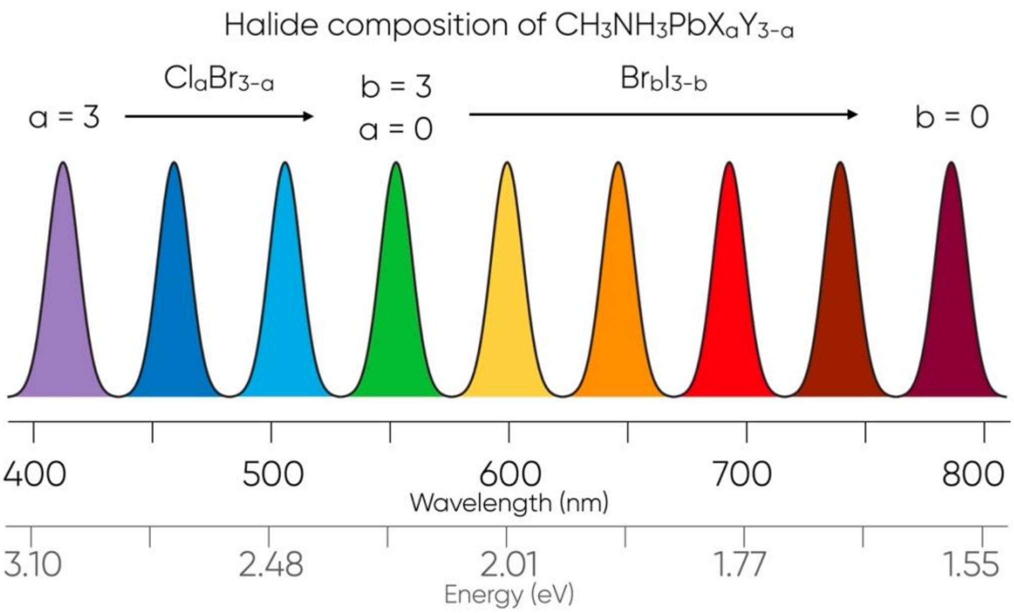

Figure 2.4 *Emission-wavelength tunability of* $CH_3NH_3PbX_aY_{3-a}$. *The emission of the MAPbXnY3−n perovskite is tunable from about 400 to about 800 nm wavelength*[71].

According to the Elliott theory, iodine-based perovskite (MAPI) exhibits the lowest exciton binding energy within the set shown in **Figure 2.5** (with a predicted value of about 25 ± 3 meV). However, experimental findings indicate that the exciton binding energy in MAPI is as low as 6 meV. This discrepancy between theory and experiment has been attributed to screening effects induced by methylammonium cation rotations and limitations of the effective mass approximation[72–75]. Nevertheless, both theoretical and experimental results indicate that the exciton binding energy in MAPI is sufficiently low to enable the formation of free electrons and holes at room temperature.

In the case of mixed halide lead perovskites containing bromine and/or chlorine, the exciton binding energies within these materials are theoretically estimated to be 64 meV for $MAPbBr_3$ and 69 meV for $MAPbCl_3$[76]. However, statistical analysis suggests that even though these values are comparable to or larger than thermal energy, free carriers still dominate over bound excitons.

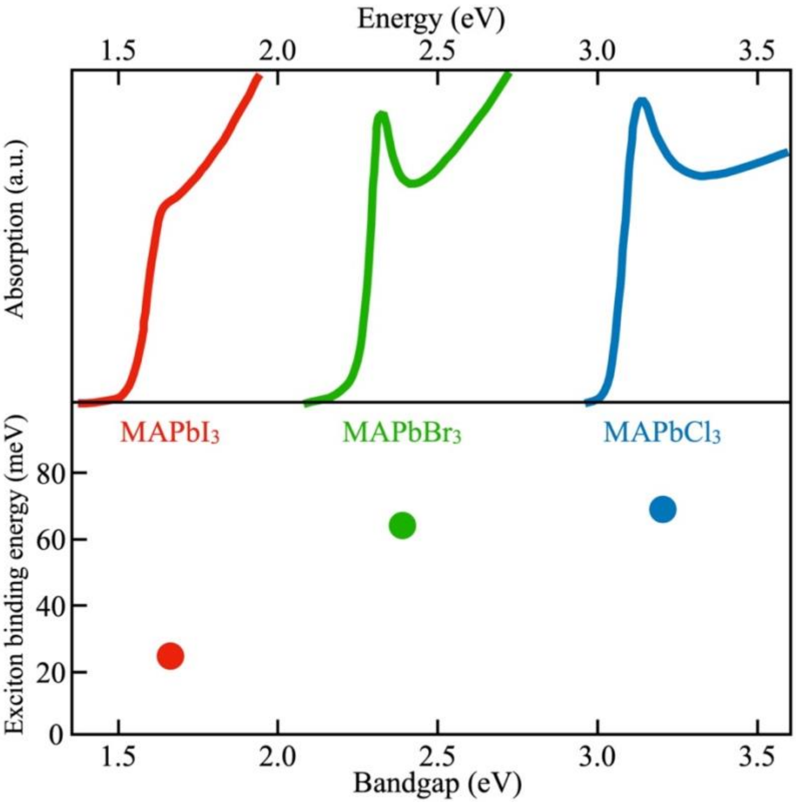

Figure 2.5 *Absorption spectra for lead halide perovskites (top panel); the exciton binding energy extracted from the Elliott formula fit as a function of the energy bandgap of the respective materials (bottom panel). Data derived from Ref.* [76]*, figure recreated by the author of this dissertation.*

2.3.2 Impact of dimensionality on bandgap and exciton binding energy

2D perovskites exhibit significant contrast of dielectric constants between organic spacers and inorganic layers[68]. The arrangement of inorganic sheets and bulky organic interlayers results in an effective multiple quantum well electronic structure[77]. The effective bandgap of this structure is parametrized by the average n value (**Figure 2.6**). However, it should be noted that the concept of an infinite well does not apply here, as the energy scaling in the approximation of an infinite well would be proportional to $1/n^2$. The data presented in **Figure 2.6** were calculated using Density Functional Theory (DFT) for a specific system of finite wells, demonstrating the deviation from the infinite well approximation. In the case of quantum confinement, the inorganic parts act as the potential "wells", while the organic barriers serve as the potential "barriers" (**Figure 2.7**).

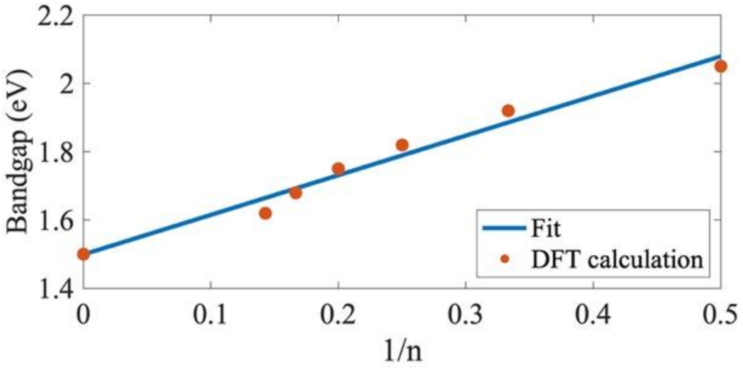

Figure 2.6 *Bandgap vs perovskite dimensionality. Based on data derived from Ref.*[66].

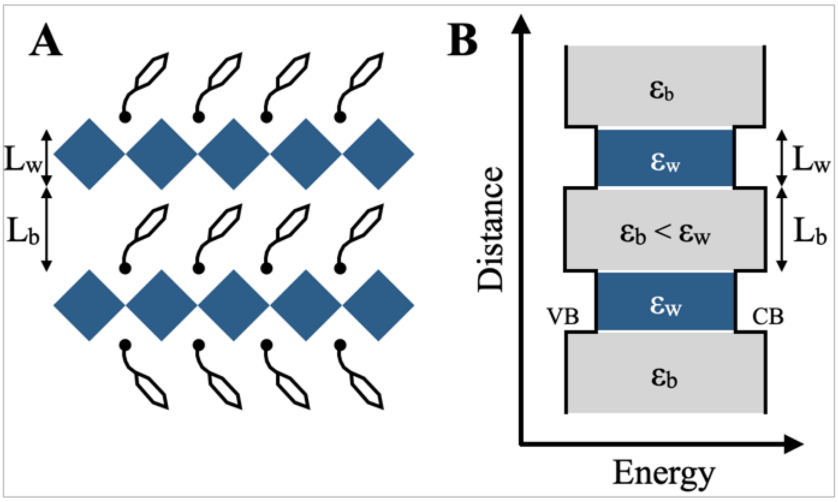

Figure 2.7 *(A) A schematic projection of the 2D-PVSK; lead halide slabs (blue) intercalated with organic barriers (black). (B) Energy diagram corresponding to the 2D-PVSK in (A). Bulky organic layers (grey region) have a dielectric constant* ε_b*, which is smaller than the dielectric constant* ε_w *of the inorganic part (blue region).*

To estimate the high-frequency dielectric constant as a function of dimensionality, a simple model can be applied[78]:

$$\varepsilon_\infty = \frac{\varepsilon_w L_w + \varepsilon_b L_b}{L_w + L_b} \qquad \text{Eq. 2.2}$$

In this equation, $\varepsilon_b = 2.1$, $\varepsilon_w = 6.5$, and a barrier width $L_b = 0.775$ nm were obtained from Ref. [68]. The well width L_w depends on dimensionality, and the values of L_w of PVSK with different n values are presented in **Table 2.1**.

***Table 2.1** Summary of width of the potential "well" (L_w) as a function of dimensionality of $BA_2MA_{n-1}Pb_nI_{3n+1}$ perovskite*[79,80].

n	**L_w (nm)**
2	1.26
3	1.89
4	2.52
5	3.15
50	31.5
∞ (3D PVSK)	315

The calculations in **Figure 2.8** show that ε_∞ increases as n value increases. The results of this simple approximation follow a similar trend as ellipsometric fitting results of ε_∞in Ref. 68

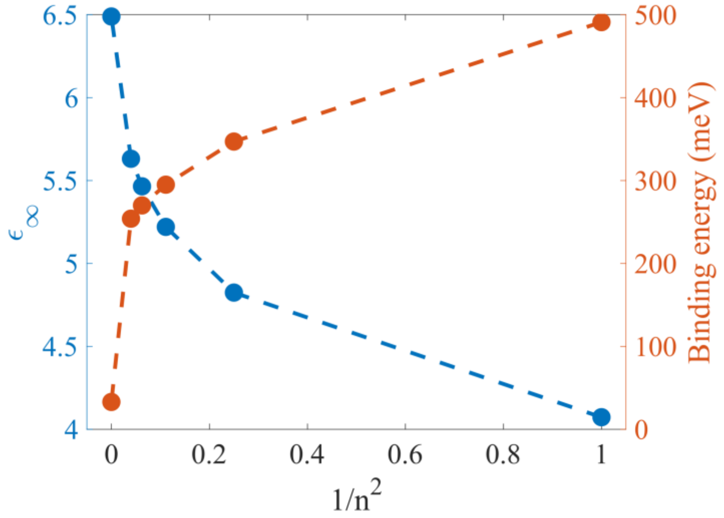

***Figure 2.8** Theoretical predictions of dielectric constant (ε_∞) and exciton binding energy as a function of $1/n^2$. The higher the n value, the higher the ε_∞, and the lower the binding energy*[68].

As a result of the decreasing dielectric constant in low n value perovskites, the exciton binding energy undergoes a significant increases in the case of 2D PVSK (n = 1) or quasi-2D PVSK (those with relatively low n values compared to 3D PVSK), ranging from tens of meV for 3D PVSK to hundreds of meV for 2D PVSK (**Figure 2.8**). However, a high exciton binding energy (relative to kT) is an undesirable material property for solar cell applications because it required additional energy for exciton dissociation into free charge carriers at the interfaces. Moreover, the wide bandgap of 2D PVSK results in a relatively low efficiency of single-junction solar cells based on these materials[65] (also refer to **Figure 1.4**, Schockley- Queisser limit, for E_g wider than 2eV). Therefore, considering both bandgap and exciton binding energy, only perovskites with $n >> 1$ are sutable candidates for the active layer of single-junction solar cells.

2.4 Perovskite solar cells

Perovskite solar cell (PSC) structures can be categorized in two types known as NIP and PIN, as shown in **Figure 2.9**. In both cases, the perovskite layer (absorbing layer) is sandwiched between P-layer and N-layer. The N-layer, also referred to as the *electron transport layer* (ETL), collects electrons generated in the perovskite layer. On the other hand, the P-layer, known as the *hole transport layer* (HTL), collects holes generated in the perovskite layer.

The main difference between the two structures lies in the direction of sunlight illumination. In the NIP structure, sunlight reaches the active layer through the ETL, while in the PIN structure, it comes through the HTL.

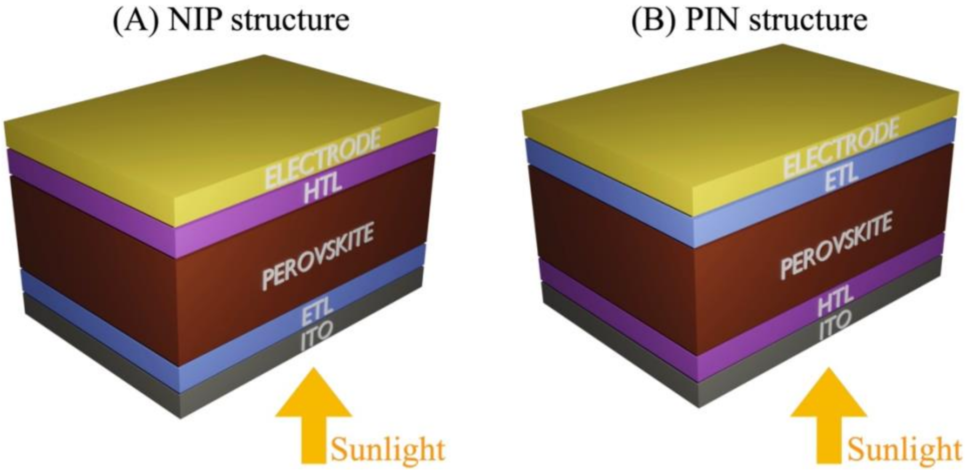

Figure 2.9 *Typical perovskite solar cell structures: (A) regular (NIP), and (B) inverted (PIN).*

Historically, the NIP structure was the first implemented structure in perovskite solar cells. It was originally inspired by the architecture of dye-sensitized solar cells[81], which is why it is also referred to as the *regular* or *standard* architecture. Currently, the highest performing perovskite solar cells are typically based on the NIP architecture[82,83]. Subsequently, inverted (PIN) structures emerged, offering advantages over NIP such as simple processability and low-temperature (100°C) fabrication[84]. Inverted structures have also been successfully integrated into multijunction tandem solar cells[85,86].

In this dissertation, perovskite solar cells based on the NIP structure were fabricated and studied, thus the focus will be on discussing this architecture in detail. The NIP structure commonly incorporates metal oxide ETLs such as mp-TiO_2[87],Zn_2SnO_4[88,89], ZnO[90–92], SnO_2[93], Al_2O_3[94–96], etc. These ELTs, due to the presence of oxygen, possess deep levels in the valance band, effectively blocking the transport of holes. On the other hand, the most extensively studied HTLs include 2,2',7,7'-Tetrakis[N,N-di(4-methoxyphenyl)amino]-9,9'-spirobifluorene (Spiro-OMeTAD)[97–101] and Poly[bis(4-phenyl)(2,4,6-trimethylphenyl)amine (PTAA)[102–104].

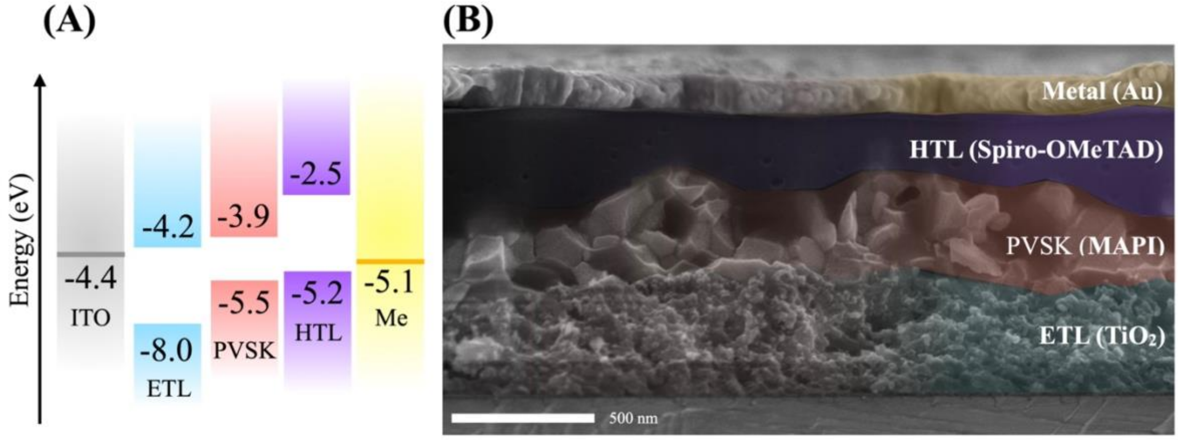

Figure 2.10 *Schematic energy diagram (A), and cross-section through the reference perovskite solar cell, with MAPI active layer, measured using SEM constructed by the author of this thesis (B).*

Figure 2.10 shows the schematic energy diagram of an NIP perovskite solar cell (PSC), along with an example cross-section through a PSC fabricated by the author of this thesis and measured using SEM. In this PhD project, a reference PSC was utilized, which comprised:

- Transparent conductive electrode – ITO,
- ETL – TiO_2,
- Active layer – MAPI ($CH_3NH_3PbI_3$),
- HTL – Spiro-OMeTAD
- Metal electrode – Au

Several strategies to improve both environmental stability and efficiency were applied, and they will be discussed in **Chapter 3.4**.

3 Problems and challenges

3.1 Solidification of perovskites

Perovskite crystallization and morphology are critical factors that influence the performance of perovskite-based solar cells. The use of an antisolvent promotes the fast initiation of perovskite crystallization and improves film morphology, leading to enhanced photovoltaic performance. The halide composition also affects solidification kinetics, thereby playing a significant role in the resulting optoelectronic properties, such as photoluminescence intensity, and the stability of perovskite materials. Mixed-halide perovskites often exhibit superior characteristics compared to their single-halide counterparts. Additionally, the addition of additives to perovskite precursors can effectively modulate the nucleation and growth of perovskite crystals, resulting in improved film quality, grain size, and device performance.

3.1.1 Influence of antisolvent

The influence of antisolvent (fabrication procedure described in **Chapter 4.1.1**) on the morphology and optoelectronic properties of perovskite has been studied in various papers[105–108]. Good antisolvent candidates are characterized by low polarity and dielectric constant, high boiling point, good miscibility with the precursor solvent, and the inability to dissolve any perovskite or related precursor phase[109,110]. Commonly used antisolvents include toluene[111], chlorobenzene[112], diethyl ether[110] and chloroform[113]. The goal of antisolvent is to induce rapid crystallization and promote high nucleation density, leading to uniform grain growth with improved morphology, surface coverage, and larger grains[114]. It has been shown that the lack of antisolvent leads to a needle-like morphology due to the formation of the orthorhombic $(MA)_2(DMF)_2Pb_3I_8$ intermediate phase[105].

The time antisolvent dripping is crucial due to the different boiling points of antisolvents and different rates of their evaporation. For example, toluene, chloroform, and chlorobenzene have boiling points of 111°C[115], 62°C[116], 132°C[117], respectively), time of antisolvent dripping is crucial. Therefore, the technology involving each antisolvent should be optimized individually.

3.1.2 Influence of additives to perovskite precursors

One approach to enhancing the intrinsic properties of perovskites and stabilize solar cell efficiency and electrical parameters is the use of specialized additives in the perovskite composition[118,119]. The literature mentions a wide variety of additives, including acids, salts, polymers, and nanoparticles[120]. These additives generally have similar effects on perovskite morphology, primarily by promoting nucleation and crystallization processes that result in larger perovskite grains. Furthermore, the additive molecules localize at the grain boundaries (GBs), passivating potential trap sites. Some additives, such as polymers, also serve as charge transport materials in interfacial layers, thereby enhancing charge separation and inhibiting the recombination process[121].

The influence of different acids in the crystallization process of perovskites has been intensively studied. According to the literature, the addition of HCl[122] or HBr[123] acids affects the morphology of the perovskite layer. These acids improve the solubility of precursors and reduce the size of colloid particles. Moreover, the evaporation of the solvent from a mixture of PbI_2 and methylammonium iodide (MAI) precursors and the crystallization process is slower when HCl or HBr acids are added, resulting in the formation of larger grains[120]. Additionally, an organic acid with a carboxylic group, such as ascorbic acid (AA), has been tried as an additive during the synthesis of the perovskite. It has been found that AA added to Pb/Sn-binary perovskite modifies the crystallization process, affecting the morphology and inhibiting the aging process of the perovskite. Solar cells with AA exhibit a long photogenerated carriers lifetime, ensuring PCE growth from 12.18 to 14.01%[124]. Su et al. has introduced trimesic acid (TMA) to the precursor solution, which enhanced PCE from 14% to about 17%. The TMA additive plays a meaningful role in the morphological changes, crystalline structure,and stability of the perovskite in air. It has been suggested that the aromatic structure of the additive and hydrogen bonding between the acid and iodine atom from the perovskite suppress ion migration in the active layer[125]. Another kind of additive incorporated into perovskites is organic acids containing sulfonic groups, such as 4-methylbenzenesulfonic acid (4-MSA)[126]. Similarly, they improve crystallinity and morphology, reduce hysteresis by reducing grain boundaries, and increase grain size.

In this work, camphorsulfonic acid (CSA) was added directly to the perovskite for the first time to study its influence on the morphology, crystallinity, and efficiency of resulting solar cells.

Another modification investigated in this thesis is the addition of tetraethoxysilane (TEOS, **Figure 3.1**) to the perovskite precursor solution. It has been shown that the addition of TEOS to the perovskite precursors may improve the material's stability[32]. Liu et al. demonstrated that encapsulation of individual perovskite grains with thin layers of amorphous silica at the nanoscale can separate perovskite from moisture and oxygen.

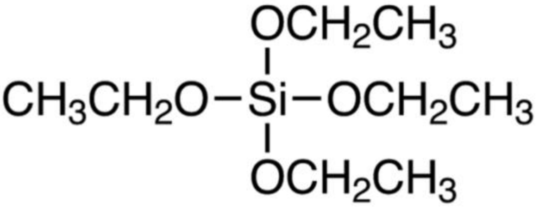

$$CH_3CH_2O-\overset{OCH_2CH_3}{\underset{OCH_2CH_3}{Si}}-OCH_2CH_3$$

Figure 3.1 *Scheme of tetraethoxysilane (TEOS) molecule*[127].

A series of hydrolysis/condensation reactions occur in the solution, converting the TEOS molecules into silica gel via Si-O-Si linkages. The chemical reactions taking place, leading to polymerization of TEOS, are given below[128,129]:

$$Si(OC_2H_5)_4 + 4H_2O \Leftrightarrow Si(OH)_4 + 4C_2H_5OH$$

$$nSi(OC_2H_5)_4 + Si(OH)_4 \ \Leftrightarrow \ (-SiO_2)_n + 4n\ C_2H_5OH$$

$$n\ Si(OH)_4 + n\ Si(OH)_4 \ \Leftrightarrow \ (-SiO_2)_n + 4nH_2O$$

After these reactions, the solution contains silica oligomers and is ready for spin coating. A series of solutions with different concentrations of TEOS (1%, 5%, and 10% v/v) were prepared, and deionized (DI) water was also added to to initiate polymerization of TEOS. In this work, silica was incorporated into the perovskite films, and stability studies were performed.

To sum up, this work investigated two additives to the perovskite solutions: the addition of CSA, which was done for the first time, to boost the efficiency of solar cells, and the implementation of TEOS to increase stability.

3.2 Influence of oxygen

It has been shown that exposure of perovskite films to light and oxygen promotes the formation of superoxide (O_2^-) species[130]. These reactive O_2^- species can deprotonate the organic component, methylammonium cation ($CH_3NH_3^+$), in photo-excited perovskite ($CH_3NH_3PbI_3^*$), resulting in perovskite degradation through the formation of PbI_2, water, methylamine, and iodine[131]. The reaction is as follows:

$$4CH_3NH_3PbI_3^* + O_2^- \rightarrow 4PbI_2 + 2I_2 + 2H_2O + 4CH_3NH_2 \qquad \textit{Eq. 3.1}$$

To investigate the degradation process of perovskites due to oxygen interaction, the energies of superoxide formation from O_2 molecules at various vacancy sites in methylammonium lead iodide structure have been calculated[131] and are presented in **Table 3.1**. The four most energy favorable locations are shown in **Figure 3.2**, and according to the data in **Table 3.1** the highest energy gain occurs when oxygen O_2 substitutes the iodine vacancy.

Table 3.1 *Formation energies of O_2^- species*[131] *at vacancy sites shown in* ***Figure 3.2****.*

Site	**A** face	**B** V_I	**C** V_{Pb}	**D** V_{MA}
O_2^- formation energy (eV)	-1.19	-1.94	+0.29	-0.23

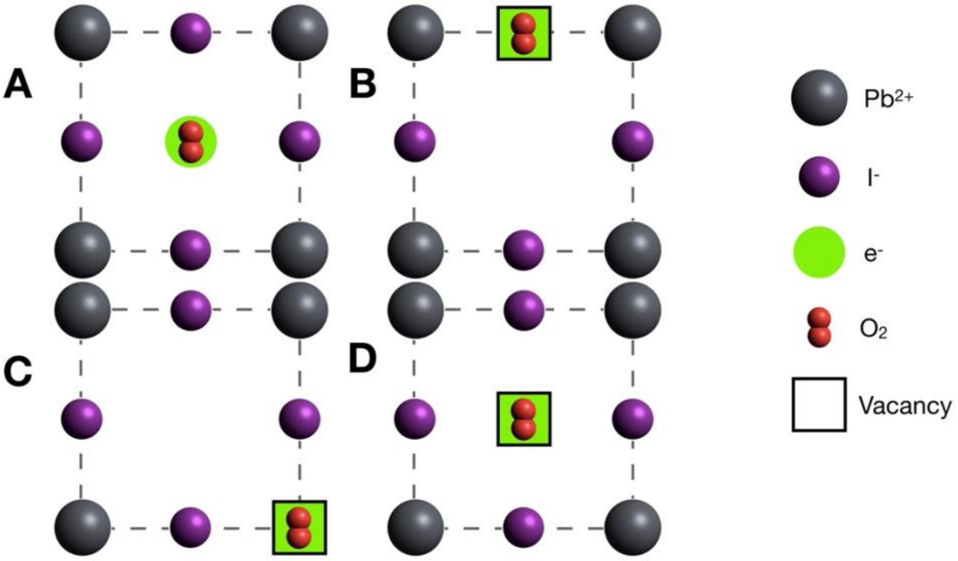

Figure 3.2 *The most energy favorable locations of O_2^- species in the perovskite structure:* ***A****- face,* ***B****- iodine vacancy (V_I),* ***C*** *lead vacancy (V_{Pb}) and* ***D****- methylammonium vacancy (V_{MA}).*

Two main findings have emerged from Ref.[130,131]. Firstly, superoxide formation is energetically favorable due to a direct electron transfer from perovskite to oxygen. Secondly, the formation energies of O_2^- species indicate that vacant iodine sites are the preferred location for the reduction process in the perovskite structure. Therefore, it seems that presence of iodine vacancies is critical for degradation process of perovskites triggered by the oxygen molecules.

3.3 Influence of moisture

The commercial applications and cost-competitive deployment of perovskite-based devices at a large scale require addressing the outstanding problem of low environmental stability of these materials. One of the most urgent challenges to overcome is poor moisture stability. The hydration of the perovskite structure can occur under certain environmental conditions, as concluded by *Leguy et al.*[132]. Their study has shown that such hydration is a two-step process. First, the crystal structure gradually saturates with one water molecule per formula unit (monohydrate phase). The second step leads to the formation of a phase with two water molecules per formula unit, which occurs after prolonged exposure to humidity (dihydrate phase)[132]. These steps can be summarized as follows:

$$1)\ \mathrm{CH_3NH_3PbI_3} + \mathrm{H_2O} \rightleftharpoons \mathrm{CH_3NH_3PbI_3 \cdot H_2O}$$

$$2)\ 4\,[\mathrm{CH_3NH_3PbI_3 \cdot H_2O}] \rightleftharpoons \mathrm{(CH_3NH_3)_4PbI_6 \cdot 2H_2O} + \mathrm{3PbI_2} + \mathrm{2H_2O}$$

The hydration of the perovskite leads to a structural deformation of $[PbI_6]^{4-}$ octahedra, converting the 3D network of $[PbI_6]^{4-}$octahedra into a one-dimensional, isolated $[PbI_3]^-$ double-chain for the monohydrate (**Figure 3.3C**), and zero-dimensional network of isolated $[PbI_6]^{4-}$ octahedra, neutralized by surrounding $CH_3NH_3^+$ cations for dihydrates (**Figure 3.3D**)[133]. Due to crystal rearrangements, each phase (mono- and dihydrate) exhibits specific Bragg peaks[132] (refer to **Figure 3.3**). While the first reaction is fully reversible, the second one promotes the formation of products that starts to decompose over time. Therefore, after prolonged exposure to moisture, hydration becomes an irreversible process that leads to the irreversible decomposition of perovskite[134]. Moreover, the relative humidity (RH) significantly impacts the hydration dynamics. Higher humidity accelerates water intercalation.

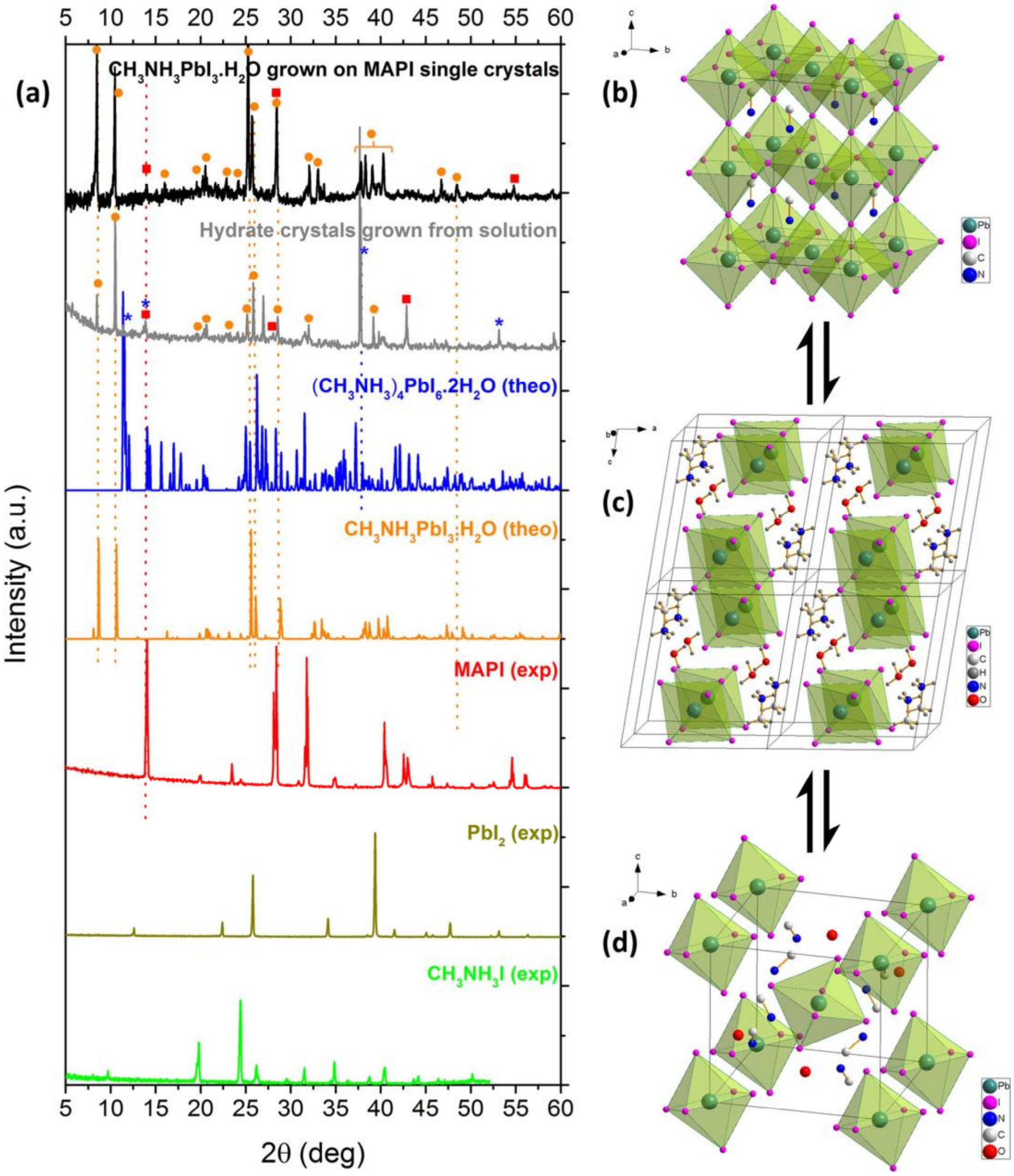

__Figure 3.3__ (a) X-ray diffraction of pristine MAPI (red diffraction) and its hydrated phases (patterns in black and grey), (b) shows the structure of the pristine 3D PVSK (MAPI), while (c) shows the structure of the mono-hydrate phase, and (d) displays the structure of the di-hydrate. The position of the hydrogens on the $CH_3NH_3^+$ *ions and the water is not assigned in (b) and (d)*[132].

3.4 Modifications of perovskite solar cell structure

3.4.1 Electron transport layer

One of the approaches to improve PCE of perovskite solar cells is the incorporation of nanoparticles with plasmonic effects within the device structure[135–139]. In this studies, gold nanoparticles (Au NPs) were chosen due to their high thermal and chemical stability, as well as their localized surface plasmon resonance (LSPR) in the visible-to-near-infrared range[138].

Three approaches of implementing plasmonic nanoparticles within the solar cell structure can be considered. First, metallic nanoparticles act as sub-wavelength light scattering centers, trapping incoming sunlight in the semiconductor layer through wide-angle scattering and effectively lengthening the optical path (an effect known as light trapping or far-field effect), as shown in **Figure 3.4(a)**. Second, metallic nanoparticles can function as subwavelength antennas that couple plasmonic near-field to the active layer, thereby increasing the effective cross-section for absorption of this layer. The near-field induces the generation of electron-hole pairs in the semiconductor, as depicted in **Figure 3.4(b)**. Third, a corrugated metal layer on the back surface of the active layer can facilitate the coupling of light and plasmons, leading to the formation of surface plasmon polaritons at the metal/semiconductor interface. Such a layer can be naturally introduced as a structured metallic contact layer (**Figure 3.4(c)**).

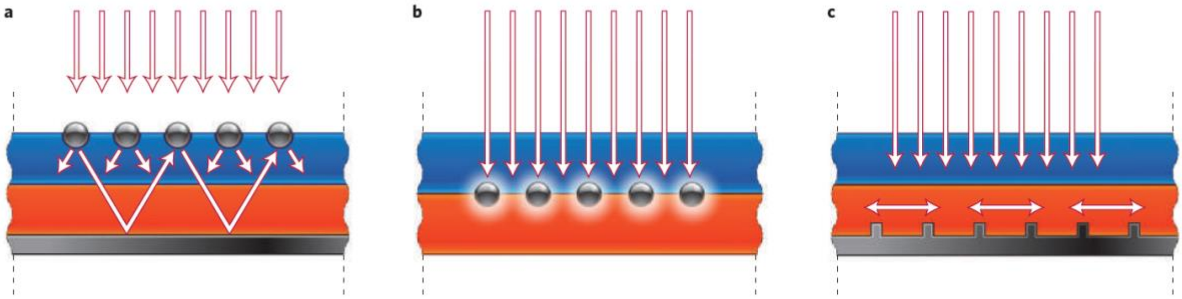

Figure 3.4 *Light trapping in the active layer of a solar cell by the three plasmonic effects described above: (a) light trapping, (b) subwave antennas, (c) surface plasmon-polaritons formation*[140].

In this study, metal nanoparticles were introduced at the interface between ETL and the perovskite layer to enhance the effective cross section for absorption (**Figure 3.5**).

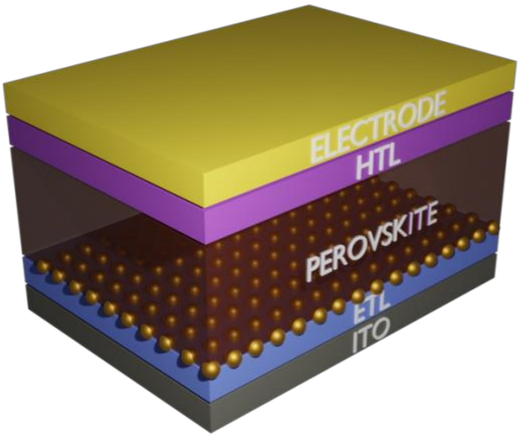

Figure 3.5 Structure of a perovskite solar cell with gold nanoparticles at the interface between ETL and the perovskite layer.

3.4.2 Hole transport layer

The commonly used HTL, Spiro-OMeTAD, has some limitations, such as high cost, which is important for large-scale applications, self-aggregation when deposited as a thin film, hygroscopic properties of Li-salts used for partial oxidation of Spiro-OMeTAD and long-term instability[141–143]. Therefore, there is a need for an alternative p-type semiconductor HTL material. Polyaniline (PANI, **Figure 3.6**) doped with PSS[144–146] or with camphorsulfonic acid (CSA)[147–149] has been reported as very attractive option owing to the high chemical and thermal stability of PANI, ease of synthesis, and solubility of the doped polymer in a wide range of solvents.

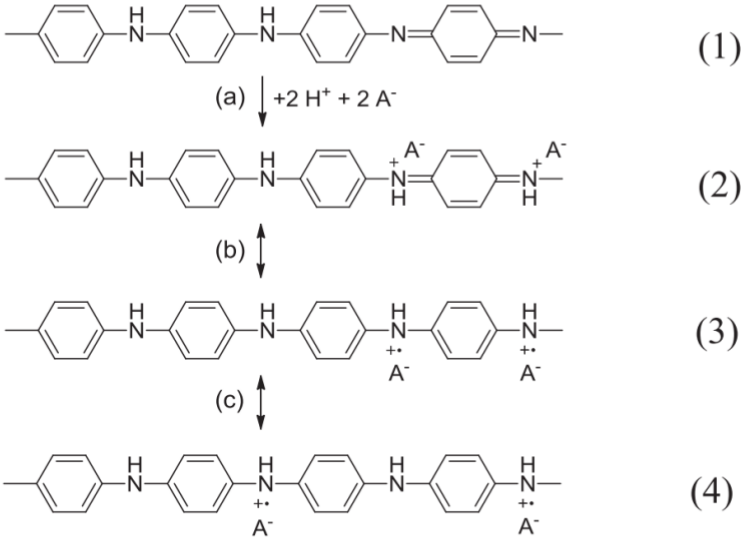

Figure 3.6 Scheme of PANI doping with a strong acid (1) and resonance structures of doped PANI in bipolaron (2) and polaron (3 and 4) forms of PANI[150].

Moreover, PANI may be readily doped over a broad range of dopant concentrations, enabling the tuning the polymer's work function[151].

In this study, polyaniline was chemically synthesized and protonated (doped) with CSA in chloroform, employing different PANI:CSA molar ratios, ranging from 6:1 to 1:4. The synthesis of polyaniline doped with CSA was conducted by our collaborators, and the detailed synthesis procedure can be found in Ref. [150].

4 Methodology

4.1 Chemical synthesis of perovskites and solar cell fabrication

4.1.1 Preparation of perovskite thin films

3D perovskites

The MAI (methylammonium iodine) and PbI_2 (lead (II) iodine) precursors were mixed in DMF/DMSO (4:1 v/v) with 1:1 molar ratio of MAI and PbI_2. The mixture was then spin coated at 1000 rpm for 10 seconds and 4000 rpm for 30 seconds on glass substrates without stopping in between. At 15 seconds before the end of the second step, 100 µl of an antisolvent (such as chlorobenzene) was dripped onto the film, followed by placement on a hotplate at 100°C for 10 minutes to convert the perovskite precursor films into $MAPbI_3$.
In case of studies with camphorsulfonic acid, different concentrations of CSA were added to the perovskite precursor solution.

Additionally, mixed halide perovskites, which involve the addition of either bromine or chlorine to the iodine-based material, were also investigated. The perovskite precursors with iodine and chlorine were purchased from Ossila.

Multidimensional perovskites

As it was discussed in **Chapter 2.2**, the general formula of multidimensional perovskites is $(RNH_3)_2A_{n-1}B_nX_{3n+1}$. In this work, materials with n = 50 were synthesized to enhance environmental stability. This means that for every 50 layers characteristic for 3D perovskite, 1 layer or bulky organic cations occurs. The rational behind this approach was to combine advantages of both 3D and 2D materials, such as bandgap and exciton binding energy of 3D perovskite, along with moisture resistivity of 2D organic spacers. In this study, RNH_3^+ cation used was the phenethylammonium cation (PEA) (see **Figure 4.1**). The precursor for this cation is phenethylamonnium iodide (PEAI).

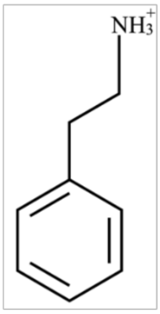

Figure 4.1 Scheme of phenethylammonium cation (PEA).

The n50 perovskites were prepared at the same conditions as the 3D materials, including spin-coating parameters, temperature and time of annealing. Due to the relatively high value of *n* in n50 perovskites, they will be also referred to as *quasi-3D perovskites* in this dissertation. **Table 4.1** summarizes chemical composition of the fabricated perovskites.

Table 4.1 Perovskites investigated in this project, MA stands for methylammonium, whereas PEA for phenethylammonium.

Short name	MAPI	MAPIB	MAPIC	N50I	N50IB
Chemical formula	$MAPbI_3$	$MAPb(I_{0.85}Br_{0.15})_3$	$MAPbI_{3-x}Cl_x$	$PEA_2MA_{49}Pb_{50}I_{151}$	$PEA_2MA_{49}Pb_{50}(I_{0.85}Br_{0.15})_{151}$
MAI (mg)	131.8	110.1	314.8	127.8	107
MABr (mg)	N/A	15.3	N/A	N/A	15
PEAI (mg)	N/A	N/A	N/A	8.2	8.2
PbI_2 (mg)	382.1	324.8	N/A	378.0	321.3
$PbBr_2$ (mg)	N/A	45.6	N/A	N/A	45.1
$PbCl_2$ (mg)	N/A	N/A	183.5	N/A	N/A

N/A – not applicable.

4.1.2 Preparation of solar cells

- **Cleaning of ITO substrates**

  The ITO-coated glass was first immersed dipped in DI water containing a Hellmanex soap and sonicated for 10 min. Then, the glass slides were sonicated for 10 min in DI water and isopropyl alcohol. After that, the glass slides were dried in filtered compressed nitrogen. Finally, the ITO-coated glass slides were exposed to UV radiation and ozone for 15 minutes prior to the deposition of TiO_2 layer.

- **ETL deposition**

  The TiO2 layer was deposited by spin-coating a 0.15 M TAA solution dispersed in anhydrous 1-butanol. It was then annealed on a hotplate at 120°C for 5 minutes to remove the remaining solvent. In the next step, mesoporous TiO2 was spin-coated and annealed at 120°C again to remove the remaining solvent. Finally, the substrates were annealed for 60 minutes at 450℃ in a furnace to crystallize the deposited amorphous TiO2.

- **Preparation of perovskite layer**

  After the TiO_2 preparation, the substrates were transferred into a glovebox with an argon atmosphere. Perovskite layers were deposited using the same thin film procedure presented in **Chapter 4.1.1**.

- **HTL deposition**

  The Spiro-OMeTAD solution was prepared by dissolving 85 mg of spiro-OMeTAD in 1 ml of chlorobenzene, along with 28.8 µl 4-tert- butyl-pyridine, a 20 µl portion of a stock solution of 500 mg/ml lithium bis(trifluoromethylsulfonyl) imide in anhydrous acetonitrile, and a 11 µl of cobalt dopant FK209 TFSI salt with concentration of 300 mg/ml in anhydrous acetonitrile. These solutions were spin-coated on the perovskite film. Alternatively, polyaniline doped with different amount of camphorsulfonic acid was used as the HTL. PANI:CSA molar ratio was varied from 6:1 to 1:6, and four independent series of the cells were prepared for each doping level.

  For each HTL layer, 50 µl of the respective solution was deposited on the perovskite layer by spin-coating at 2000 rpm for 30 seconds.

- **Metal electrode evaporation**

  Finally, an 80 nm thick Au electrode was deposited via thermal evaporation. This step was carried out with the support of prof. dr hab. Krzysztof P. Korona.

4.2 Atomic Layer Deposition

Atomic Layer Deposition (ALD) is a gas-phase chemical process utilized for thin-film deposition. Most of ALD systems employ two precursor chemicals, which react with the material surface individually, during the growth process. The deposition cycle consists of the following steps:

- Pulse of the first precursor,
- Purging the chamber with inert gas (N_2),
- Pulse of the second precursor,
- Purging the chamber with inert gas (N_2).

The cycle is repeated N times until the desired thickness is achieved. The purpose of the purging step is to eliminate unreacted residual precursor and possible by-products. A scheme of the single cycle is shown in **Figure 4.2**.

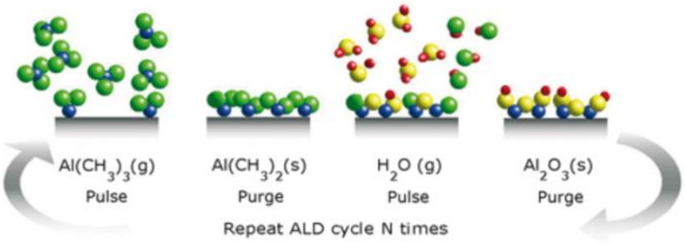

Figure 4.2 *Scheme of the ALD deposition cycle*[152].

Properties of Atomic Layer Deposition:

- Chemisorption of precursors with a substrate provides great adhesion,
- Sequential growth results in a great thickness accuracy,
- Growth during a cycle is precise and repeatable, thickness of a layer in a single cycle is about 0.1 nm,
- Operation at relatively low temperatures (typically starting from 25°C[153]) which proves advantageous when working with soft substrates,
- Capability to coat not only flat substrates but also complex shapes.

The Beneq TFS200 system (**Figure 4.3**) was employed in this studies to deposit thin films of Al_2O_3. These films were used to encapsulate perovskite films and perovskite solar cells, enhancing their environmental stability.

Figure 4.3 *Beneq TSF200, ALD system at the Faculty of Physics, University of Warsaw.*

<u>Parameters of Al_2O_3 growth for encapsulation of perovskites:</u>

- Temperature: 65 °C
- Number of cycles: 300
- Aluminum precursor: Trimethylaluminium (TMA)
- Oxygen precursor: deionized water
- TMA pulse duration: 200 ms
- H_2O pulse duration: 200 ms
- Purge time between pulses: 5s
- Final Al_2O_3 thickness: $d = 90$ nm

Al_2O_3 coatings of perovskite films were done by dr Rafał Pietruszka, Institute of Physics PAS, and perovskite solar cells were encapsulated by mgr Maciej Krajewski, Faculty of Physics UW.

4.3 X-Ray Diffraction

X-ray diffraction measurements were carried out using X'Pert Philips diffractometer with Cu Kα as a source of radiation. X-Ray Diffraction (XRD) is a technique which provides information about the atomic and molecular structure of a crystal. Atoms forming a crystalline structure diffract a beam of incident X-rays into specific directions. The detected angles and intensities of these diffracted beams are fingerprints for a particular crystal. The interaction of the incident beam with the sample leads to constructive interference and the formation of diffracted beams, as governed by Bragg's law:

$$2d\sin\theta = n\lambda \qquad \textit{Eq. 4.1}$$

Here, n is a positive integer, λ is the wavelength of the incident wave, and d is the interplanar distance. Bragg's law establishes a relationship between the wavelength of electromagnetic radiation, the diffraction angle, and the lattice spacing in a crystalline sample. The diffracted X-ray photons are detected and counted. By scanning the sample across a range of angles, the data from all possible crystallographic directions of the lattice can be collected due to the polycrystalline character of perovskite layers. However, in partially ordered polycrystalline materials, certain diffraction peaks may exhibit enhancements, while others may disappear. This aspect will be further discussed in the subsequent text.

A measured specimen can be identified by comparing the obtained diffraction pattern with a reference spectrum, such as those contained in the Powder Diffraction File. XRD measurements also provide information about grain sizes, which are related to a full width at half maximum (FWHM) of specific diffraction peaks and their position. This relationship follows the Scherrer equation:

$$\tau = \frac{K\lambda}{\beta\cos\theta} \qquad \textit{Eq. 4.2}$$

Where:

- τ is the mean size of the crystalline domains,
- K is a dimensionless shape factor, with a value close to unity,
- λ is the X-ray wavelength,
- β is the line broadening at half the maximum intensity (FWHM),
- θ is the Bragg angle.

XRD measurements, including hydration and long-term stability studies, were conducted at the University of Louisville by the author of this thesis under the supervision of Dr. Jacek Jasinski. Initial material characterization was performed at the Faculty of Physics, UW, by Dr. Mateusz Tokarczyk.

4.4 Electron Microscopy

Electron microscopy is a crucial technique for studying and analyzing the surface areas of nanostructured materials (SEM), as well as thin samples obtained from solid materials (TEM, STEM). The optics in electron microscopy are similar to those in optical microscopy, with the main distinction being the much shorter wavelength of accelerated electrons compared to visible light or UV photons, and the utilization of electromagnetic or electrostatic lenses. This shorter wavelength enables electron microscopy to achieve much higher resolution. Additionally, electrons exhibit stronger interaction with matter compared to photons, necessitating the use of vacuum environment of at least 10^{-4} Pa in electron microscope[154]. Due to their charge, electrons can be focused by magnetic or electric fields, making it easier to control the electron beam in scanning mode in electron microscopes.

4.4.1 Scanning Electron Microscopy

In Scanning Electron Microscopy (SEM), a focused beam of accelerated electrons (typically 1-30 keV) is directed onto the surface of a sample, interacting with it and resulting in the emission of secondary electrons (SEs) across a broad energy spectrum. These secondary electrons are primarily ejected from the K shell of the specimen atoms. The SEs are collected by the Everhart-Thornley detector, and the signal is converted and displayed as a digital image[14]. The signal reflects the topography of the measured sample, offering topography contrast. SEM allows for a wide range of magnifications (about 6 orders of magnitude), from approximately 10 to 500,000 times.

Another type of electrons used for imaging in SEM is backscattered electrons (BSEs), which possess high energy[155] and low density compared to secondary electrons. Backscattered electrons are primary electrons (beam electrons) that undergo elastically scattering from the sample. The backscattering coefficient strongly depends on the atomic number Z of the investigated material. Sample regions containing elements with higher atomic numbers backscatter more electrons, appearing as brighter spots in BSE images. BSE images provide important information about variations in the composition of the sample, offering chemical contrast.

4.4.2 Transmission Electron Microscopy

A transmission electron microscope (TEM) is a tool used to visualize the internal microstructure of very thin samples. The acceleration voltage in TEM is typically much higher than in SEM, typically 100-400 kV, although specialized high voltage devices operating at 1MV or higher exist[156]. The advantage of high voltage is the increased image resolution (up to atomic resolution), thanks to the shorter wavelength of electrons and the increased penetration depth.

4.4.3 Energy-dispersive X-Ray Spectroscopy

Energy-dispersive X-ray Spectroscopy (EDS or EDX) allows for identification of elements within a sample. To induce the emission of characteristic X-rays from a specimen, a high-energy beam of charged particles (such as electrons or protons) or X-rays is focused onto the sample. In this work, EDS was employed as part of Scanning or Transmission Electron Microscopes, inducing the emission of characteristic X-rays using accelerated electrons. If a reference material is available, the method can be used for quantitative elemental analysis. When as sample is at rest, all atoms within it possess ground state electrons. The incident beam can excite an electron from its initial state (in an inner shell), causing it to be ejected from the shell. This process creates an electron-hole pair, with the hole subsequently being filled by an electron from an outer, higher-energy shell. The energy difference between the higher-energy shell and the lower energy shell is released as an X-ray. The energy of the emitted X-rays is characteristic for each element and can be measured by an energy-dispersive spectrometer, providing information about the elemental composition of the specimen. Additionally, this technique enables the mapping of the chemical composition of a sample.

SEM studies were performed at the University of Louisville by the author of this thesis. TEM measurements were done by both the author and Dr. Jacek Jasiński.

4.5 X-Ray Photoelectron Spectroscopy

X-Ray photoelectron spectroscopy (XPS) is a technique used to analyze the surface chemistry of materials. The information obtained from XPS relates to the top 2-5 nm layer of a sample. In XPS, a surface is irradiated with X-rays (commonly Al Kα or Mg Kα line) in an ultra-high vacuum (UHV). When an X-ray photon hits the sample, it transfers its energy to a core-level electron of a specific atom, causing the electron to be ejected from its initial state with a kinetic energy E_k dependent on the incident X-ray energy and the binding energy of the atomic orbital from which it originates (**Figure 4.4**).

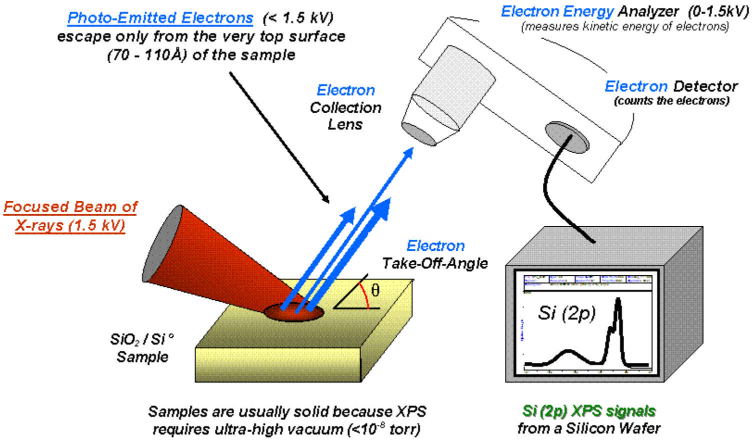

Figure 4.4 *Operating principle of XPS*[157].

The detector measures the kinetic energy E_k of the emitted photoelectrons which corresponds to their binding energy (E_B) in the solid according to Eq. 4.3:

$$E_B = h\upsilon - E_K - \phi \qquad \text{Eq. 4.3}$$

where ϕ is the material work function and $h\upsilon$ is the energy of the incident X-ray photons.

One advantage of XPS is its ability to provide information not only about the presence of elements but also their amounts within the sample.

XPS analysis chambers operate under ultra-high vacuum (UHV) conditions to minimize adsorbed gas on the sample surface and to prevent disturbance of ejected electrons on their way to the detector. And as a result, a broad spectrum of peaks from 0 to more than 1 keV can be collected. The presence of Auger electrons must also be considered. Fortunately, in the case of perovskites, there is no overlap between perovskite peaks and a Auger peaks. To determine which peaks (and hence, electrons) are important for further analysis, the X-ray source can be changed (to a source producing X-rays of a different energy), leading to a shift of the background signal while the material peaks remain at the same positions.

When collecting the XPS spectrum, it is possible that peaks may be shifted from their expected binding energy positions. This phenomenon occurs due to a positive charge build-up at the surface of non-conducting (or poorly conducting) samples. In such cases, the rate of photoelectron loss at the surface exceeds the rate of their replacement within the sample, resulting in a retarding field at the surface that lowers the kinetic energy of ejected electrons and shifts the measured peaks. The issue can be addressed by using a known peak as a reference. The carbon C1s peak is often used for calibration, as all samples contain carbon to some extent. Setting this peak to 285.0 eV provides the binding energy calibration for all peaks originating from other elements.

A survey scan is carried out in a broad energy range to assess the elements present, followed by more high-resolution scans within energy areas of interest.

XPS measurements enable the determination of the chemical composition in a particular sample. The amount of each element can be calculated using the following formula (Eq. 4.4):

$$X_i[\%] = \frac{\frac{1}{ASF_i} I_i}{\sum_{i=1}^{N} \frac{1}{ASF_i} I_i} * 100 \qquad \textit{Eq. 4.4}$$

where $X_i[\%]$ is the atomic percentage of a particular i-element within a sample, I_i is an integrated area of a specific energy region corresponding to the element, ASF_i is atomic sensitivity factor, specific for each element, and N is the number of all the elements within the sample[158].

XPS experiments were performer at the University of Louisville by the author of this thesis under a supervision of Dr. Jacek Jasiński.

4.6 In-situ photoluminescence and climate chamber

In-situ photoluminescence (PL) experiments are particularly powerful for because PL evolution allows to investigate the nucleation and growth of perovskites, and provides information on the nanoscale nucleation and further nuclei densification within seconds. In situ PL measurements were acquired using a home-built confocal setup in the Molecular Foundry at Lawrence Berkeley National Laboratory. The setup includes a 532 nm laser diode, a plano-convex lens above the substrate, a 550 nm long-pass filter, and a fiber coupled Ocean Optics spectrometer (Flame). During the measurements, a maximum laser power density of 30 mW cm^{-2} was used. In-situ PL spectra were collected every 200 ms within a range of 1.2 eV to 2.5 eV. In-situ PL was utilized for investigating of crystallization processes during film annealing and reversible hydration studies.

For investigating hydration processes within perovskites, the author of this dissertation built a climate chamber (**Figure 4.5**). The chamber is controlled by Arduino MEGA 2560 Rev 3 microcontroller and employs a DHT11 digital sensor to measure temperature and humidity. The chamber displays key parameters (temperature, humidity) on displays and saves data to a micro-SD card. Additionally, the chamber is equipped with a water reservoir, an ultrasonic piezo component, and a feedback loop that stabilizes the humidity inside the box to the value set by the user. The box was 3D printed, and the entire chamber was entirely built by the author, including the Arduino script controlling the chamber, the conceptualization of electrical circuits and connections, and the 3D printed project.

Figure 4.5 *Climate chamber with controlled humidity for studies of perovskite hydration dynamics. The chamber dimensions: 20cm x 15cm x 30cm.*

The *in-situ* PL experiments were performed at Lawrence Berkeley National Laboratory by the author of this thesis.

4.7 Current-voltage (IV) characteristics

Current-voltage characteristics were measured by means of Keithley 2450 Source Meter with Kickstart PC software, and using Ossila 8-pixel test board. A Newport VeraSol-2 LED Class AAA Solar Simulator, providing 1000 W/m^2 power output and an AM1.5G spectrum, was used as the source of illumination.

A current–voltage characteristic, or I–V curve, describes the relationship between the applied voltage and the corresponding current through a solar cell. To faciliate cell comparison, it is convenient to present the current density instead of the current vs voltage characteristics, where the electric current is divided by the area of a solar cell.

Performing this type of measurement allows for extraction of main parameters characteristic for a solar cell, such as J_{sc},V_{oc}, fill factor, and power conversion efficiency (η), which were discussed in **Chapter 1.4.1**.

Typically, applied voltages for perovskite solar cells range from -0.2 to 1.2 V, and corresponding current densities reach about $25\mathrm{mA/cm^2}$.

IV characteristics were collected at the Faculty of Physics UW by the author of this thesis. Moreover, the author wrote a MATLAB code to analyze the performance of perovskite solar cells.

4.8 Summary of the Author's input in technology and techniques used in the thesis

In this thesis, the author employed a comprehensive approach to study perovskite materials and their application in solar cells. The author developed and synthesized his own perovskite materials, prepared perovskite thin films, and fabricated solar cells based on these materials. A wide range of techniques and methodologies were utilized, including atomic layer deposition, X-ray diffraction, electron microscopy (scanning and transmission electron microscopy), and energy-dispersive X-ray spectroscopy for the characterization of perovskite materials. Furthermore, the author employed X-ray photoelectron spectroscopy and *in-situ* photoluminescence to investigate the materials' properties.

To analyze the performance of the solar cells, the author developed a custom MATLAB code that was applied to the current-voltage (IV) characteristics data. Additionally, the author constructed a climate chamber for conducting degradation studies, providing valuable insights into the long-term stability and performance of perovskite-based solar cells.

5 Studies of perovskites morphology and crystal structure

5.1 Dynamics of antisolvent processed perovskite

The impact of chlorobenzene antisolvent on the perovskite morphology is shown in **Figure 5.1**. Firstly, lack of chlorobenzene (**Figure 5.1(a)**) leads to a needle-like morphology. Similar structures have been observed in the literature, which has been explained as the formation of the orthorhombic $(MA)_2(DMF)_2Pb_3I_8$ intermediate phase[105]. Therefore, it was concluded that a similar process took place in the studies presented in this thesis. Secondly, when antisolvent is dripped too early, the nucleation density is relatively poor, resulting in bigger grains but the film contains pinholes (**Figure 5.1(b)**). Thirdly, if chlorobenzene is dripped at an optimum time which is 15s before the end of the second spin-coating step in this study (perovskite synthesis described in **Chapter 4.1.1**), it leads to the formation of a compact, pinhole-free film.

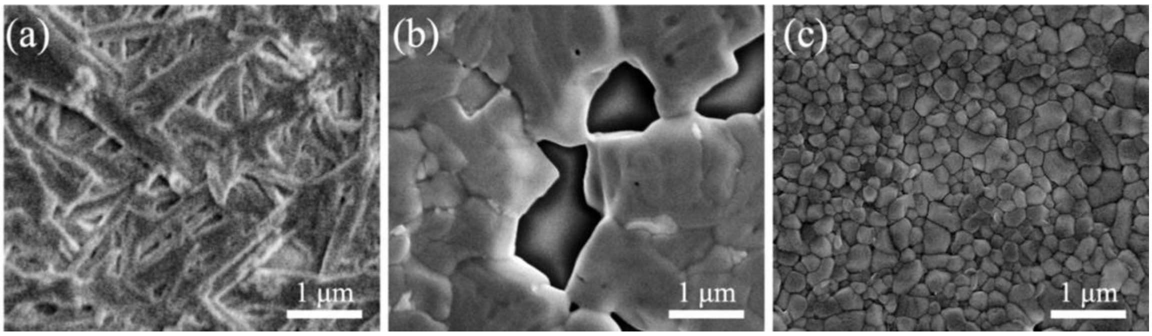

Figure 5.1 *SEM images of $MAPbI_3$ films: (a) without antisolvent, (b) antisolvent dripped too early, (c) proper antisolvent dripping time.*

Additionally, two other antisolvents, toluene and chloroform, were used to find an ideal candidate for further studies. Together with chlorobenzene (CB) mentioned above, **Figure 5.2** shows the resulting morphology. The antisolvent dripping time was the same for all the chemicals, based on the optimum time previously established for chlorobenzene (15s before the end of the second spin-coating step). It was found that for both toluene and chloroform (**Figure 5.2(b)** and **(c)**, respectively) the perovskite films contained pinholes, similar to films with CB dripped too early. As indicated in **Chapter 3.1.1**, the boiling points of these antisolvents are lower than that of CB, which may indicate their faster evaporation.

Therefore, if, for any reasons, an antisolvent other than CB needs to be used, the optimum dripping time must be established individually. However, since the addition of CB led to good quality films in this investigation, all further studies were conducted using this chemical.

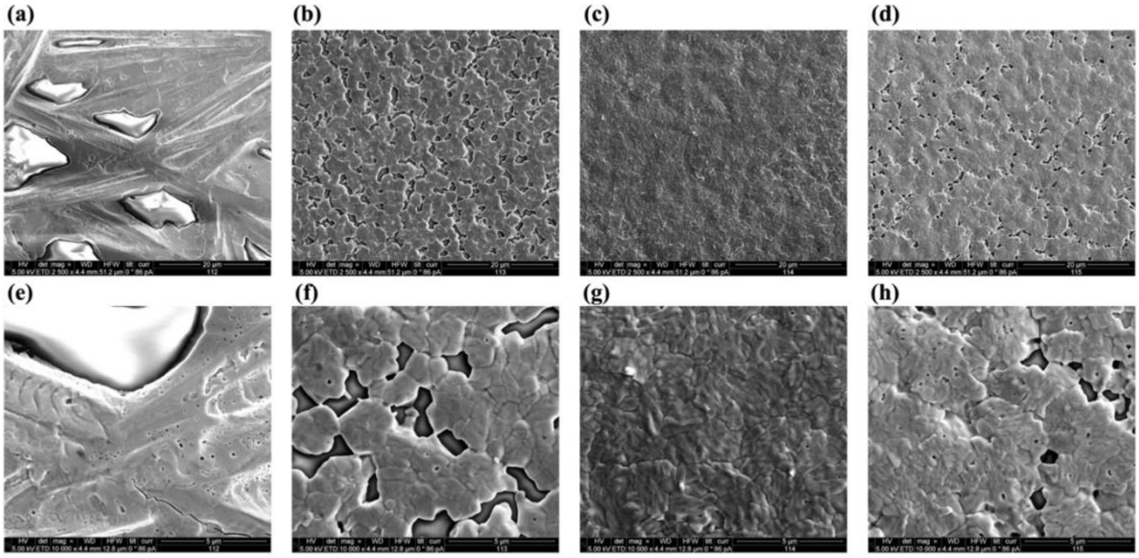

Figure 5.2 *SEM images of $MAPbI_3$ with different antisolvents: (a) without antisolvent, (b) toluene, (c) chlorobenzene, (d) chloroform. (e-h) magnified regions of images from above. Time of antisolvent dripping was optimized for CB only.*

To conclude, it was found that the lack of antisolvent leads to crystallization of needle-like perovskite structures. Secondly, the CB dripping time was optimized to be 15s before the end of the second spin-coating step. Finally, the choice of antisolvent has a significant impact on the film morphology, and fabrication parameters need to be optimized separately for different chemicals. Due to lower boiling points of toluene and chloroform compared to chlorobenzene, it is recommended to drip them slightly later than CB.

5.2 Halide composition

In this chapter, the impact of bromine addition to the typical perovskite formulation, MAPI, was studied (chemical compositions were previously summarized in **Table 4.1**). In short, MAPI contains only iodine, whereas MAPIB has 15% of bromine and 75% of iodine according to the stoichiometry of the prepared precursor mixture.

5.2.1 Influence on the morphology

SEM images of perovskites with and without the addition of bromine are shown in **Figure 5.3**. First of all, a significant difference in grain sizes between MAPI shown in

Figure 5.1(c) and MAPIB shown in **Figure 5.3(a)** can be noticed. The exact mechanism behind this phenomenon is difficult to explain. Over the years of these studies, perovskite precursors, mainly PbI_2, were purchased from various suppliers. Due to supply chain issues, especially during the COVID-19 pandemic, it was sometimes impossible to obtain the exact same materials. They differed in terms of purity and also the form of the chemical (powder vs granules). Therefore, no direct comparisons between perovskites based on precursors from different suppliers will be made in this dissertation.

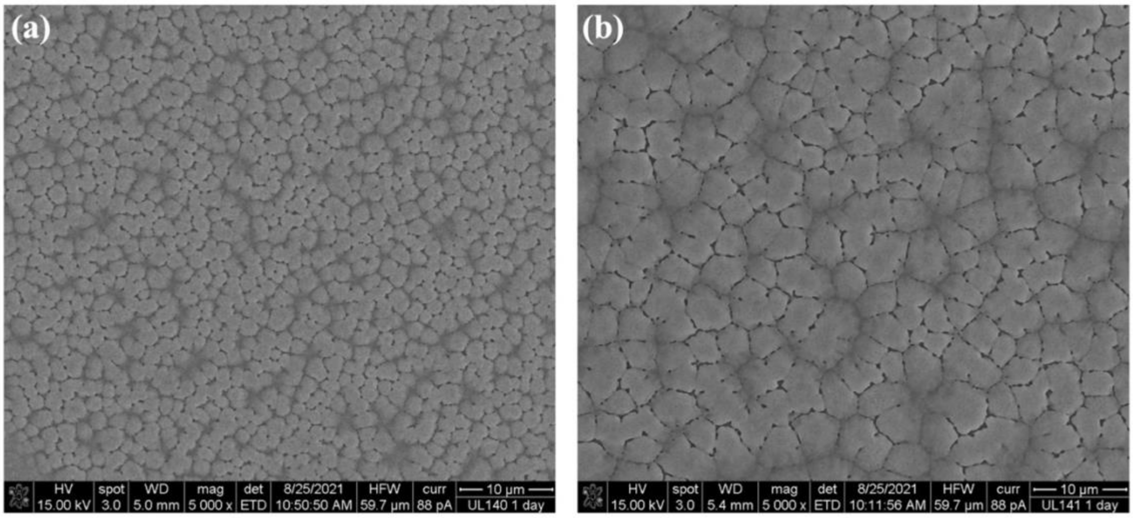

Figure 5.3 *SEM images of: (a) MAPI, and (b) MAPIB.*

It can be observed that mixed-halide perovskite films reveal larger grains compared to iodine-based species (MAPI (a) vs MAPIB (b) in **Figure 5.3**). To quantitatively analyze the average grain size, a Fast Fourier Transform (FFT) of the SEM images was performed, as shown in **Figure 5.4**. The FFT technique in image processing is a useful approach to determine the crystal structure in reciprocal space, similar to its use in High-Resolution Transmission Electron Microscope (HRTEM). The technique has been described in detail by Jin-Gyu et al.[159]. In this study, FFT was applied to extract the average grain sizes of fabricated perovskite films based on the SEM images, as traditional granulometry failed due to weak contrast between grains and their boundaries.

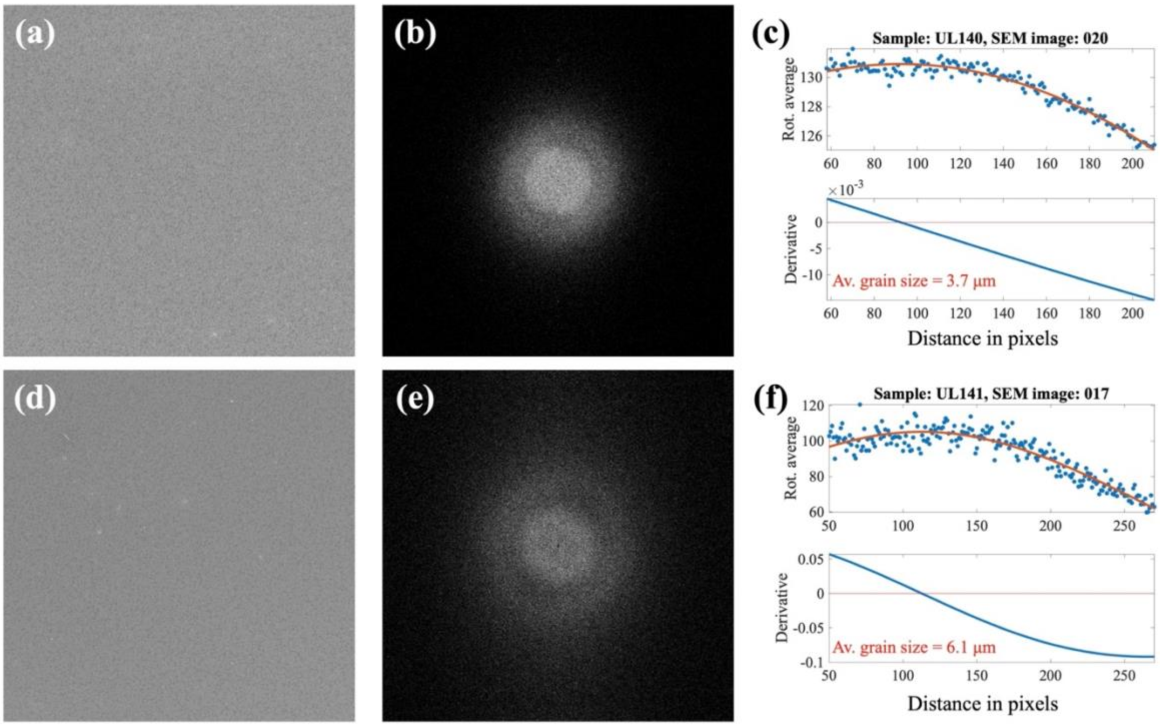

***Figure 5.4** SEM images of MAPI (a), MAPIB (d), FFT of MAPI (b), FFT of MAPIB (e), FFT analysis of MAPI image (c), FFT analysis of MAPIB image (f).*

Figure 5.4(a,d) shows SEM images at very low magnification (1000x for MAPI and 500x for MAPIB). Then, FFT was performed on these images (**Figure 5.4(b,e)**). Finally, **Figure 5.4(c,f)** shows cross-sections through generated images in reciprocal space **(b,e)**. The average size of MAPI grains was found to be 3.7 μm, while average MAPIB grains measured 6.1 μm. An explanation for such a significant grain size differences has been shown by Huang et al.[160]. They used Density Functional Theory to calculate the interaction energies of PbX_2 (X denote either I or Br) species with DMSO (one of the perovskite precursor solvents). Huang et al. found that DMSO forms stronger bonds with PbI_2 (0.84 eV) than with $PbBr_2$ (0.77eV), indicating that Br-rich species have lower solubility and are therefore thermodynamically more favored to form and potentially nucleate before iodide-containing species. If nucleation starts earlier for Br-containing species, it allows them more time to grow, leading to the formation of larger grains within the film. Further discussion of these results requires supplementary *in-situ* photolumienscence experiments. Therefore, it will be continued in **Chapter 6.2**.

5.2.2 Influence on the crystal structure

XRD patterns of fresh samples are presented in **Figure 5.5**.

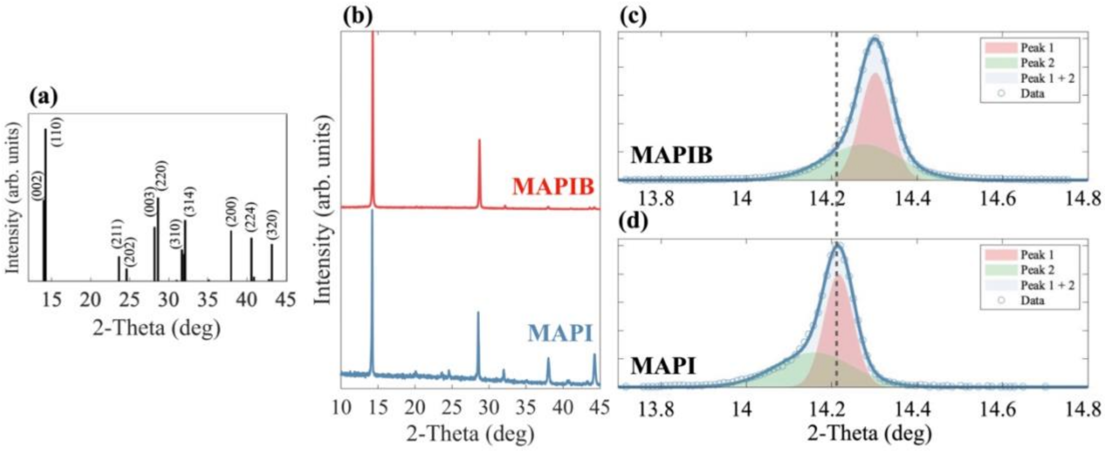

Figure 5.5 *XRD patterns of studied samples: (a) theoretical peak positions derived from JCPDS No. 01-084-7607, (b) XRD patterns in a wide 2-Theta angle, (c-d) diffraction zoomed on (002)/(110) peak.*

The XRD pattern of the MAPI sample, i.e., the sample with the simplest chemical composition, shows most of the diffraction peaks allowed for the perovskite structure. This indicates the highly polycrystalline morphology of the film, with grains oriented close to (but not fully) random orientation. In contrary, for MAPIB, the small number of observed XRD peaks (mostly of the (*hk0*)-type) provides evidence of highly textured grain orientation, with most grains having their [110] crystallographic direction perpendicular to the film plane (**Figure 5.5(b)**). **Figure 5.5(c,d)** show the deconvolution of the lowest angle perovskite peak (about 14 deg). It can be observed that this peak is asymmetric due to presence of two components: the main peak 1 – (110), and peak 2 at lower angle – (002) according to the reference in **Figure 5.5(a)**). Moreover, XRD peaks of the sample with the addition of bromine (i.e., MAPIB) are shifted towards higher 2-Theta angles, indicating a reduced lattice parameter for these samples (**Figure 5.5(c-d)**). At room temperature, MAPI crystallizes in tetragonal phase, I4/mcm[161]. Based on the Bragg's law and the peak positions in **Figure 5.5(c-d)**, the d-spacings (the distance between members of families of parallel planes) of MAPI and MAPIB were calculated and compared with the results reported in Ref. [161] (**Table 5.1**).

Table 5.1 *d-spacing of the most intense XRD peak (110).*

Sample	**d (110) (Å)**
MAPI (reference)[161]	6.2225
MAPI	6.2281
MAPIB	6.1873

The d-spacing for MAPI in the presented results is very close to the reference value (6.2281Å and 6.2225Å, respectively). A slight difference may be associated with inaccurate XRD calibration and the determination of the position of peak maximum. As observed, the distance between (110) planes in MAPIB is smaller than in MAPI. Due to smaller atomic radius of Br compared to I (115 pm vs 140 pm[162]), as well as stronger Coulomb interactions originating from the greater electronegativity of bromine compared to iodine, the mixed-halide perovskite contains, on average, more tightly packed unit cell than in the case of iodine-based material. These effects (smaller Br atom and stronger Coulomb interactions) lead to reduction of the interplanar distance and are responsible for the shift of the XRD towards higher 2-Theta angles.

Additionally, using the shift calibration data for the (110) diffraction peak, which follows Vegard's law, as provided by Lehmann et al.[163], the bromine concentration in MAPIB was determined to be 12%. This is slightly smaller value than expected based on the stoichiometry (15%), possibly due to potential inaccuracies in XRD calibration, as well as the inaccuracy of precursor scaling during synthesis.

5.2.3 Influence on the bandgap

As discussed in **Chapter 2.3.1**, the halide composition has an impact on the perovskite's bandgap. The photoluminescence spectra of MAPI and MAPIB are shown in **Figure 5.6**.

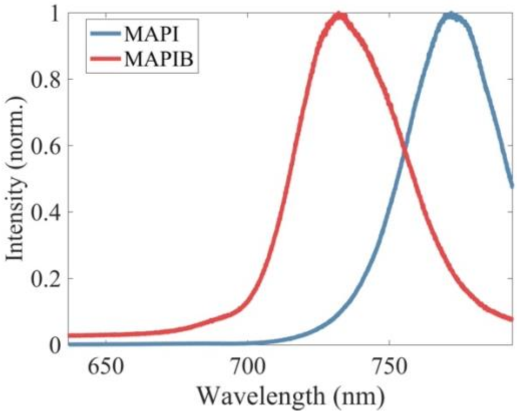

Figure 5.6 *Photolumiencence of MAPI and MAPIB.*

As expected, the PL maximum of the mixed-halide perovskite (MAPIB) is blueshifted, indicating a wider bandgap compared to the iodine-based perovskite (MAPI). Systematic studies of band-to-band luminescence as a function of bromine content have already been condcuted[164], and they were utilized for the MAPIB sample to calculate the halide composition in this thesis. Based on the PL peak maximum presented in **Figure 5.6**, the bromine content has been estimated to be about 15.9%. However, PL provides information from a relatively small area compared to XRD, which averages the signal across the entire volume of the sample. Considering several PL spectra measured at different locations on the sample (**Figure 5.7**), the average concentration of bromine within MAPIB, based on PL maxima, was found to be about 13%.

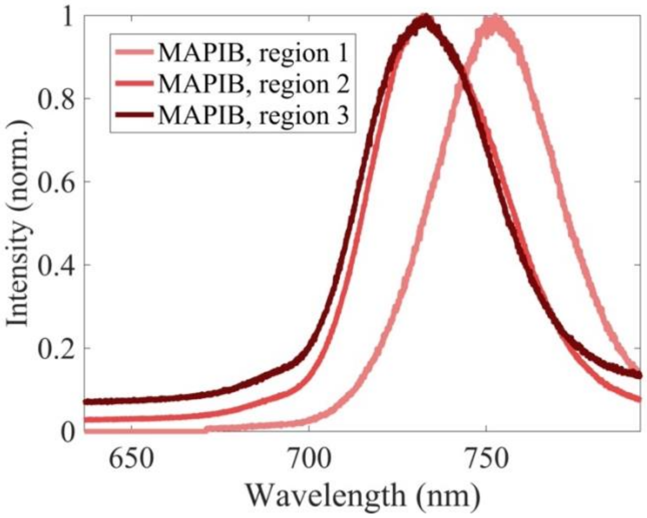

Figure 5.7 *MAPIB PL at different places on the sample.*

Interestingly, the PL peak of MAPIB in **Figure 5.6** is asymmetric, and its deconvolution is shown in **Figure 5.8**.

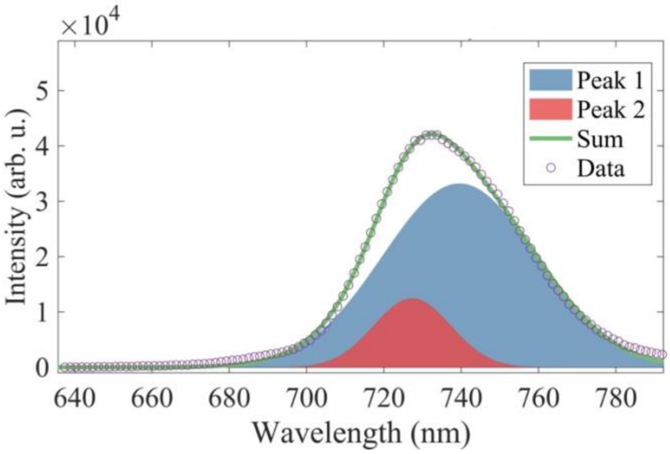

Figure 5.8 *MAPIB PL peak deconvolution.*

The appearance of two Gaussian peaks within PL spectrum suggests halide heterogeneity, indicating the formation of two perovskite clusters: one with lower Br content and the other with higher Br content (peak 1 and peak 2 in **Figure 5.8**, respectively). This will be discussed in the next chapter.

5.2.4 Chemical heterogeneity

To study halide distribution within the samples, TEM experiments were conducted. **Figure 5.9(a-b)** shows an image of the analyzed region, where two subregions (red and blue) can be distinguished. They differ in terms of halide composition, and quantitative studies were condcuted on both subregions (**Figure 5.9(c,d)**). The main part of the analyzed image (red) contains 89.0% of iodine and 11.0% of bromine. On the other hand, the blue subregion consists of 70.4% of iodine and 29.6% of bromine. These results are qualitatively consistent with the PL deconvolution in **Figure 5.8**, confirming the existence of the phase separation into subregions of different stoichiometry.

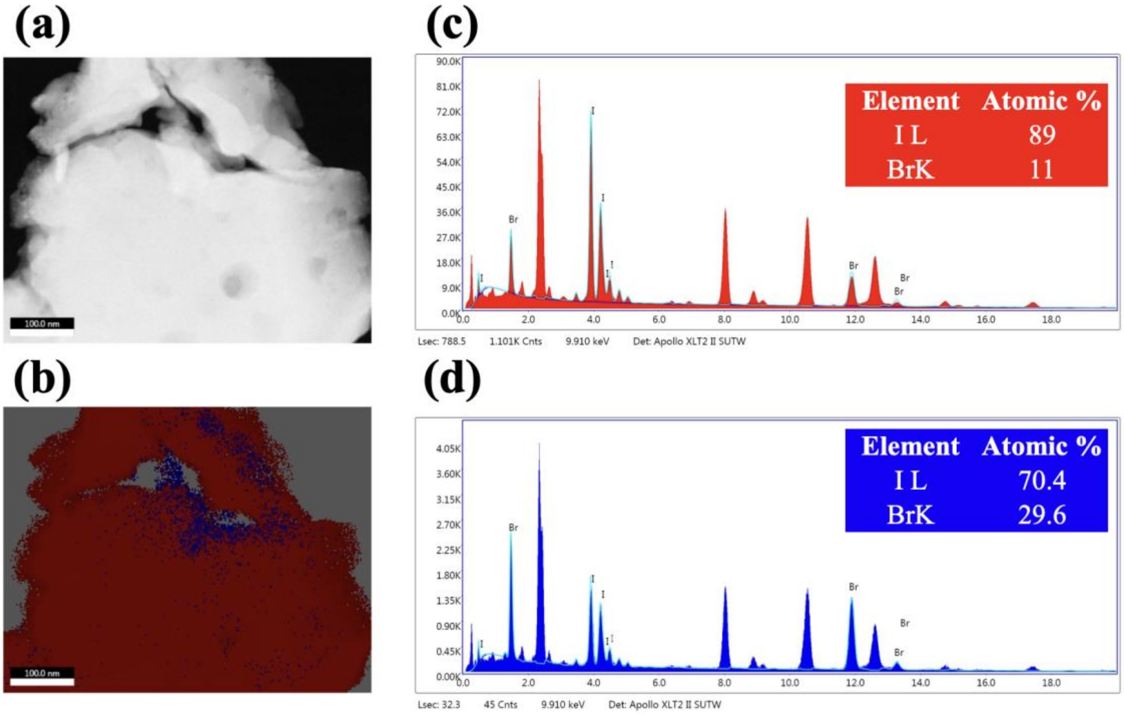

Figure 5.9 TEM images of MAPIB. (a) analyzed region, (b) image with colors indicating phase heterogeneity, (c-d) EDX spectra of analyzed subregions (red and blue in (b)).

Interestingly, even more explicit halide segregation was observed for aged samples. Examples of EDX maps collected after 14 days of aging in air are shown in **Figure 5.10**. Regions (a), (b), and (c) in **Figure 5.10** are included for statistical purposes to highlight the formation of Br-rich clusters within different parts of the sample after prolonged exposure to air. These observations align with the interpretation that halide migration could be the potential cause of the observed heterogeneity[165].

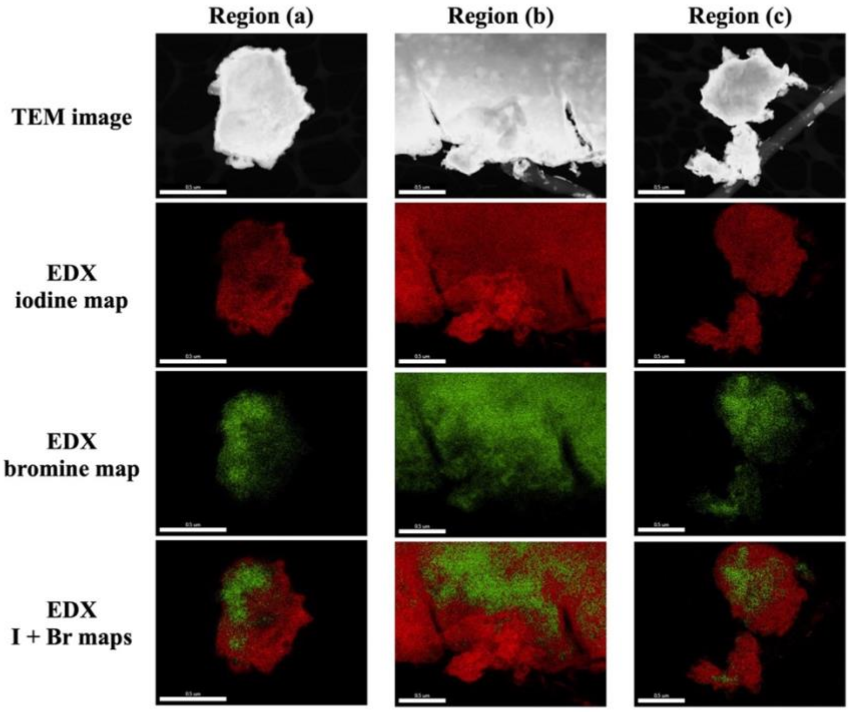

Figure 5.10 *TEM images of aged MAPIB (14 days).*

To study the bromine content within the MAPIB film, XPS measurements were also conducted. **Figure 5.11** shows the XPS spectrum in the iodine region, where two lines occur due to spin-orbit interaction – I3d$_{3/2}$ and I3d$_{5/2}$. The splitting equals 11.5 eV.

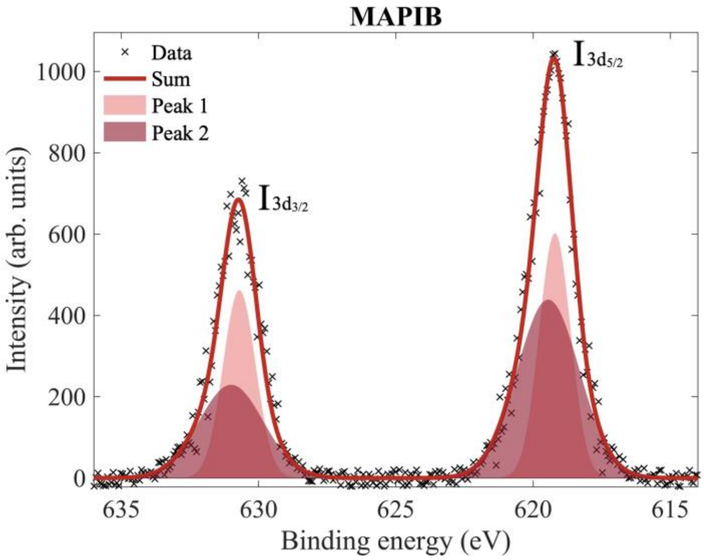

Figure 5.11 *XPS spectrum in the iodine (I3d) energy region for MAPIB.*

Following Eq. 4.4, bromine content was found to be 19% from XPS. It is worth mentioning, that XPS is a surface technique and provides information from the top 2 nm of the film. Since the bromine content obtained from XPS experiments is higher than that obtained from other techniques (XRD – 12%, PL – 13%, TEM – 11%), it was concluded that bromine migrates to the top of the MAPIB film. A bromine concentration of 11.0% in

TEM was obtained from the main portion of the sample and is statistically the most representative value for comparison with other techniques.

5.3 Dimensionality

5.3.1 Influence on the morphology

It is well known that morphology plays a significant role in the performance of solar cells, including the presence of pinholes in the perovskite film[166] and the grain size or the film roughness[68]. Quasi-3D perovskites synthesized in these studies characterize "amorphous" morphology (meaning that single grains are hard to distinguish, not a crystal form of the material, which we already know it exist based on XRD). SEM images of n50I and n50IB are shown in **Figure 5.12**. Traces of small pinholes can be observed in both films. The grains of the multidimensional perovskites are challenging to distinguish compared to their 3D counterparts (**Figure 5.3**), but they appear to be smaller than those in MAPI or MAPIB (a rough approximation of the distance between darker regions in images suggests a grain/crystallite size of about 1-3 µm).

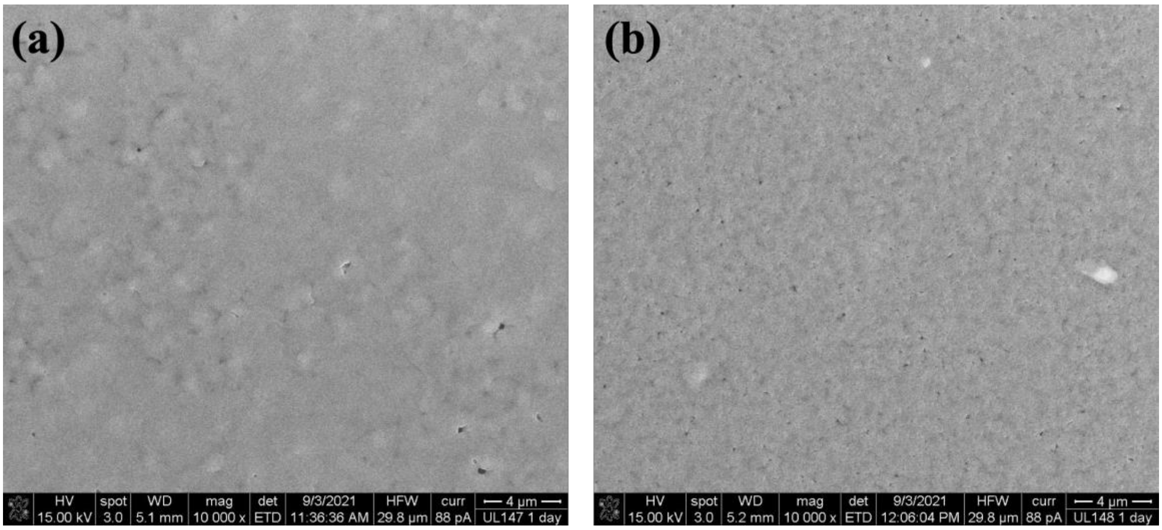

Figure 5.12 *SEM images of: (a) n50I, (b) n50IB.*

5.3.2 Influence on the crystal structure

The XRD patterns of quasi-3D perovskites is shown in **Figure 5.13**. Additionally, XRD patterns of 3D materials were included for comparison of 3D vs quasi-3D films. The quasi-3D perovskites, similar as MAPIB, exhibit only a few XRD diffraction peaks compared to MAPI, indicating a highly textured crystallite orientation. Moreover, the XRD peaks of the sample with the addition of bromine (i.e., n50IB) are shifted towards higher 2-Theta angles, indicating a reduced lattice parameter. However, the shift is slightly smaller for n50IB than for MAPIB (**Figure 5.13(b)**). Therefore, the lattice parameter decreased compared to MAPI but not as much as in MAPIB. The d-spacing results of the entire set of samples are shown in **Table 5.2**.

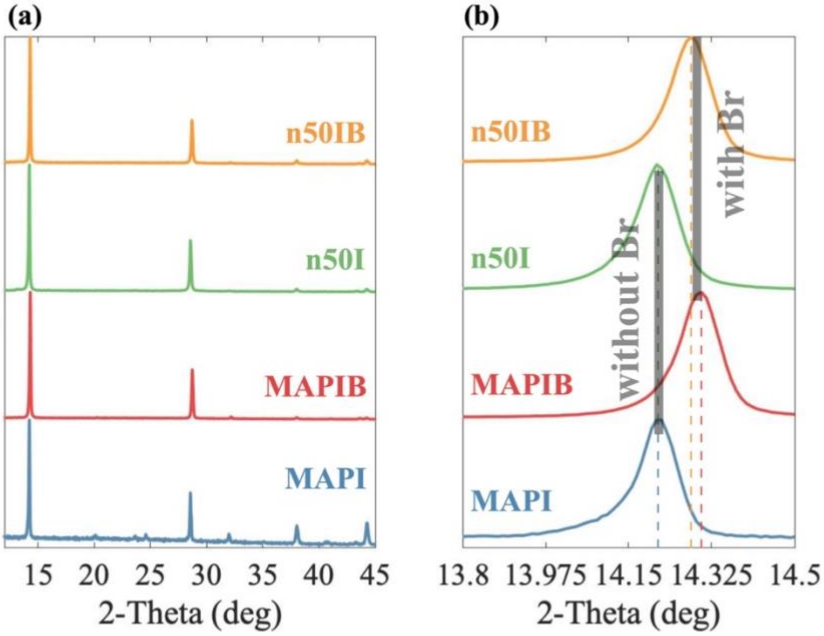

Figure 5.13 XRD *patterns of investigated samples. 3D perovskites (MAPI, MAPIB) were added for comparison: (a) wide angle range, (b) position of (110) perovskite peak.*

Table 5.2 *d-spacing of the most intense XRD peaks (110) within the entire set of samples.*

Sample	**d (110) (Å)**
MAPI (reference)[161]	6.2225
MAPI	6.2281
MAPIB	6.1873
n50I	6.2281
n50IB	6.1963

The calculated bromine content within n50IB sample, based on the shift of the XRD peaks[163], was found to be 9%.

5.3.3 Influence on the bandgap

In a case of quasi-3D perovskites, both dimensionality and halide composition have an impact on the bandgap. However, in these studies, perovskites with n = 50 were fabricated, and referring to the bandgap vs n-value results (**Figure 2.6**), it can be noticed that for such a high n-number, the impact of dimensionality on the bandgap is negligible. Therefore, the main contribution to the PL maximum shift should be related to the presence of bromine in n50IB. **Figure 5.14** presents the PL of the four studied perovskites (note that due to the halide heterogeneity of MAPIB, different spectra could be plotted for this material. Thus, only region 1 from **Figure 5.7** was arbitrarily selected to show here).

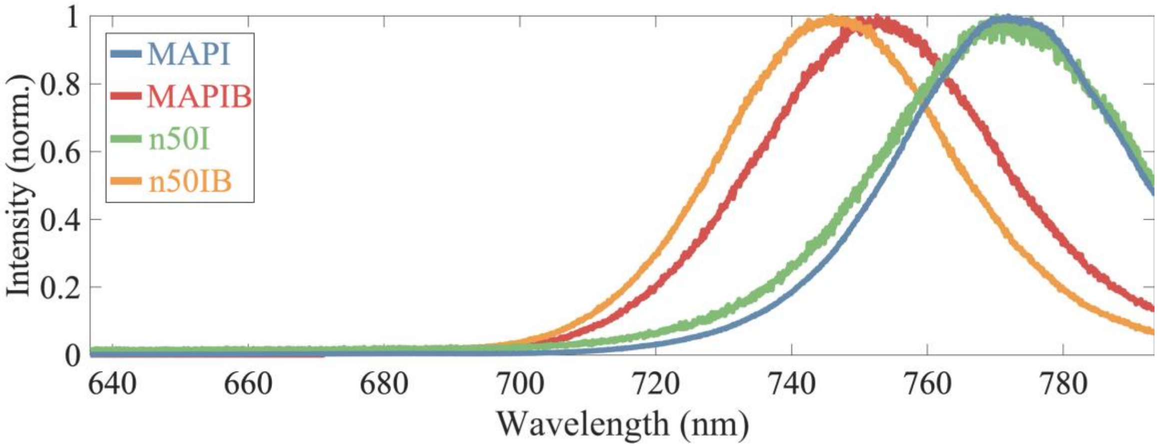

***Figure 5.14** Photolumienscence spectra of the entire set of samples. Shift towards higher energies was observed for bromine-containing perovskites, i.e. MAPIB and n50IB.*

First, the position of the PL maximum of n50I lies at the same position as MAPI, confirming that dimensionality has little impact on the bandgap in this case.

Second, a blueshift was observed for n50IB, and the concentration of bromine was found to be approximately 10%. Interestingly, in n50IB, all the PL spectra collected at different parts of the sample have their maxima at similar positions, suggesting lack of halide heterogeneity in n50IB, contrary to its 3D counterpart (MAPIB) (**Figure 5.15**). This observation was further supported by TEM experiments.

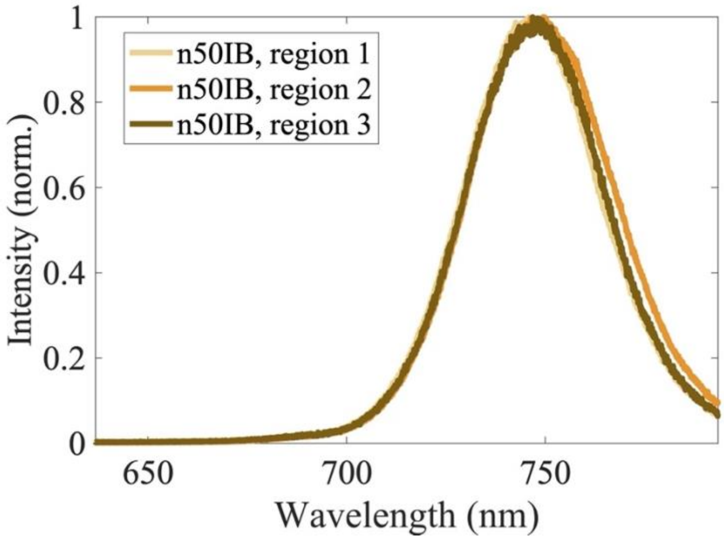

***Figure 5.15** n50IB PL at different places on the sample.*

Figure 5.16 shows TEM images of n50IB perovskite. The halide distribution in the analyzed region is relatively uniform, with a few small sub-regions of bromine excess. The halide composition was found to be 89.8% iodine and 10.2% bromine, as confirmed by

EDS chemical analysis, which is consistent with PL halide evaluation, both qualitatively and quantitatively.

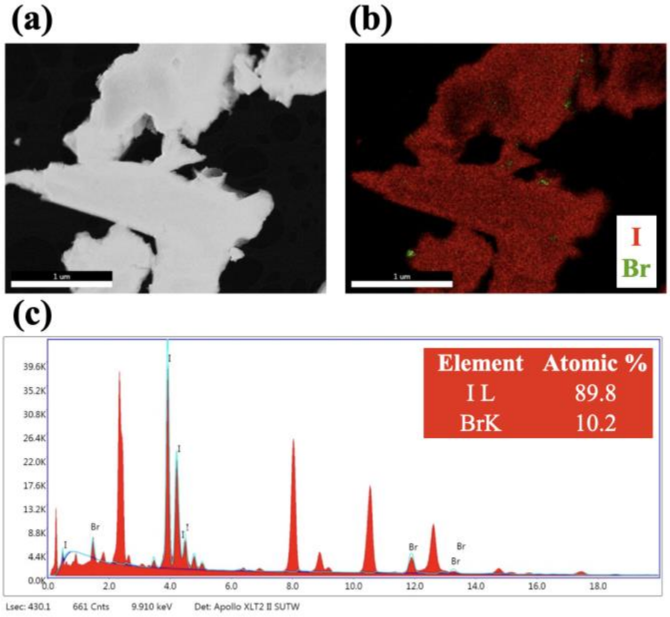

Figure 5.16 *TEM image of n50IB perovskite: (a) analyzed region, (b) EDS map (iodine – red, bromine – green), (c) EDS spectrum with calculated halide composition.*

To evaluate the bromine distribution in the top ~2nm layer of n50IB, XPS measurements were also performed, and the iodine XPS spectrum is shown in **Figure 5.17**.

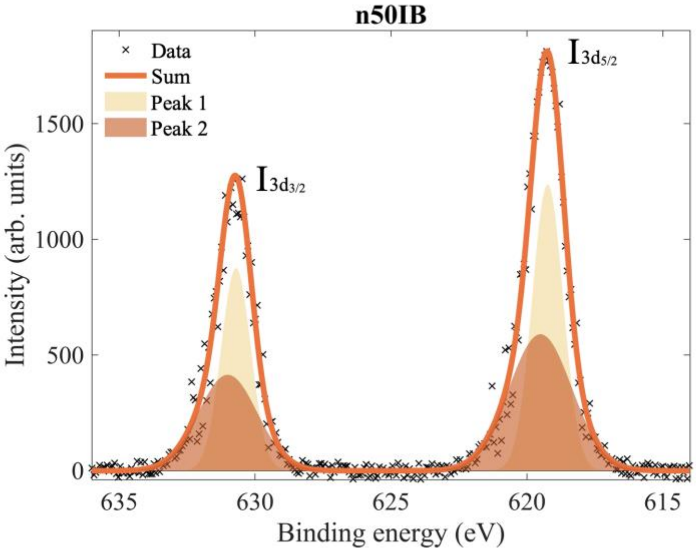

Figure 5.17 *XPS spectrum in the iodine (I3d) energy region for n50IB.*

In the case of n50IB, the bromine content determined by XPS is 10%. Therefore, all the techniques used for chemical analysis revealed similar numbers suggesting a uniform halide distribution.

The Br contents established using XRD, PL, TEM and XPS are summarized in **Table 5.3**.

Table 5.3 Summary of bromine content evaluated using four different techniques.

	% of Br in MAPIB	% of Br in n50IB
XRD	12	9
PL	13	10
TEM	11.0	10.2
XPS	19	10

5.4 Camphorsulfonic acid additive

As discussed in **Chapter 3.1.2**, one approach to improve the intrinsic properties of perovskites that affect the stabilization of solar cell efficiency and electrical parameters is the use of special additives to the perovskite precursors[166,167]. Here, the influence of the addition of camphorsulfonic acid (CSA, **Figure 5.18**) to the perovskite precursor on the morphology and crystallinity of the perovskite will be discussed. The results presented in this chapter have already been published, and the author of this dissertation is the first author of the manuscript[168] (the author initiated these studies, conducted experiments, and lead the discussion of the results).

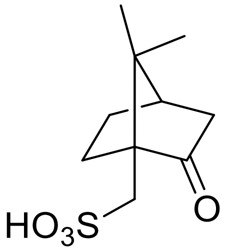

Figure 5.18 Scheme of camphorsulfonic acid molecule.

5.4.1 Influence on the morphology

SEM images of the obtained perovskites with different CSA contents are presented in **Figure 5.19**. It was found that for a relatively high concentration of CSA, acid precipitates occurred on the surface of the samples. This was easily noticeable for samples with CSA concentration equal to or higher than 3 mg/mL, and the areas with CSA crystallites are marked with red squares in **Figure 5.19**. The higher the CSA concentration, the greater the surface area of the perovskite covered with acid crystallites. No traces of CSA precipitation on perovskite films were observed, with CSA up to 2 mg/mL, based on CSA properties (melting and boiling points of 196–200 °C and 344 °C[169], respectively), we suppose that it remains dissolved in the film (perovskites are annealed at the significantly lower temperature of 100 °C).

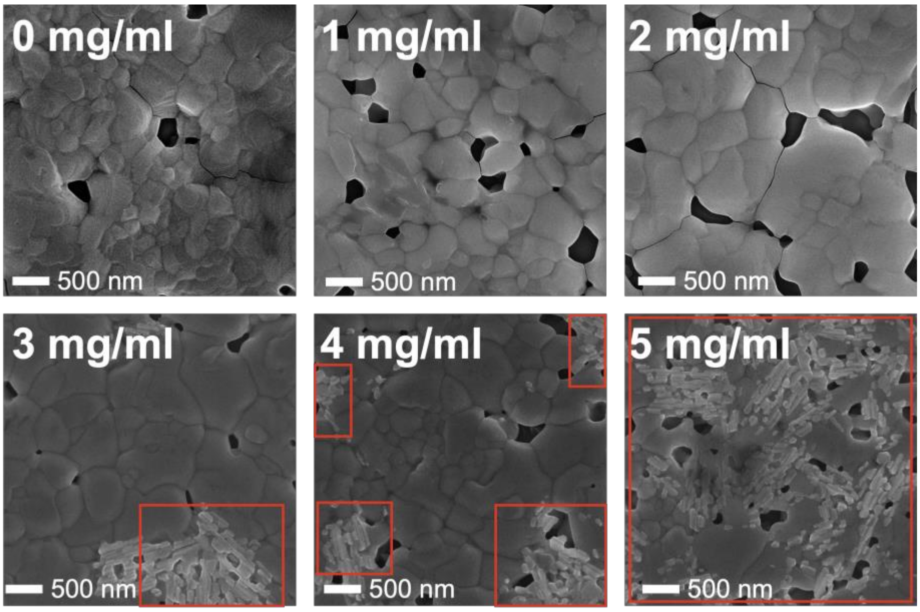

Figure 5.19 *SEM images of MAPI: CSA samples. Areas with CSA crystallites are marked with red squares.*

Moreover, in **Figure 5.19**, a gradual increase in the average grain size of the perovskite material from 320 nm for samples with no CSA (0 mg/mL) up to 480 nm for samples with 3 mg/mL CSA can be observed. For samples with higher CSA content (4 and 5 mg/mL), a plateau of grain sizes was reached at a level of about 480 nm (**Figure 5.20**). The increase in size with increasing CSA is related to the interaction between CSA and the perovskite precursors in the solution.

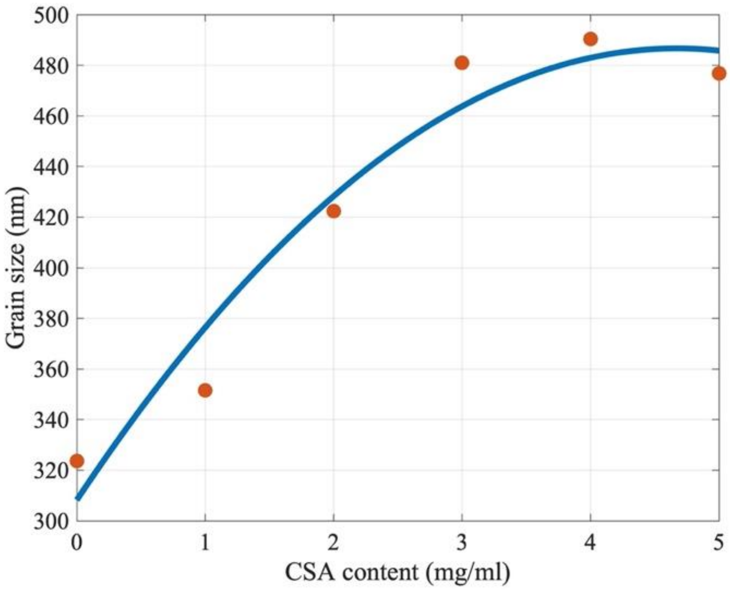

Figure 5.20 *Perovskite grain sizes as a function of CSA content. The red dots are experimental data, and the solid line is a guide for the eye.*

According to the literature, the SO_3^- groups of 4-methylbenzenesulfonic acid (4-MSA) may interact with methylammonium ion (MA^+) in the solution, resulting in a number of MA^+ ions surrounded by additives containing SO_3^- [126]. During crystallization, the interaction between methylammonium iodine (MAI) and 4-MSA promotes the growth of large perovskite grains. The CSA used in our studies also contains SO_3^- group. Therefore, it is supposed that the same mechanism is responsible for the increase in perovskite grain size with increasing CSA concentration in the precursor solution.

On the other hand, PbI_2 is likely to bond with Lewis bases[170]. CSA is a Lewis base. In chemistry, a Lewis base and a Lewis acid are chemical species which can interact with their surrounding using an electron pair (2 electrons). A Lewis acid is able to accept a pair of electrons from another molecule, resulting in a bond formation. This definition is in contrast to the traditional definition of an acid, which refers to a substance that donates protons or hydrogen ions. Lewis acids are named after the American chemist Gilbert N. Lewis, who proposed the concept in 1923. Lewis bases, on the other hand, are chemical species that are able to donate a pair of electrons to form a bond with a Lewis acid. This definition is in contrast to the traditional definition of a base, which refers to a substance that can accept protons or hydrogen ions. Lewis bases are often molecules or ions with a lone pair of electrons that can be donated to a Lewis acid to form a new covalent bond. The concept of Lewis acids and bases is important in understanding the mechanisms of many chemical reactions, and it provides a more general and comprehensive approach to acid-base chemistry than the traditional definitions of acids and bases. Lewis acids and bases are often used in organic chemistry to explain the mechanisms of chemical reactions, and they are also useful in inorganic chemistry for understanding the behavior of coordination complexes.

CSA, being a Lewis base and having three oxygen atoms with lone electron pairs, may interact strong with PbI_2, the perovskite precursor, in solution. It has been shown that the addition of DMSO (a Lewis base) to DMF used as the solvent of perovskite precursors affects PbI_2-DMF cluster formation at the molecular level because DMSO shows much stronger coordination capability to PbI_2 than DMF[171]. Since CSA is also a Lewis base and has three oxygen atoms with lone electron pairs, it may interact even stronger with PbI_2 than DMSO, leading to smaller colloid particles that act as nucleation centers during the perovskite formation.

To summarize the possible interactions discussed above between additives and perovskite precursors, it is believed that both SO_3^- group interactions with $CH_3NH_3^+$ from MAI and Lewis acid–base interactions between Pb^{2+} from PbI_2 and CSA lead to better dispersion of the perovskite precursor molecules, promoting the growth of the larger perovskite grains upon annealing compared to the those that grow without CSA. The optimum CSA concentration regarding the grain size was found to be in the range of 3–4 mg/mL (**Figure 5.20**). However, it should be remembered that starting from a 3 mg/mL CSA content, the problem with CSA precipitation begins.

5.4.2 Influence on the crystal structure

The XRD patterns of the fabricated perovskite films with different concentrations of CSA are shown in **Figure 5.21**. They all reveal most of the diffraction peaks characteristic for the perovskite structure and indicate the highly polycrystalline morphology of the films, with close to (but not full) random grain orientation. The dominance of (110) and (220) reflexes indicates the partial texturization of the solidified perovskites. There is no evidence of additional phases such as PbI_2 or CSA[168].

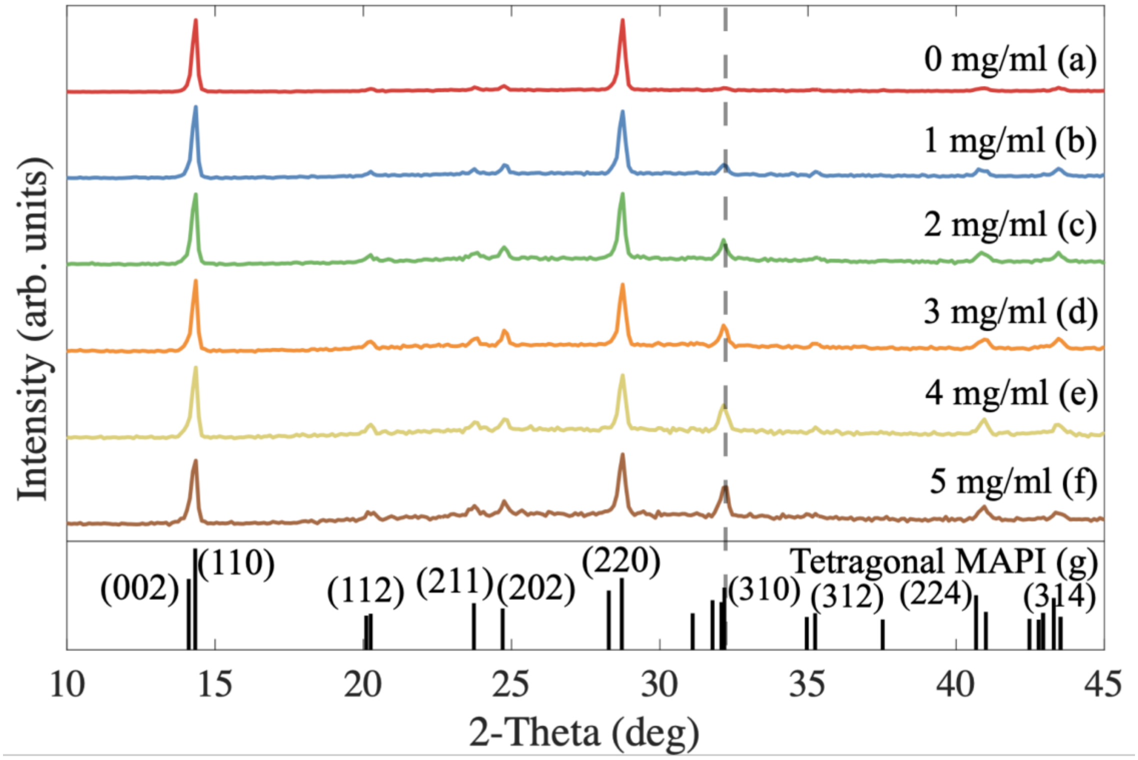

***Figure 5.21** XRD patterns (Cu K-alpha radiation) of MAPI with different amounts of CSA (a-f), reference derived from JCPDS No. 01-084-7607 **(g)**. Dashed line represents a sample diffraction pattern, in which contribution increases with CSA content.*

Interestingly, the higher the concentration of CSA within the perovskite, the stronger the additional peaks were compared to the main (110) and (220) diffraction peak intensities, such as the exemplar (310) peak marked with a dashed line in **Figure 5.21**.

Figure 5.22 shows its relative intensity to the (110) diffraction peak intensity as a function of CSA content. The almost linear increase indicates a reduction of the degree of solidified perovskite texturization with increasing CSA amounts added to the precursor solution.

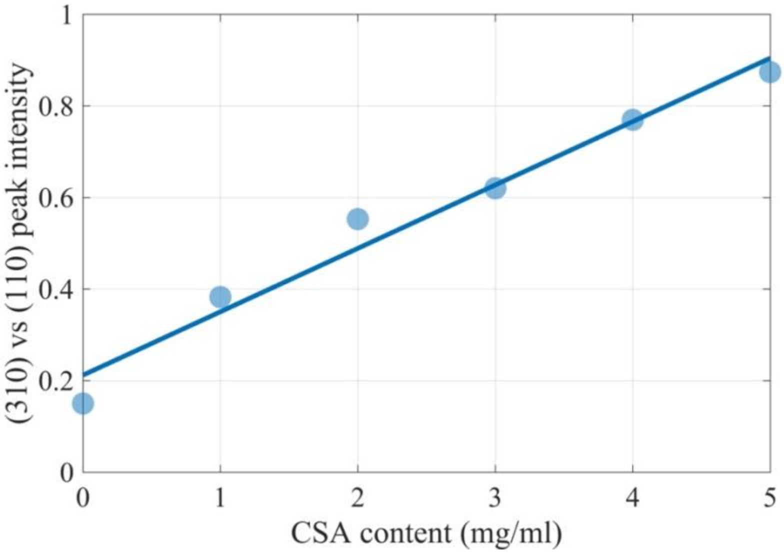

Figure 5.22 *Peak intensity of (310) vs. (110) as a function of CSA content.*

This result is evidence of the increasing randomization of grain orientation. Interestingly, it has been reported that additives such as 4-methylbenzenesulfonic acid (4-MSA) improve the perovskite's crystallinity[126]. Due to its aromatic character, 4-MSA may intercalate the structure of the perovskite, leading to materials' growth according to the 4-MSA orientation within the film. On the contrary, the CSA used in our studies is not an aromatic compound; it contains a sulfonic $-SO_3^-$ group that may interact with Pb^{2+} ions. According to Liu et al.[172], the density of Pb atoms in the perovskite is the largest on (110) and (002) facets. Therefore, in the presence of the additive containing a sulfonic group (3-(decyldimethylammonio)-propane-sulfonate inner salt in Ref. [172]), the growth of these facets may be slowed down and result in higher randomization of crystallites growing in the presence of CSA. In general, from the point of view of the material's electrical properties, texturization would be the preferred form of crystallization[173], as it should enhance the mobility of carriers along the plane of the perovskite layer. For the perovskite solar cells, however, the mobility across the layer is important, so the observed texturization should not be of any significance for the operation of the cells.

5.5 Tetraethoxysilane additive

5.5.1 Influence on the morphology

For these SEM/EDX studies, glass substrates were replaced by copper sheets due to presence of Si in glass, which would provide relatively strong silicon signal from the substrate compared to Si present in the perovskite film. Interestingly, a choice of substrate has a significant influence on the film morphology (**Figure 5.23**), as reported in the literature[174].

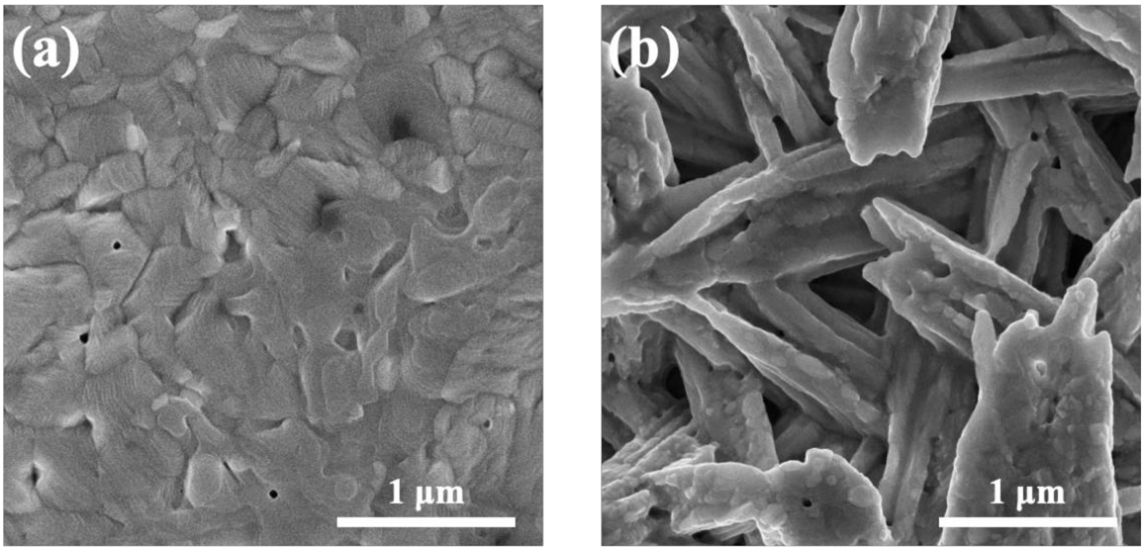

Figure 5.23 *SEM images of MAPI on: (a) glass substrate, (b) copper substrate.*

A model of nucleation and growth for thin films has already been established, dividing the perovskite formation into several steps, with the first one being the formation of crystal nucleus[175,176]. According to the model, the Gibbs free energy for heterogeneous nucleation can be expressed as the equation below:

$$\Delta G_{heterogeneous} = \Delta G_{homogeneous} \times f(\theta)$$

wherein $f(\theta) = (2 - 3\,cos\theta + cos^3\theta)/4$

and θ is the contact angle of the precursor solution[177]

The conclusion that arises from the equation above is that a smaller contact angle (which depends on the substrate and especially the adhesion to this substrate) results in reduced Gibbs free energy for heterogeneous nucleation meaning it assists the nucleation process. Therefore, the morphology of the film may strongly depend on the choice of the substrate. Here, no further studies devoted to the influence of substrates were done.

The idea was to provide a “proof-of-concept” of TEOS implementation into the perovskite film. However, the explanation of the origin of different morphology than presented in previous chapters was needed. SEM images of MAPI with different content of TEOS on copper substrates are shown in **Figure 5.24**.

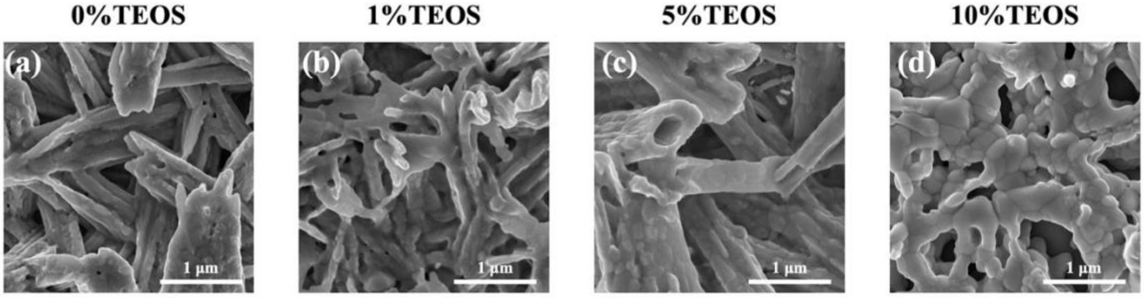

Figure 5.24 *SEM images of MAPI with different contents of TEOS.*

They all display a similar needle-like morphology. MAPI film with 10% of TEOS (**Figure 5.24(d)**) looks slightly different than other films. It still maintains a needle-like morphology, but these needles seem to have a grained structure. Chemical analysis was also conducted to determine location of silica within the films (Figure 5.25). The samples with the highest TEOS contents (5 and 10%, Figure **5.25(b)** and **(c)**, respectively) show bright precipitates, suggesting the formation of silica agglomerates. However, a linear EDS analysis does not support this hypothesis (Figure **5.25(d,e)**). A homogeneous distribution of Si along the analysis line is observed, with a minimum occurring at the point of precipitation, which may probably be a residue of the components of the TEOS solution. No spatial agglomerates of silica were observed in the other samples either. Additionally, it must be borne in mind that the depth of interaction of the electron beam with the sample is up to several micrometers. Therefore, the analyzed signal comes from the entire thickness of the layer (about 100 nm). There are no well-defined crystal domains in the analyzed samples. Therefore, it was impossible to perform granulometry to determine their sizes and surface density. The lack of clear boundaries of the domains also prevented the analysis of the presence of silica, which is supposed to be a binder protecting the perovskite from external factors.

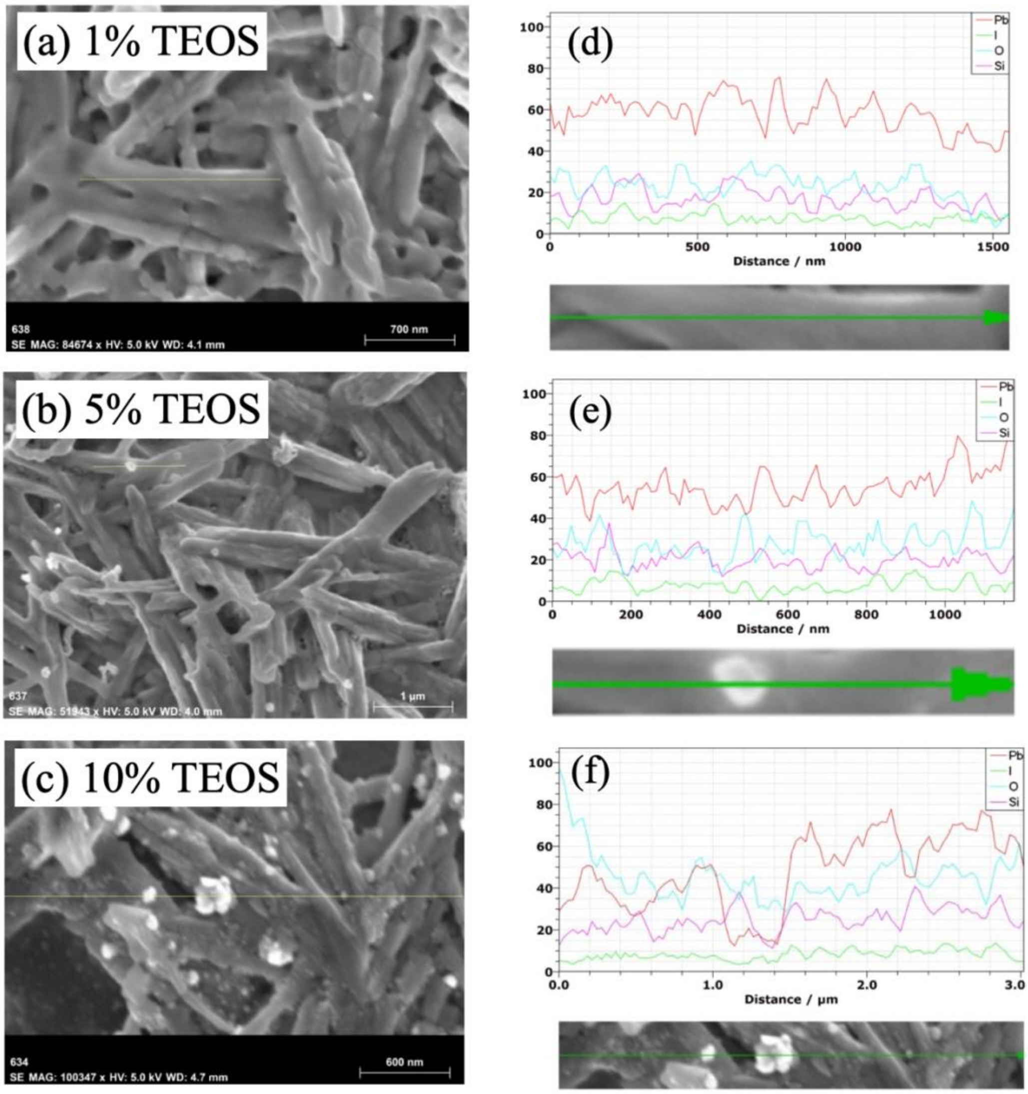

Figure 5.25 *SEM images of MAPI with different contents of TEOS (a-c), and EDS cross-section through corresponding films (d-f).*

5.5.2 Influence on the crystal structure

The XRD patterns of the set of TEOS-containing samples are shown in **Figure 5.26**. Interestingly, all the diffraction patterns reveal an additional non-perovskite peak (marked by a dashed line in **Figure 5.26**), which originates from PbI_2. As already studied, this may originate from either a product of perovskite degradation or non-stoichiometric concentration of PbI_2[178]. It is worth mentioning that the samples fabricated in the studies related to the addition of TEOS were made at the beginning of the author's PhD program. Therefore, errors due to inexperience in perovskite synthesis at the early stage might have occurred, potentially resulting in the presence of PbI_2.

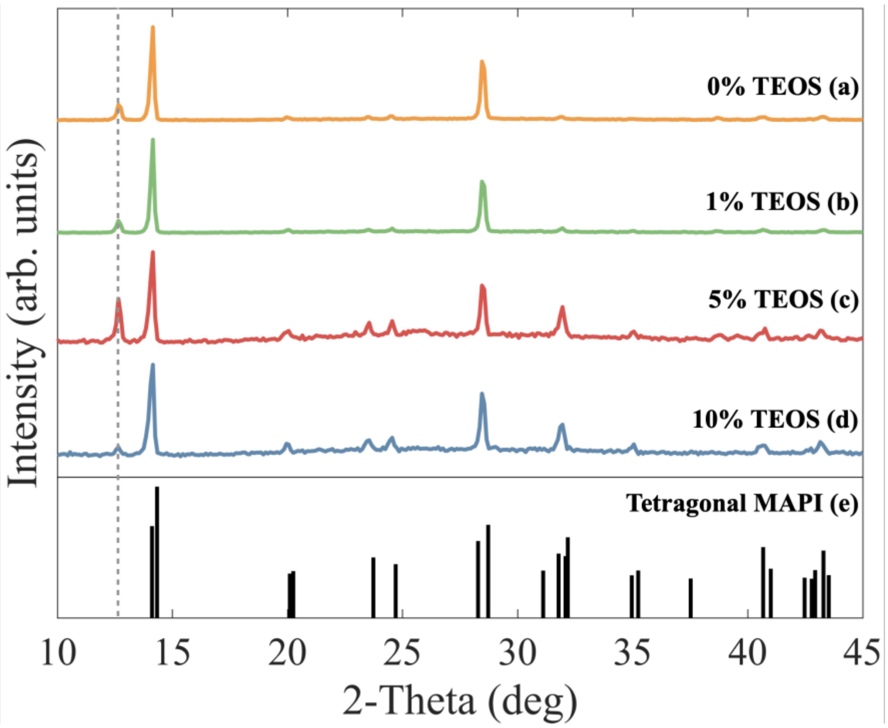

Figure 5.26 *XRD patterns (Cu K-alpha radiation) of MAPI with different amounts of TEOS (a-d), reference derived from JCPDS No. 01-084-7607 (**e**). Dashed line indicates a peak originating from a perovskite degradation product (PbI_2).*

The lack of compact, grained structure may result in materials' susceptibility to water and oxygen diffusion through such massive pin-holes (of the order of hundreds of nanometers). As a consequence, degradation started immediately within all the films leading to formation of PbI_2.

Environmental stability studies of silica-containing MAPI films were conducted, and XRD evolution of all the samples is shown in **Figure 5.27(a-d)**. Two XRD peaks are presented in figures (a-d): the one at the lower angle (about 12.6°) is the PbI_2 (001) diffraction peak, whereas the other at the higher angle (about 14.2°) is the (110) perovskite diffraction peak.

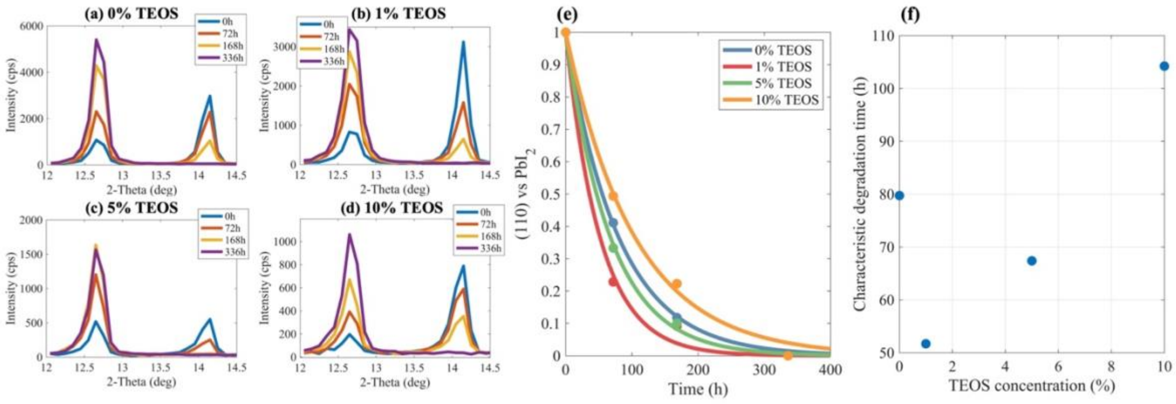

Figure 5.27 *Degradation analysis of TEOS containing PVSK films: (a-d) XRD, (e) perovskite line decay, (f) characteristic degradation times.*

It is evident that during exposure to air, a decomposition of all perovskites to PbI_2 took place. The observed decrease of the (110) perovskite diffraction peak was accompanied by an increase in the diffraction peak related to (001) PbI_2 planes. After 336 hours the perovskite peak entirely vanished within all the samples. To analyze evolution of the XRD patterns quantitatively, intensities of perovskite (110) and PbI_2 (001) diffraction peaks were integrated for all the investigated samples and plotted as a function of air exposure time in graphs presented in **Figure 5.27(e)**. Interestingly, the observed decays of perovskite peaks could be described by first order kinetics of reaction with a rate directly proportional to the momentary amount of perovskite. Fitting to the experimental data of both perovskites with exponential curves described by the formula:

$$N(t) = N_0 exp\left(-\frac{t}{\tau_p}\right)$$

yielded the characteristic degradation times τ_p shown in **Figure 5.27(f)**.

First, τ_p of perovskites with 1% (52h) and 5% (67h) of TEOS are shorter than τ_p of the TEOS-free reference (80h) meaning they decomposed even faster than unmodified material. Second, τ_p of the perovskite with 10% of TEOS was longer than that of the reference (104h vs 80h) indicating slightly better stability of the material with silica.

The relationship of characteristic degradation times is seen to scale proportionally with the concentration of TEOS. At lower concentrations (1 and 5%), the characteristic degradation times are shorter in comparison to the reference material devoid of TEOS. The introduction of TEOS itself induces additional effects, resulting in shorter degradation times at low TEOS concentrations. It is only when the TEOS concentration is significantly high (10%) that the characteristic degradation times exceed those of the material without such inclusions. Therefore, it was shown that the addition of TEOS to the perovskite solution improves material's stability, but only at a relatively high concentration of TEOS.

5.6 Chapter summary

In this chapter, perovskite materials with various chemistry modifications were introduced. First, the influence of an antisolvent on the film's morphology was shown. The studies suggest that the lack of an antisolvent leads to a needle-like morphology due to the formation of the orthorhombic $(MA)_2(DMF)_2Pb_3I_8$ intermediate phase, similar to Ref. [107]. Moreover, when antisolvent is dripped too early, the nucleation density is relatively poor, creating bigger grains, but the film contains pinholes. Finally, if the antisolvent is dripped at an optimum time, the formation of a compact, pinhole-free film is achieved. Additionally, the influence of different antisolvents (chlorobenzene, toluene, chloroform) on morphology was investigated. The results indicate the highest quality of the film when chlorobenzene is used. However, toluene and chloroform could potentially also be applied, but the dripping time should be optimized individually for each antisolvent.

Second, the influence of the addition of bromine was investigated. It was found that the presence of bromine induces the growth of perovskite grains almost two times larger compared to Br-free material. It may be associated with lower solubility of bromine-rich species and the more favored formation and nucleation compared to I-containing species. Earlier nucleation and crystallization of Br-containing species give them more time to grow and may lead to the formation of bigger grains within the film.

Third, multidimensional perovskites were synthesized. Their grains are hard to distinguish compared to their 3D counterparts, but they seem to be smaller than in MAPI or MAPIB.

Forth, the halide composition was studied within both 3D (MAPIB) and 2D/3D (n50IB) kinds of perovskites. To determine the exact content of bromine within analyzed materials, four techniques were used: XRD (based on the shift of the diffraction peaks), PL (based on the luminescence maximum position), and XPS and TEM-based EDS analysis/mapping (based on chemical analysis).

It was found that in multidimensional perovskite (n50IB), the bromine content evaluated via XRD, PL, EDS, XPS, remains similar. On the contrary, in 3D perovskite significant differences can be observed: PL and EDS mapping revealed phase separation into Br-rich regions. XPS unveiled the highest Br content among all the techniques. The last approach provided information from top ~2nm; therefore, it was concluded that bromine in 3D perovskite (MAPIB) prefers to remain close to the top of the sample or it migrates from the volume to the surface.

Fifth, the addition of camphorsulfonic acid (CSA) to MAPI was investigated. It was found that the higher the CSA content, the bigger the perovskite grains. However, after a threshold found to be at about 3 mg/ml, CSA precipitates occur on the surface. Additionally, the increasing randomization of grain orientation by means of XRD was observed in a function of increasing CSA concentration.

Sixth, addition of tetraethoxysilane (TEOS) to MAPI was studied. This research revealed slightly better environmental stability of perovskite with the TEOS addition in comparison to pristine MAPI. However, the observed differences were not significant, and the entire process requires extensive optimization. Specifically, it is crucial to consider chemistry modifications to address the issue of needle-like morphology. TEOS may be an interesting approach to boost perovskite stability, but it will not be used in further studies due to better candidates, such as CSA.

6 Revealing the dynamics of perovskite formation via in-situ photoluminescence

In-situ photoluminescence (PL) was used to monitor nucleation and the perovskite crystallization process in real time. This technique provides information on radiative recombination processes and kinetics, such as the evolution of the bandgap during growth. The bandgap is primarily influenced by the halide ratio and dimensionality within the studied perovskites. Therefore, *in-situ* PL is valuable for investigating the formation dynamics associated with the halide elements.

6.1 Formation dynamics of MAPI

In-situ PL studies of MAPI were performed. **Figure 6.1** shows the *in-situ* PL results of MAPI. Spectra were collected during annealing of spin-coated precursor mixture, and the perovskite formation started after about 7.2 seconds – this is the time needed to heat the substrate to the temperature at which crystallization process starts.

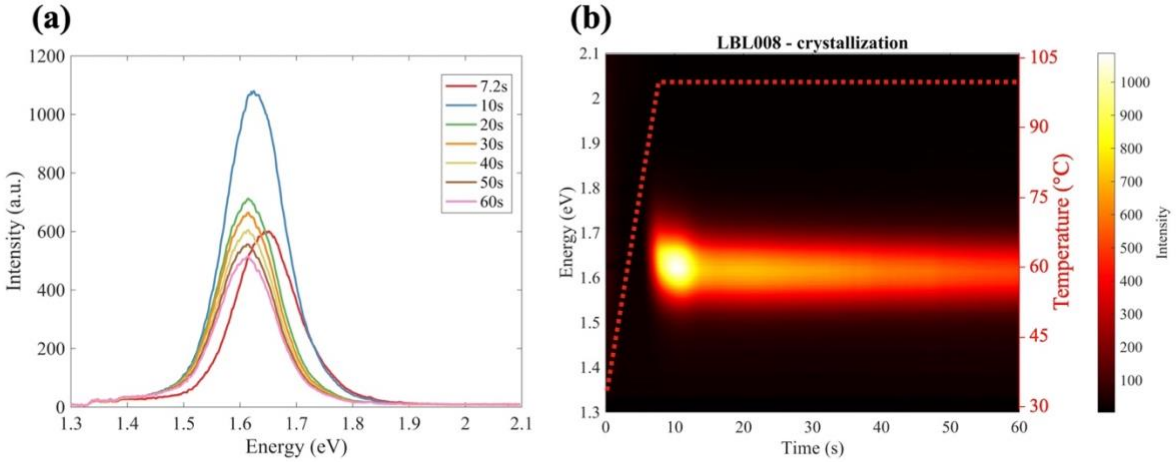

***Figure 6.1** In-situ PL measurements of MAPI during annealing: (a) example photoluminescence spectra, (b) in-situ PL map together with the substrate temperature (right y-axis).*

Gaussian fitting of the *in-situ* PL spectra was applied to extract the evolution of the peak energy position, its intensity, and full width at half maximum (FWHM) of the PL signal over time (**Figure 6.2**). It was observed that the PL initiated at a higher energy (1.653 eV) compared to the final bandgap of the bulk perovskite film (1.611 eV). Therefore, the energy redshifted by 0.042 eV upon annealing. It has been speculated that the emission peak shifting, especially at the early growth stage of perovskites, could be attributed to the quantum confinement of the nanograins[160]. In this thesis, the results of PL behavior are explained in the same way.

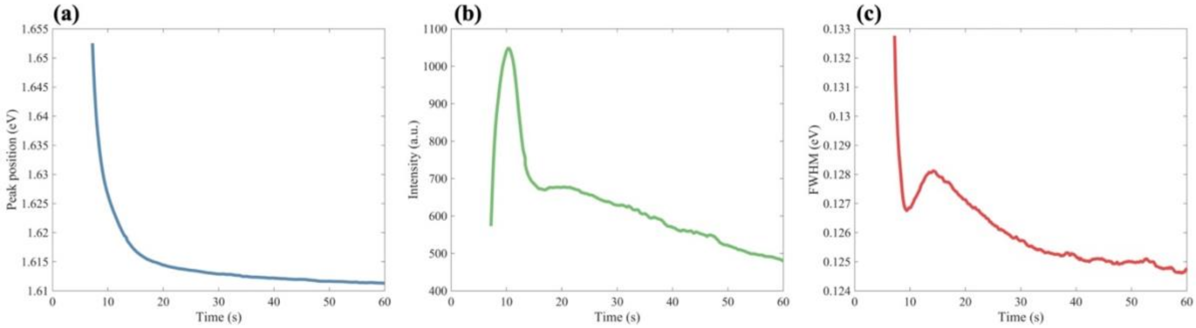

Figure 6.2 The extracted values of emission peak position (a), PL intensity (b), and FWHM (c) from the in-situ PL measurements of MAPI.

Growth modes and quantum confinement in ultrathin vapour-deposited MAPI films have already been studied[179] and experimental results have followed a simple approximation of the quantum confinement fit (**Figure 6.3**), shown in **Eq. 6.1**.

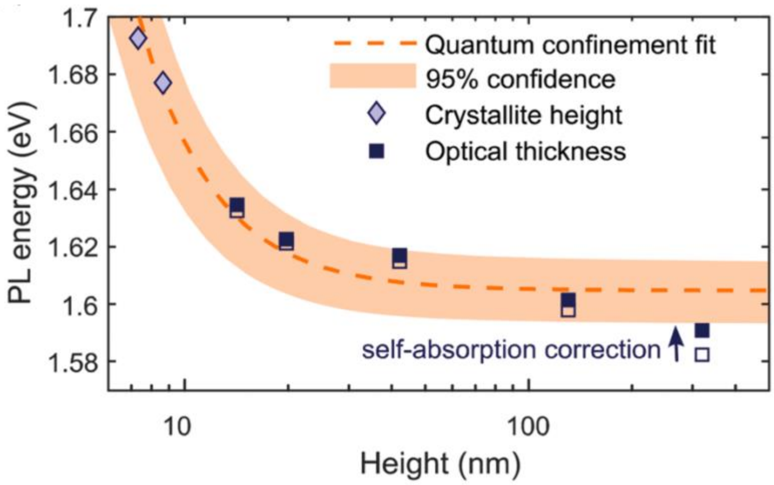

***Figure 6.3** PL peak energy as a function of crystalline size, d. The data are fitted with an equation for quantum confinement $E = E_g + b/d^{2[179]}$.*

$$E = E_g + \frac{\hbar^2 \pi^2}{2\mu \, d^2} \qquad \textbf{\textit{Eq. 6.1}}$$

where $\mu = 0.075 m_e$[179]

and **d** stands for a crystallite size.

Based on the initial PL position in **Figure 6.2(a)** and using **Eq. 6.1**, the corresponding grain size in MAPI was estimated to be about 10.9 nm.

The PL intensity (**Figure 6.2(b)**) observed during the annealing behaved non-monotonically. First, the PL intensity was increasing from the beginning of annealing and reached its maximum after 10.4 s. The rise of intensity is attributed to increasing amounts of highly illuminating perovskite phase crystals in the early stage of crystallization. Then, the PL intensity was decreasing until 16s, which may be related to: (i) an increasing number of trap-assisted nonradiative recombination centers as the size and specific area of the crystalline perovskite change during growth, which is in agreement with the conclusions in Ref.[160]), or (ii) self-absorption – the higher energy photons emitted by smaller grains are reabsorbed by larger perovskite crystallites, similarly explained in Ref.[179]. Finally, from about 20 s to the end of annealing (60s), a systematic intensity decay was observed. This is possibly due to partial degradation of the material under the laser beam where both heat on the hot-plate and the laser electromagnetic radiation are present, which may initiate the degradation process.

The time required to reach the intensity maximum is defined in this thesis as the crystal growth time (i.e., the earlier it reaches the intensity maximum, the faster is the growth time). Analyzing the FWHM (**Figure 6.2(c)**), the PL signal achieved a relatively sharp peak after 10 s, so at the PL intensity maximum. Then, from 10 s to 16 s, the FWHM slightly rose. However, the FWHM changes were relatively small, i.e., the peak intensity almost doubles in its extremes, whereas the FWHM decreased only by a few percent. Overall, the decrease in FWHM may suggest grain size homogenization over time.

6.2 Formation dynamics in mixed-halide perovskites

In-situ PL results of mixed-halide perovskite (MAPIB) are shown in **Figure 6.4**. The crystallization process started after 2.8s, much earlier than for MAPI (7.2s) and at a lower temperature. Interestingly, the evolution of the PL position revealed not only a redshift, as in MAPI, but also a blueshift (**Figure 6.5(a)**).

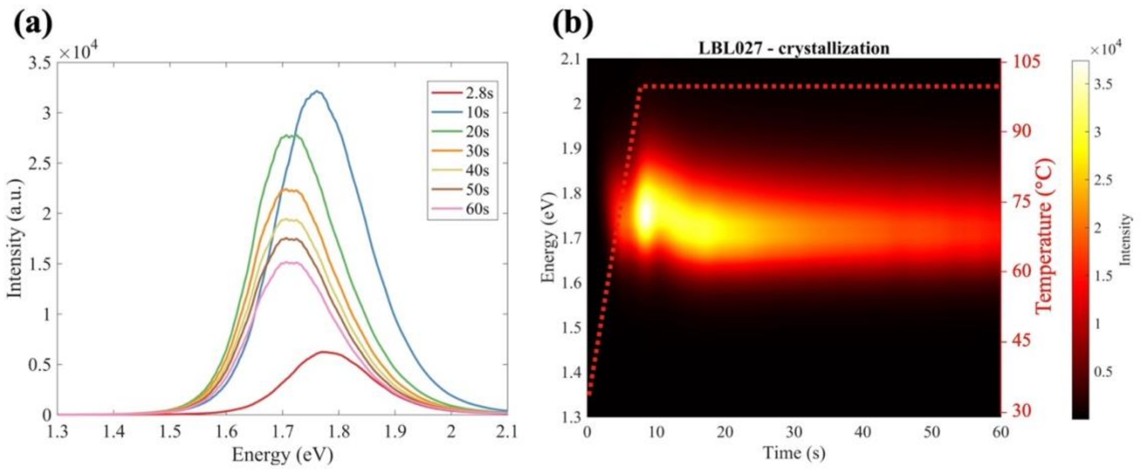

***Figure 6.4** In-situ PL measurements of MAPIB during annealing: (a) example photoluminescence spectra, (b) in-situ PL map together with the substrate temperature (right y-axis).*

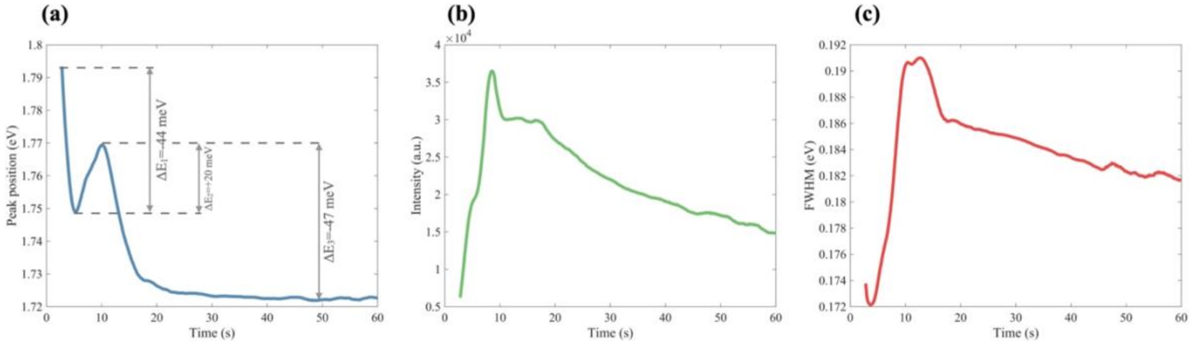

***Figure 6.5** The extracted values of emission peak position (a), PL intensity (b), and FWHM (c) from the in-situ PL measurements.*

The PL position, similar to MAPI, initiated at higher energy (1.793eV) compared to the final bandgap of the bulk perovskite film (1.722eV). Therefore, the energy shifted by 0.071eV upon annealing. Due to the quantum confinement, a larger energy shifting in MAPIB than in MAPI (0.071 eV and 0.042 eV, respectively) suggests a smaller initial crystal size in mixed halide perovskite than in iodine-only based material. Based on **Eq. 6.1**, the crystal size of 8.4 nm was calculated, which is less than in MAPI (10.9 nm). Three PL position regions in **Figure 6.5(a)** can be highlighted: (i) redshift ΔE_1 = -0.044eV, (ii) blueshift ΔE_2 = +0.020eV, and (iii) redshift ΔE_3 = -0.047eV. It was already speculated that redshifts are related to the quantum confinement of the nanograins. On the other hand, blueshift may be associated with a compositional evolution during perovskite formation. Huang et al.[160] have found by means of DFT calculations that DMSO (a solvent of the perovskite precursors) bonds most strongly with PbI_2 (0.84eV), followed by PbIBr (0.79eV), and has the weakest bond with $PbBr_2$ (0.77eV) (results obtained from the optimized molecular configuration and bond distances are shown in **Figure 6.6**).

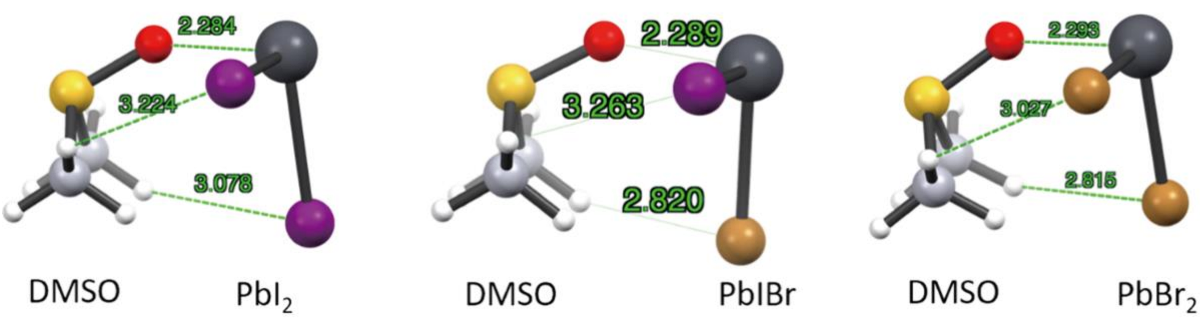

Figure 6.6 *Molecular configuration and interaction distance of coordinating solvent DMSO and PbXX′ molecules. X and X' denote either I or Br. Figure and DFT results originate from Ref.* [160].

Furthermore, the formation energies for the PbXX′:DMSO (X,X' different halides) adduct crystals have been also calculated. The formation energies decreased as I was gradually replaced by Br (−0.18 eV for PbI_2:DMSO, −1.10 eV for PbIBr:DMSO, and −1.32 eV for $PbBr_2$:DMSO). Therefore, their results suggest that Br-containing intermediate adduct phases are more thermodynamically favored to form compared to pure I-based material. Thus, in the case of mixed halides as in this thesis, it can be expected that during the solidification process, crystals richer in bromine will first form, and then the concertation of halide will change and finally settle at that resulting from the ratio of bromine and iodine precursors. These calculations are in agreement with the trend of PL position evolution for MAPIB in **Figure 6.5(a)**. The perovskite crystallization started earlier in the case of MAPIB than in MAPI (2.8 s and 7.2 s, respectively) indicating that Br-rich species potentially nucleate first during supersaturation. Then, from 5.2 s to 10 s, the bandgap of MAPIB increased by $\Delta E_2 = 0.020$ eV, suggesting faster crystallization of Br-rich species. The crystallization process can be imagined first as the crystallization of small grains at nucleation centers and then their preferential selection with bromine, and afterwards, this concentration evens out.

The PL intensity maximum (**Figure 6.5(b)**) was reached after 8.4 s from the beginning of annealing (or in 5.6 s after the start of crystallization), indicating a slightly slower growth time in MAPIB compared to MAPI (3.2 s). Finally, from about 20 s until the end of annealing, a systematic intensity decay was observed, similar to that in MAPI, and it was associated with perovskite degradation under the laser beam. FWHM reaches the highest value at about 10 seconds (**Figure 6.5(c)**), suggesting a relatively high distribution of grain sizes. Then, the FWHM slightly decreases as the grains tend to achieve similar sizes.

6.3 Formation dynamics in camphorsulfonic acid – doped perovskites

In **Chapter 5.4**, the influence of camphorsulfonic acid (CSA) on the perovskite film's morphology and crystal structure was discussed. Here, the formation dynamics of perovskite doped with CSA will be discussed. In *in-situ* PL studies, CSA concentration of 1 mg/ml was selected due to its promising properties discussed in **Chapter 5.4**. On one hand, a positive influence of CSA on both morphology and crystal structure was observed. On the other hand, this is a safe concentration in terms of potential CSA precipitates, which could additionally impact the *in-situ* PL behavior.

As it was already discussed in **Chapter 3.1.2**, CSA is a Lewis base, similar as DMSO, having three oxygen atoms with lone electron pairs. It may interact even stronger with PbI_2 than DMSO, increasing the activation energy of crystallization. Therefore, it is supposed that the growth time in the case of perovskites with CSA will be longer than in unmodified materials.

6.3.1 Formation dynamics in MAPI:CSA

Figure 6.7 shows *in-situ* PL results of MAPI doped with CSA (MAPI:CSA). Spectra were collected during annealing, and the perovskite formation started after about 5.8 seconds.

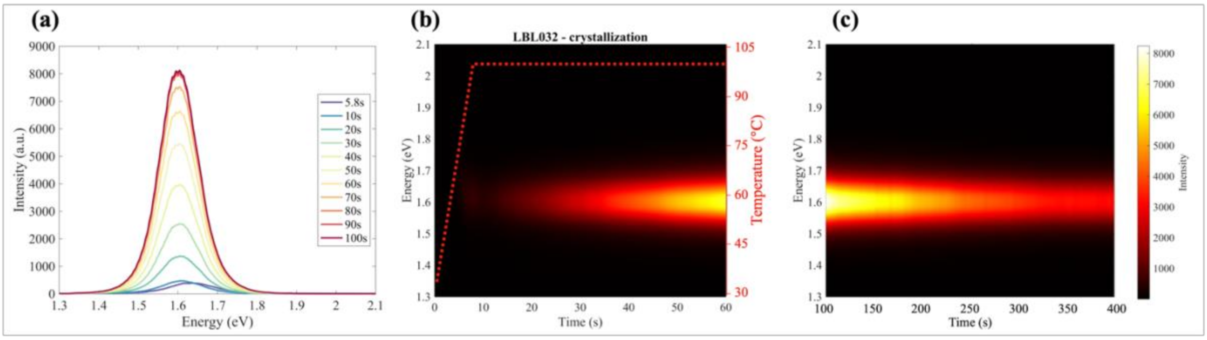

Figure 6.7 *In-situ PL measurements of MAPI:CSA during annealing: (a) example photoluminescence spectra, (b) in-situ PL map together with the substrate temperature (right y-axis), (c) longer timescale of in-situ PL experiment.*

The formation dynamics in MAPI:CSA clearly differs from pristine MAPI (**Figure 6.1**). The entire process is significantly longer than in MAPI therefore, the *in-situ* PL evolution of MAPI:CSA was also displayed in a longer timescale (**Figure 6.7(c)**).

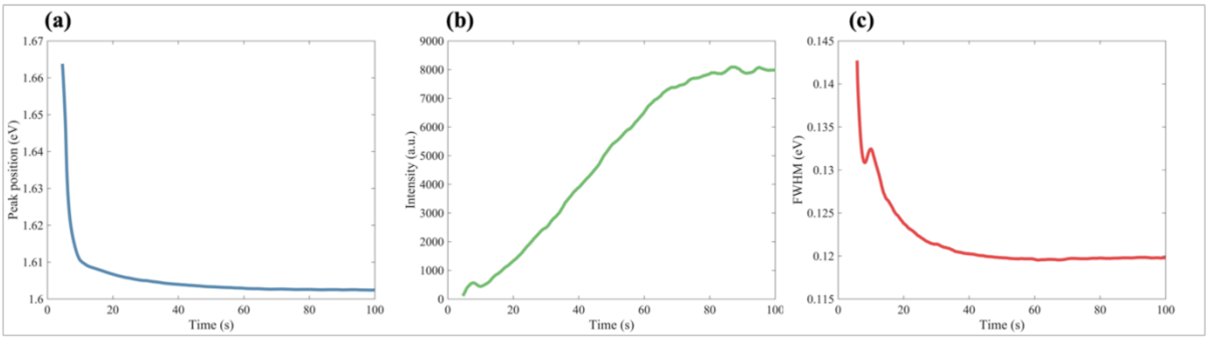

Figure 6.8 *The extracted values of emission peak position (a), PL intensity (b), and FWHM (c) from the in-situ PL measurements of MAPI:CSA.*

Similarly, as in the previous samples (MAPI, MAPIB), it was observed that the PL maximum initiated at higher energy (1.664 eV) compared with the final bandgap of the bulk perovskite film (1.602 eV) (**Figure 6.8(a)**). Therefore, the energy shifted by 0.062 eV upon annealing. Based on **Eq. 8.1.**, the initial grain size was estimated to be about 9.0 nm. The PL intensity maximum (**Figure 6.8(b)**) was reached after about 88 s from the beginning of annealing (or in 82.2 s after the start of crystallization). Interestingly, this material seems to be more resistant to degradation than CSA-free MAPI because the intensity decay started after about 100 s in the case of MAPI:CSA, compared to 20 s in unmodified MAPI. Bigger grains of MAPI:CSA (morphology discussion in **Chapter 5.4.1**) than in pristine MAPI may cause a better thermal conductance of MAPI:CSA than MAPI[180,181]. Therefore, thermal energy dissipation in the case of MAPI:CSA is more efficient and prevents local overheating under the laser beam.

6.3.2 Formation dynamics in MAPIB:CSA

Figure 6.9 shows the *in-situ* PL results of MAPIB doped with CSA (MAPIB:CSA). Spectra were collected during annealing, and the perovskite formation started after about 2.6 seconds.

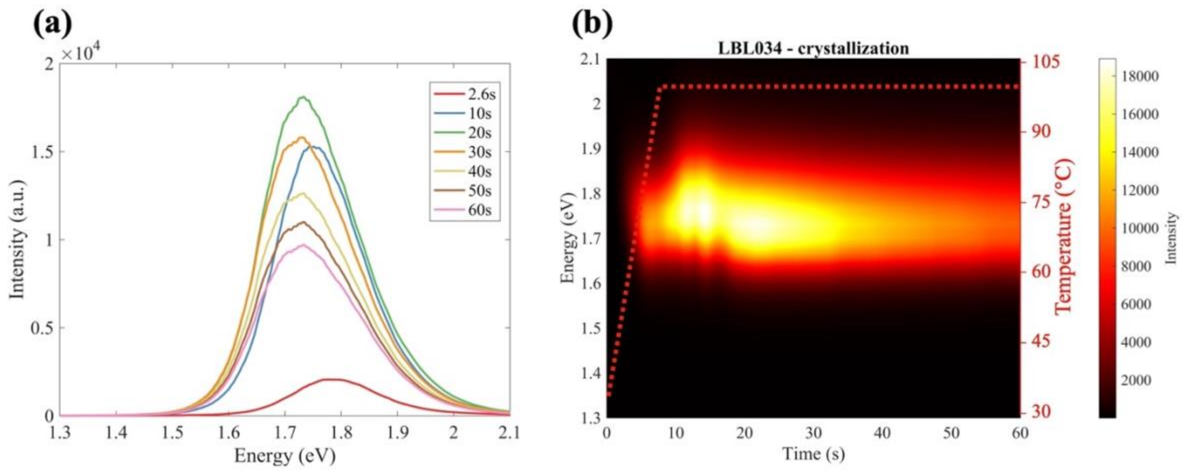

Figure 6.9 In-situ PL measurements of MAPIB:CSA during annealing: (a) example photoluminescence spectra, (b) in-situ PL map together with the substrate temperature (right y-axis).

Both blueshift and redshift are observed (**Figure 6.9(b)**), which are related to the compositional evolution during perovskite formation, dominated by an initial higher bandgap species (blueshift) and quantum confinement of initial nanograins (redshift).

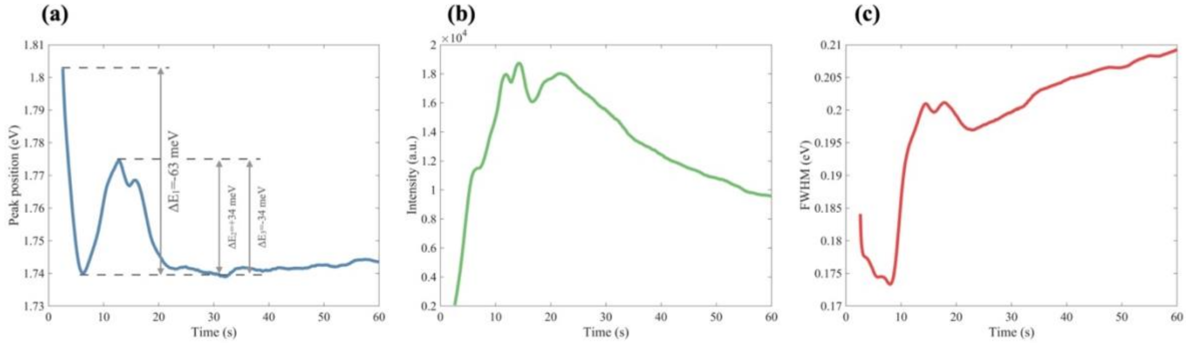

***Figure 6.10** The extracted values of emission peak position (a), PL intensity (b), and FWHM (c) from the in-situ PL measurements of MAPIB:CSA.*

Similarly, as in the all previously introduced samples, it was observed that the PL maximum initiated at higher energy (1.803eV) compared to the final bandgap of the bulk perovskite film (1.742eV) (**Figure 6.10(a)**). Therefore, the energy shifted by 0.061eV upon annealing. Based on **Eq. 8.1.**, the initial grain size was estimated to be about 9.1 nm.

From the beginning of the crystallization until 6 seconds, a gradual redshift of 0.063 eV was observed (**Figure 6.10(a)**). Then, from 6 to 12.7s, a blueshift of 0.034 eV occurred, indicating faster growth time of Br-rich species compared to iodine-based components within this time window, influencing the material's bandgap. Additionally, a local slight decrease followed by an increase of the bandgap between 12.7 to 15.9s may be related to evaporation of residual solvents (DMF, DMSO) trapped by CSA or indicates an anion exchange–like halide homogenization process, which is necessary to attain the final stoichiometry from the initial bromide-rich phase. This observation is similar to studies in Ref.[160], but they investigated different material, without CSA.

The PL intensity maximum (**Figure 6.10(b)**) was reached after about 14.3 s from the beginning of annealing (or in 11.7 s after the start of crystallization). Interestingly, the PL intensity between 15 and 22 seconds experienced a local minimum. This “intensity valley” partially overlaps with fluctuations of the bandgap discussed above (12.7 s to 15.9 s in **Figure 6.10(a)**) which suggests that this effect may also be related to the halide homogenization process at this growth stage. These claims are also indirectly supported by results on bromine-free perovskite (MAPI), where neither bandgap fluctuations nor intensity fluctuations were observed (**Figure 6.2**, **Figure 6.8**), suggesting that both effects are related to the presence of bromine within the MAPIB perovskite.

6.3.3 Discussion of in-situ PL measurements of 3D perovskites

The influence of CSA on perovskite formation dynamics was observed, and key parameters extracted from *in-situ* PL experiments are summarized in **Table 6.1** and **Figure 6.11**. First, the PL maximum initiated at a higher energy compared with the final bandgap of the bulk perovskite film within all the samples, which was associated with quantum confinement of the nanograins at the early growth stage (**Figure 6.11(a)**). Second, the initial grain size was relatively similar in all samples, so the influence of CSA was negligible in this respect. Third, within all the samples with CSA (MAPI:CSA and MAPIB:CSA), the crystallization started earlier (at lower temperature) compared to unmodified perovskites (5.8 s vs. 7.2 s in MAPI and MAPI:CSA, respectively; and 2.6 s vs. 2.8 s in MAPIB and MAPIB:CSA, respectively). It has been speculated that CSA with three oxygen atoms with lone electron pairs may interact even stronger with PbX_2 than DMSO[168] suggesting that CSA-containing species have lower solubility and therefore potentially nucleate faster than CSA-free ones. Moreover, the growth time was longer in CSA-containing samples compared to unmodified materials (82.2 s vs. 3.2 s in MAPI, and 11.7 s vs. 5.6 s in MAPIB, **Figure 6.11(b)**), which suggests the origin of larger final MAPI:CSA grains compared with CSA-free species.

***Table 6.1** Summarized results of in-situ PL on 3D perovskites with and without CSA.*

	MAPI	**MAPI:CSA**	**MAPIB**	**MAPIB:CSA**
Initial PL peak position (eV)	1.653	1.664	1.793	1.803
PL peak position in the bulk (eV)	1.611	1.602	1.722	1.742
Energy shift upon annealing(eV)	-0.042	-0.062	-0.071	-0.061
ΔE_1 (eV)	N/A	N/A	-0.044	-0.063
ΔE_2 (eV)	N/A	N/A	+0.020	+0.034
ΔE_3 (eV)	N/A	N/A	-0.047	-0.034
Initial grain size (nm)	10.9	9.0	8.4	9.1
Crystallization beginning time (s)	7.2	5.8	2.8	2.6
Growth time (s)	3.2	82.2	5.6	11.7

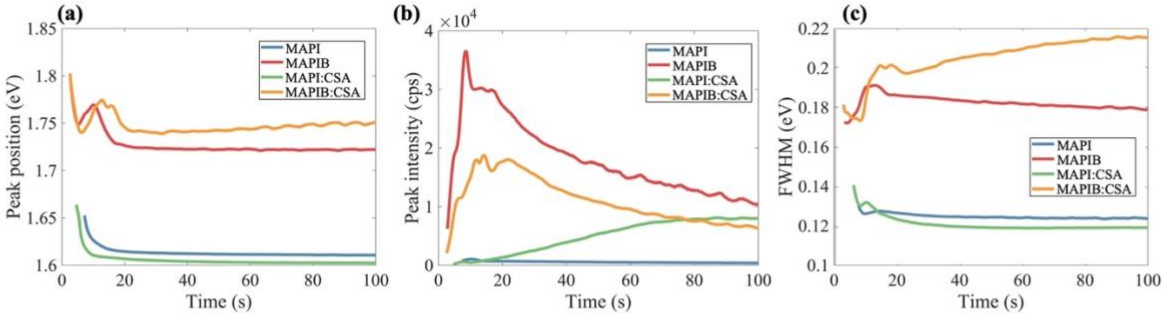

***Figure 6.11** Summarized in-situ PL results for 3D perovskites: (a) peak position, (b) PL intensity, (c) FWHM.*

Perovskite crystallization involves many steps, and the behavior of these materials is not fully understood.

In the performed research, some aspects of the crystallization process were shown and discussed. But it is still a topic that needs more research.

6.4 Formation dynamics in quasi-3D perovskites

In-situ PL studies were also done for quasi-3D perovskites (**Figure 6.12**). The chemical composition of these materials was summarized in **Table 4.1**. In short, they contain a small addition of large organic cations, phenethylammonium (PEA), compared to already analyzed 3D perovskites. Moreover, they are divided into iodine-based quasi-3D perovskites (n50I), and perovskites with the addition of bromine (n50IB), with a similar concentration of halides as in their 3D counterparts. Moreover, the influence of CSA on formation dynamics was studied similarly as in 3D perovskites.

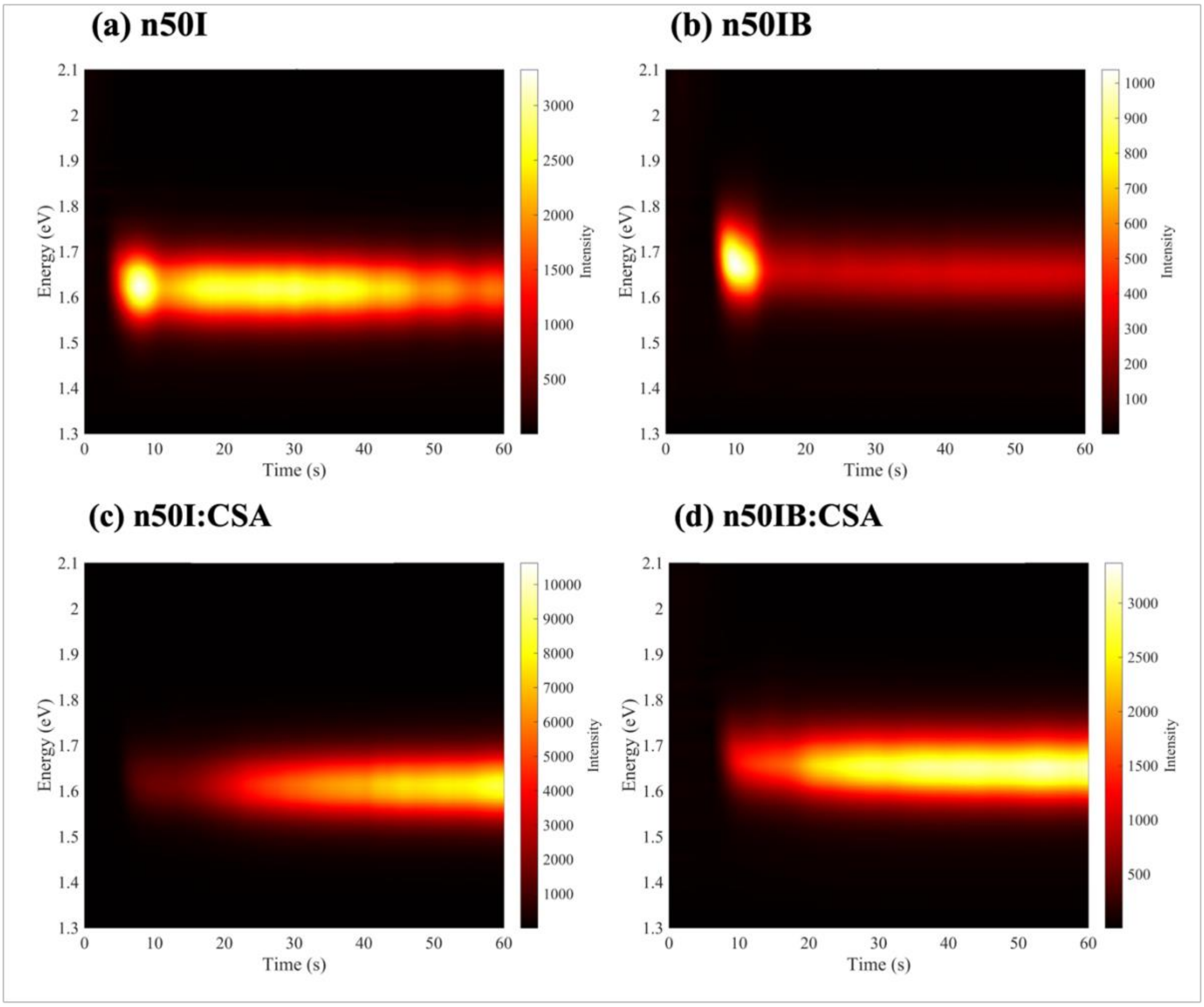

Figure 6.12 In-situ PL maps of quasi-3D perovskites with and without addition of CSA during annealing at 100 °C .

Figure 6.12 depicts the PL spectra evolution during annealing of quasi-3D perovskites without and with addition of CSA.

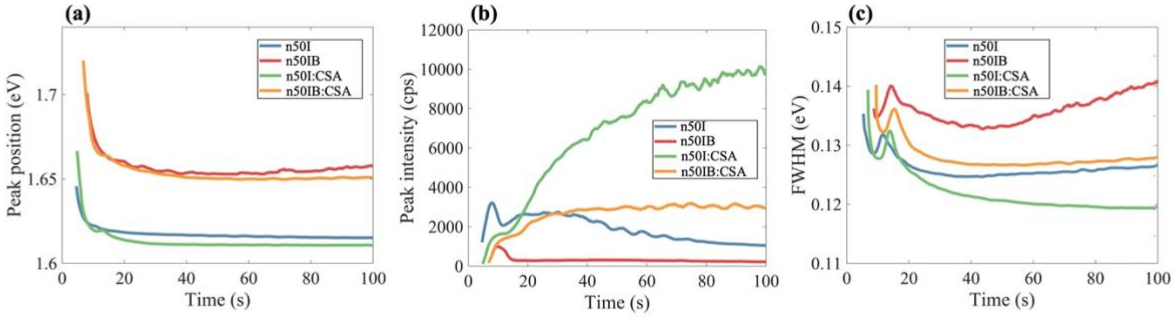

Figure 6.13 *Summarized in-situ PL results for quasi-3D perovskites: (a) peak position, (b) PL intensity, (c) FWHM.*

In both cases, i.e., iodine-based quasi-3D perovskite (n50I) and mixed-halide quasi-3D perovskite (n50IB), the addition of CSA results in the PL peak appearance at a slightly higher energy than in CSA-free films: 1.669 eV vs. 1.647 eV in n50I:CSA vs n50I, and 1.725 eV vs. 1.705 eV in n50IB:CSA vs. n50IB, see **Figure 6.13** (values summarized in **Table 6.2**).

The addition of CSA results in nucleation in the form of smaller grains, which may be a consequence of better dispersion of precursors in the initial solution when CSA is present in it.

Similarly as in the case of 3D perovskites, PL signals of all quasi-3D species initiated at a higher energy compared to the final bandgap of the bulk perovskite films, resulting in energy shifts upon annealing displayed in **Table 6.2**. By the formula in **Eq. 6.1**, the smallest initial grain size within the set was found in n50IB:CSA, followed by n50I:CSA, n50IB, and n50I (see **Table 6.2** for exact values). Therefore, the addition of CSA to both quasi-3D perovskites resulted in a decrease in initial grain sizes, but these differences were not significant. However, this effect was consistently visible for all materials.

On the contrary to MAPIB/MAPIB:CSA, neither in n50IB nor in n50IB:CSA blueshifts were observed. An increase in the bandgap in MAPIB/MAPIB:CSA was associated with faster nucleation of bromine rich species. Therefore, it is possible to conclude that good phase homogeneity from the early growth stage takes place in quasi-3D samples.

Interestingly, crystallization began earlier in quasi-3D iodine-based perovskites (4.3 s and 4.6 s in n50I and n50I:CSA, respectively) than in mixed-halide ones (7.8 s and 6.6 s in n50IB and n50IB:CSA, respectively), which is the opposite relationship than in their 3D counterparts. It is unclear at the moment if PEA cation influences PbI_2:DMSO formation energies stronger than $PbBr_2$:DMSO ones, leading to faster nucleation in n50I species. The growth time was significantly affected by the addition of CSA in both cases. The presence of camphorsulfonic acid slowed down crystallization by about 30 times compared to pristine species. PL intensity fluctuations can be observed within almost all the samples (**Figure 6.13(b)**), which may be related to either dimensionality, halide reorganization, or experimental artifacts.

__Table 6.2__ Summarized results of in-situ PL on quasi-3D perovskites with and without CSA.

	n50I	**n50I:CSA**	**n50IB**	**n50IB:CSA**
Initial PL peak position (eV)	1.647	1.669	1.705	1.725
PL peak position in the bulk (eV)	1.615	1.611	1.660	1.652
Energy shift upon annealing(eV)	0.032	0.058	0.045	0.073
Initial grain size (nm)	12.5	9.2	10.5	8.2
Crystallization beginning time (s)	4.3	4.6	7.8	6.6
Growth time (s)	3.6	100.6	2.0	68.2

Similarly as in the case of 3D perovskites, changes of FWHM were insignificant in quasi-3D materials, and observed small trends may require further in-depth studies.

6.5 Chapter summary

In this chapter, formation dynamics of perovskites was discussed and influence of bromine, dimensionality, and CSA was investigated. The most pronounced difference was observed between species with and without CSA. Presence of CSA leads to the nucleation of smaller *grains* than in the case of their counterparts (materials without CSA and Br). That said, addition of CSA promotes the growth of bigger grains in the final material (at the end of the formation process). The growth time in CSA-doped samples was significantly longer compared to CSA-free perovskites, indicating slower crystallization. CSA has three oxygen atoms with lone electron pairs which may strongly interact with PbX_2 compared to DMSO, leading to an increase in the activation energy for crystallization and slowing down nuclei densification. These results correlate with electron microscopy analysis presented in **Chapter 5.4.1**, revealing larger grains of CSA-doped perovskites.

Finally, in 3D mixed-halide perovskites (MAPIB/MAPIB:CSA), the character of the PL signal vs. time was more complex, especially considering blueshift and fluctuations of the PL intensity, being an indication of the halide homogenization process and self-diffusion of the anions during nucleation and growth. This is not the case in n50IB/n50IB:CSA therefore, they follow their target stoichiometry with good phase homogeneity from the early growth stage. These claims are also supported by chemical analysis by means of XRD, TEM-based EDS, and XPS (summarized in **Chapter 5.2** and **Chapter 5.3**), displaying homogeneous halide distribution in n50IB, and on the other hand, the formation of Br-rich clusters on the top of the film in MAPIB. Traces of halide homogenization were observed in MAPIB by *in-situ* PL studies, but research on the final materials' form (XRD, TEM-based EDS, XPS) suggests that this process does not lead to the target stoichiometry and halide uniformity.

In conclusion, CSA-containing perovskites may be good candidates for solar cell applications, among others due to larger grains, possibly affecting electrical properties of these species. *In-situ* PL studies provided deep insights into the formation dynamics in such materials and partially explained the origin of modified morphology of CSA-doped films.

7 Influence of oxygen on the degradation dynamics

7.1 Introduction

In this chapter, the influence of oxygen on the degradation dynamics perovskite will be discussed. The studies have already been published, and the author of this dissertation is the first author of the manuscript, who initiated and conducted experiments[178]. The model of oxygen-induced degradation mechanism developed by Aristidou[130] was introduced in **Chapter 3.2.** Here, the basic assumptions will be highlighted.

It has been demonstrated that exposure of MAPI layers to light and oxygen leads to the formation of superoxide species (O_2^-) and the decomposition of the perovskite film according to the following reaction:

$$4CH_3NH_3PbI_3^* + O_2^- \rightarrow 4PbI_2 + 2I_2 + 2H_2O + 4CH_3NH_2$$

Aristidou et al.[131] have shown that vacant iodine sites are the preferred location for the degradation mechanism to start. Moreover, it has been shown that the addition of chlorine leads to the substitution of iodine atoms in the perovskite lattice[182]. Therefore, in this thesis it was speculated that chlorine boosts the stability by reducing the concentration of iodine vacancy sites and suppressing the diffusion of oxygen into the perovskite layers.

7.2 Influence of Cl addition on perovskite grain structure

To check the influence of chlorine on perovskite stability and the suppression of oxygen diffusion, a material with the addition of Cl (referred to as MAPICl in this chapter) was grown. The XRD patterns of the measured samples (MAPI and MAPICl) are presented in **Figure 7.1(a)** and **(b)**, and **Figure 7.1(c)** shows the reference X-ray powder diffraction pattern of MAPI in the tetragonal structure[183]. The presence of numerous peaks originating from the perovskite structure and the absence of some low-intensity reflections indicates that the film is polycrystalline, with a close-to-random grain orientation. There is no evidence of additional phases such as PbI_2 within the sample.

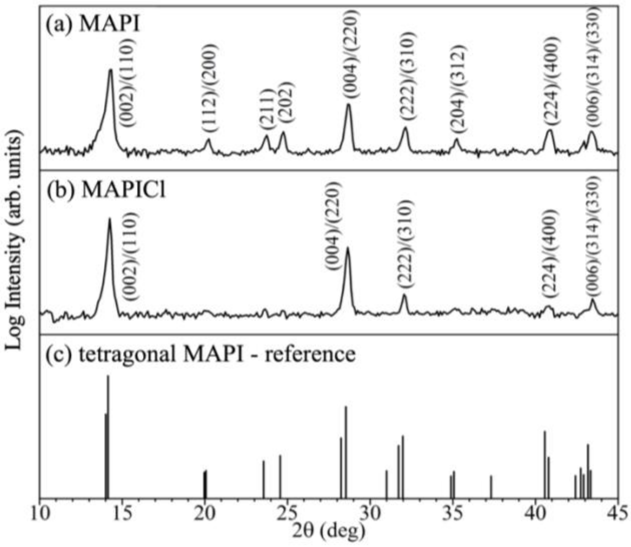

Figure 7.1 *XRD pattern of MAPI (a), MAPICl (b), and (c) the MAPbI3 reference X-ray powder diffraction powder*[183].

A smaller number of diffraction peaks and strong intensity of diffraction from (110) and its second and third order lattice planes are observed for MAPICl (**Figure 7.1(b)**). However, the peak positions are approximately the same as in the case of MAPI, indicating only a slight influence of chlorine addition on crystal lattice parameters, therefore a low doping level of chlorine. The small number of the observed XRD peaks is evidence of a highly textured film with significantly more uniform grain orientation compared to MAPI.

Moreover, it was observed that the perovskite grain boundaries in the MAPICl sample are not as clearly visible as in MAPI (**Figure 7.2**). However, even in this selected region, it can be seen that the grains are larger than those in MAPI (**Figure 7.2**). For the mixed perovskite (MAPICl) sample, its grains show average areas of about 3800 μm^2 (**Figure 7.2(c)**, red bars). They are significantly bigger than the average grain areas (about 500 μm^2, **Figure 7.2(c)**, black bars) observed for the iodide perovskite (MAPI) sample. This observation is in line with the common trend of improving the crystal quality for chloride-containing perovskites, and in general, grain enlargement has been found to be beneficial in terms of efficiency increase for both perovskite and organic solar cells[184,185].

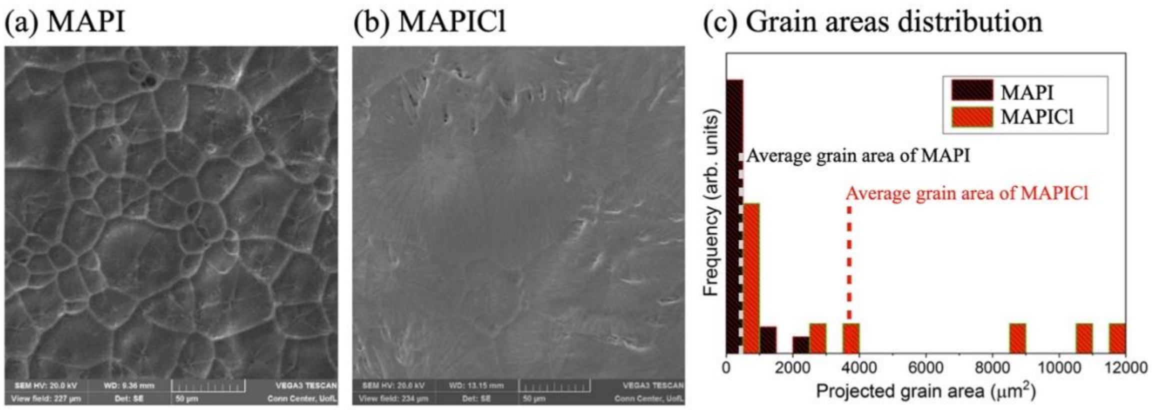

Figure 7.2 SEM images of (a) MAPI, (b) MAPICl. (c) shows grain areas distribution within MAPI and MAPICl.

Recently the role of grain boundaries in perovskite degradation has been identified and reported[186,187]. Firstly, the diffusion of oxygen can be substantially enhanced through the transport along the grain boundaries, as previously shown for inorganic perovskites[186]. We believe a similar mechanism takes place also in organic-inorganic hybrid perovskites. Secondly, grain boundaries can serve as easy pathways for iodine migration to the surface[187]. Both processes contribute to the degradation of perovskite films.

7.3 XPS studies of oxygen concentration evolution within perovskite film over time

After finding larger grains in chlorine mixed perovskite, further studies were conducted to investigate the influence of chlorine on perovskite stability using XPS measurements. XPS analysis was performed for MAPI and MAPICl formulations to track the degradation process. In XPS experiments, the carbon C1s peak at 285.5 eV is typically used for binding energy (BE) calibration. However, the C1s spectrum in our samples consists of four Gaussian components, indicating different carbon species in the measured material (**Figure 7.3**). Consistent with the literature reports, the second-highest BE peak (peak 3, orange curve in **Figure 7.3**) is related to carbon in methylammonium (MA)[98]. The most intense carbon peak component (peak 1, red curve in **Figure 7.3**) and also peak 2 (blue curve in **Figure 7.3**) could be attributed to adventitious, residual surface carbon. The 282 eV line (peak 4, green curve in **Figure 7.3**) can be regarded as a background, an artifact related to a non-monochromatic X-ray source (Al Kα line is approximately 10–15 times stronger than K-beta). It has been shown by G. Greczynski and L. Hulman that in the case of a non-monochromatic X-ray, two satellites occurred. Kα3 is shifted by approximatelly 3 eV, and Kα4 is shifted by approximatelly 9 eV from the main peak[188]. In our case, peak 4 in **Figure 7.3** corresponds to the Kα3 line discussed by Greczynski et al.

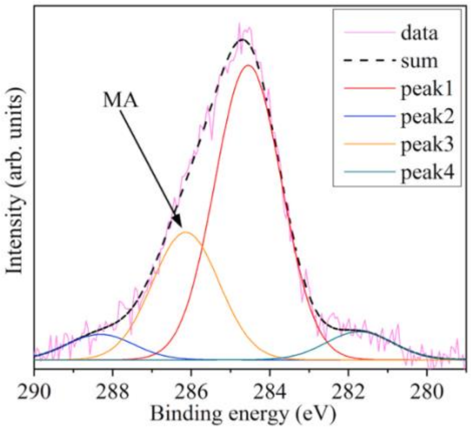

Figure 7.3 *High-resolution XPS spectrum in the energy range of carbon C1s peak (magenta solid line). The black dashed curve represents the fitted data being a sum of four Gaussian peaks. Peak 3 (orange) corresponds to carbon in methylammonium (MA)*[98]*, whereas peaks 1,2 represent other carbon species, peak 4 is an artifact related to a non-monochromatic X-ray source.*

Since the peak 1 has the most significant impact on the experimental C1s spectrum, an alternative approach for BE calibration was applied, and the iodine 3d line was used instead.

The investigated samples (MAPI, MAPICl) did not have any surface coating layers. As the degradation model involves oxygen diffusion, the amount of oxygen in these samples was probed by tracing the intensity of the oxygen O1s XPS peak. The O1s spectrum corresponding to the fresh MAPI sample is presented in **Figure 7.4**.

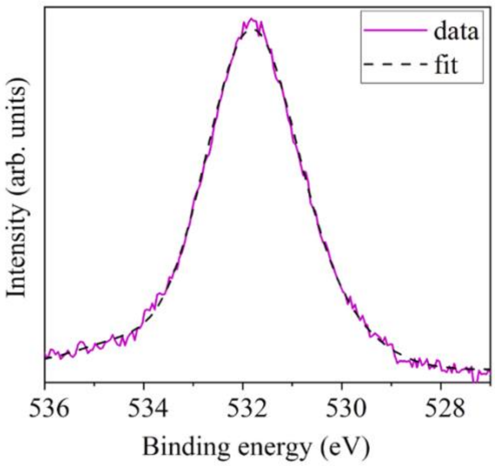

Figure 7.4 XPS spectrum of fresh MAPI sample in the energy range corresponding to oxygen O1s peak (magenta solid line). The black dashed curve represents the fitted data.

Using Atomic Sensitivity Factors (introduced in **Chapter 4.5**), the relative intensity of the O1s peak was converted into oxygen content (atomic percentage of oxygen compared to signals originating from all the elements present within the perovskite) in the subsurface layer (**Figure 7.4**). The XPS experiment showed that the amount of oxygen for MAPI considerably increased in the top surface layer with exposure time to air, by about 23% and 47% after 7 and 20 hours of aging, respectively (**Figure 7.5**). For MAPICl, the increase in the surface concentration of oxygen was much more moderate, by about 8% and 25% after 7 and 20 hours, respectively (**Figure 7.5**). It can be then concluded that the presence of chlorine within perovskite slows down oxygen diffusion into the layer.

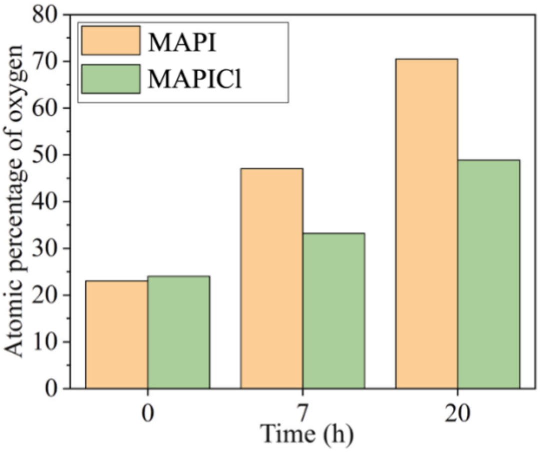

Figure 7.5 Amount of oxygen in the surface layer of MAPbI3 and MAPbI3-xClx samples for fresh materials, and after 7 h and 20 h of exposure to air. The bars represent intensities of O1s peaks from the respective XPS spectra.

Assuming the model describing influence of oxygen in the degradation process proposed by Aristidou et al.[130], the addition of chlorine should lead to improved stability and slow down the degradation induced by the generation of superoxide species. However, it needs to be emphasized that XPS is a surface technique, and the presented bar graphs in **Figure 7.5** do not represent the amount of oxygen within the entire volume of the sample but rather in the top ~2 nm-thick layer only. Nevertheless, the degradation process begins at the surface, and a 20-hour time was found to be enough for even the mixed perovskite with unprotected surface to show the substantial increase of oxygen within the sub-surface layer.

7.4 Reduction of Pb^{2+} to Pb^0 as a sign of slower oxygen diffusion in MAPICl

Interestingly, during the aging experiment, significant changes in the lead Pb4f signal for the MAPICl sample were observed (**Figure 7.6(b)**), while in the case of MAPI perovskite, a slight shift towards higher BEs was only noticed (**Figure 7.6(a)**).

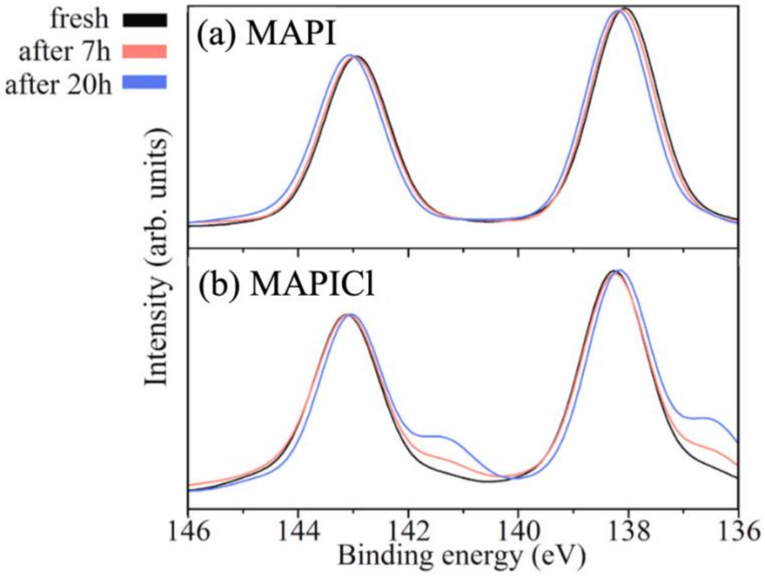

Figure 7.6 *Time evolution of the XPS spectrum of (a) MAPI, and (b) MAPICl, in the energy range of Pb4f peak.*

It is worth mentioning that Pb4f line splitting is due to spin-orbit interaction, with Pb4f7/2 - Pb4f5/2 doublet separation of ~4.86 eV[189] and a theoretical intensity ratio between the two components of 4:3. As these parameters are approximately constant, they were used as constrains during line deconvolution of Pb4f spectra from samples MAPICl and MAPI. The changes of the Pb4f signal were monitored as an additional probe of the processes occurring during degradation of the layer. It was observed that an additional double-peak structure at a lower BE shoulder appeared already in fresh MAPICl sample and was more pronounced after the sample exposure to air. The intensity of this structure increased with time during the aging experiment. As an example, deconvolution of the Pb4f spectrum for the MAPICl sample is presented in **Figure 7.7** (for the sample after 20 hours of exposure to air). The spectrum was deconvoluted into two dominant doublet Gaussian lines and a weaker third one at higher BE, which will not be discussed further.

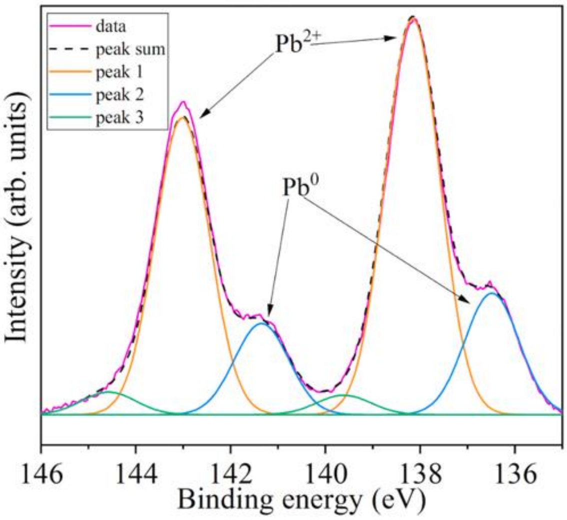

***Figure** 7.7 XPS spectrum in the lead energy region for MAPICl sample after 20 h of exposure to air. Double peak 1 (red) - simulation of lead Pb^{2+} originating from perovskite, double peak 2 (blue) - simulation of reduced lead Pb^0 [98]. Additional, double peak 3 (green) also occurred.*

The strongest doublet (orange line, peak 1 in **Figure 7.7**) can be assigned to Pb^{2+}, being a regular cation in perovskite. For identification of the other pronounced doublet, the shifting of the XPS peak to lower BE indicating the reduction process of a particular element was recalled. Thus, we agree with the already proposed interpretation[98] that the discussed Pb doublet corresponds to metallic lead Pb^0 being a product of the reduction reaction:

$$Pb^{2+} + 2e \rightarrow Pb^0$$

Another possible interpretation of the discussed doublet is its link to lead oxide. However, according to the literature[190–192], the position of Pb4f7/2 peak in lead oxide ranges from 137.6 eV to 138.2 eV. Moreover, such a significant XPS line shift should be linked to a change of the element charge. It has been reported that the Pb4f peak position in metallic lead is 136.4 eV[193]. The XPS calibration error in our case does not exceed 0.5 eV. Therefore, based on the literature data and the three-sigma rule, we are convinced that the identification of 136.48 eV observed in our experiment should be interpreted as the presence of Pb^0.

The interpretation of the reason for Pb^0 appearance in MAPICl is not obvious. One of the reasons for such behavior, meaning reduction of Pb^{2+} to Pb^0, may be a fact that Cl-free perovskite possibly provides an oxidizing environment due to more efficient oxygen diffusion into the perovskite layer than in the case of Cl-containing one. Therefore, in-diffused oxygen in MAPI oxidizes lead originating from perovskite decomposition. Consequently, Pb^0 is not observed in MAPI XPS measurement. It seems therefore that for the MAPICl, the process of lead reduction from Pb^{2+} to metallic lead Pb^0 takes place during exposure to air.

Based on the obtained XPS spectra, the ratio of the amount of metallic lead to the total lead content within the top layer of the sample was calculated and the results are shown in **Figure 7.8**.

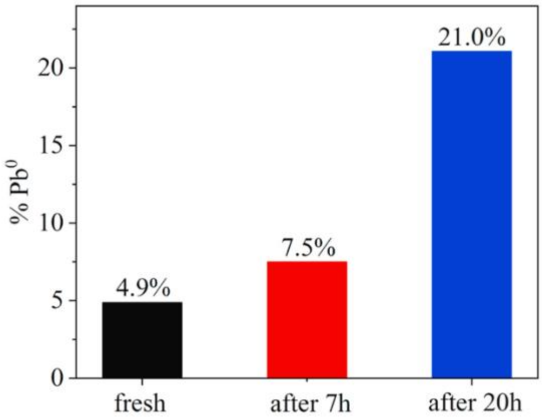

Figure 7.8 *A bar graph showing change of metallic lead Pb^0 amount in MAPICl with time. $\%Pb^0$ means the percentage amount of Pb^0 vs whole lead content in the specimen.*

As can be seen, the amount of metallic lead Pb^0 increased with the ageing time. For the fresh sample, this value was 4.9%, while after 7 hours of air exposure, it increased to 7.5%, and after 20 hours, it reached 21% of the total lead concentration. We tried to understand the lead behavior in the MAPICl sample. One possibility is that it is caused by the evaporation of volatile compounds or elements. It could be assumed that chlorine or iodine evaporates during aging, leaving metallic lead behind. However, according to the respective XPS peaks, it is evident that a change of iodine concentration takes place for both samples, whereas lead reduction is observed for the mixed perovskite only. Therefore, it can be concluded that aging process of the mixed perovskite is associated with lead reduction, but the mechanism responsible for this phenomenon remains unclear.

7.5 Degradation kinetics

The degradation process and chlorine influence on it was also observed over a timescale of two weeks for MAPI and MAPICl by means of an XRD experiment. Using this technique, changes in materials occurring in the volume were traced. The penetration depth of X-rays is of the order of micrometers, while the thickness of the perovskite layer was of about 100 nm. Thus, the XRD measurement results applied to the entire volume of the sample, not just its surface layer only, as in the case of XPS measurements. **Figure 7.9** presents the XRD pattern for angles corresponding to PbI_2 (perovskite degradation product) and perovskite. The observed diffraction peaks were identified as the (001) lattice plane peak for PbI_2 and the (110) lattice plane peak of perovskite.

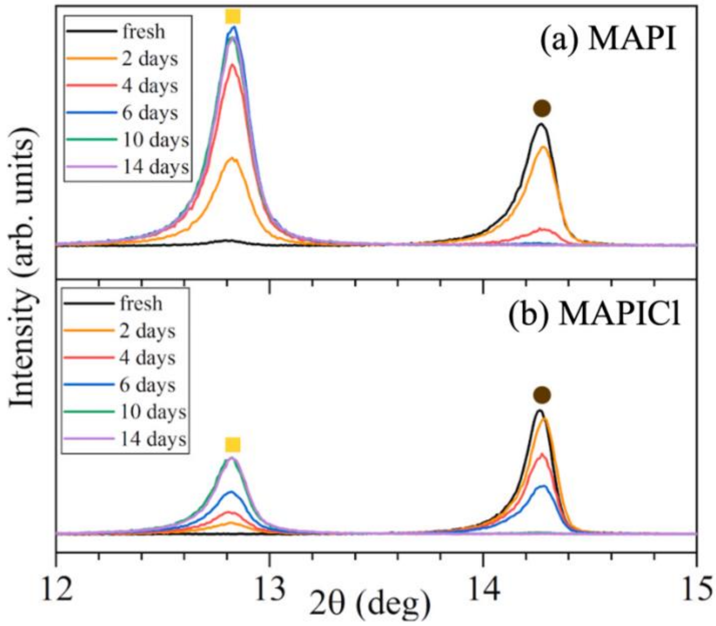

Figure 7.9 *XRD of MAPI (a) and MAPICl (b) in a low angle region. The first peak (marked with a square) originates from PbI_2 (degradation product), whereas the second one (marked with a circle) was due to diffraction from (110) lattice planes of perovskite. Evolution of these diffraction curves is shown in a time-scale up to 14 days.*

It is worth noticing that the perovskite peak shown in **Figure 7.9** consists of two components with different intensities which causes asymmetry of the resulting overlapping peak ((002) and (110))[194]. From the diffraction data for MAPI it was evident that during exposure to air decomposition of iodide perovskite to PbI_2 took place. The observed decrease of the (110) perovskite diffraction peak was accompanied by the increase of the diffraction peak related to (001) PbI_2 planes. The (001) peak of PbI_2 grew significantly - after 2 days of exposure to air it was almost as intense as the (110) perovskite peak and after 6 days the perovskite peak almost entirely vanished. Moreover, at the end of the experiment (14th day), the (001) PbI_2 peak intensity was significantly higher than the intensity of the perovskite peak for the fresh sample. The behavior was quite different for the mixed perovskite layer. In this case, degradation was also evident by the decrease of the (110) perovskite diffraction peak. However, after 6 days the perovskite peak could be still observed and its intensity was almost the same as that of the PbI_2 peak. Also, final intensity of the PbI_2 peak was about half of the initial perovskite peak intensity.

To analyze evolution of the XRD patterns quantitatively, intensities of the perovskite (110) and PbI_2 (001) diffraction peaks were integrated for both MAPI and MAPICl, and plotted as a function of air exposure time in graphs presented in **Figure 7.10**. Interestingly, the observed decay of perovskite peaks (**Figure 7.10(a)** and **(c)**) could be described by a reaction exhibiting first order kinetics, whose rate is directly proportional to the momentary amount of perovskite. Fitting to the experimental data of both perovskites with exponential curves described by the formula:

$$N(t) = N_0 exp\left(-\frac{t}{\tau_p}\right)$$

yielded the characteristic degradation times τ_p shown in **Table 7.1**.

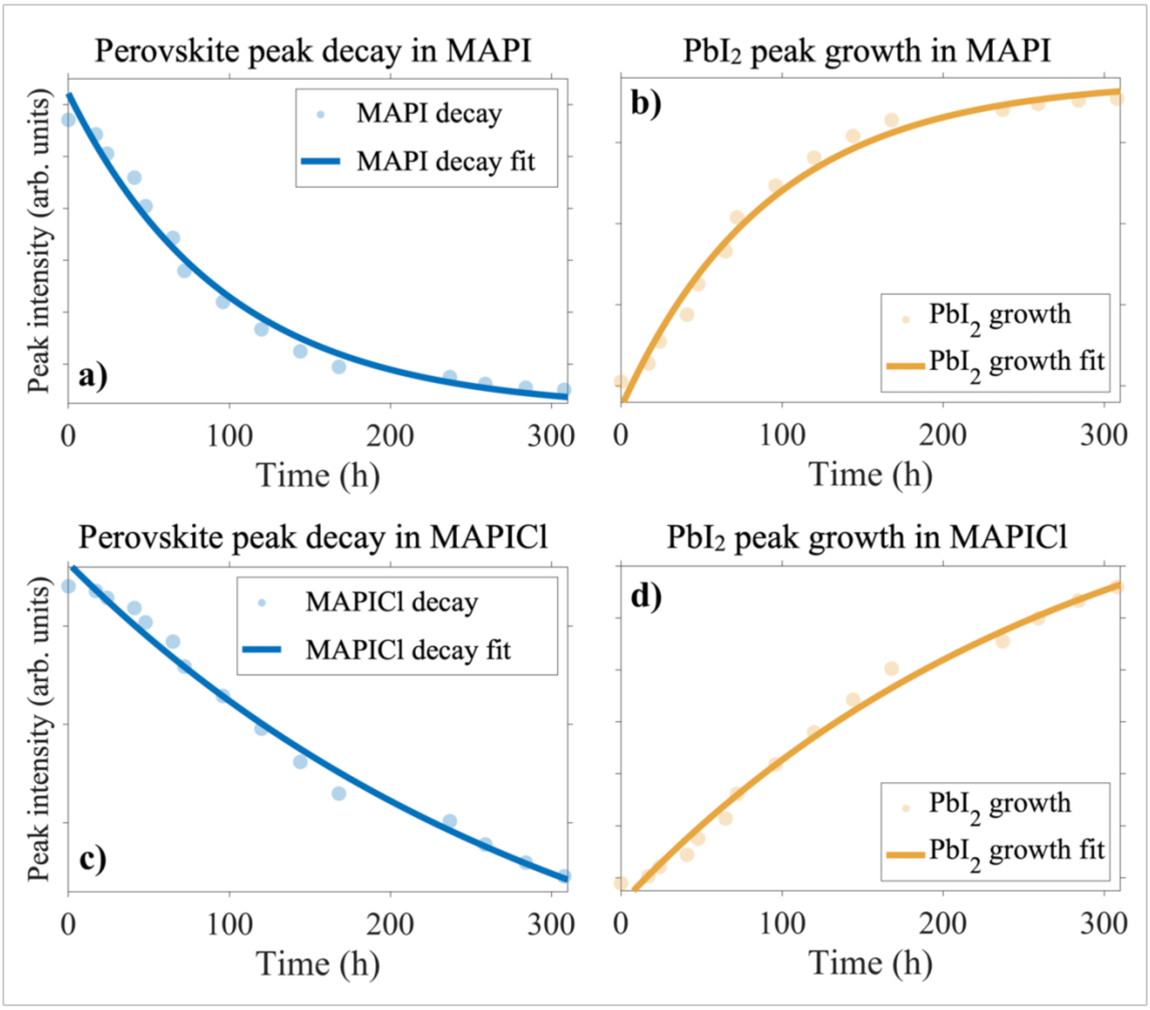

Figure 7.10 Integrated XRD peak intensities (points) and fitted kinetic reaction curves (solid lines). (a) MAPI perovskite integrated peak decay and b) PbI_2 integrated peak growth in MAPI; (c) MAPICl perovskite integrated peak decay and d) MAPICl PbI_2 integrated peak growth.

In case of MAPICl, this time was about twice as long as for MAPI. Here, N(t) represents momentary amount of perovskite, while N_0 is the initial amount of fresh perovskite. The fitted curves are shown in **Figure 7.10**. They describe the process of degradation of both perovskites reasonably well. A more realistic model should take into account diffusion processes (most probably oxygen diffusion) starting at the surface and leading to perovskite layer degradation. However, such a model would include parameters that may be difficult to estimate. Also, the formula describing the time dependence of perovskite decomposition may be very complex. For example, in-depth studies of oxygen diffusion in inorganic perovskites[186,195,196] have indicated several mechanisms of diffusion, including bulk diffusion with diffusion coefficient depending on concentration of vacancies, which are sites for oxygen to occupy, fast (with a few orders of magnitude higher diffusion coefficient) grain boundary diffusion or diffusion along dislocations. Nevertheless, the experimental data can be described with the proposed simplified model, and the determined time constants (the only fitting parameter except for the normalizing factor and possible background), which characterize the degradation times of the measured materials, are easy to compare. However, it should be noted that the introduced model is very simplified. The real process of perovskite decomposition starts at the surface and the decomposition is not uniform throughout entire volume of the perovskite film.

The analysis showed that the increase of the PbI_2 diffraction peak intensity during aging experiment was fully correlated with the decay of the perovskite peak. Specifically, the increase of the PbI_2 peak (**Figure 7.10(b)** and **(d)**) could be described the following formula corresponding to the first order kinetics of compound creation:

$$n(t) = n_0\left(1 - exp\left(-\frac{t}{\tau_i}\right)\right) + y_0$$

Here, n(t) represents momentary amount of PbI_2, n_0 is the final amount of created PbI_2 during the degradation process, y_0 is the initial amount of PbI_2 due to excess of lead (II) iodide precursor (it was the case for some samples in which unreacted PbI_2 precursor was present) and τ_i is the characteristic time of PbI_2 formation. The obtained τ_i are shown in **Table 7.1**.

Table 7.1 *Characteristic times of both perovskite degradation (τ_p) and PbI_2 formation (τ_i).*

	MAPI	**MAPICl**
τ_p (hours)	97 ± 11	313 ± 83
τ_i (hours)	92 ± 10	275 ± 58

The times τ_p and τ_i for each sample are similar within the experimental errors (97h and 92h in MAPI, and 313h and 275h in MAPICl), indicating that the degradation of perovskites was directly related to the formation of PbI_2. The analysis also showed that, both perovskite degradation and PbI_2 formation times were three times longer for the MAPICl than for the MAPI, proving therefore better stability of mixed perovskite over the pure iodine one.

In order to understand kinetics and possible correlation of oxygen diffusion to the sub-surface layer and degradation process in the entire volume of perovskite films, results of XPS and XRD analysis were compared. **Figure 7.11** shows the integrated intensities of PbI_2 (001) XRD peaks as a function of air exposure time for MAPI and MAPICl, similarly as the data shown in **Figure 7.10(b)** and **(d)**, respectively, but measured for the first 70 hours only.

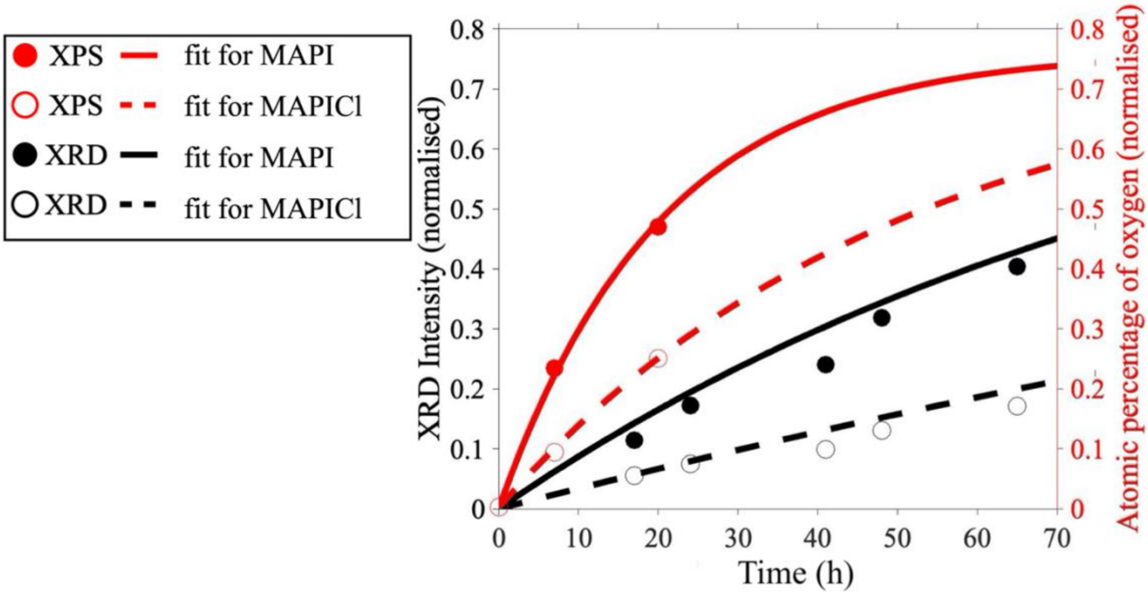

Figure 7.11 *Comparison of XRD and XPS data for air-exposed films. Time evolution of PbI_2 (001) XRD peak intensities (black symbols) and surface oxygen concentration (red symbols) for MAPI (full dots) and MAPICl (open dots) samples. Lines represent curve fitting using formulas described in the text.*

The surface oxygen concentration change in time obtained from the XPS analysis of these samples is also presented in **Figure 7.11**. The following two observations can be made based on this comparison. Firstly, XPS and XRD provide complementary information on the perovskite degradation process. XPS probes changes in oxygen concentration within a thin sub-surface layer, and therefore, the observed processes are faster than the degradation phenomena, which take place in the entire volume, monitored by XRD. Although the data obtained from XPS was limited only to three points per sample (as shown in **Figure 7.5**), we described them using a first order kinetics model. This allowed to estimate the characteristic times of oxygen build-up in the sub-surface layer. The increase of the sub-surface oxygen concentration was fitted using the formula:

$$n(t) = n_0\left(1 - exp\left(-\frac{t}{\tau_{ox}}\right)\right) + y_0$$

where n(t) is the momentary atomic percentage of oxygen, n_0 is the final concentration of oxygen and τ_{ox} is the characteristic time of oxygen diffusion into the perovskite layer. The measured kinetic times corresponding to oxygen build-up differed between samples. In the case of iodine perovskite (MAPI), the time was significantly shorter (~20 h), than in the case of mixed perovskite (MAPICl) films (~51 h). This shows that the oxygen diffusion was slowed down significantly (about three times) in the mixed perovskite as compared to that in pure iodine perovskite material. Our data indicates that in mixed perovskites (i.e., for the MAPICl sample) the oxygen diffusion is less effective than in the case of pure iodine perovskite (i.e., MAPI) sample suggesting that the number of vacancies is reduced due to chlorine presence. Therefore, these findings are in agreement with the previous theoretical works[131,182], proving important role of vacancies in the oxygen diffusion process. Although, there were only few XPS experimental points and the precision of the quantitative determination of characteristic oxygen diffusion times was limited, the analysis showed unequivocally that τ_{ox} for pure iodide perovskite material was significantly shorter than τ_{ox} for the mixed material. However, stabilization of iodide perovskite by chlorine addition may be due to an additional mechanism besides the mentioned reduction of iodine vacancy concentration. Namely, as can be seen from the diffraction patterns in **Figure 7.1(a)** and **(b)**, and also, from SEM images (**Figure 7.2**), chlorine addition improves the perovskite crystal quality and leads to increased grain size, which may result in slower oxygen diffusion due to the reduced number of grain boundaries. Diffusion across grain boundaries is significantly faster than through the bulk material, which makes the effect of larger grains potentially more important than the concentration of iodine vacancies in the material.

The characteristic times associated with oxygen diffusion in the sub-surface layer should be compared with the degradation times of the entire perovskite film. The data is summarized in **Table 7.2**. It can be seen, that the oxygen built-up in the sub-surface layer occurred about 5 times faster than the degradation in the entire perovskite volume.

***Table* 7.2** *Comparison of the characteristic times associated with oxygen diffusion in the sub-surface layer (τ_{ox}) and the degradation times of the entire perovskite film (τ_i).*

sample	MAPI	MAPICl
τ_{ox} (hours)	20 ± 1	50 ± 2
τ_i (hours)	95 ± 10	275 ± 58

Therefore, it is believed that these two processes are related, and the degradation of perovskite is the result of oxygen diffusion. The times characterizing oxygen diffusion into the sub-surface area are approximately five times shorter than the ones characterizing the degradation of the entire perovskite volume for both measured materials. Moreover, perovskite degradation times shows a similar trend as the one describing oxygen diffusion, i.e., the material with the addition of chlorine show slower oxygen diffusion and better stability. Having said that, oxygen diffusion is not the only factor responsible for perovskite decomposition and degradation. The organic cations in perovskite's structure are very hygroscopic and therefore, the presence of moisture might lead to the material's degradation (this process will be discussed in the next Chapter)[197]. Although the role of water diffusion in degradation processes will be explored in subsequent chapters of this thesis, it should be noted that this factor becomes significant only under conditions where humidity exceeds 50%. In contrast, the current experiment was conducted under relative humidity levels of less than 40%. This condition, according to the results presented in the next Chapter, **Chapter 8**, effectively mitigates the impact of moisture on degradation processes. Therefore, within the parameters of this experiment, oxygen emerges as the dominant agent contributing to the degradation of the perovskite materials.

Additionally, it has been shown that MAPI perovskite decomposes and converts into lead iodide under UV light even without the presence of moisture and oxygen[198]. XPS helps to monitor the changes in oxygen concentration within a thin sub-surface layer. On the other hand, XRD provides information from the entire volume of the layer. In agreement with the Non-Steady-State diffusion model[199], the observed oxygen diffusion in subsurface layer is significantly faster in than the degradation of the entire layer, monitored by XRD (**Table 7.2**). This also indicates that the oxygen diffusion was considerably faster than any other possible degradation processes, which could originate from other environmental factors (e.g., humidity, UV illumination, etc.). Therefore, for the overall conclusion of this study, it seems justifiable to neglect these other factors, especially since all samples were kept under the same environmental conditions.

7.6 Chapter summary

In this work, films of methylammonium lead iodide perovskite and mixed perovskite with chlorine were prepared and analyzed in terms of their structure and stability. XRD analysis performed on these samples confirmed that all perovskite films were synthesized successfully and that they crystallized in the tetragonal structure. The obtained films of mixed perovskite were highly textured and displayed only strong diffraction peaks from the (1 1 0) and (2 2 0) lattice planes, whereas the films without chlorine were less ordered and consisted of smaller, randomly oriented grains showing all allowed peaks in their XRD patterns.

According to the mechanism of perovskite degradation, proposed by Aristidou N.[131], oxygen plays a crucial role in perovskite decomposition, which means the degradation kinetics should depend on the number of iodine vacancies, which are preferential sites for oxygen diffusion. Chlorine, when added to iodide perovskite, substitutes for iodine and improves material stability, most likely due to the reduction of the iodine vacancy number and/or better crystalline quality. The Aristidou's model and its conclusions were successfully verified by our experiments. In particular, it was proven that the addition of chlorine slows down the oxygen diffusion inside the perovskite structure. Furthermore, the XRD studies showed higher stability of the films with chlorine (i.e., mixed perovskite) compared to the films of pure iodine-based material. As measured, the decay of the perovskite XRD pattern and the simultaneous growth of the PbI_2–related signal were considerably faster in the case of chlorine-free material, which showed the characteristic degradation time of about 95 hours, i.e., much lower than the time of about 300 hours measured for the mixed perovskite films. It should be emphasized that the results obtained from the XPS and XRD measurements provided complementary information on the degradation process in perovskite films, as XPS is a surface technique, while XRD allows probing the entire volume of the samples. Therefore, the kinetics of processes related to oxygen diffusion into subsurface region were faster when probed by XPS than degradation processes measured by XRD. The characteristic times of oxygen diffusion into the sub-surface layer (probed by XPS) of perovskite films were about 5 times shorter than the characteristic volume degradation times (measured in XRD) in these materials. However, we provide arguments that these processes are related, and indeed oxygen diffusion leads to perovskite degradation. During ageing of mixed perovskite, the change of the XPS spectrum of lead was noticed: the additional peaks associated with metallic lead were observed, and their concentration increased with time. However, the exact mechanism of Pb reduction reaction accompanying degradation of perovskite mixed with chlorine remains unclear.

8 Perovskite reversible hydration dynamics

Understanding the process of water intercalation in perovskite films is of the key importance for improving the long-term stability of perovskite solar cells. In this work, we investigated the hydration dynamics in the state-of-the-art 3D and newly developed quasi-3D perovskite films based on methylammonium lead halides.

The mechanism of perovskite's reversible hydration was discussed in **Chapter 3.3**.

The aim of this study was to substantially enhance perovskite stability by combining and testing different approaches (and their synergy), including: (i) addition of bromine to iodine-based perovskite and (ii) usage of bulky organic spacers. These materials were evaluated under hydrous conditions. The samples used in these studies were MAPI, MAPIB, n50, and n50IB, as summarized earlier in **Chapter 4.1.1** and **Table 4.1**.

8.1 X-Ray Diffraction

To study the influence of water vapor, samples were kept for weeks under a humid atmosphere in the dark, and their XRD patterns, as well as relative humidity (RH) data, were systematically recorded over time.

Figure 8.1(a) shows a time-resolved (TR)-XRD map of the perovskite sample. It was observed that under conditions of relative humidity (RH) lower than 45%, no hydration process was observed (no additional XRD peaks from the hydrated form from 0 to 12 days in **Figure 8.1(a)**).

After exposing the sample to an airflow with >45% RH (maximum 50% RH) for 15 days, the sample exhibited several XRD peaks related to its degradation. In addition to the characteristic diffraction peaks of pristine perovskite (labeled as **PVSK** in **Figure 8.1(a)**) and its well-known degradation product, **PbI_2**, two additional clearly visible diffraction peaks apperared at 8.7° and 10.6°, respectively (labeled as **HP** in **Figure 8.1(a)**), indicating the formation of hydrated perovskite phases[200]. A TR-XRD cross section after 18 days is shown (in a logarithmic scale) in **Figure 8.1(b)**. Besides peaks from the monohydrate phase, some traces of dihydration (X-ray peaks at 11.8°, 12.3° and 14.0°) were also observed, albeit with significantly weaker intensities (labeled as 2HP in **Figure 8.1(b)**).

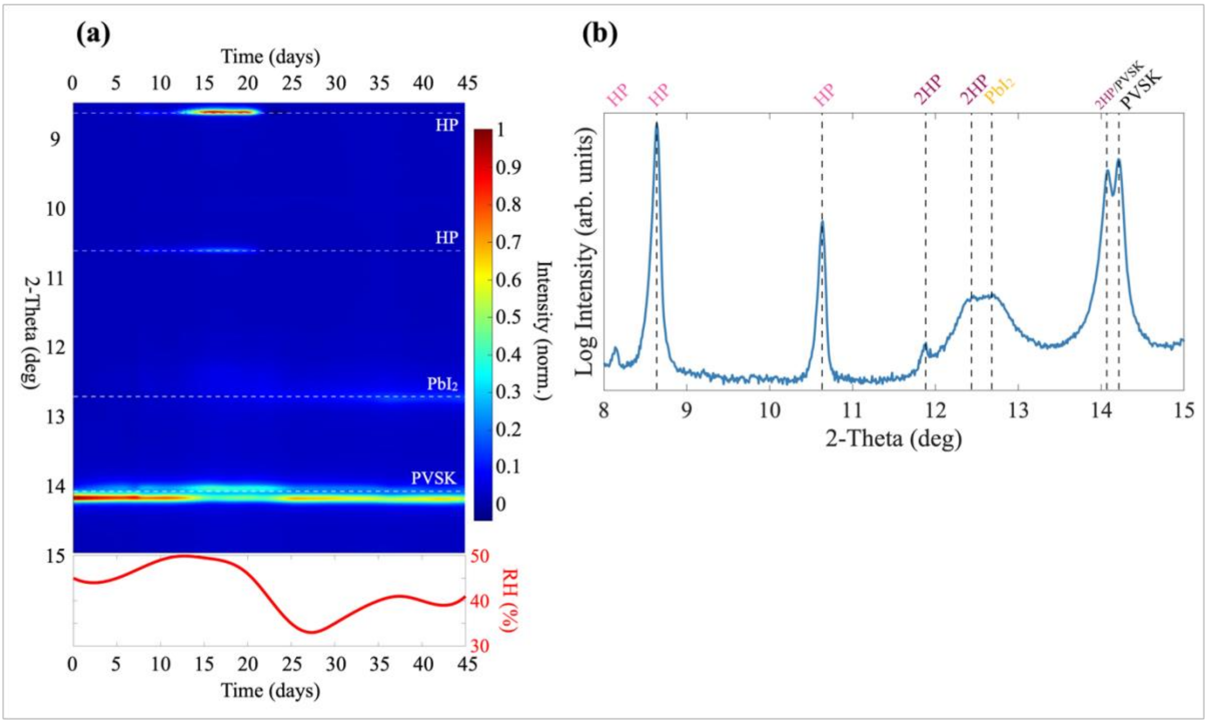

Figure 8.1 *(a) Exemplar time Resolved X-Ray Diffraction for perovskite material with peaks from:* ***PVSK*** *–perovskite,* ***PbI₂*** *–product of degradation,* ***HP*** *–hydrated phases. The time humidity profile (bottom panel) and X-ray peak intensity scale (right) are also included. (b) XRD pattern after 18 days of exposure to humid air.*

Furthermore, the study demonstrated that even a slight reduction of the humidity can trigger a reversal of the hydration process. In fact, dehydration of the sample was observed when the humidity was reduced by less than 10% (<40% RH). The HP and 2HP peaks completely disappeared after 20 days under such conditions (**Figure 8.1(a)**), indicating that the observed hydration was a fully reversible process. A similar hydration and the emergence of XRD peaks of mono- and dihydrate phases, albeit at a much faster rate (within 30 mins of exposure), were recently reported by *Leguy et al.*[132] for perovskite films subjected to an airflow of higher humidity (80±5 % RH). The drastic difference in the hydration rate observed in our, lower-humidity study (i.e., 50% RH) and the experiments reported by *Leguy et al.*[132] indicates the key role that the RH value plays in controlling the kinetics of the hydration process[134]. To confirm that the kinetics indeed strongly depend on the RH value, we conducted our own additional control XRD measurements on our perovskite films (MAPI), this time subjected to high humidity of 85% RH, and compared the results with those from the lower humidity conditions (i.e, 50% RH).

Figure 8.2 shows a time series of XRD patterns obtained in the high-humidity experiment. For the first 30 minutes, the RH was kept below 80%, and then, at t = 30 min, it was sharply increased to 85% and maintained at this level for another 30 minutes (i.e., until t = 60 min). Interestingly, the first XRD pattern measured under this elevated humidity (at t = 45 min) already showed well-developed monohydrate peaks, labeled as “HP” in **Figure 8.2**.

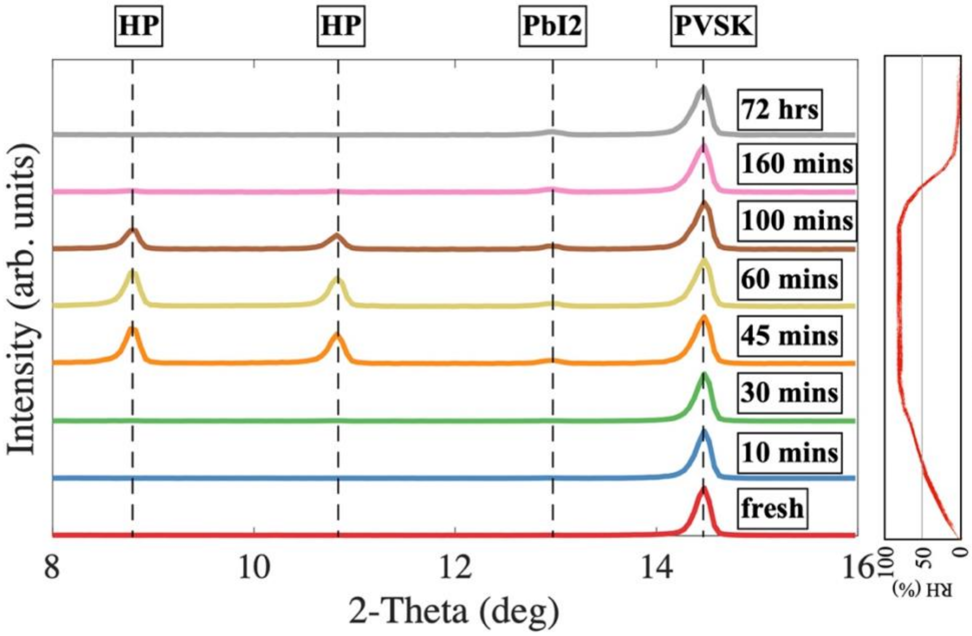

Figure 8.2 Hydration and dehydration of MAPI at humidity of 85%. The changes in the humidity level are schematically shown on the right side.

The second XRD pattern, acquired 15 minutes later (i.e., at t = 60 min), exhibited practically the same intensities of these two peaks, indicating that the hydration had already reached its saturation level. Therefore, at this time (at t = 60 min), we initiated the dehydration stage of the experiment by replacing the humid airflow with dry N_2 gas. The XRD pattern collected after 40 minutes under such conditions (i.e., at t = 100 min) showed both monohydrate peaks significantly reduced, and after an additional 60 minutes (at t = 160 min), these peaks were practically gone, and the entire film transformed back to the perovskite structure. This high-humidity experiment was consistent with the hydration rate reported by *Leguy et al.*[132]. Indeed, when combined with our results discussed earlier from the low-humidity (50% RH) study, these results confirmed that by controlling the humidity, the rate of perovskite hydration can be widely tuned over orders of magnitude.

Figure 8.3 presents TR-XRD maps of the four investigated samples (maximum humidity 50%). It can be observed that hydration reactions took place only in the iodine-based samples only (MAPI and n50I in **Figure 8.3**). Interestingly, the XRD pattern of the MAPI sample revealed only one peak, at 8.7°, associated with the hydration, while the n50I sample showed this peak and a weak peak at 10.6°. The peak at 8.7° was stronger than

10.6°, and in the initial stage of hydration only this stronger peak was visible. Therefore, it seems that the peak at 8.7° may indicate the early stage of the hydration process. A similar observation of a delayed occurrence of the 10.6° peak was reported in Ref. [132].

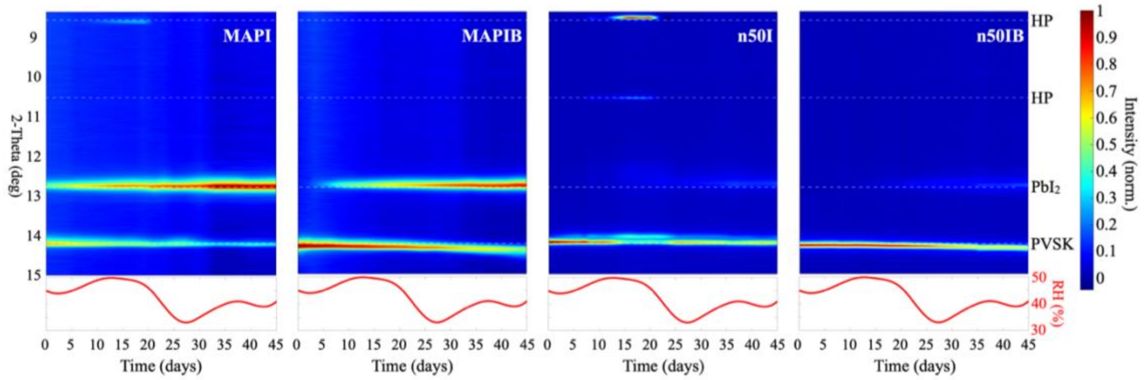

Figure 8.3 Time resolved X-ray Diffraction with peaks from: ***PVSK*** *–perovskite,* ***PbI_2*** *– product of degradation,* ***HP*** *–hydrated phases*[200]*. The time humidity profile (bottom panel) and X-ray peak intensity scale (right) are also included.*

Conversely, the XRD peak of PbI_2 in the MAPI sample (i.e., 3D PVSK) was already well developed at the onset of the monohydrate peaks formation, while it was not yet present in the n50I sample (i.e., quasi-3D PVSK) (see **Figure 8.3**). This means that significant decomposition of the perovskite and formation of PbI_2 in the MAPI sample were already taking place well before any noticeable hydration occurred, and that not only water but also other species (e.g., oxygen) were involved in the decomposition process. As a matter of fact, this observation strongly suggests that under 45% RH, water is not noticeably influencing the degradation process.

In addition, the overall weak intensities of the monohydrate peaks, after they fully developed in the XRD pattern of the MAPI sample, indicate that the degradation product (i.e., PbI_2) formed a natural encapsulation around MAPI grains and prevented water molecules from entering and hydrating the perovskite structure.

The TR-XRD results for the mixed perovskites samples (i.e., MAPIB and n50IB) showed that these materials were water-resistant under the conducted conditions, for RH < 50%. Thus, water resistance appeared exclusively for mixed perovskites with bromine addition. The lack of any observed water intercalation in such materials was most likely due to the unit cell contraction because of iodine atoms partially substituted by smaller bromine atoms. This led to a shrinkage of channels that would normally facilitate water diffusion.

A more detailed explanation of this phenomenon includes a discussion of the difference in crystal structure for iodine- and bromine-based perovskites. Iodine-based PVSK has the

$I4/mcm$ tetragonal space group, whereas bromine-based PVSK crystallizes in the $Pm\overline{3}m$ cubic space group[163]. What is also known that within the composition range of up to about 30% of $MAPbBr_3$ molar fraction, mixed crystals (i.e., with both halogens) form a single-phase material, following Vegard's law[163]. Therefore, based on Ref. [163], our perovskites with Br concentrations of about 15% form a single-phase material that still holds the tetragonal structure of MAPI but with a smaller lattice parameter and strained structure. The higher the bromine concentration, the closer the material's structure to the (pseudo)cubic lattice (its tolerance factor increases as the halide ionic radii decreases[201]). The reduced ionic radius of bromine compared to iodine contributes to its heightened electronegativity when compared to iodine. Consequently, bromine fosters more potent interactions due to this higher electronegativity. This results in mixed perovskites forming more tightly packed unit cells and smaller lattice constant compared to their iodine-based counterparts[202], which may further prevent the water diffusion and the hydration reaction from occuring.

When considering the diffusion mechanisms, one should also take into account the possibility of diffusion through grain boundaries, and therefore, it is important to compare the crystal sizes and the density of grain boundaries in the studied samples. Indeed, in the case of MAPIB perovskite, the average grain size was bigger than in the MAPI sample (about two times, **Figure 5.4** in **Chapter 5.2.1**), which resulted in a reduced density of grain boundaries and could limit the diffusion of water molecules.

However, although the grains of quasi-3D PVSK films (i.e., n50I and n50IB) had similar sizes, hydration occurred for the n50I sample only (morphology discussed in **Chapter 5.3.1**, see **Figure 5.12**). It signifies that the grain size is not the pervasive factor affecting water intercalation into perovskite structure, but rather more compact Br-containing PVSK unit cells are of primarily importance. However, one cannot forget that bromine fills iodine vacancies and thus reduces the diffusion coefficient.

The dynamics of the hydration process strongly depends on the level of humidity. When PVSK films were exposed to an air flow with a relatively low humidity (25% RH), no traces of hydration reaction were observed after 45 days, even for highly susceptible samples such as n50I (see **Figure 8.4**).

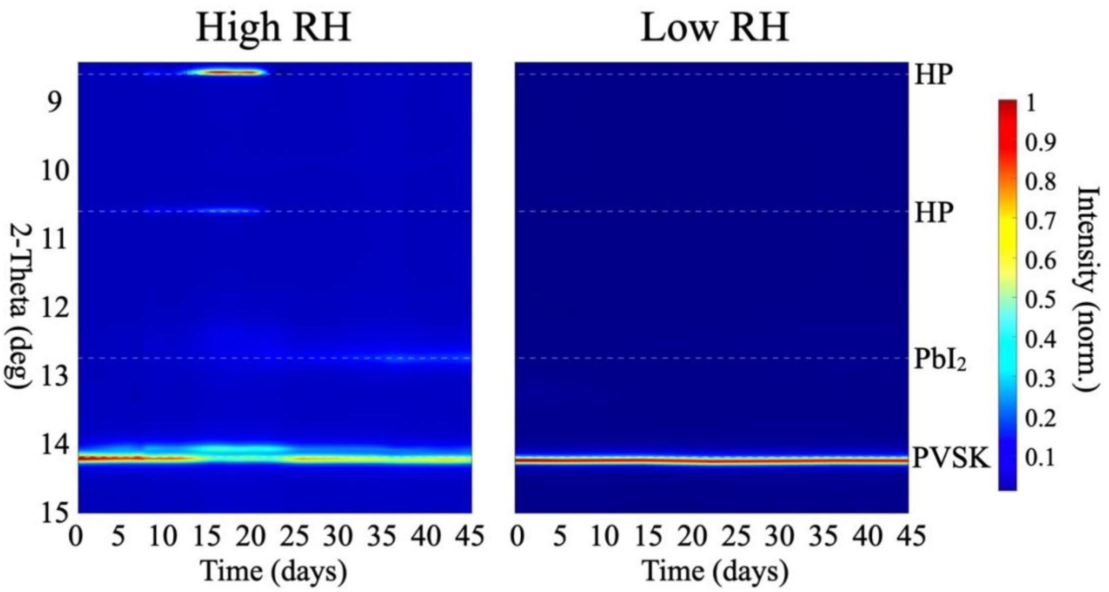

Figure 8.4 *TR-XRD of n50I. Comparison of samples stored at relatively high humidity (~50% RH, left), and low humidity (~25% RH, right).*

Figure 8.5 shows water diffusion dynamics for MAPI samples at different moisture conditions (45% vs 85%). Relative monohydrate peak intensities (y-axis in **Figure 8.5**) were calculated as the intensity of monohydrate XRD peak at 8.6° versus the intensity of pristine perovskite XRD peak at 14.2°. Diffusion currents were estimated based on slopes of the monohydrate contribution increase, which were found to be 0.01 and 48.13 day^{-1} for 45%RH and 85%RH, respectively. Assuming hydration level of perovskite kept at about 20%RH, the gradient of water concentration in environment 85% and 45% differs of a factor of two. Therefore, the diffusion coefficient, which is the ratio of diffusion current and concentration gradient, is about 2500 times greater in the lattice exposed at 85%RH compared to 45%RH.

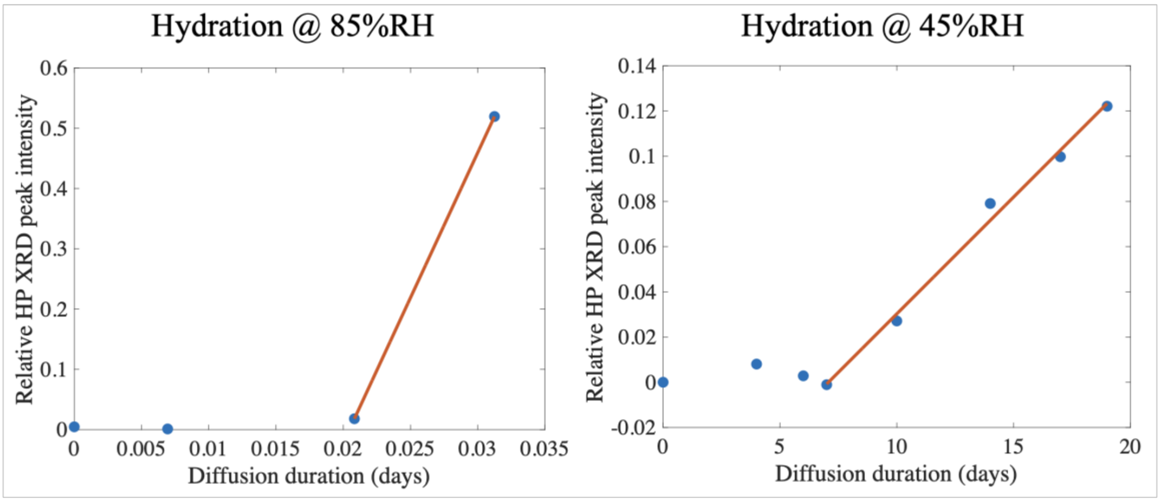

Figure 8.5 *Water diffusion dynamics for MAPI samples at different moisture conditions.*

Thus, the water concentration gradient increased of a factor of 2-3 by changing the environment from 85%RH to 45%RH.

The theoretical justification for the growth of XRD peak intensities as a function of time would necessitate a more comprehensive understanding of the long-term behavior of this relationship. However, the current scope of this study is limited to the presentation of experimental results without interpretation due to the lack of adequate data for extended durations.

However, a possible explanation for the lower diffusion coefficient for the material under relatively low RH, is the formation of PbI_2, which grows from the surface, constitutes an additional shield and reduces the diffusion coefficient in slow-running processes (allowing the formation of a protective layer). Thus, the hydration processes for lower values of relative humidity are strongly slowed down by the decomposition of the perovskite (in our case most probably due to oxygen) and for 25% RH, we do not practically observe the hydration because decomposition was ahead of the water diffusion process.

A very important result of these studies is the fabrication of the novel quasi-3D perovskite film (n50IB), which shows superior stability compared to 3D perovskites. Its resistance to hydration process was presented above. But what is equally important, the material (together with n50I) was resistant to other degradation factors, such as oxygen. The decomposition of perovskite results in the formation of lead iodide documented with an appropriate XRD peak growth. After 45 days of exposure, the intensity of the PbI_2 peak in quasi-3D perovskites was still relatively weak compared to that of the PVSK peak (**Figure 8.3**, n50I and n50IB). In contrast, the PbI_2 peak was significantly stronger than the PVSK peak for the MAPI as well as MAPIB samples (**Figure 8.3**, MAPI and MAPIB). The study showed that after 45 days of exposure, most of the 3D perovskite films were degraded into PbI_2, while the quasi-3D films were only slightly decomposed.

Thus, the very important conclusion from these studies is that the quasi-3D n50IB perovskite is a panacea for the degradation problems resulting from oxygen diffusion (mainly due to reduced dimensionality) and from water diffusion (mainly due to bromine content and reduction in unit cell size and probably also decreasing the number of iodine vacancies).

8.2 In-situ photoluminescence

Early hydration processes under extremely high relative humidity (approximately 70% and 95%) were investigated using *in-situ* photoluminescence (PL) measurements because lab-based XRD measurements were not fast enough to track hydration-induced changes. PL has shown to be very sensitive to small changes in halide perovskites, including nucleation, growth, and degradation processes[203]. Experiments were conducted in a modified climate chamber built by the author of this dissertation (**Figure 4.5**). The *in-situ* photoluminescence research was conducted by the author at the Lawrence Berkeley National Laboratory, within Professor Carolin Sutter-Fella's group.

8.2.1 Hydration dynamics in MAPI

Figure 8.6 illustrates the evolution of the MAPI PL signal during the hydration experiment. To avoid potential degradation artifacts resulting from interactions with oxygen, the experiments were conducted in a nitrogen atmosphere.

The humidity changes during the experiment can be divided into five distinct steps (**Figure 8.6**):

- **Step 1**: The sample was kept in a dry nitrogen atmosphere. However, due to the chamber not being completely sealed, the initial RH was set between 20 and 40%,
- **Step 2**: The sample was kept at a nitrogen atmosphere with gradually increasing RH from the initial value of 40% in **Figure 8.6**,
- **Step 3**: The sample was kept in a nitrogen atmosphere with increasing RH from 70% to 95%,
- **Step 4**: The RH was maintained at 95% for about 1 minute. This time was short enough to prevent irreversible hydration process,
- **Step 5**: The chamber was dried with nitrogen, causing the RH to decrease from 95% to the initial value observed in Step 1.

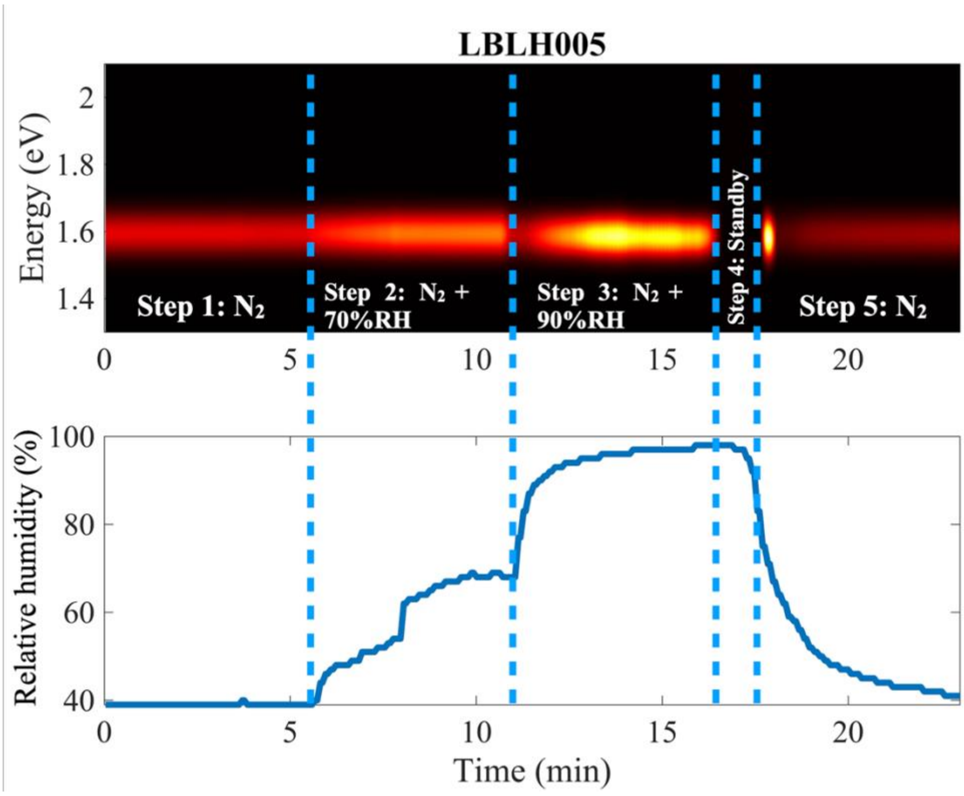

Figure 8.6 *Reversible hydration of MAPI studied by means of in-situ PL.*

The dynamics of material solidification processes considered so far (**Chapter 6**) are not visible on these PL maps because the hydration process begins at the point when the material is already fully crystallized and placed in the climate chamber. The evolution of the PL fitted parameters in MAPI is shown in **Figure 8.7**. The impact of moisture on the PL signal was observed after 5 minutes, meaning when the RH started to increase. A gradual redshift, and increase in PL intensity, and slight peak narrowing can be noticed between 5 and 11 minutes (**Figure 8.7** blue, red and green curves). Next, a sudden drop in the PL intensity around 11 minutes is probably an artifact related to the humidifier turning on. Then, from 11 to 17 minutes, these trends (i.e., redshift, PL enhancement, peak broadening) were even more noticeable due to the rapid increase of RH from 70 to 95%. This indicates that the RH level considerably impacts the hydration dynamics of perovskites.

One possible explanation for the redshift between 5 and 11 minutes is the role water plays as it diffuses into the material. As water permeates through the material's structure, it induces a change in the lattice constant and introduces stress. The extension of the bonds within the material influences its energy gap, leading to a decrease (and thus a PL redshift). However, it is important to note that this is not the sole mechanism that could explain the observed behavior.

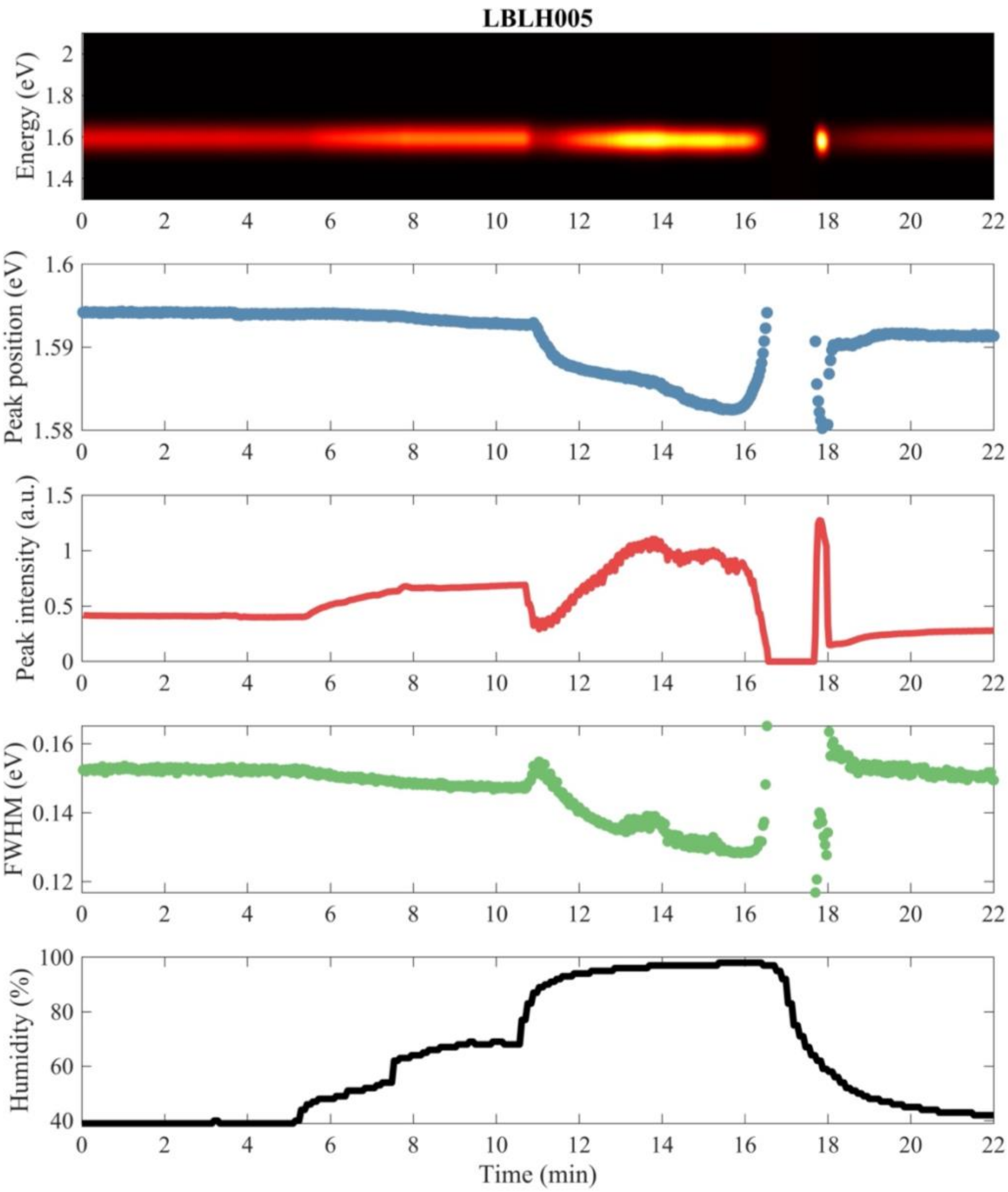

Figure 8.7 *PL parameters evolution in MAPI during hydration and dehydration processes.*

The alternative explanation involves the solubility of perovskite components in water. It has been shown that H_2O molecules can incorporate into the crystal lattice dissolving MA^+ cations and causing an increase in the number of vacancies in the crystal lattice. This may create shallow trap states, which are the energy levels near the valence band[204]. These trap states can act as radiative recombination channels, emitting photons with less energy than those emitted during the transition from the conduction band to the valence band, resulting in the redshift of the PL spectra[205]. Moreover, these vacancies can cause a shift in the positions of atoms in the crystal structure, as observed in Raman spectroscopy[206].

This may be the case in MAPI (**Figure 8.7**), as a redshift of 0.01eV was observed (peak position at the beginning of the experiment was 1.594eV, and after 15 minutes it was 1.584eV), suggesting the formation of shallow defect states near either the valance or conduction band.

On the other hand, deep trap states, which are energy levels located away from the band edges, can cause non-radiative recombination pathways[207]. It is believed that deep centers in perovskites have high formation energies. However, on the other hand, resistance measurements as a function of temperature indicate the presence of a defect 0.4 eV below the conduction band, showing that there are centers in the energy gap. Therefore, the enhancement of peak intensity (the intensity doubled from the pristine MAPI emission (0 min) to the hydrated form (14 min) in **Figure 8.7**) may be attributed to the passivation of non-radiative charge recombination sites by water molecules.

Similar trends (redshift and PL enhancement) have already been observed in MAPI by others[206]. However, results in this dissertation are the first attempts of systematic, real-time hydration studies, investigated by means of *in-situ* PL. They not only confirm these trends but also indicate the dynamics of the processes at different levels of RH.

An intriguing PL evolution took place between steps 3 and 4 (16.5 min in **Figure 8.7**). PL spectra rapidly disappeared in just 1 minute (**Figure 8.8**). According to the hydration reactions discussed in **Chapter 3.3**, the presence of moisture leads to the formation of so-called monohydrates followed by dihydrate species created after prolonged exposure to water vapour. Their bandgaps have been found to be 3.1 eV[132] and 3.87 eV[208] for monohydrate and dihydrate, respectively. In studies conducted in this thesis, a green laser of 523 nm (2.37eV) was used. Therefore, it would not be possible to observe traces of hydrated species even if radiated band-to-band transitions are present in them. However, the rapid decay of PL in the measured region suggests the formation of either mono- or dihydrates. The results indicate that at 95% RH, hydration reactions take place in just 1 minute, turning a regular perovskite phase entirely into hydrated species.

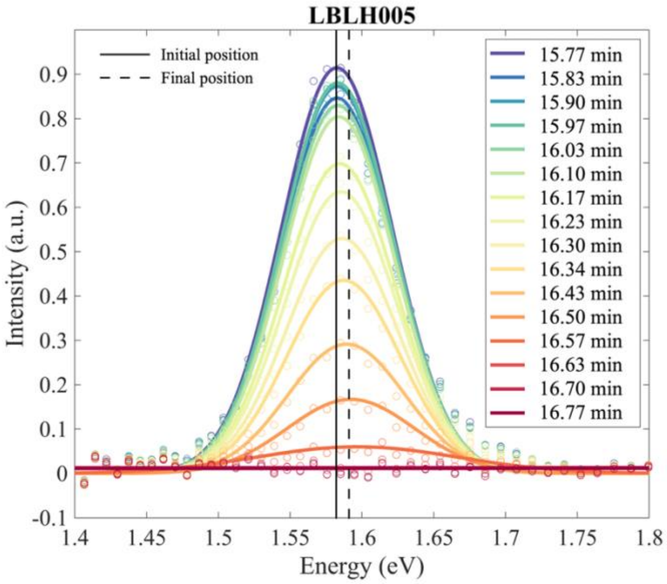

Figure 8.8 *in-situ PL decay in MAPI between the hydration steps 3 and 4.*

During the hydration reactions a blueshift of about 0.01eV was observed (as shown by the blue curve at about 16 minutes in **Figure 8.7**, and in **Figure 8.8**). The exact mechanism behind this shift remains unclear, but it might be related to a sudden transition to the hydrated phase, which has a different structure than pristine perovskite. As water is released from the perovskite cells, the lattice contracts, which in turn results in a shift of the photoluminescence to higher energy.

Finally, after complete disappearance of the PL signal, drying procedure began. When the RH dropped to about 60%, a strong PL recovery occurred at the energy range of MAPI (17.8 min in **Figure 8.7**). Then, the PL saturated at about 1.591eV. Interestingly, the final bandgap of the material after the hydration procedure was slightly smaller (of about 0.003 eV) than in the pristine film (1.594 eV), indicating that not all the shallow defect states were healed after dehydration. According to the literature[206], they are caused by the formation of methylammonium vacancies. Therefore, a shifted bandgap of the film after hydration compared to the pristine one may indicate that not all MA cations could return to their initial positions after the hydration procedure.

8.2.2 Hydration dynamics in MAPIB

Figure 8.9 illustrates the *in-situ* PL evolution in MAPIB during the hydration experiment. The PL intensity significantly increased (almost seven times) and redshifted by 0.03 eV with increasing RH (spectra at 0 min and 7 min in **Figure 8.10**). Both parameters, intensity and emission energy, showed a stronger evolution in MAPIB compared to MAPI. In MAPIB, there was a sevenfold increase in PL intensity and 0.03 eV energy shift, while in MAPI, the increase in PL intensity was twofold the energy shift was 0.01 eV.

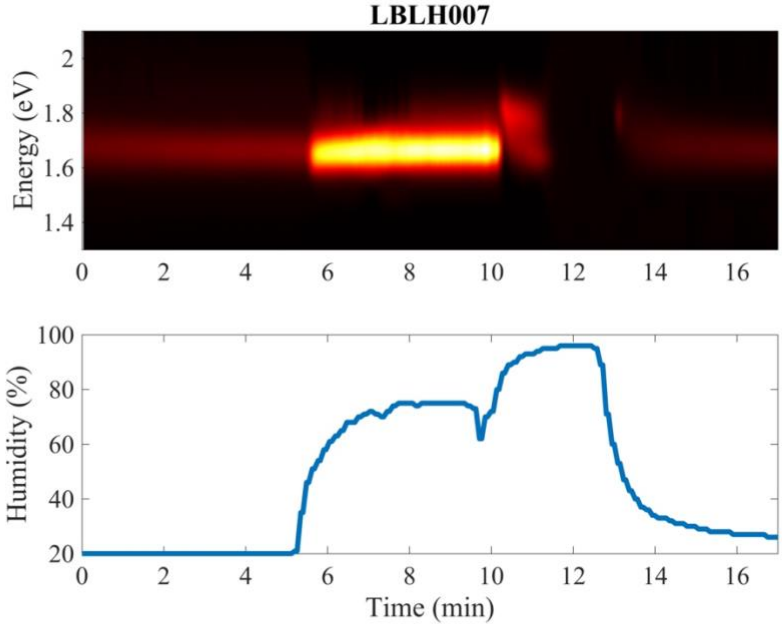

Figure 8.9 Reversible hydration of MAPIB studied by means of in-situ PL.

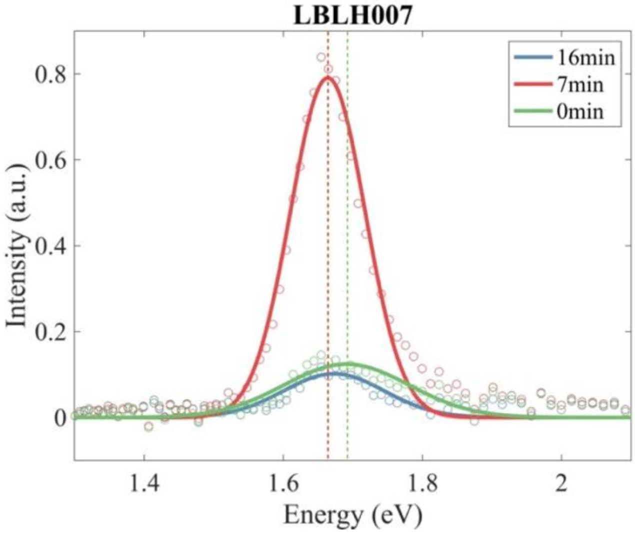

Figure 8.10 Example PL spectra for MAPIB during hydration experiment.

Interestingly, traces of halide heterogeneity occurred after about 11 minutes (**Figure 8.9**). PL spectra between 9 and 12 min of hydration are shown in **Figure 8.11**.

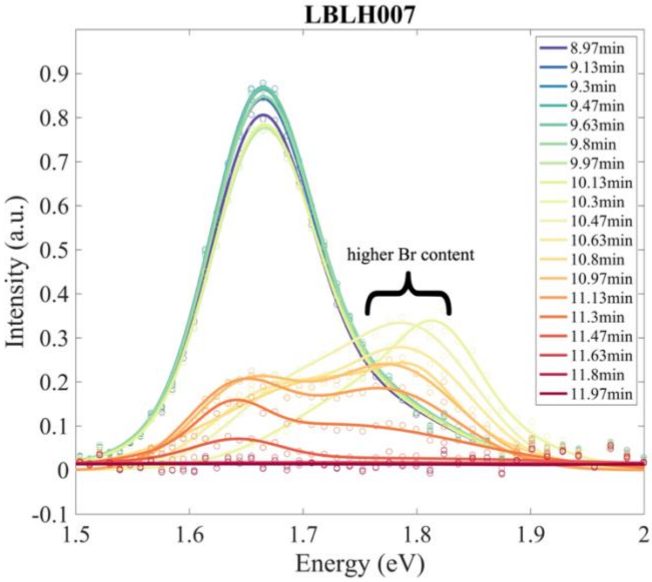

Figure 8.11 *Example spectra of MAPIB during hydration between 9 and 12 minutes.*

The main perovskite PL peak at about 1.67 eV rapidly decreased, revealing a component at higher energy (~1.8 eV). This result suggests that after 10 minutes, most of the iodine-based perovskite fraction turned into its hydrated phase, as evidenced by the significant decrease of the lower energy perovskite peak. Moreover, the peak at 1.67 eV corresponds to a mostly iodine-based film, indicating better stability of bromine-based perovskites. After 10.5 minutes, mostly a peak at about 1.8 eV is visible in **Figure 8.11**.

8.2.3 Hydration dynamics in n50I

Figure 8.12 shows the evolution of PL in the n50I film during the hydration experiment. Contrary to its 3D counterparts (MAPI and MAPIB), the PL almost did not change in the initial stage of hydration (RH increased from 20 to 80% between 5 and 10 minutes in **Figure 8.12**). This indicates higher moisture resistivity of quasi-3D film compared to the 3D film. However, during this hydration stage (5-10min), a slight decrease in FWHM was observed, indicating a sharper PL peak.

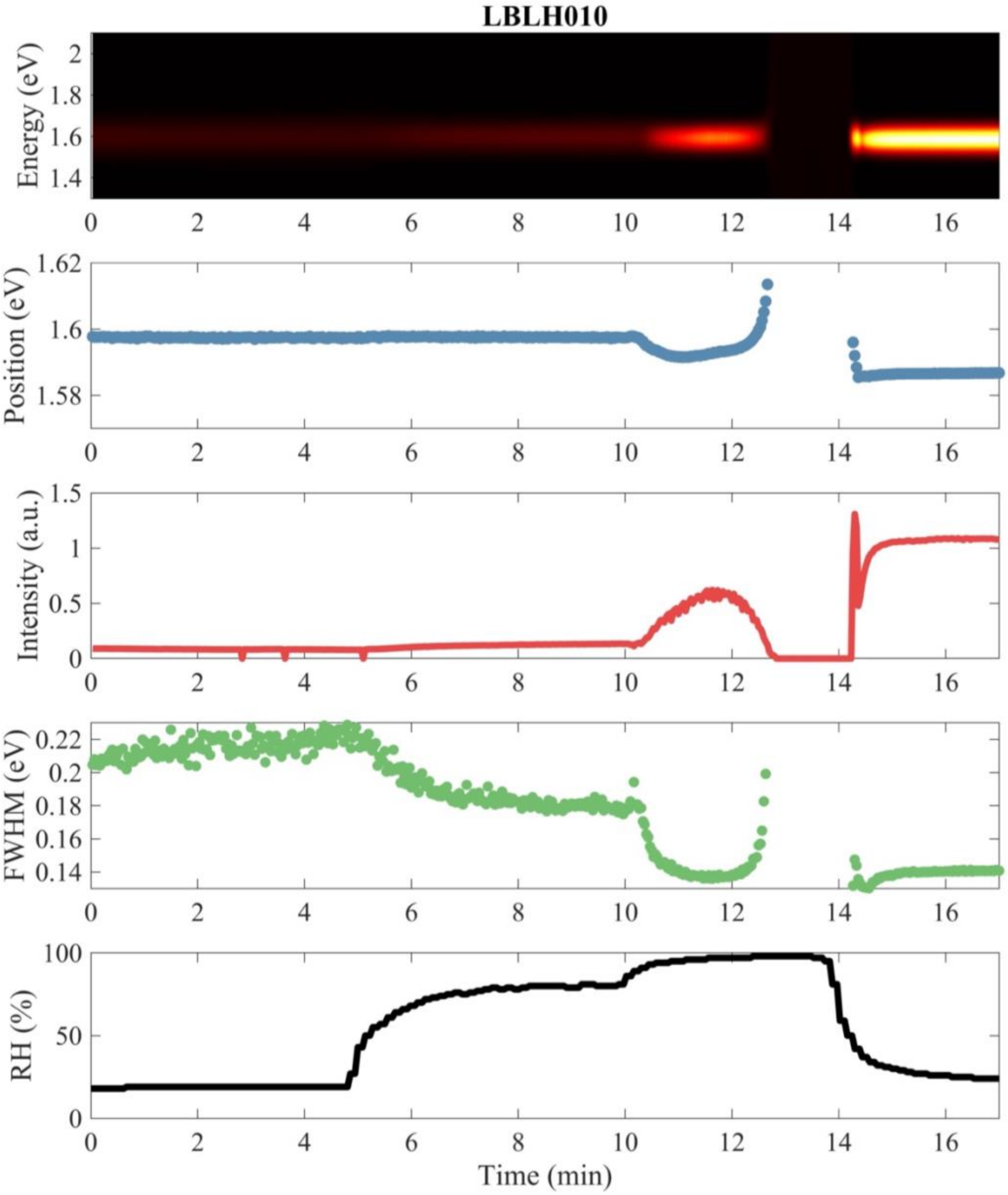

Figure 8.12 *Reversible hydration of n50I studied by means of PL.*

At higher humidity (starting at 10 minutes in **Figure 8.12**), the PL evolved in a similar way as in 3D species, with a redshifted of about 0.01 eV and a sevenfold enhancement compared to the untreated perovskite. Quantitatively, a redshift in n50I was exactly the same as in MAPI, suggesting a similar shallow defect concentration or a similar rate of lattice expansion due to water diffusion. Regarding PL intensity, the PL in n50I enhanced sevenfold, while in MAPI, it only doubled. This indicates stronger passivation of non-radiative charge recombination sites by water molecules in the quasi-3D film compared to the 3D film.

A very interesting result is that the PL intensity significantly enhanced after the hydration procedure (a recovery step at about 15 minutes in **Figure 8.12**). This suggests that moisture treatment of n50I permanently passivates non-radiative charge recombination sites, which may be beneficial for future devices such as PV and LEDs based on these materials. Additionally, the emission energy shifted by 0.15 eV after the hydration procedure compared to the untreated film (0 min vs 16 min in **Figure 8.12**).

8.2.4 Hydration dynamics in n50IB

Figure 8.13 shows the evolution of PL in the n50IB film during the hydration experiment. The PL intensity doubled and redshifted by 0.01 eV during the first hydration step (see also spectra at 0 min and 8 min in **Figure 8.14**). Moreover, a sharper PL peak (decrease of FWHM) was observed between 5 and 10 minutes in **Figure 8.13** (green curve) compared to the pristine perovskite. During the second hydration step (RH increased from 10 to 12 min), rapid PL decay occurred, indicating a fast transition to the hydrated phase of the perovskite. Contrary to its 3D counterpart (MAPIB), the PL consisted of only one Gaussian component, indicating a homogeneous transition to the hydrated phase (**Figure 8.15**). Similarly to the iodine-based quasi-3D perovskite (n50I), the PL enhanced after recovery and further redshifted compared to the pristine perovskite.

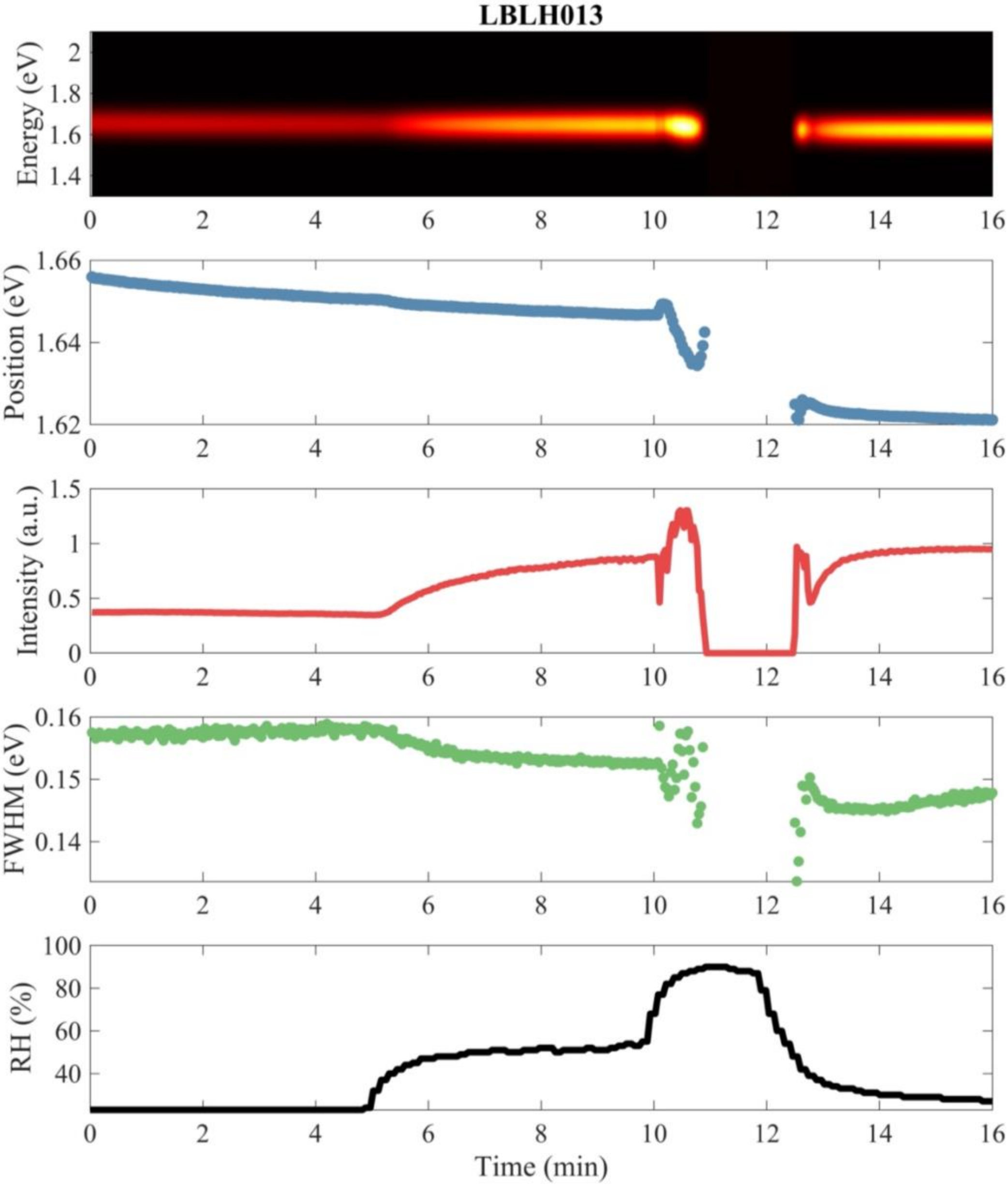

Figure 8.13 *Reversible hydration of n50IB studied by means of PL.*

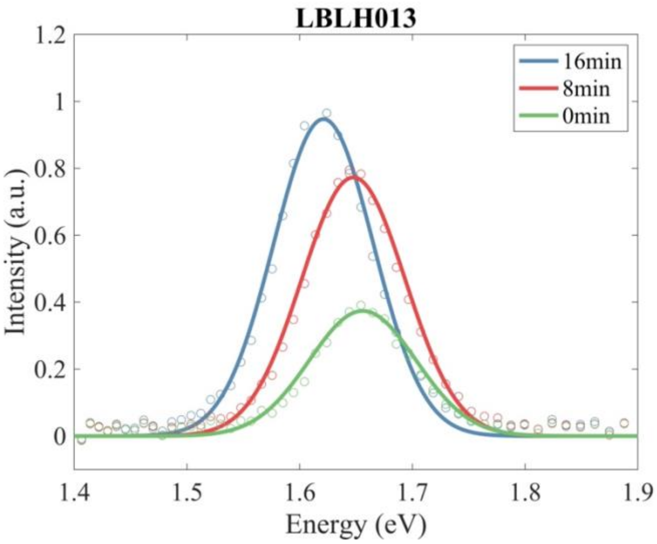

Figure 8.14 *PL spectra of n50IB during hydration experiment (fresh sample – 0 min, after the first hydration step – 8 min, and after recovery – 16 min).*

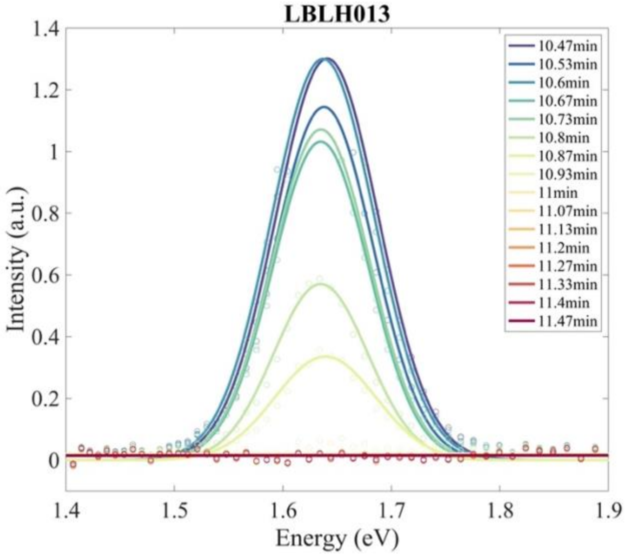

Figure 8.15 *Example spectra of n50IB during hydration between 10 and 12 minutes.*

8.3 Chapter summary

In this work, films of the novel quasi-3D perovskites were prepared and analyzed in terms of their susceptibility to water and were compared with the state-of-the-art 3D materials.

It was shown that humid air induces rearrangement of the perovskite crystal structure. The evolution of the XRD patterns was observed when the samples were exposed to an air flow with about 50% RH and higher, indicating the formation of perovskite hydrated phases. Interestingly, the water intercalation in long-term studies (XRD) took place only for iodine-based perovskites (both quasi-3D and 3D films), whereas the mixed perovskites (both quasi-3D and 3D films with bromine content about 10%) were water resistant, and the hydration reaction was not observed for these films when exposed to around 50% RH. However, samples exposed to relative humidity close to 100%RH (studies by means of *in-situ* PL) revealed that hydration occurred within all the samples, including MAPIB and n50IB. These results suggest that Br-containing samples are more water-resistant than pure I-based species, but there is still a threshold of this resistivity, and they not entirely stable in highly hydrous conditions. Therefore, the addition of bromine does not protect against hydration before humidification at significantly higher than 50% humidity .

XRD studies were conducted at lower RH compared to *in-situ* PL; therefore, hydration reactions were slowed down, and perovskite degradation due to oxygen exposure was more likely to occur. It was speculated that product of degradation (i.e., PbI_2) formed a natural encapsulation around PVSK grains, preventing water molecules from entering and hydrating the perovskite structure. This was not the case in *in-situ* PL because the hydration reaction took minutes, and there was no time for perovskite degradation to PbI_2, which would encapsulate the material and further slow down or prevent hydration. This is probably why hydration in MAPIB and n50IB was not observed in long XRD studies (days, RH 65%) but was present in short *in-situ* PL studies (minutes, RH ~90%).

Moreover, the studies confirmed that the hydration reaction was a reversible process, and both XRD patterns and PL spectra returned to their initial form, showing peaks originating from the perovskite structure (and PbI_2 in XRD) only after exposure to moisture followed by the drying process.

The kinetics of the hydration processes in perovskites is very dependent on the relative humidity, changing the effective diffusion coefficients hundreds of times with a change in humidity from 45 to 85%. This can be explained by the fact that during slow water diffusion processes (studied here by means of XRD), an additional, sufficiently thick, impermeable surface layer is created from PbI_2, which is a product of perovskite decomposition. The studies that the size of crystals and the number of grain boundaries are not as critical to the perovskite hydration processes as the size of the unit cell and lowered iodine vacancies concentration in Br-containing species.

One of the most important results of the work is the fabrication of novel quasi-3D perovskite (n=50) with superior stability compared to 3D perovskites, especially in long-term studies revealed by means of XRD. Additionally, *in-situ* PL provided new and interesting results concerning enhancement of PL after hydration in quasi-3D films, suggesting that moisture-treatment of both n50I and n50IB permanently passivates non-radiative charge recombination sites, which may be beneficial for future devices such as PV and LEDs based on these materials.

9 Studies of long-term perovskite stability

9.1 Introduction

In this chapter, studies devoted to long-term stability of perovskites will be presented. Impact of dimensionality and halide composition will be discussed based on the set of samples: MAPI, MAPIB, n50I, and n50IB.

All the samples were stored at dark, in air with humidity of about 40% and temperature of 25°C. It is worth noticing that samples investigated in **Chapter 7.5** were exposed to higher humidity than here, of about 50% RH and therefore, the processes of degradation were accelerated in those studies.

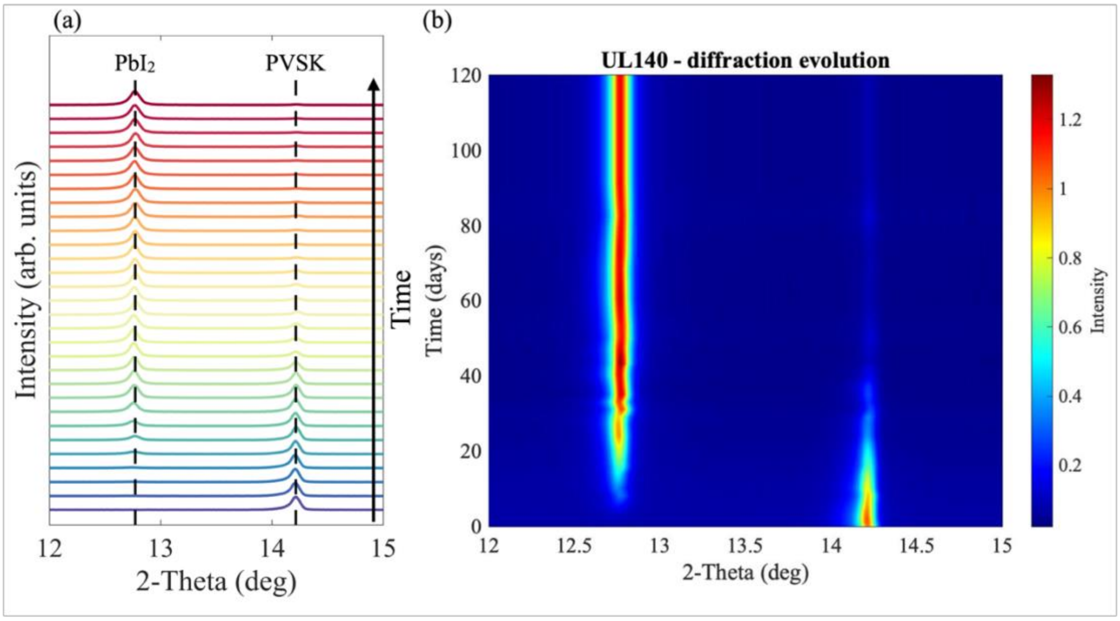

Figure 9.1 Example X-ray diffraction evolution over time of MAPI and its degradation product PbI_2 *indicated (a), diffraction map (b).*

Figure 9.1(a) presents the XRD pattern for angles corresponding to PbI_2 and perovskite diffractions (PVSK) from (001) and (110) lattice planes, respectively. From the diffraction data for MAPI sample it was evident that during exposure to air decomposition of iodide perovskite to PbI_2 took place. The process of decomposition is also visualized using X-ray diffraction map with a time-scale on y-axis, as shown in **Figure 9.1(b)**.

9.2 Long-term degradation studies of the entire set

X-ray diffraction maps over 120 days of degradation studies of the entire set of samples are shown in **Figure 9.2**. The fastest degradation was observed for 3D perovskites (MAPI and MAPIB), since after 120 days peaks originating from perovskites at about 14.2° almost completely disappeared. On the other hand, quasi-3D materials revealed better stability compared to their 3D counterparts, maintaining significant intensity of the perovskite peak after 120 days, but degradation to PbI_2 was evident at that point.

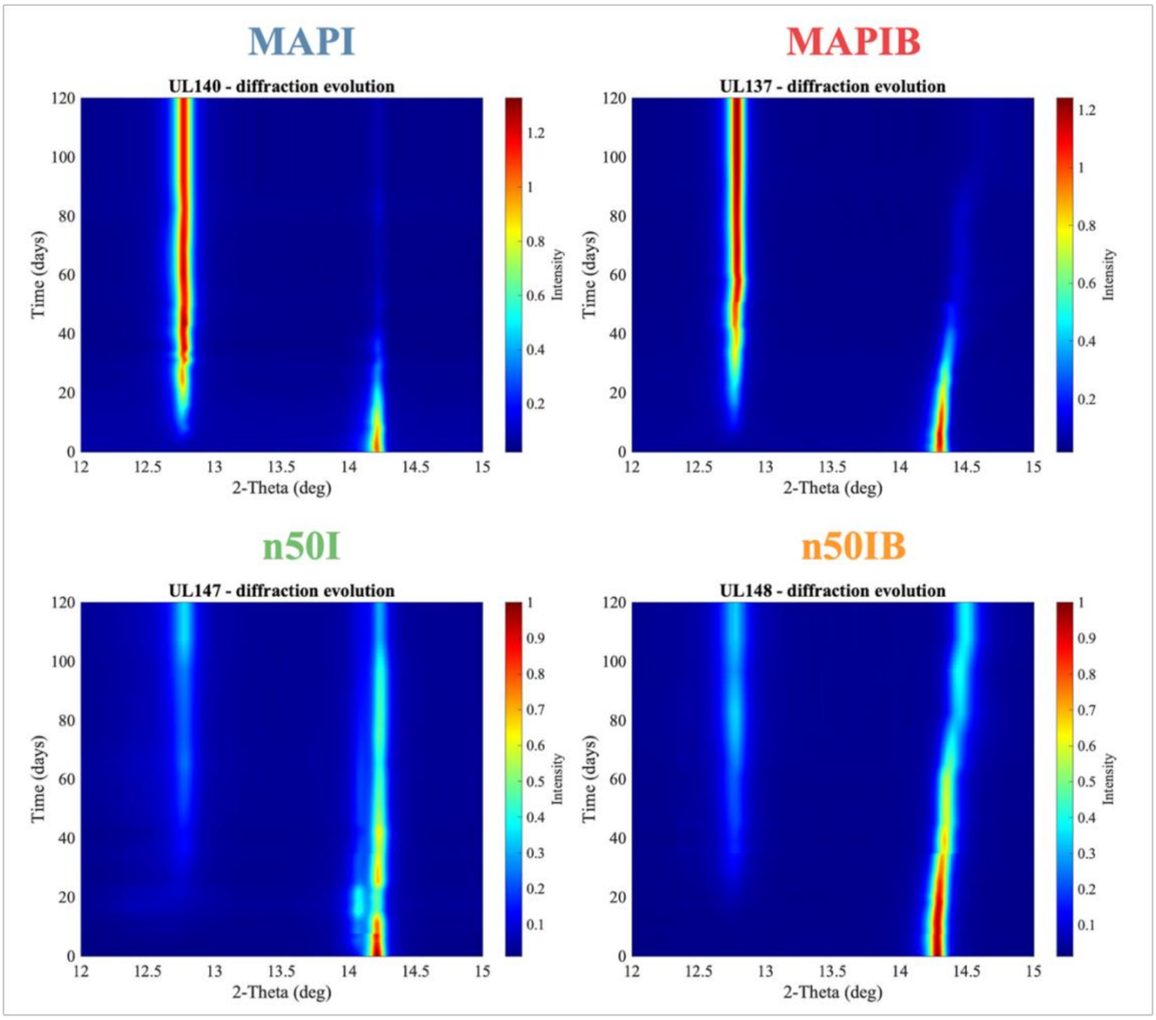

Figure 9.2 *X-ray diffraction maps of the entire set of perovskites. Peak at lower angle originates from PbI2, whereas at higher angle from perovskite.*

It is worth noting that after 20 days (see **Figure 9.2**), an accidental hydration occurred in the n50I sample, but it quickly reversed and had no effect on further, multi-day aging experiments. To analyze evolution of the XRD patterns quantitatively, intensities of perovskite (110) and PbI_2 (001) diffraction peaks were integrated in a similar manner as discussed in **Chapter 7.5**, but in a longer timescale. Perovskite contribution within the film at a particular time was defined by the formula:

$$C = \frac{\int_{\theta_a}^{\theta_b} PVSK(\theta)d\theta}{\int_{\theta_a}^{\theta_b} PVSK(\theta)d\theta + \int_{\theta_c}^{\theta_d} PbI_2(\theta)d\theta}$$

Where:

C is perovskite contribution,

$\int_{\theta_a}^{\theta_b} PVSK(\theta)d\theta$ is the integrated perovskite peak,

$\int_{\theta_c}^{\theta_d} PbI_2(\theta)d\theta$ is the integrated PbI_2 peak.

In that way, all the decays are normalized since at the pristine film (time equals 0) only perovskite peaks were present within all the samples and $\int_{\theta_c}^{\theta_d} PbI_2(\theta)d\theta$ equaled 0. The results of C(t) are shown in **Figure 9.3** (dots).

Fitting to the experimental data of all perovskites with exponential curves is described by the formula:

$$N(t) = N_0 exp\left(-\frac{t}{\tau_p}\right)$$

Fitting decays are presented as solid lines in **Figure 9.3**, and corresponding characteristic degradation times, τ_p, are summarized in **Table 9.1**. This quantitative analysis reveals that 3D perovskites decompose about 6 times faster than their quasi-3D counterparts. Additionally, within 3D species, MAPI degrade slightly faster ($\tau_p = 20$ days) than MAPIB ($\tau_p = 31$ days). It is worth commenting on the significant difference in the characteristic degradation times presented here (on the order of days) compared to those discussed in **Chapter 7.5** (on the order of hours). This discrepancy probably arises from the fact that the studies in **Chapter 7.5** were conducted at the beginning of the PhD research, where not all elements of the degradation mechanisms were known/taken into consideration. It is likely that during that time, the stored samples were not kept in the dark but rather had limited exposure to light, which could have influenced the degradation dynamics.

The possible reason of that may originate from two factors: morphology and crystal structure. First, as it was shown in **Chapter 5.2.1** in **Figure 5.3**, grain sized of MAPI are about two times smaller than of MAPIB. Water and oxygen diffusion proceeds through grain boundaries therefore, material's penetration by these species may be more efficient in iodine-based perovskite MAPI than in mixed-halide MAPIB due to these differences in grain sizes. At the same time, it is probable that bromine can partially heal iodine vacancies. Second, the unit cell of MAPIB is more compact than MAPI, as analyzed in **Chapter 5.2.2**.

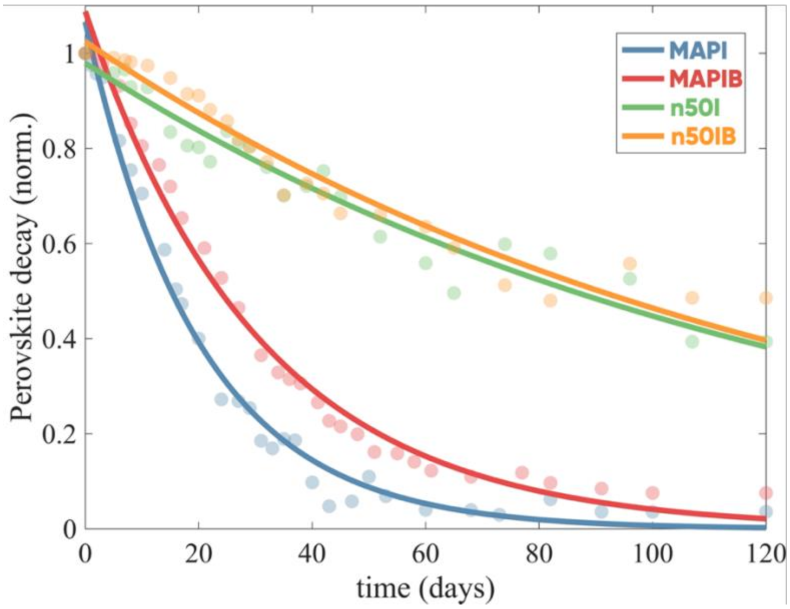

Figure 9.3 *Perovskites decomposition over time. Dots represent the results of peaks integration, whereas solid lines correspond to decay fitting.*

Table 9.1 *Characteristic degradation times derived from decay fits.*

	MAPI	**MAPIB**	**n50I**	**n50IB**
τ_p (days)	20	31	128	126

Due to smaller atomic radius of Br than I, 115 pm vs 140 pm[162], respectively, but also stronger Coulomb interactions originating from the greater electronegativity of bromine compared to iodine, the mixed-halide perovskite contains more tightly packed unit cell with less of iodine vacancies. These effects (smaller Br atom and stronger Coulomb interactions) lead to reduction of the interplanar distance and therefore, water (especially under experimental conditions, RH = 40%) and oxygen diffusion into the perovskite structure is slowed down in MAPIB compared to MAPI.

However, the most evident stability improvement was achieved in quasi-3D perovskites. First, the morphology of these perovskites discussed in **Chapter 5.3.1** revealed compact films without easily distinguishable grains. Therefore, water and oxygen diffusion may be significantly slower than in 3D species because pathways of penetration through grain boundaries is harder to occur. Moreover, a hydrophobic large organic molecule in quasi-3D films, phenylethylammonium cation, has a low affinity for water, reducing water diffusion and hydration reactions to occur.

Additionally, an interesting process of XRD perovskite peak shift into higher angles over time in both mix-halide perovskites (MAPIB and n50IB) was observed (**Figure 9.2**).

Using the shift calibration data for (110) diffraction peak, which follow Vegard's law, provided by Lehmann et al.[163], the bromine concentration over time in these species was calculated and the results are shown in **Figure 9.4**.

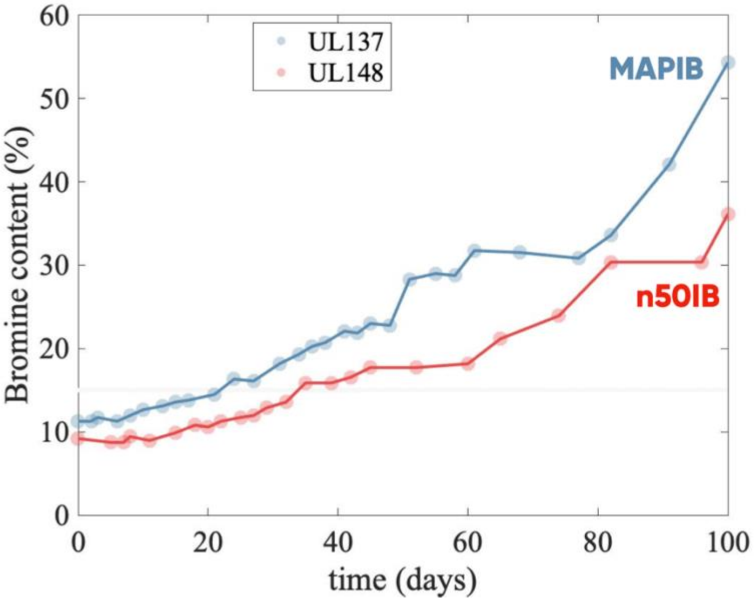

Figure 9.4 *Bromine content within mix-halide perovskites over time.*

This result indicates that in time, the content of bromine within the perovskite chemical composition increased about 5 times in MAPIB, and about 3.5 times in n50IB due to decomposition of iodine species to lead (II) iodine. No traces of lead (II) bromine were observed. Therefore, a better stability of bromine-based perovskites was shown.

9.3 Chapter summary

This chapter presented research on the long-term stability of perovskites, with a focus on the impact of dimensionality and halide composition. The study was conducted using a set of samples which were stored at a dark, humid environment of 40% and 25°C. X-ray diffraction was used to analyze the samples over time, and the results showed that 3D perovskites degrade faster than their quasi-3D counterparts.

This was evident in the XRD patterns, where the peaks originating from perovskites in 3D samples almost completely disappeared after 120 days, while the quasi-3D samples still maintained significant intensity of the perovskite peak. The analysis also revealed that within the 3D species, MAPI degraded slightly faster than MAPIB.

The characteristic degradation time for MAPI was found to be 20 days and for MAPIB is 31 days. Characteristic degradation times of quasi-3D species were about 6 times longer than of 3D samples, 128 and 126 days in n50I and n50IB, respectively.

It is believed that the main factors contributing to better perovskite stability are: grain size and size of the unit cell. The bigger the grains, the slower the degradation due to reduced concentration of grain boundaries through which oxygen and water diffusion proceeds.

10 Perovskite solar cells

10.1 Introduction

In this Chapter, results of studies on perovskite solar cells will be discussed. Several approaches were applied to boost both efficiency and stability. The investigated structure modifications were discussed in **Chapter 3.1.2** and **3.4**.

It is important to note that not all the investigated perovskite solar cells changes resulted in increased efficiency. In fact, some approaches were not successful in the performance enhancement. However, even if a particular modification did not result in increased efficiency, it can still provide valuable information for researchers. By identifying a scientific "dead-end", researchers can avoid going down a similar path in their own work, and instead focus on approaches that are more likely to be successful. Additionally, this information can be used to guide future research and development efforts, allowing scientists to learn from past mistakes and improve their chances of success in the future.

10.2 Au nanoparticles – modification of electron transporting layer

10.2.1 Synthesis of gold nanoparticles by photoreduction of tetrachloroauric acid

In these studies, gold nanoparticles (AuNPs) were synthesized through the photoreduction of a gold precursor, such as $HAuCl_4$ (tetrachloroauric acid). In this process, a substrate coated with TiO_2 was submerged in a 9mM solution of $HAuCl_4$ and illuminated with UV light for 2 minutes. The UV light excited electrons from the valence band to the conduction band in TiO_2, which then transferred to the $HAuCl_4$, causing the reduction of the gold to metallic gold nanoparticles.

To increase the efficiency of this reaction, a hole scavenger (methanol 5% v/v) was added to the solution. The function of the hole scavenger is to accept holes from the valence band of the TiO_2 during the absorption of UV light, which can improve the yield of the gold nanoparticles formation.

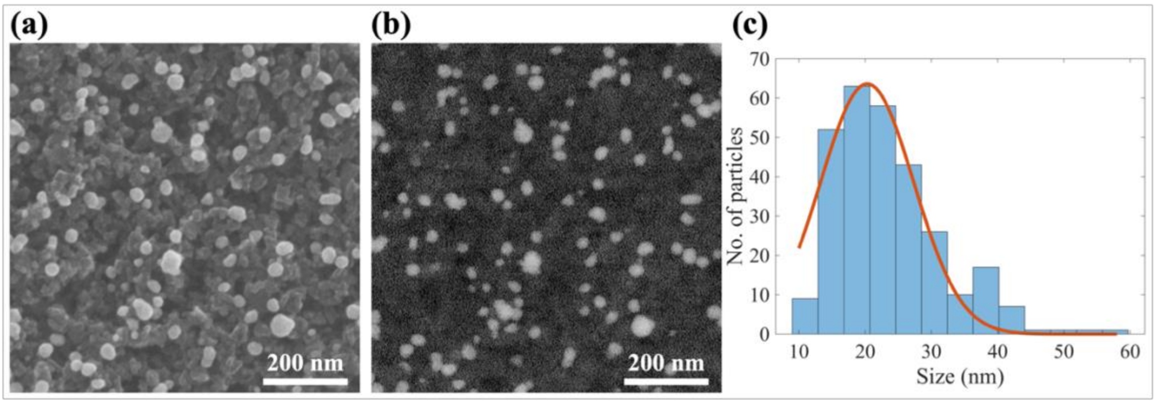

Figure 10.1 *SEM images of TiO_2 with Au nanoparticles: (a) secondary electron image, (b) backscattered electron image, (c) NPs size analysis.*

Figure 10.1(a-b) shows SEM images of gold nanoparticles at TiO_2 (AuNPs@TiO_2). Granulometry revealed the average size of AuNPs of about 20 nm (**Figure 10.1(c)**). It has been found that nanoparticles of about 5-20 nm may serve as sub-wave antennas and effectively store incoming sunlight energy in localized plasmonic modes and increase perovskite absorption by the near-field effect[209,210].

10.2.2 Impact of plasmonic nanoparticles on efficiency of perovskite solar cells

Perovskite solar cells with gold nanoparticles on TiO_2 (AuNPs@TiO2) were fabricated and the J-V curves of the best reference (without AuNPs) and modified (with NPs) cells are shown in **Figure 10.2**, and derived parameters are summarized in **Table 10.1**.

Unfortunately, despite several trials and fabrication of tens of solar cells with AuNPs, their efficiency was significantly lower than in the reference devices. The main parameters which contributed to decrease of performance of modified cells were: current density and fill factor (which is a consequence of both relatively high series resistance and low shunt resistance).

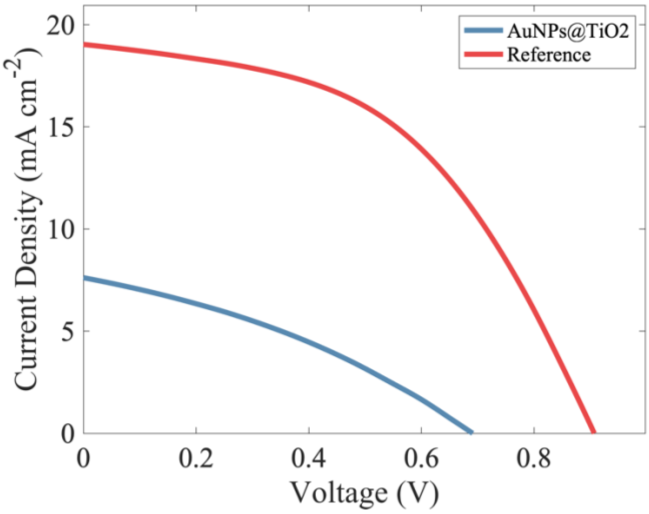

Figure 10.2 *J-V characteristics of solar cells with AuNPs (blue curve), and the reference cell without AuNPs (red).*

Table 10.1 *Photovoltaic parameters of perovskite solar cells:* V_{oc} *- open circuit voltage,* J_{sc} *- short circuit current, FF - fill factor, PCE - power conversion efficiency,* ρ_s *- series surface resistivity;* ρ_{sh} *shunt surface resistivity.*

	V_{oc} (V)	**Jsc (mA cm^{-2})**	**FF (%)**	**ρ_s (Ω cm2)**	**ρ_{sh} (Ω cm^2)**	**PCE (%)**
Reference	0.91	19.03	48.46	8.58	284.60	8.36
AuNPs@TiO2	0.69	7.62	33.96	23.76	157.12	1.79

A low J_{sc} compared to the reference may indicate the decomposition of the absorbing layer (perovskite). This low current was due to less material able to absorb photons. Additionally, if the decomposition occurs at the interface between AuNPs@TiO2 and perovskite, a series resistance may increase due to the presence of resistive PbI_2. Both effects were observed in AuNPs@TiO2 samples (**Table 10.1**). One potential reason for perovskite decomposition at the interface could be the presence of residual $HAuCl_4$ acid at the TiO_2 surface, which etches perovskite. It is speculated that submerging the TiO2 substrate in methanol or ethanol as a means of "cleaning" the material from residual acid after photoreduction may potentially be beneficial in enhancing the performance of cells with NPs. The mesoporous structure of titanium dioxide in perovskite solar cells can pose challenges when attempting to remove acid residues. It is suggested that since $HAuCl_4$ is soluble in alcohols, submerging the TiO_2 substrate in methanol or ethanol immediately after photoreduction may be an effective method for removing residual acid and "cleaning" the material. However, further experimental investigation and validation are necessary to ascertain the actual effectiveness and optimize the cleaning process. Given the relatively weak performance, the exploration of nanoparticles in this context was discontinued. The solar cells with AuNPs consistently demonstrated efficiency significantly lower than the reference devices, which steered the focus of the research towards alternative avenues.

10.3 Polyaniline – modification of hole transporting layer

10.3.1 Introduction

The results presented in this Chapter were already published, and the author of this dissertation has equal contribution as first authors to the manuscript with other two PhD candidates[150]. Studies on perovskite solar cells were done exclusively by the author of this thesis.

In the pursuit of improved stability in solar cells, the use of polyaniline doped with camphorsulfonic acid (PANI:CSA) was investigated in this thesis as a potential alternative to Spiro-OMeTAD, the traditional hole transport layer (HTL). Spiro-OMeTAD, while commonly utilized, suffers from oxidation over time, leading to its degradation. As a PANI application as HTL, the doping process, which involves varying the molar ratio of PANI to CSA, is critical in achieving the desired conductivity of HTL. The objective of the research was to find the optimal concentration of CSA that would enhance the conductivity of PANI without compromising stability. The CSA doping impacts the HOMO (highest occupied molecular orbital) level of the HTL. Through the doping process, the HOMO level is lowered, as illustrated in **Figure 10.3**, further contributing to the improved performance of the solar cells due to a better adjustment of energy levels within the solar cell structure.

The perovskite solar cells in configuration ITO/TiO_2/perovskite/HTL/Au (the energy diagram is shown in **Figure 10.3(a)**, and a schematic illustration of the device in **Figure 10.3(b)** were prepared according to the procedure described in **Chapter 4.1.2**. In these studies, polyaniline doped with camphorsulfonic acid with PANI:CSA molar ratio ranging from 6:1 to 1:4 was used as the HTL, while in the reference cell this layer was prepared using Spiro-OMeTAD.

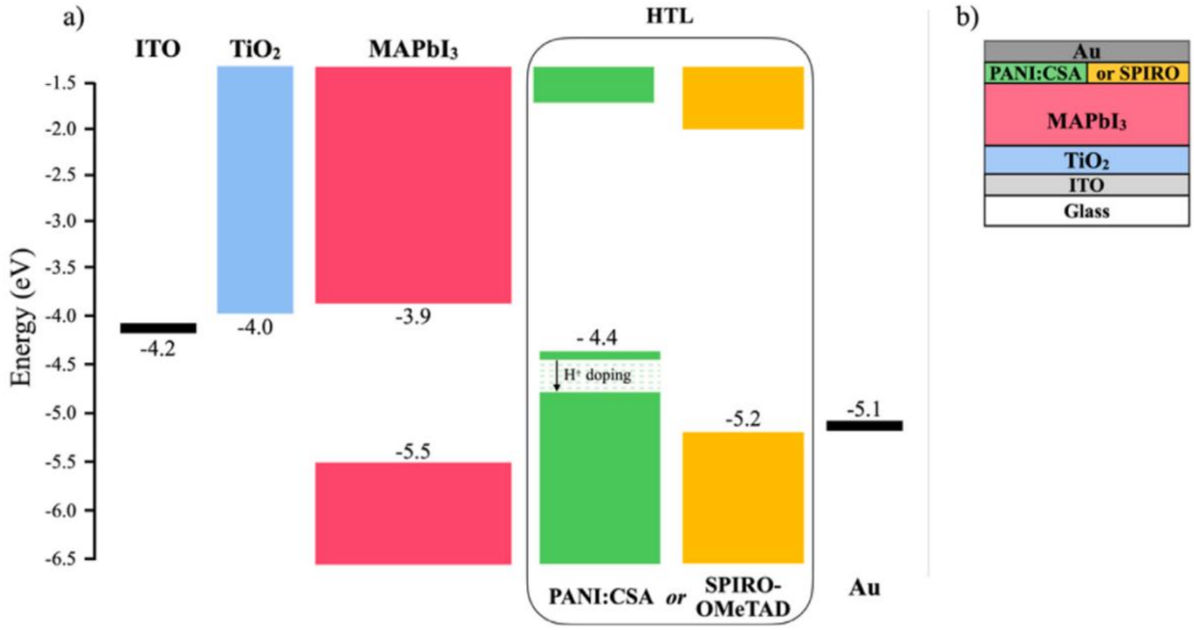

Figure 10.3 *An energy diagram (a), and schematic illustration of the planar heterojunction perovskite solar cells (b).*

10.3.2 Photovoltaic parameters

In this study, the best perovskite solar cells that contained PANI:CSA as the HTL had J-V characteristics that resembled diodes (**Figure 10.4**), but their efficiencies were at most two times lower than performance of the reference cell with Spiro-OMeTAD. The cells with the highest open circuit voltage (V_{oc}) of around 0.75 V were those with PANI:CSA molar ratios of 2:1, and 2.5:1. However, the short circuit current (J_{sc}) for these cells did not exceed 10 mA cm^{-2}. On the other hand, the cells with the highest J_{sc} values of over 20 mA cm^{-2} had a higher content of CSA in the HTL (PANI:CSA molar ratios 1:1 and 1:2.5). Unfortunately, these cells had low V_{oc} values, below 0.5 V. The photovoltaic parameters of the cells presented in **Figure 10.4**, determined from the J-V characteristics, are summarized in **Table 10.2**.

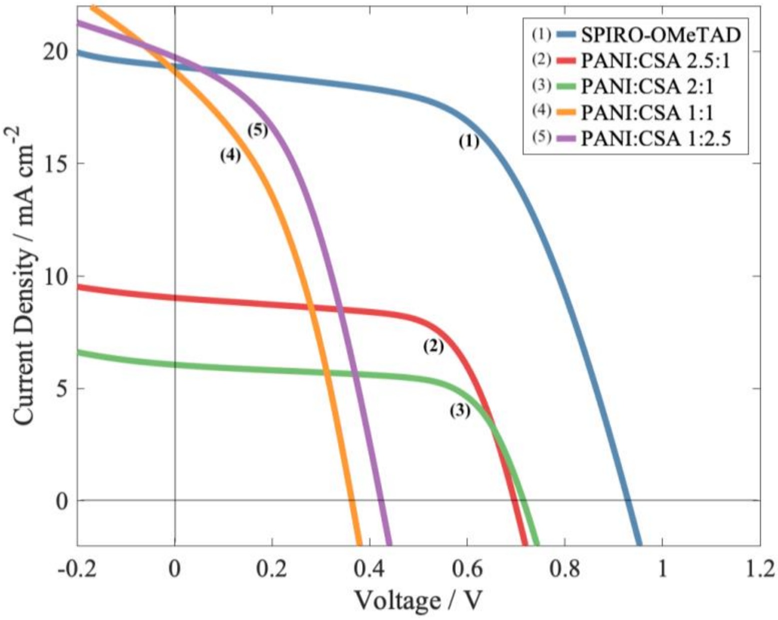

Figure 10.4 *J-V characteristics of perovskite solar cells with different HTLs: Spiro-OMeTAD (line 1), and PANI:CSA at various molar ratios: 2.5:1 (line 2), 2:1 (line 3), 1:1 (line 4) and 1:2.5 (line 5).*

Table 10.2 *Photovoltaic parameters of different investigated perovskite solar cells:* V_{oc} *- open circuit voltage,* J_{sc} *- short circuit current, FF - fill factor, PCE - power conversion efficiency,* ρ_s *- series surface resistivity;* ρ_{sh} *shunt surface resistivity.*

	V_{oc} (V)	J_{sc} (mA cm^{-2})	FF (%)	ρ_s (Ω cm^2)	ρ_{sh} (Ω cm^2)	PCE (%)
Spiro-OMeTAD	0.93	19.34	57.26	6.73	320.20	10.28
PANI:CSA 2.5:1	0.70	9.03	65.05	4.41	404.76	4.09
PANI:CSA 2:1	0.71	6.05	66.35	4.92	355.28	2.87
PANI:CSA 1:1	0.36	19.12	39.88	3.36	60.72	2.58
PANI:CSA 1:2.5	0.42	19.75	44.19	3.99	130.28	3.69

To understand how the PANI doping level affects solar cells' performance, the ratio of PANI to CSA in the HTL was varied from 6:1 to 1:4. Four separate sets of cells were also made for each PANI level, as some cells, especially those with a high amount of CSA, did not perform well. The results shown below are the average values of these four sets, after the data from cells that did not work correctly was excluded.

The plot in **Figure 10.5(a)** shows that, for a low level of CSA doping, the PCE (power conversion efficiency) values increase as the PANI:CSA molar ratio decrease (from 6:1 up to 2:1). The efficiency reaches a maximum in the range of 2:1 to 1:1 and then gradually decreases to zero for higher CSA content. It is worth noting that the highest PCE value recorded was 4.1% and that the data shown in **Figure 10.5(a)** are the average values obtained from multiple measurements of the cells. To better understand the trend in the plot shown in **Figure 10.5(a)**, the V_{oc} (open-circuit voltage) and J_{sc} (short-circuit current density) values were analyzed as a function of the PANI:CSA ratio.

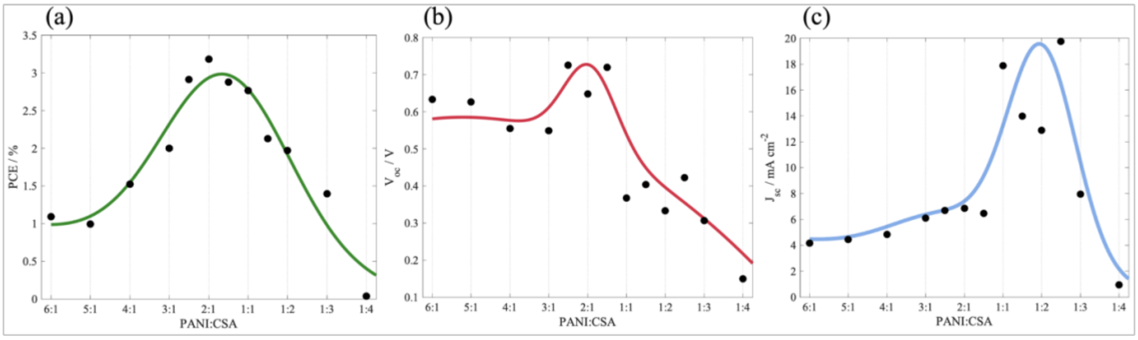

Figure 10.5 The changes of perovskite solar cells parameters: power cell efficiency (a), open circuit voltage (b), and short-circuit current density (c), as a function of PANI:CSA ratio. Points correspond to average experimental data, whereas the solid lines are the guide for the eye.

The open circuit voltage (V_{oc}) of a low doping level of PANI with CSA was found to be in the range of 0.5-0.6V (**Figure 10.5(b)**), which is consistent with the energy difference between the conduction band of TiO_2 (-4.0 eV in relation to the vacuum level) and the highest occupied molecular orbital (HOMO) level of slightly doped PANI (-4.5 to -4.4 eV vs. vacuum level)[151]. Increasing the doping level of PANI with CSA led to an increase in V_{oc} to approximately 0.75 V, with the maximum value achieved at a PANI:CSA molar ratio of about 2:1, which is considered the optimal doping level for hole transport in the hole transport layer. Doping PANI with CSA in m-cresol is known to lower its HOMO energy level to around -4.78 eV in relation to the vacuum level for fully protonated (doped) PANI[151]. This behavior may explain the mentioned above increase of V_{oc} to c.a. 0.75 V for PANI:CSA molar ratio of about 2:1, which corresponds to full doping of PANI. Thus, it seems that for the solar cells with higher CSA content in HTL, i.e. with PANI:CSA ratio lower than 1:1, one could expect stabilization of the open circuit voltage, since V_{oc} value should be approximately related to the potential difference between the conduction band of

TiO_2 and HOMO level of fully doped PANI. As can be seen from **Figure 10.5(b)** this was not however the case because the increasing content of CSA gave rise to significant decrease of V_{oc} and this tendency was observed for all the cells in different series. For high CSA doping level, the decrease of V_{oc} was correlated with a decrease of cell shunt resistivity. Namely, the ρ_{sh} dropped down to several dozen Ω cm^2 for the cells with low V_{oc}, while for the reference cell and for cells with PANI:CSA molar ratio greater than 1:1 it was in the order of several hundred Ω cm^2. The decrease of V_{oc} with decrease of shunt resistivity suggests formation of defects in the solar cells, which are responsible for the flow of photogenerated charge carriers by alternate paths under external voltage. The J-V characteristics show a deviation from the flat shape of the current under external voltage (as shown by curves 4 and 5 in **Figure 10.4**). It is believed that these defects may be caused by the uncontrolled deterioration of the perovskite layer due to excess CSA accumulation at the hole transport layer (HTL)/perovskite interface.

The short-circuit current density values were relatively low, around 4 mA cm^{-2}, for cells with a low doping level of PANI (shown in **Figure 10.5(c)**). This may be due to the low conductivity of the HTL at this doping level[150]. However, the short-circuit current density increased as the CSA concentration increased, reaching its maximum value of up to 20 mA/cm2 for a wide range of PANI:CSA ratios from 2:1 to 1:2.5. This increase may be attributed to a decrease in the cell's series resistivity, which decreased by half compared to the reference solar cell (**Table 10.2**).

However, the position and value of the maximum short-circuit current density (J_{sc}) varied between different series of solar cells. If the resistivity of the HTL had been the main factor influencing the increase in J_{sc}, the maximum current density would have been observed at a PANI:CSA molar ratio of 2:1. However, it was evident that the maximum was shifted to higher CSA concentrations. This suggests that a slight excess of this acid may have a positive impact on cell performance regarding J_{sc}.

For solar cells with a high content of CSA, the short-circuit current density (J_{sc}) dropped to zero, which may be due to the crystallization of an excessive amount of CSA[150]. This may lead to uncontrolled interactions between CSA and the perovskite layer and the creation of defects at the HTL/perovskite interface, which may be responsible for uncontrolled short circuits at various locations in the perovskite layer.

The reference perovskite solar cell with an HTL made of Spiro-OMeTAD had a power conversion efficiency (PCE) of 10.3% (shown in **Figure 10.4**, blue curve), an open-circuit voltage (V_{oc}) of 0.93 V, a short-circuit current density (J_{sc}) of 19.4 mA/cm^2, a surface series resistivity (ρ_s) of 6.7 Ω cm^2, and a surface shunt resistivity (ρ_{sh}) of 320 Ω cm^2. The open-circuit voltage was higher than for cells with an HTL made of PANI:CSA, likely due to the lower HOMO level of SPIRO compared to the HOMO level of doped PANI. The typically higher values of short-circuit current were probably due to the higher conductivity of SPIRO and the better properties of the interface between SPIRO and the perovskite layer compared to PANI:CSA. It would be difficult to significantly increase the open-circuit voltage in the case of PANI cells, but the short-circuit current can still be optimized.

Based on the research that has been conducted so far, it can be concluded that the use of PANI:CSA as an HTL in perovskite solar cells instead of SPIRO may make sense, particularly if the durability of such cells can be improved. This is an area of further research, and preliminary results are promising (**Figure 10.6**).

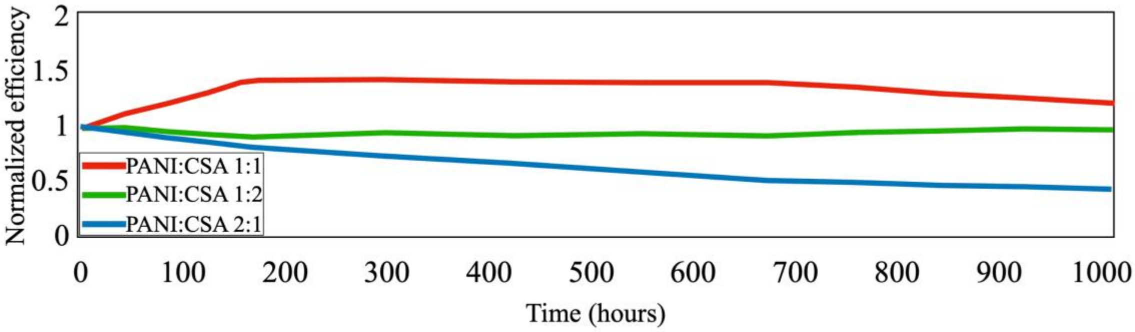

Figure 10.6 *Ageing of perovskite solar cells with PANI:CSA as a HTL.*

Ageing studies over 1000 hours show that for some PANI:CSA ratios (such as PANI:CSA 1:2 in **Figure 10.6**), solar cells are stable and no drop of the efficiency is observed.

10.4 Active layer doped with camphorsulfonic acid

The studies presented in this subchapter have already been published, and the author of this dissertation is the first author of the manuscript, who initiated and conducted experiments[194].

10.4.1 Photovoltaic parameters

In these studies, CSA acid was added to the perovskite active layer. Examples of the J-V characteristics of perovskite-based devices with different CSA concentration are compared in **Figure 10.7**. As can be observed, all the cells revealed a proper, diode-like characteristics with electrical parameters presented in **Table 10.3.** The most important parameter of the solar cell is its efficiency. As can be seen from **Table 10.3**, the addition of CSA to the active layer improved the performance of perovskite solar cells. The highest power conversion efficiency PCE = 11.73% was observed for the sample with CSA concentration of 2 mg/ml.

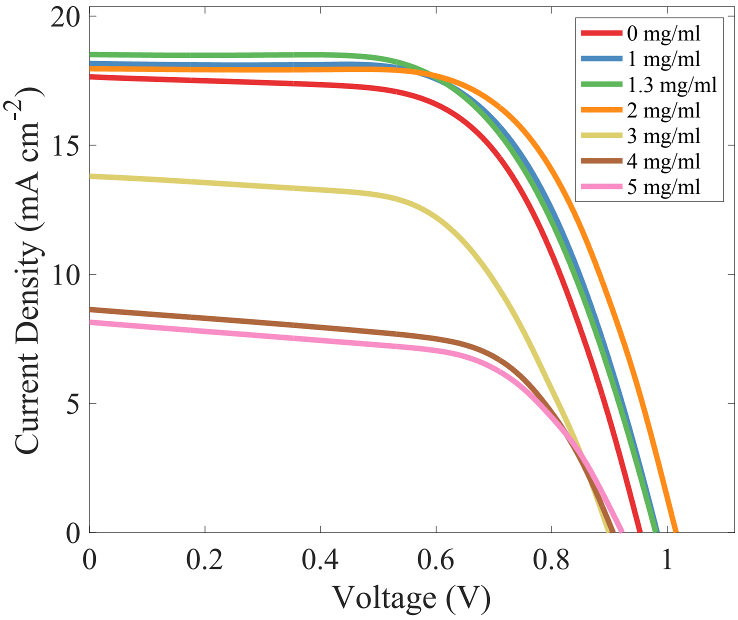

Figure 10.7 *J-V characteristics of the perovskite solar cells with different CSA content.*

Table 10.3 *Photovoltaic parameters of the best perovskite solar cells for a given CSA content: PCE – power conversion efficiency; V_{oc} - open circuit voltage; J_{sc} - short circuit current; FF- fill factor; ρ_s - series resistance; ρ_{sh} - shunt resistance.*

CSA content (mg/ml)	**Max PCE (%)**	**V_{oc} (V)**	**J_{sc} (mA cm^{-2})**	**FF (%)**	**ρ_s (Ω cm^2)**	**ρ_{sh} (Ω cm^2)**
0	10,40	0,95	17,65	61,8	6,4	1297
1	11,17	0,98	18,16	62,6	6,6	3880
1.3	11,03	0,98	18,51	60,8	6,8	7026
2	**11,73**	**1,02**	**17,96**	**64,3**	**7,0**	**5370**
3	7,35	0,90	13,80	59,2	8,7	816
4	4,78	0,91	8,64	61,1	8,8	585
5	4,47	0,92	8,15	59,5	10,9	562

This cell had an open-circuit voltage V_{oc} = 1.02V, short-circuit current density J_{sc} = 17.96 mA cm^{-2}, surface serial resistivity ρ_s = 7.0 Ω cm^2, and surface shunt resistivity ρ_{sh} = 5370 Ω cm^2. However, the highest average PCE based on 8 pixels of each device was obtained for the perovskite cell with CSA concentration of 1 mg/ml. **Table 10.4** contains the average values of the photovoltaic parameters of the investigated set of solar cells.

Table 10.4 *Mean photovoltaic parameters of perovskite solar cells. PCE, efficiency;* V_{oc}*, open circuit voltage;* J_{sc}*, short circuit current; FF, fill factor;* ρ_s*, series resistance;* ρ_{sh}*, shunt resistance.*

CSA content (mg/ml)	**PCE (%)**	**Voc (V)**	**Jsc (mA cm^{-2})**	**FF (%)**	**ρ_s (Ω cm2)**	**ρ_{sh} (Ω cm^2)**
0	8,74	0,93	16,41	57,1	11,7	359
1	**10,56**	**0,98**	**17,58**	**61,4**	**12,3**	**1222**
1.3	10,32	0,96	17,58	60,9	11,5	1042
2	9,19	0,98	16,25	57,8	12,7	670
3	6,34	0,87	12,84	56,6	13,7	577
4	4,11	0,91	7,36	61,5	17,4	451
5	3,89	0,91	7,19	59,6	17,7	414

The reference cell without CSAThe normalized average efficiencies of the cells are shown in **Figure 10.8**. CSA of concentration 1 mg/ml within the perovskite precursor improved the PCE by 20% compared to the reference cell. A sample with 1.3 mg/ml of CSA was made to potentially maximize the efficiency, but it ended up being slightly lower than the sample with 1 mg/ml, suggesting that 1 mg/ml is close to the optimal concentration of CSA. In general, the average efficiency of devices with CSA-doped perovskite up to 2 mg/ml was improved compared to the reference cell without CSA.

The increase in efficiency of perovskite cells with CSA was due to a higher short-circuit current density and improved open circuit voltage, as well as a significant increase in shunt resistance. The larger grain size of the perovskite material also improved charge transport and led to higher mobility. In addition, the reduced amount of grain boundaries likely contributed to an increase in shunt resistance and improved fill factor.

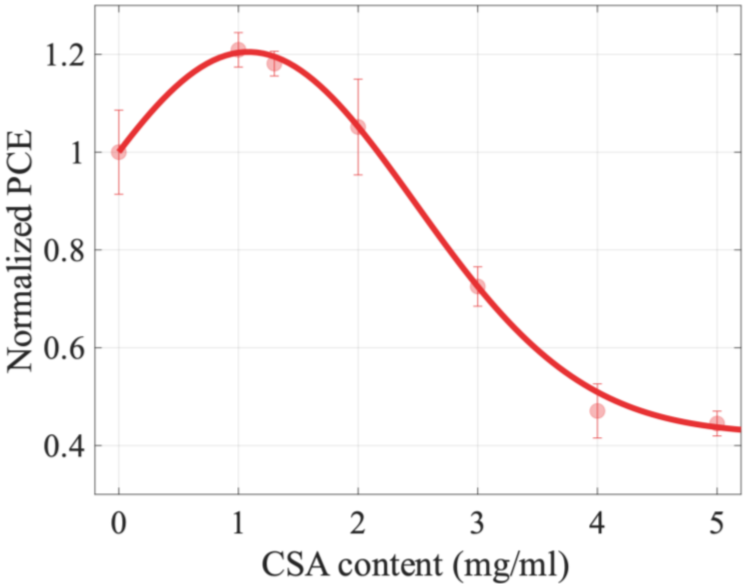

Figure 10.8 *The normalized PCE vs CSA content within perovskite precursors. Error bars represent a standard deviation. The red dots are experimental data and the solid line is a guide to the eye.*

It has already been shown that perovskite grain size affects PCE[55,211]. We suspect that bigger grains of perovskites with 1, 1.3, and 2 mg/ml of CSA discussed in **Chapter 5.4.1** had a positive impact on the performance of the cells based on these materials.

For cells with CSA concentrations of 3, 4, and 5 mg/ml, the efficiency was lower than the reference device. In particular, the cells with the two highest CSA concentrations only retained half of their original efficiency. The decrease in efficiency was mainly due to a decrease in current density (**Figure 10.9(a)**) and an increase in series resistance (**Figure 10.9(b)**). As shown, the trend of the dependence of J_{sc} on CSA content is similar to the trend of changes in efficiency, with J_{sc} values of samples with CSA up to 2 mg/ml being equal to or higher than the reference cel value. The J-V characteristic of the perovskite cell with 3 mg/ml CSA showed about 80% of the J_{sc} value of the cell without CSA.

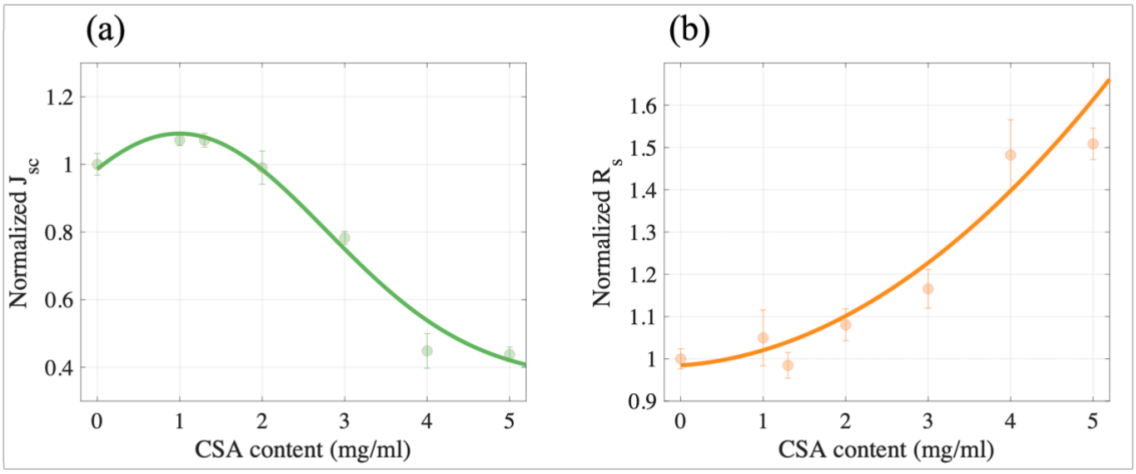

Figure 10.9 *Normalized current density (J_{sc}) vs CSA content (a), normalized series resistance (R_s) vs CSA content (b).*

Finally, materials with CSA concentrations of 4 and 5 mg/ml resulted in devices with about half the J_{sc} of the reference cell. In terms of series resistance, cells with CSA up to 2 mg/ml had similar or slightly higher ρ_s values compared to the reference cell. However, perovskite solar cells with CSA concentrations of 4 and 5 mg/ml showed a relatively high ρ_s value, representing an increase of about 50% compared to the reference cell.

Despite the fact that the perovskite grains were about 50% larger in cells with higher concentrations of CSA (3, 4, and 5 mg/ml), the cell parameters deteriorated and the efficiency dropped by more than a factor of two. It is believed that the presence of CSA precipitates on the film surfaces of perovskites with high CSA content (morphology discussed in **Chapter 5.4.1**) formed non-conductive interfaces between the perovskite layer and the HTL (Spiro-OMeTAD) or CSA precipitates within the perovskite bulk, resulting in an increase in serial resistance and a decrease in current density, which significantly reduced the efficiency of the cells. CSA is considered an insulator, thus an explanation involving isolating precipitates and the increase in series resistance could potentially offer a plausible explanation.

10.4.2 Aging studies

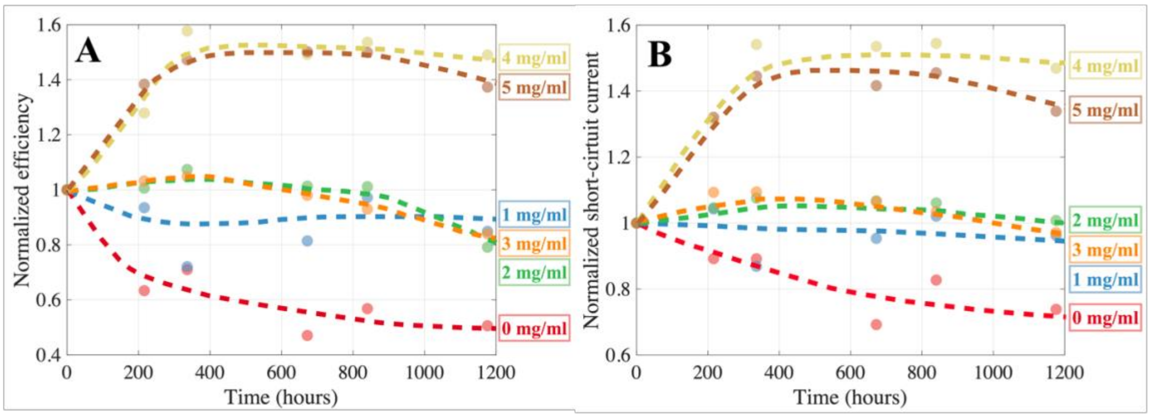

Figure 10.10 *Ageing of perovskite solar cells: efficiency (A), and short-circuit current (B).*

The changes in normalized efficiency over time, as shown in **Figure 10.10(a)**, indicate that the degradation dynamics depend on the concentration of CSA in the perovskite layer. The reference sample with 0 mg/ml CSA showed the fastest decay, reaching about half of its initial efficiency after 1200 hours. Cells with moderate CSA concentrations (1, 2, 3 mg/ml) were more stable than the reference, retaining about 80% of their initial efficiency at the end of the aging experiment. It is known that perovskites are sensitive to oxygen and moisture, which can lead to their gradual decomposition. It has been shown that the increase of the perovskite grain size (which is a case in CSA-doped perovskites as discussed in **Chapter 5.4.1**) can significantly reduce oxygen diffusion and considerably slow down the degradation[131]. We found that a moderate concentration of CSA promotes the growth of large perovskite grains, which are expected to be more stable than the reference material. As a result, devices made with these materials show better environmental stability compared to cells with pristine perovskite.

Finally, the cells with the highest CSA concentrations (4 and 5 mg/ml) behaved significantly differently from the others. Their efficiencies gradually increased, reaching about 1.5 times their initial efficiency after 400 hours, and then saturated at this level. The increase in efficiency was mainly due to an increase in J_{sc} (**Figure 10.10(b)**). It is believed that this increase was caused by interactions between CSA precipitates and Spiro-OMeTAD. The addition of acids can catalyze the oxidation process of Spiro-OMeTAD[99], and the presence of CSA precipitates on the surface of the perovskite films at high acid concentrations (discussed in **Chapter 5.4.1**, see also **Figure 5.19**) suggests that CSA excess at the interface between the perovskite film and HTL (Spiro-OMeTAD) could migrate to the HTL, promoting its oxidation and improving its conductivity. However, it is worth noting that although the relative increase in efficiency was the highest for cells with 4 and

5 mg/ml of CSA, the maximum absolute efficiency of these devices was lower than that of cells with 2 mg/ml of CSA.

10.5 Al_2O_3 coverage – a promising and efficient device's encapsulation

Fragments of this chapter have already been published, and the author is the first author in the publication[212]. The other strategy to improve the stability of iodide perovskite films, besides bromine/chlorine addition or CSA doping, is to deposit a water and oxygen resistant top layer. Atomic layer deposition (ALD) is a very promising technique for new generation solar cell fabrication. ALD has been applied for both deposition of the electron transport layer[213] and also to stabilize the devices[101]. It has been shown that the encapsulation of perovskite solar cells by atomic layer deposition of Al_2O_3 thin films is an efficient approach to perovskite solar cell stability improvement[100]. The architecture of a typical perovskite solar cell provides a partial protection of perovskite absorber film because the absorber film is sandwiched between two charge transporting layers. However, an additional encapsulation of the device is needed to prevent the oxygen and water diffusion through the side edges of the structure. Furthermore, some layers, such as commonly used SPIRO-OMeTAD (a hole-transporting layer material) can spontaneously oxidize on contact with oxygen from air, or degrade due to hygroscopicity of dopant salts[34], which might negatively impact its conductivity and therefore, negatively affect the power conversion efficiency of the solar cell.

Al_2O_3 coating was used to study its effect on the stability of perovskite films. For this experiment MAPI, showing a relatively fast degradation without coating, was selected. A layer of Al_2O_3 was deposited on top of this sample using ALD technique, as described in **Chapter 4.2**. The stability of such structure was monitored by collecting XRD patterns several times during 50 days of exposure to air. For comparison, an uncoated MAPI was also exposed to the same environmental conditions and monitored by XRD. These measurements indicate a very slow kinetics of the degradation process with the characteristic time of at least several months. The XRD patterns for both, uncoated and Al_2O_3-coated films, collected at different stages of aging experiment, are compared in **Figure 10.11**.

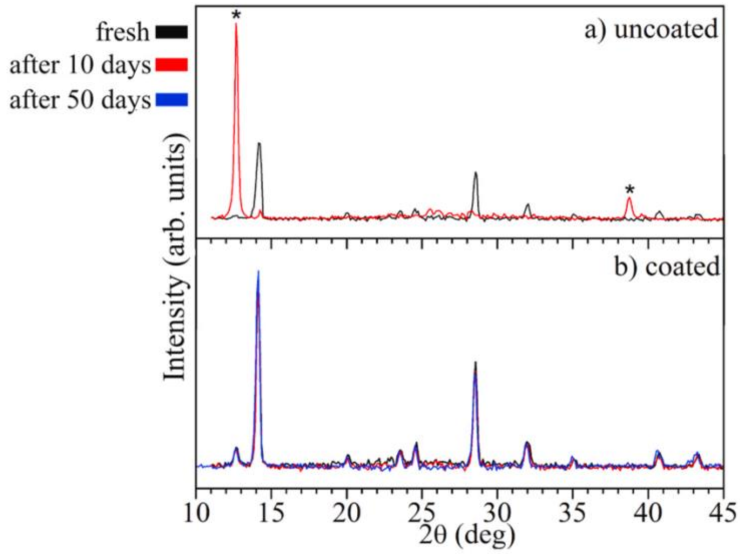

Figure 10.11 *Influence of Al_2O_3 coating on the durability of MAPI. Figure shows a) uncoated, and b) coated samples. * denotes peaks originating from PbI_2.*

It can be seen there that for the uncoated MAPI film, perovskite structure peaks were completely absent from the XRD pattern already after 10 days of air exposure (**Figure 10.11**, red diffraction curve). This is evidence of complete degradation of perovskite material. After these 10 days there were only two strong peaks present in the XRD pattern, one at ~13° and other one at ~39°, originating from PbI2 (001) and (003) planes[214], respectively. This was an evidence of iodide perovskite degradation to PbI_2.

Significantly different behavior was observed for the MAPI film coated with an Al_2O_3 layer. XRD diffraction pattern measured for this sample did not change, even after 50 days of exposure to air; all perovskite diffraction peaks were unchanged and their relative intensities were preserved (**Figure 10.11**), which was evidence of no change in material structure and composition. Thus, greatly improved stability of the perovskite film coated with Al_2O_3 was achieved and demonstrated.

After a successful encapsulation of the perovskite films with Al_2O_3, impact of such a coverage on stability of perovskite solar cells was investigated. A protective Al_2O_3 layer was deposited on the top of the device and aging experiments were conducted for over 1000 hours. **Figure 10.12** shows how normalized efficiency evolved over time for the reference cell, namely exposed to air (60%RH, 25°C) without any protection (red curve) and the encapsulated, covered with Al_2O_3 cell (green curve). Both samples were stored in the dark, and were illuminated only during daily J-V measurements.

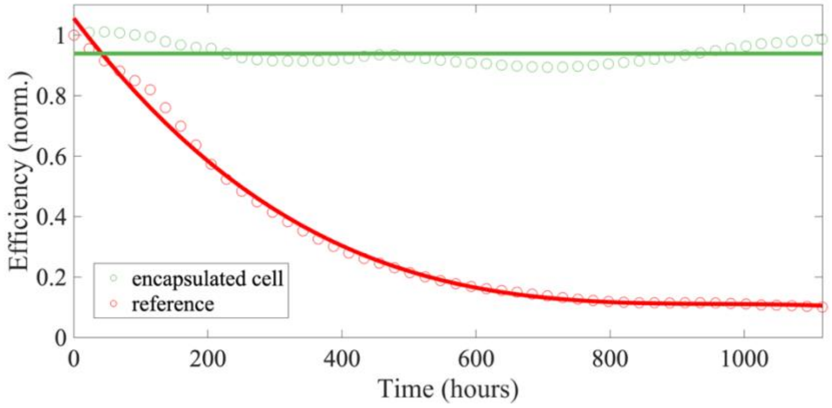

Figure 10.12 *Perovskite solar cells efficiency evolution over time: reference (red), and covered with Al_2O_3 (green). Dots represent the average efficiency of 8 samples.*

It was found the efficiency almost did not change over more than 1000 hours for the encapsulated cell (green curve). Insignificant efficiency fluctuations were observed, which may occur due to slight changes of humidity or temperature in the aging environment. This is evidence of successful protection of the device against degradation factors such as oxygen or moisture. On the other hand, uncovered cell degraded relatively fast, and after 1000 hours maintained about 10% of the initial efficiency (red curve).

Therefore, it was shown that additional protection of the device is needed, and Al_2O_3 deposited using ALD is an efficient approach to stabilize perovskite solar cells.

10.6Chapter summary

This chapter presented the results of studies on perovskite solar cells, in which several approaches were applied to boost both efficiency and stability. The results show that not all the investigated changes in the perovskite solar cells resulted in increased efficiency.

First, a modification of electron transport layer was analyzed. This study investigated impact of plasmonic gold nanoparticles (AuNPs) on the efficiency of perovskite solar cells. Unfortunately, despite several trials and fabrication of many solar cells with AuNPs, their efficiency was significantly lower than in the reference devices. The main parameters which contributed to decrease of performance of modified cells were: current density and fill factor. The low J_{sc} compared to the reference may indicate the decomposition of the absorbing layer (perovskite) due to the presence of residual HAuCl4 acid at the TiO_2 surface. The mesoporous structure of titanium dioxide in the perovskite solar cell can make it difficult to remove the acid.

Secondly, chemically synthesized polyaniline protonated with camphorsulfonic acid in chloroform substituted state-of-the art hole transport layer, Spiro-oMeTAD, in perovskite solar cells. The cells with the highest open-circuit voltage (Voc) were those with PANI:CSA molar ratios of 1.5:1, 1:1, and 2.5:1, but they had relatively low short-circuit current (J_{sc}) values. On the other hand, the cells with the highest Jsc values had a higher content of CSA in the HTL, but they had low V_{oc} values (1:2.5 PANI:CSA). The results of the study showed that the power conversion efficiency (PCE) of the cells increased as the PANI:CSA molar ratio increased from 6:1 to 2:1, reached a maximum in the range of 2:1 to 1:1, and then gradually decreased to zero for higher CSA content. The highest PCE value recorded was 4.1%. Even though the efficiency was lower than in the reference, PANI:CSA has its advantages over Spiro-OMeTAD like better environmental stability. And once the structure is optimized, it may be a very promising candidate for a future HTL material.

Third, studies of a set of perovskite solar cells with a modified active layer by adding CSA acid to perovskite precursor showed the average improvement of their efficiency by 20% for 1 mg/ml CSA. The systematic characterization of the influence of CSA acid on the active layer film quality and photovoltaic parameters of the devices as a function of CSA content was performed. It was observed (as presented in **Chapter 5.4.2**) that the higher the CSA content, the more random the grain orientation within the film was. Additionally, it was found that higher concentration of CSA led to increase of grain sizes (by 50% compared to the reference with no CSA). However, starting from the perovskite with 3 mg/ml of CSA, precipitations of this acid were observed on the surface of the active layer material. These CSA precipitations formed insulating islands at some places of interface between the perovskite films and Spiro-OMeTAD within a cell, which resulted in a significant increase in series resistance, thereby reduced the open circuit current, and as a consequence led to decrease in the efficiency. Aging experiments showed that the cells based on perovskites with moderate concentrations of CSA reveal better environmental stability compared to the reference device. For cells with the highest concentrations of CSA, a gradual increase of PCE over time was observed, which was attributed to CSA migration from its precipitates to Spiro-OMeTAD, promoting Spiro-OMeTAD oxidation, and as a consequence improving its conductivity.

Finally, a water and oxygen-resistant top layer (Al_2O_3) using atomic layer deposition (ALD) technique was deposited on the perovskite films and perovskite solar cells. The stability of the films was monitored by collecting XRD patterns several times during 50 days of exposure to air. The results indicated that the uncoated MAPI film degraded completely after 10 days of air exposure, but the MAPI film coated with Al_2O_3 did not change, even after 50 days of exposure to air. These studies showed that the Al_2O_3 coating greatly improved the stability of the perovskite film. The impact of the Al_2O_3 coating on the stability of perovskite solar cells was also investigated and it was found that the efficiency of the encapsulated cells almost did not change over more than 1000 hours, while the efficiency of the reference cells decreased significantly.

11 Summary

This thesis focuses on perovskites and perovskite photovoltaic cells, which have received extensive research attention in recent years due to their potential for achieving high efficiencies while offering inexpensive and eco-friendly fabrication. The primary challenges faced by this generation of cells include the lack of repeatability in the technology, degradation issues, and ongoing efforts to improve efficiency.

Several attempts were made to modify both the cell layers (ETL and HTL) and, specifically, the active layer, with the aim of enhancing efficiency. The best efficiencies were achieved by incorporating CSA in the cells. *In-situ* studies demonstrated that the presence of CSA significantly slowed down perovskite crystallization, resulting in improved material quality and the growth of larger grains. Adding CSA to the active layer enhanced the performance of perovskite solar cells by 20% compared to the CSA-free reference.

The second approach involved substituting the commonly used HTL with chemically synthesized polyaniline protonated with camphorsulfonic acid (PANI:CSA). It was demonstrated that this new HTL can be used in perovskite solar cells, although with lower efficiency compared to the reference. The promise of this approach lies in the improved environmental stability of PANI:CSA, as commercial SPIRO tends to oxidize uncontrollably and lose its optimal properties.

A significant portion of the research was dedicated to tracking the degradation processes of perovskites. It is generally accepted that oxygen and water are the main degradation factors. The presented research examined the impact of oxygen and water, while the influence of illumination was not analyzed. It was observed that water significantly affects perovskite stability when humidity levels exceed approximately 40% RH. Below this value, oxygen becomes the main degrading factor. Importantly, the study demonstrated that hydration processes are reversible as long as the material is not exposed to high humidity for extended periods. The experiments showed that subjecting the material to high humidity close to 100% RH for a few minutes and subsequent drying with nitrogen allowed for complete dehydration and restoration of the material to its original form. Furthermore, in partially degraded materials, the presence of a PbI_2 layer (a degradation product) surrounding the pristine perovskite, significantly slowed down the hydration process by limiting water diffusion.

Kinetic models of degradation processes were developed, enabling the determination of characteristic degradation times and facilitating comparisons of degradation dynamics among different modified materials.

The study also revealed that oxygen diffusion leads to irreversible processes and material degradation. Considering the difficulty in preventing oxygen diffusion into the material, the possibility of protecting the cells with an Al_2O_3 layer deposited using ALD was examined. The research confirmed the effective protection and significantly improved stability, potentially limiting both oxygen and water diffusion in solar cells.

Moreover, it was observed that water, contrary to expectations, has a positive impact on quasi-3D perovskites. After hydration and restoration to the initial perovskite structure, a more ordered material with a significant improvement in luminescence (a novel observation) was obtained. This discovery opens up possibilities for utilizing quasi-3D perovskites in LEDs.

The study also demonstrated that the presence of bromine slows down crystallization and promotes the growth of larger perovskite grains, similar to the addition of CSA acid.

Other strategies for modifying perovskites and solar cells were also explored, such as incorporating plasmonic nanoparticles (AuNPs) on the surface of the electron-transporting layer or adding tetraethoxysilane (TEOS) to perovskites. These studies showed potential but require further optimization. Solar cells with the addition of AuNPs exhibited low efficiency compared to the reference. The presence of TEOS indicated increased stability of perovskites, but only at relatively high concentrations of TEOS.

12 Publications of the author

1. **Wincukiewicz, A.**; Wierzyńska, E.; Bohdan, A.; Tokarczyk, M.; Korona, K.P.; Skompska, M.; Kamińska, M. Enhanced Performance of Camphorsulfonic Acid-Doped Perovskite Solar Cells. *Mol. 2022, Vol. 27, Page 7850* **2022**, *27*, 7850, doi:10.3390/MOLECULES27227850
2. Łempicka-Mirek, K.; Król, M.; Sigurdsson, H.; **Wincukiewicz, A.**; Morawiak, P.; Mazur, R.; Muszyński, M.; Piecek, W.; Kula, P.; Stefaniuk, T.; et al. Electrically Tunable Berry Curvature and Strong Light- Matter Coupling in Birefringent Perovskite Microcavities at Room Temperature. *Sci. Adv.* **2022**, *8*, 7533
3. Kwiatkowska, E.; Mech, W.; **Wincukiewicz, A.**; Korona, K.P.; Zarębska, K.; Kamińska, M.; Skompska, M. Investigation of Polyaniline Doped with Camphorsulfonic Acid in Chloroform Solution as a Hole Transporting Layer in PTB7: PCBM and Perovskite-Based Solar Cells. *Electrochim. Acta* **2021**, *380*, 138264, doi:10.1016/J.ELECTACTA.2021.138264
4. **Wincukiewicz, A.**; Jasinski, J.B.; Tokarczyk, M.; Pietruszka, R.; Godlewski, M.; Kaminska, M. The Effects of Doping and Coating on Degradation Kinetics in Perovskites. *Sol. Energy Mater. Sol. Cells* **2021**, *230*, 111142, doi:10.1016/j.solmat.2021.111142
5. Mech, W.; Borysiuk, J.; **Wincukiewicz, A.**; Bożek, R.; Trautman, P.; Tokarczyk, M.; Kamińska, M.; Korona, K.P. Influence of Active Layer Processing on Electrical Properties and Efficiency of Polymer- Fullerene Organic Solar Cells. *Jaszowiec* **2019**, *136*, doi:10.12693/APhysPolA.136.579
6. **Wincukiewicz, A.**; Mech, W.; Grankowska, S.; Wolos, A.; Drabinska, A.; Slupinski, T.; Korona, K.P.; Kaminska, M. Radiative Recombination and Other Processes Related to Excess Charge Carriers, Decisive for Efficient Performance of Electronic Devices. *Lith. J. Phys.* **2018**, *58*, 49–61, doi:10.3952/PHYSICS.V58I1.3651

13 List of figures

14 List of tables

15 References

1. Krajewski, M. Lewarowanie półprzewodnikami. Część 1. *Strategy&Future* https://strategyandfuture.org/lewarowanie-polprzewodnikami-czesc-1/ (2021).
2. Dole, S. H. Habitable Planets for Man. *Habitable Planets Man* (2007) doi:10.7249/CB179-1.
3. Kopparapu, R. K. A REVISED ESTIMATE OF THE OCCURRENCE RATE OF TERRESTRIAL PLANETS IN THE HABITABLE ZONES AROUND KEPLER M-DWARFS. *Astrophys. J. Lett.* **767**, L8 (2013).
4. Lewis, N. S. *et al.* Basic Research Needs for Solar Energy Utilization. Report of the Basic Energy Sciences Workshop on Solar Energy Utilization, April 18-21, 2005. (2005).
5. International Renewable Energy Agency. FUTURE OF SOLAR PHOTOVOLTAIC - Deployment, investment, technology, grid integration and socio-economic aspects. https://www.irena.org/-/media/Files/IRENA/Agency/Publication/2019/Nov/IRENA_Future_of_Solar_PV_2019.pdf (2019).
6. Energy Information Administration, U. Cost and Performance Characteristics of New Generating Technologies, Annual Energy Outlook 2022. (2022).
7. Altermatt, P. P., Schenk, A., Geelhaar, F. & Heiser, G. Reassessment of the intrinsic carrier density in crystalline silicon in view of band-gap narrowing. *J. Appl. Phys.* **93**, 1598 (2003).
8. Rangel, T. *et al.* Band structure of gold from many-body perturbation theory. *Phys. Rev. B - Condens. Matter Mater. Phys.* **86**, 125125 (2012).
9. Ullah, S. Optical control and detection of spin coherence in multilayer systems. **3**, (2017).
10. Gao, S. P. Band gaps and dielectric functions of cubic and hexagonal diamond polytypes calculated by many-body perturbation theory. *Phys. Status Solidi Basic Res.* **252**, 235–242 (2015).
11. Shockley, W. The Theory of p-n Junctions in Semiconductors and p-n Junction Transistors. *Bell Syst. Tech. J.* **28**, 435–489 (1949).
12. Shockley, W. & Queisser, H. J. Detailed balance limit of efficiency of p-n junction solar cells. *J. Appl. Phys.* **32**, 510–519 (1961).
13. Shockley–Queisser limit - Wikipedia. https://en.wikipedia.org/wiki/Shockley–Queisser_limit.
14. Mark Geoghegan, Hamley Ian W. & Kelsall Robert W. *Nanotechnologie*. (2008).
15. Rühle, S. Tabulated values of the Shockley-Queisser limit for single junction solar cells. *Sol. Energy* **130**, 139–147 (2016).
16. Guan, L. *et al.* Effect of atomic configuration on band gap behaviour in CH3NH3SnxPb1−xI3 perovskites. *Phys. Lett. A* **384**, 126173 (2020).
17. Gueymard, C. A., Myers, D. & Emery, K. Proposed reference irradiance spectra for solar energy systems testing. *Sol. Energy* **73**, 443–467 (2002).
18. Belghachi, A. Theoretical Calculation of the Efficiency Limit for Solar Cells. *Sol. Cells - New Approaches Rev.* (2015) doi:10.5772/58914.
19. Sze, S. M. & Ng, K. K. Physics of Semiconductor Devices. *Phys. Semicond. Devices* (2006)

doi:10.1002/0470068329.

20. Kroon, M. A. & Van Swaaij, R. A. C. M. M. Spatial effects on ideality factor of amorphous silicon pin diodes. *J. Appl. Phys.* **90**, 994 (2001).

21. Xiong, C., Sun, J., Yang, H. & Jiang, H. Real reason for high ideality factor in organic solar cells: Energy disorder. *Sol. Energy* **178**, 193–200 (2019).

22. Kim, K. *et al.* Performance prediction of chalcopyrite-based dual-junction tandem solar cells. *Sol. Energy* **155**, 167–177 (2017).

23. This Month in Physics History. https://www.aps.org/publications/apsnews/200904/physicshistory.cfm.

24. A Limitless Resource: Solar Energy; In a world that needs more and more power, intensive research goes forward on methods of 'harnessing' the sun. - The New York Times. https://www.nytimes.com/1956/03/18/archives/a-limitless-resource-solar-energy-in-a-world-that-needs-more-and.html.

25. Jaeger, J. Explaining the Exponential Growth of Renewable Energy. (2021).

26. Best Research-Cell Efficiency Chart | Photovoltaic Research | NREL. https://www.nrel.gov/pv/cell-efficiency.html.

27. Green, M. A. *et al.* Solar cell efficiency tables (Version 60). *Prog. Photovoltaics Res. Appl.* **30**, 687–701 (2022).

28. Monocrystalline vs Polycrystalline Solar Panels | American Solar Energy Society. https://ases.org/monocrystalline-vs-polycrystalline-solar-panels/.

29. Amorphous silicon - Wikipedia. https://en.wikipedia.org/wiki/Amorphous_silicon.

30. Wu, C. G., Chiang, C. H. & Chang, S. H. A perovskite cell with a record-high-Voc of 1.61 v based on solvent annealed CH3NH3PbBr3/ICBA active layer. *Nanoscale* **8**, 4077–4085 (2016).

31. Xiang, S. *et al.* Highly Air-Stable Carbon-Based α-CsPbI3Perovskite Solar Cells with a Broadened Optical Spectrum. *ACS Energy Lett.* **3**, 1824–1831 (2018).

32. Liu, T. *et al.* Stable Formamidinium-Based Perovskite Solar Cells via In Situ Grain Encapsulation. *Adv. Energy Mater.* **8**, 1–9 (2018).

33. Grätzel, M. The light and shade of perovskite solar cells. *Nat. Mater. 2014 139* **13**, 838–842 (2014).

34. Kim, N.-K. *et al.* Investigation of Thermally Induced Degradation in CH3NH3PbI3 Perovskite Solar Cells using In-situ Synchrotron Radiation Analysis. *Sci. Rep.* **7**, 4645 (2017).

35. Babbe, F., Masquelier, E., Zheng, Z. & Sutter-Fella, C. M. Flash Formation of I-Rich Clusters during Multistage Halide Segregation Studied in MAPbI1.5Br1.5. *J. Phys. Chem. C* **124**, 24608–24615 (2020).

36. Phuong, L. Q., Nakaike, Y., Wakamiya, A. & Kanemitsu, Y. Free Excitons and Exciton-Phonon Coupling in CH3NH3PbI3 Single Crystals Revealed by Photocurrent and Photoluminescence Measurements at Low Temperatures. *J. Phys. Chem. Lett.* **7**, 4905–4910 (2016).

37. Chi, L. *et al.* The ordered phase of methylammonium lead chloride CH3ND 3PbCl3. *J. Solid State Chem.* **178**, 1376–1385 (2005).

38. Ke, W. *et al.* Narrow-bandgap mixed lead/tin-based 2D Dion-Jacobson perovskites boost the performance of solar cells. *J. Am. Chem. Soc.* **142**, 15049–15057 (2020).

39. Aftab, A. & Ahmad, M. I. A review of stability and progress in tin halide perovskite solar cell. *Sol. Energy* **216**, 26–47 (2021).

40. Gupta, S., Bendikov, T., Hodes, G. & Cahen, D. CsSnBr $_3$, A Lead-Free Halide Perovskite for Long-Term Solar Cell Application: Insights on SnF $_2$ Addition. *ACS Energy Lett.* **1**, 1028–1033 (2016).
41. Leijtens, T. *et al.* Overcoming ultraviolet light instability of sensitized TiO2 with meso-superstructured organometal tri-halide perovskite solar cells. *Nat. Commun. 2013 41* **4**, 1–8 (2013).
42. Liang, C. *et al.* One-Step Inkjet Printed Perovskite in Air for Efficient Light Harvesting. *Sol. RRL* **2**, 1700217 (2018).
43. Ghahremani, A. H. & Druffel, T. Realizing Perovskite Solar Cells on Roll Roll-to-Roll Compatible Processes. *Conf. Rec. IEEE Photovolt. Spec. Conf.* **2**, 3433–3437 (2019).
44. Gong, J., Darling, S. B. & You, F. Perovskite photovoltaics: life-cycle assessment of energy and environmental impacts. *Energy Environ. Sci.* **8**, 1953–1968 (2015).
45. Iwan, A. & Instytut Elektrotechniki (Warszawa). Oddział Technologii i Materiałoznawstwa Elektrotechnicznego (Wrocław). Nowe polimerowe ogniwa fotowoltaiczne : badanie wpływu budowy polimeru, architektury ogniwa oraz rodzaju domieszki na sprawność polimerowych ogniw słonecznych opartych na poliazometinach i politiofenach : praca zbiorowa. (2015).
46. Green, M. A. *et al.* Solar cell efficiency tables (version 59). *Prog. Photovoltaics Res. Appl.* **30**, 3–12 (2022).
47. Everything you ever wanted to know about perovskite. *Science, Volume 358, Issue 6364* https://www.youtube.com/watch?v=5oZWLKSDVBk (2017).
48. An, Y. *et al.* Structural Stability of Formamidinium- And Cesium-Based Halide Perovskites. *ACS Energy Lett.* **6**, 1942–1969 (2021).
49. Li, Z. *et al.* Stabilizing Perovskite Structures by Tuning Tolerance Factor: Formation of Formamidinium and Cesium Lead Iodide Solid-State Alloys. *Chem. Mater.* **28**, 284–292 (2016).
50. Fan, Z., Sun, K. & Wang, J. Perovskites for photovoltaics: a combined review of organic–inorganic halide perovskites and ferroelectric oxide perovskites. *J. Mater. Chem. A* **3**, 18809–18828 (2015).
51. Ma, C. *et al.* 2D/3D perovskite hybrids as moisture-tolerant and efficient light absorbers for solar cells. *Nanoscale* **8**, 18309–18314 (2016).
52. Kim, W. *et al.* Oriented Grains with Preferred Low-Angle Grain Boundaries in Halide Perovskite Films by Pressure-Induced Crystallization. *Adv. Energy Mater.* **8**, 1702369 (2018).
53. Zhang, J. *et al.* Hole-conductor-free perovskite solar cells prepared with carbon counter electrode. *Appl. Surf. Sci.* **430**, 531–538 (2018).
54. Bera, S. *et al.* Review of defect engineering in perovskites for photovoltaic application. *Mater. Adv.* **3**, 5234–5247 (2022).
55. Nukunudompanich, M., Budiutama, G., Suzuki, K., Hasegawa, K. & Ihara, M. Dominant effect of the grain size of the MAPbI3 perovskite controlled by the surface roughness of TiO2 on the performance of perovskite solar cells. *CrystEngComm* **22**, 2718–2727 (2020).
56. Nandal, V. & Nair, P. R. Ion induced passivation of grain boundaries in perovskite solar cells. *J. Appl. Phys.* **125**, (2019).
57. Li, B. *et al.* Surface passivation engineering strategy to fully-inorganic cubic CsPbI3perovskites for high-performance solar cells. *Nat. Commun.* (2018) doi:10.1038/s41467-018-03169-0.
58. Dou, L. Emerging two-dimensional halide perovskite nanomaterials. *J. Mater. Chem. C* **5**, 11165–11173 (2017).
59. Quan, L. N. *et al.* Ligand-Stabilized Reduced-Dimensionality Perovskites. *J. Am. Chem. Soc.* **138**,

2649–2655 (2016).

60. Yuan, J. *et al.* Two-dimensional perovskite capping layer for stable and efficient tin-lead perovskite solar cells. *Sci. China Chem. 2019 625* **62**, 629–636 (2019).
61. Grancini, G. *et al.* One-Year stable perovskite solar cells by 2D/3D interface engineering. *Nat. Commun.* **8**, 1–8 (2017).
62. Dehghanipour, M., Behjat, A. & Amrollahi Bioki, H. Fabrication of stable and efficient 2D/3D perovskite solar cells through post-treatment with TBABF4. *J. Mater. Chem. C* **9**, 957–966 (2021).
63. Quan, L. N. *et al.* Ligand-Stabilized Reduced-Dimensionality Perovskites. *J. Am. Chem. Soc.* **138**, 2649–2655 (2016).
64. Kim, E.-B., Akhtar, M. S., Shin, H.-S., Ameen, S. & Nazeeruddin, M. K. A review on two-dimensional (2D) and 2D-3D multidimensional perovskite solar cells: Perovskites structures, stability, and photovoltaic performances. *J. Photochem. Photobiol. C Photochem. Rev.* 100405 (2021) doi:10.1016/j.jphotochemrev.2021.100405.
65. Han, F., Yang, W., Li, H. & Zhu, L. Stable High-Efficiency Two-Dimensional Perovskite Solar Cells Via Bromine Incorporation. *Nanoscale Res. Lett.* **15**, (2020).
66. Ge, C., Xue, Y. Z. B., Li, L., Tang, B. & Hu, H. Recent Progress in 2D/3D Multidimensional Metal Halide Perovskites Solar Cells. *Front. Mater.* **7**, (2020).
67. Zhang, L. & Liang, W. How the Structures and Properties of Two-Dimensional Layered Perovskites MAPbI3 and CsPbI3 Vary with the Number of Layers. *J. Phys. Chem. Lett.* **8**, 1517–1523 (2017).
68. Liu, B. *et al.* Optical Properties and Modeling of 2D Perovskite Solar Cells. *Sol. RRL* **1**, 1–8 (2017).
69. Jeon, N. J. *et al.* Compositional engineering of perovskite materials for high-performance solar cells. *Nature* **517**, 476–480 (2015).
70. Yang, W. S. *et al.* High-performance photovoltaic perovskite layers fabricated through intramolecular exchange. *Science (80-.).* **348**, 1234–1237 (2015).
71. Sutherland, B. R. & Sargent, E. H. Perovskite photonic sources. *Nat. Photonics* **10**, 295–302 (2016).
72. Kim, H. S., Im, S. H. & Park, N. G. Organolead halide perovskite: New horizons in solar cell research. *J. Phys. Chem. C* **118**, 5615–5625 (2014).
73. Miyata, A. *et al.* Direct measurement of the exciton binding energy and effective masses for charge carriers in organic–inorganic tri-halide perovskites. *Nat. Phys. 2014 117* **11**, 582–587 (2015).
74. Even, J., Pedesseau, L. & Katan, C. Analysis of multivalley and multibandgap absorption and enhancement of free carriers related to exciton screening in hybrid perovskites. *J. Phys. Chem. C* **118**, 11566–11572 (2014).
75. Bakulin, A. A. *et al.* Real-Time Observation of Organic Cation Reorientation in Methylammonium Lead Iodide Perovskites. *J. Phys. Chem. Lett.* **6**, 3663–3669 (2015).
76. Saba, M., Quochi, F., Mura, A. & Bongiovanni, G. Excited State Properties of Hybrid Perovskites. *Acc. Chem. Res.* **49**, 166–173 (2016).
77. Davy, M. M., Jadel, T. M., Qin, C., Luyun, B. & Mina, G. Recent progress in low dimensional (quasi-2D) and mixed dimensional (2D/3D) tin-based perovskite solar cells. *Sustain. Energy Fuels* **5**, 34–51 (2021).
78. Ishihara, T., Takahashi, J. & Goto, T. Optical properties due to electronic transitions in two-dimensional semiconductors (CnH2n+1NH3)2PbI4. *Phys. Rev. B* **42**, 11099–11107 (1990).
79. Stoumpos, C. C. *et al.* Ruddlesden−Popper Hybrid Lead Iodide Perovskite 2D Homologous

Semiconductors. (2016) doi:10.1021/acs.chemmater.6b00847.

80. Stoumpos, C. C. *et al.* High Members of the 2D Ruddlesden-Popper Halide Perovskites: Synthesis, Optical Properties, and Solar Cells of (CH3(CH2)3NH3)2(CH3NH3)4Pb5I16. *Chem* **2**, 427–440 (2017).
81. De Angelis, F. Modeling Materials and Processes in Hybrid/Organic Photovoltaics: From Dye-Sensitized to Perovskite Solar Cells. (2014) doi:10.1021/ar500089n.
82. Yoo, J. J. *et al.* Efficient perovskite solar cells via improved carrier management. *Nature* **590**, 587–593 (2021).
83. Warby, J. *et al.* Understanding Performance Limiting Interfacial Recombination in pin Perovskite Solar Cells. *Adv. Energy Mater.* **12**, 2103567 (2022).
84. Momblona, C. *et al.* Efficient vacuum deposited p-i-n and n-i-p perovskite solar cells employing doped charge transport layers. *Energy Environ. Sci.* **9**, 3456–3463 (2016).
85. Al-Ashouri, A. *et al.* Monolithic perovskite/silicon tandem solar cell with >29% efficiency by enhanced hole extraction. *Science* **370**, 1300–1309 (2020).
86. Al-Ashouri, A. *et al.* Conformal monolayer contacts with lossless interfaces for perovskite single junction and monolithic tandem solar cells. *Energy Environ. Sci.* **12**, 3356–3369 (2019).
87. Liu, H. *et al.* Thickness-dependent photovoltaic performance of TiO2blocking layer for perovskite solar cells. *J. Alloys Compd.* **736**, 87–92 (2018).
88. Mali, S. S., Shim, C. S. & Hong, C. K. Highly porous Zinc Stannate (Zn2SnO4) nanofibers scaffold photoelectrodes for efficient methyl ammonium halide perovskite solar cells. *Sci. Reports 2015 51* **5**, 1–14 (2015).
89. Shin, S. S. *et al.* High-performance flexible perovskite solar cells exploiting Zn2SnO4 prepared in solution below 100 °C. *Nat. Commun.* **6**, (2015).
90. Liu, C. *et al.* Effective stability enhancement in ZnO-based perovskite solar cells by MACl modification. *J. Mater. Chem. A* **9**, 12161–12168 (2021).
91. Liu, G. *et al.* Highly efficient and stable ZnO-based MA-free perovskite solar cells via overcoming interfacial mismatch and deprotonation reaction. *Chem. Eng. J.* **431**, 134235 (2022).
92. Pezhooli, N., Rahimi, J., Hasti, F. & Maleki, A. Synthesis and evaluation of composite TiO2@ZnO quantum dots on hybrid nanostructure perovskite solar cell. *Sci. Reports 2022 121* **12**, 1–9 (2022).
93. Min, H. *et al.* Perovskite solar cells with atomically coherent interlayers on SnO2 electrodes. *Nat. 2021 5987881* **598**, 444–450 (2021).
94. Lee, M. M., Teuscher, J., Miyasaka, T., Murakami, T. N. & Snaith, H. J. Efficient hybrid solar cells based on meso-superstructured organometal halide perovskites. *Science* **338**, 643–647 (2012).
95. Zhang, J. *et al.* Al2O3 Underlayer Prepared by Atomic Layer Deposition for Efficient Perovskite Solar Cells. *ChemSusChem* **10**, 3810–3817 (2017).
96. Mahmoudi, T., Wang, Y. & Hahn, Y. B. SrTiO3/Al2O3-Graphene Electron Transport Layer for Highly Stable and Efficient Composites-Based Perovskite Solar Cells with 20.6% Efficiency. *Adv. Energy Mater.* **10**, 1903369 (2020).
97. Rombach, F. M., Haque, S. A. & Macdonald, T. J. Lessons learned from spiro-OMeTAD and PTAA in perovskite solar cells. *Energy Environ. Sci.* **14**, 5161–5190 (2021).
98. Christians, J. A. *et al.* Tailored interfaces of unencapsulated perovskite solar cells for >1,000 hour operational stability. *Nat. Energy* **3**, 68–74 (2018).

99. Li, Z. *et al.* Acid Additives Enhancing the Conductivity of Spiro-OMeTAD Toward High-Efficiency and Hysteresis-Less Planar Perovskite Solar Cells. *Adv. Energy Mater.* **7**, 1–8 (2017).

100. Ramos, F. J. *et al.* Versatile perovskite solar cell encapsulation by low-temperature ALD-Al2O3 with long-term stability improvement. *Sustain. Energy Fuels* **2**, 2468–2479 (2018).

101. Choi, E. Y. *et al.* Enhancing stability for organic-inorganic perovskite solar cells by atomic layer deposited Al2O3 encapsulation. *Sol. Energy Mater. Sol. Cells* **188**, 37–45 (2018).

102. Hu, L. *et al.* High efficiency perovskite solar cells with PTAA hole transport layer enabled by PMMA:F4-TCNQ buried interface layer. *J. Mater. Chem. C* **10**, 9714–9722 (2022).

103. Wang, Y. *et al.* PTAA as Efficient Hole Transport Materials in Perovskite Solar Cells: A Review. *Sol. RRL* **6**, 2200234 (2022).

104. Knight, A. J. & Herz, L. M. Preventing phase segregation in mixed-halide perovskites: A perspective. *Energy Environ. Sci.* **13**, 2024–2046 (2020).

105. Song, T.-B. *et al.* Dynamics of Antisolvent Processed Hybrid Metal Halide Perovskites Studied by In Situ Photoluminescence and Its Influence on Optoelectronic Properties. *ACS Appl. Energy Mater.* **3**, 2386–2393 (2020).

106. Song, T. Bin *et al.* Revealing the Dynamics of Hybrid Metal Halide Perovskite Formation via Multimodal In Situ Probes. *Adv. Funct. Mater.* **30**, 1908337 (2020).

107. Pratap, S. *et al.* Out-of-equilibrium processes in crystallization of organic-inorganic perovskites during spin coating. *Nat. Commun. 2021 121* **12**, 1–9 (2021).

108. Wang, L. *et al.* Pinhole-Free Perovskite Films by Methylamine Iodide Solution-Assisted Repair for High-Efficiency Photovoltaics under Ambient Conditions. *ACS Appl. Mater. Interfaces* **8**, 30920–30925 (2016).

109. Li, J. *et al.* Optimization of anti-solvent engineering toward high performance perovskite solar cells. *J. Mater. Res.* **34**, 2416–2424 (2019).

110. Xiao, M. *et al.* Selection of an anti-solvent for efficient and stable cesium-containing triple cation planar perovskite solar cells. *Nanoscale* **10**, 12141–12148 (2018).

111. Jeon, N. J. *et al.* Solvent engineering for high-performance inorganic–organic hybrid perovskite solar cells. *Nat. Mater. 2014 139* **13**, 897–903 (2014).

112. Xiao, M. *et al.* A fast deposition-crystallization procedure for highly efficient lead iodide perovskite thin-film solar cells. *Angew. Chem. Int. Ed. Engl.* **53**, 9898–9903 (2014).

113. Higgins, K., Ziatdinov, M., Kalinin, S. V. & Ahmadi, M. High-Throughput Study of Antisolvents on the Stability of Multicomponent Metal Halide Perovskites through Robotics-Based Synthesis and Machine Learning Approaches. *J. Am. Chem. Soc.* **143**, 19945–19955 (2021).

114. Prochowicz, D. *et al.* Understanding the effect of chlorobenzene and isopropanol anti-solvent treatments on the recombination and interfacial charge accumulation in efficient planar perovskite solar cells. *J. Mater. Chem. A* **6**, 14307–14314 (2018).

115. The MAK-Collection for Occupational Health and Safety. *MAK-Collection Occup. Heal. Saf.* (2002) doi:10.1002/3527600418.

116. ICSC 0027 - CHLOROFORM. https://www.ilo.org/dyn/icsc/showcard.display?p_version=2&p_card_id=0027.

117. ICSC 0642 - CHLOROBENZENE. https://www.ilo.org/dyn/icsc/showcard.display?p_version=2&p_card_id=0642.

118. Wang, D., Wright, M., Elumalai, N. K. & Uddin, A. Stability of perovskite solar cells. *Sol. Energy Mater. Sol. Cells* **147**, 255–275 (2016).

119. Shang, Y. *et al.* Efficient and photostable CsPbI2Br solar cells realized by adding PMMA. *J. Semicond.* **42**, 050501 (2021).

120. Liu, S. *et al.* A Review on Additives for Halide Perovskite Solar Cells. *Adv. Energy Mater.* **10**, 1902492 (2020).

121. Kim, K., Han, J., Maruyama, S., Balaban, M. & Jeon, I. Role and Contribution of Polymeric Additives in Perovskite Solar Cells: Crystal Growth Templates and Grain Boundary Passivators. *Sol. RRL* **5**, 2000783 (2021).

122. Pan, J. *et al.* Room-Temperature, Hydrochloride-Assisted, One-Step Deposition for Highly Efficient and Air-Stable Perovskite Solar Cells. *Adv. Mater.* **28**, 8309–8314 (2016).

123. Heo, J. H., Song, D. H. & Im, S. H. Planar CH3NH3PbBr3 Hybrid Solar Cells with 10.4% Power Conversion Efficiency, Fabricated by Controlled Crystallization in the Spin-Coating Process. *Adv. Mater.* **26**, 8179–8183 (2014).

124. Xu, X. *et al.* Ascorbic acid as an effective antioxidant additive to enhance the efficiency and stability of Pb/Sn-based binary perovskite solar cells. *Nano Energy* **34**, 392–398 (2017).

125. Su, L. *et al.* Performance enhancement of perovskite solar cells using trimesic acid additive in the two-step solution method. *JPS* **426**, 11–15 (2019).

126. Han, F. *et al.* A functional sulfonic additive for high efficiency and low hysteresis perovskite solar cells. (2017) doi:10.1016/j.jpowsour.2017.05.084.

127. Tetraethyl orthosilicate 99.999 trace metals 78-10-4. https://www.sigmaaldrich.com/PL/pl/product/aldrich/333859.

128. Buckley, A. M. & Greenblatt, M. The Sol-Gel Preparation of Silica Gels. *J. Chem. Educ.* **71**, 599–602 (1994).

129. Huang, S. *et al.* Enhancing the Stability of CH3NH3PbBr3 Quantum Dots by Embedding in Silica Spheres Derived from Tetramethyl Orthosilicate in 'waterless' Toluene. *J. Am. Chem. Soc.* **138**, 5749–5752 (2016).

130. Aristidou, N. *et al.* The Role of Oxygen in the Degradation of Methylammonium Lead Trihalide Perovskite Photoactive Layers. *Angew. Chemie Int. Ed.* **54**, 8208–8212 (2015).

131. Aristidou, N. *et al.* Fast oxygen diffusion and iodide defects mediate oxygen-induced degradation of perovskite solar cells. *Nat. Commun.* **8**, 15218 (2017).

132. Leguy, A. M. A. *et al.* Reversible hydration of CH3NH3PbI3 in films, single crystals, and solar cells. *Chem. Mater.* **27**, 3397–3407 (2015).

133. Mazumdar, S., Zhao, Y. & Zhang, X. Stability of Perovskite Solar Cells: Degradation Mechanisms and Remedies. *Front. Electron.* **2**, 1–34 (2021).

134. Christians, J. A., Miranda Herrera, P. A. & Kamat, P. V. Transformation of the excited state and photovoltaic efficiency of CH3NH3PbI3 perovskite upon controlled exposure to humidified air. *J. Am. Chem. Soc.* **137**, 1530–1538 (2015).

135. Ai, B., Fan, Z. & Wong, Z. J. Plasmonic–perovskite solar cells, light emitters, and sensors. *Microsystems Nanoeng. 2022 81* **8**, 1–28 (2022).

136. Omrani, M. K., Keshavarzi, R., Abdi-Jalebi, M. & Gao, P. Impacts of plasmonic nanoparticles incorporation and interface energy alignment for highly efficient carbon-based perovskite solar cells.

Sci. Reports 2022 121 **12**, 1–10 (2022).

137. Gao, Y. *et al.* Plasmon-Enhanced Perovskite Solar Cells with Efficiency Beyond 21 %: The Asynchronous Synergistic Effect of Water and Gold Nanorods. *Chempluschem* **86**, 291–297 (2021).
138. Lee, T. C. *et al.* Enhanced efficiency and stability of planar perovskite solar cells using a dual electron transport layer of gold nanoparticles embedded in anatase TiO2 films. *ACS Appl. Energy Mater.* **3**, 9568–9575 (2020).
139. Juan, F. *et al.* Plasmonic Au Nanooctahedrons Enhance Light Harvesting and Photocarrier Extraction in Perovskite Solar Cell. *ACS Appl. Energy Mater.* **4**, 3201–3209 (2021).
140. Atwater, H. A. & Polman, A. Plasmonics for improved photovoltaic devices. *Nat. Mater. 2010 93* **9**, 205–213 (2010).
141. Chen, J., Seo, J. Y. & Park, N. G. Simultaneous Improvement of Photovoltaic Performance and Stability by In Situ Formation of 2D Perovskite at (FAPbI3)0.88(CsPbBr3)0.12/CuSCN Interface. *Adv. Energy Mater.* **8**, 1702714 (2018).
142. Li, M. *et al.* Copper Salts Doped Spiro-OMeTAD for High-Performance Perovskite Solar Cells. *Adv. Energy Mater.* **6**, 1601156 (2016).
143. Wang, R. *et al.* A Review of Perovskites Solar Cell Stability. *Adv. Funct. Mater.* **29**, 1808843 (2019).
144. Lim, T. H., Oh, K. W. & Kim, S. H. Effect of self-assembly supramolecules on the electrical properties of polyaniline based hole transport layer. *Synth. Met.* **162**, 268–275 (2012).
145. Jung, J. W., Lee, J. U. & Jo, W. H. High-efficiency polymer solar cells with water-soluble and self-doped conducting polyaniline graft copolymer as hole transport layer. *J. Phys. Chem. C* **114**, 633–637 (2010).
146. Ecker, B. *et al.* Degradation Effects Related to the Hole Transport Layer in Organic Solar Cells. *Adv. Funct. Mater.* **21**, 2705–2711 (2011).
147. Lee, B. H., Park, S. H., Back, H. & Lee, K. Novel Film-Casting Method for High-Performance Flexible Polymer Electrodes. *Adv. Funct. Mater.* **21**, 487–493 (2011).
148. Abdulrazzaq, O. *et al.* Optimization of the Protonation Level of Polyaniline-Based Hole-Transport Layers in Bulk-Heterojunction Organic Solar Cells. *Energy Technol.* **1**, 463–470 (2013).
149. Lee, K. *et al.* Efficient and moisture-resistant hole transport layer for inverted perovskite solar cells using solution-processed polyaniline. *J. Mater. Chem. C* **6**, 6250–6256 (2018).
150. Kwiatkowska, E. *et al.* Investigation of polyaniline doped with camphorsulfonic acid in chloroform solution as a hole transporting layer in PTB7: PCBM and perovskite-based solar cells. *Electrochim. Acta* **380**, 138264 (2021).
151. Abdulrazzaq, O. *et al.* Tuning the work function of polyaniline via camphorsulfonic acid: an X-ray photoelectron spectroscopy investigation. *RSC Adv.* **5**, 33–40 (2014).
152. Atomic Layer Deposition (ALD) - Technolutions. https://technolutions.pl/atomic-layer-deposition-ald/.
153. BENEQ TFS200.
154. Yougui Liao. *Practical Electron Microscopy and Database - An Online Book*. (2006).
155. Frank, L., Müllerová, I. & Delong, A. Microscopy with slow electrons. *Czechoslov. J. Phys. 1994 443* **44**, 195–238 (1994).
156. Kawasaki, T. *et al.* Development of a 1 MV field-emission transmission electron microscope. *J. Electron Microsc. (Tokyo).* **49**, 711–718 (2000).

157. XPS operating principle. https://commons.wikimedia.org/wiki/File:System2.gif.
158. Moulder, J. F., Stickle, W. F., Sobol, P. E. & Bomben, K. D. Handbook of X-ray Photoelectron Spectroscopy. *Surf. Interface Anal.* **3**, v–v (1979).
159. Kim, J.-G., Yoo, S. J., Kim, C.-Y. & Jou, H.-T. Circular Fast Fourier Transform Application: A Useful Script for Fast Fourier Transform Data Analysis of High-resolution Transmission Electron Microscopy Image. *Appl. Microsc.* **44**, 138–143 (2014).
160. Huang, T. *et al.* Performance-limiting formation dynamics in mixed-halide perovskites. *Sci. Adv.* **7**, 1–10 (2021).
161. Kong, W. *et al.* Characterization of an abnormal photoluminescence behavior upon crystal-phase transition of perovskite CH3NH3PbI3. *Phys. Chem. Chem. Phys.* **17**, 16405–16411 (2015).
162. Slater, J. C. Atomic Radii in Crystals. *J. Chem. Phys.* **41**, 3199 (2004).
163. Lehmann, F. *et al.* The phase diagram of a mixed halide (Br, I) hybrid perovskite obtained by synchrotron X-ray diffraction. *RSC Adv.* **9**, 11151–11159 (2019).
164. Prathapani, S., Bhargava, P. & Mallick, S. Electronic band structure and carrier concentration of formamidinium–cesium mixed cation lead mixed halide hybrid perovskites. *Appl. Phys. Lett.* **112**, 092104 (2018).
165. Slotcavage, D. J., Karunadasa, H. I. & McGehee, M. D. Light-Induced Phase Segregation in Halide-Perovskite Absorbers. *ACS Energy Lett.* **1**, 1199–1205 (2016).
166. Wang, D., Wright, M., Elumalai, N. K. & Uddin, A. Stability of perovskite solar cells. *Sol. Energy Mater. Sol. Cells* **147**, 255–275 (2016).
167. Shang, Y. *et al.* Efficient and photostable $CsPbI_2Br$ solar cells realized by adding PMMA. *J. Semicond. 2021, Vol. 42, Issue 5, Pages 050501-050501-4* **42**, 050501-050501–4 (2021).
168. Wincukiewicz, A. *et al.* Enhanced Performance of Camphorsulfonic Acid-Doped Perovskite Solar Cells. *Mol. 2022, Vol. 27, Page 7850* **27**, 7850 (2022).
169. (1S)-(+)-Camphor-10-sulphonic acid | 3144-16-9. https://www.chemicalbook.com/ChemicalProductProperty_EN_CB0395928.htm.
170. Ahn, N. *et al.* Highly Reproducible Perovskite Solar Cells with Average Efficiency of 18.3% and Best Efficiency of 19.7% Fabricated via Lewis Base Adduct of Lead(II) Iodide. *J. Am. Chem. Soc.* **137**, 8696–8699 (2015).
171. Li, L. *et al.* The Additive Coordination Effect on Hybrids Perovskite Crystallization and High-Performance Solar Cell. *Adv. Mater.* **28**, 9862–9868 (2016).
172. Liu, Y. *et al.* Ligand assisted growth of perovskite single crystals with low defect density. *Nat. Commun.* **12**, 4–11 (2021).
173. Wang, S. *et al.* Improving perovskite solar cell performance by compositional engineering via triple-mixed cations. *Sol. Energy* **220**, 412–417 (2021).
174. Yang, D. *et al.* High efficiency planar-type perovskite solar cells with negligible hysteresis using EDTA-complexed SnO2. *Nat. Commun. 2018 91* **9**, 1–11 (2018).
175. Zhumekenov, A. A. *et al.* The Role of Surface Tension in the Crystallization of Metal Halide Perovskites. *ACS Energy Lett.* **2**, 1782–1788 (2017).
176. Zhao, H. *et al.* Enhanced stability and optoelectronic properties of MAPbI3 films by a cationic surface-active agent for perovskite solar cells. *J. Mater. Chem. A* **6**, 10825–10834 (2018).
177. Salim, T. *et al.* Perovskite-based solar cells: impact of morphology and device architecture on device

performance. *J. Mater. Chem. A* **3**, 8943–8969 (2015).

178. Wincukiewicz, A. *et al.* The effects of doping and coating on degradation kinetics in perovskites. *Sol. Energy Mater. Sol. Cells* **230**, 111142 (2021).
179. Parrott, E. S. *et al.* Growth modes and quantum confinement in ultrathin vapour-deposited MAPbI3 films. *Nanoscale* **11**, 14276–14284 (2019).
180. Haeger, T., Heiderhoff, R. & Riedl, T. Thermal properties of metal-halide perovskites. *J. Mater. Chem. C* **8**, 14289–14311 (2020).
181. He, J., Zhang, L. & Liu, L. Thermal transport in monocrystalline and polycrystalline lithium cobalt oxide. *Phys. Chem. Chem. Phys.* **21**, 12192–12200 (2019).
182. Mosconi, E., Amat, A., Nazeeruddin, M. K., Grätzel, M. & De Angelis, F. First-principles modeling of mixed halide organometal perovskites for photovoltaic applications. *J. Phys. Chem. C* **117**, 13902–13913 (2013).
183. *JCPDS No. 01-084-7607.*
184. Fan, L. *et al.* Elucidating the role of chlorine in perovskite solar cells. *J. Mater. Chem. A* **5**, 7423–7432 (2017).
185. Mech, W. *et al.* Influence of Active Layer Processing on Electrical Properties and Efficiency of Polymer-Fullerene Organic Solar Cells. *Jaszowiec* **136**, (2019).
186. Slouka, C. *et al.* The Effect of Acceptor and Donor Doping on Oxygen Vacancy Concentrations in Lead Zirconate Titanate (PZT). *Mater. 2016, Vol. 9, Page 945* **9**, 945 (2016).
187. Zhou, Y. *et al.* Enhancing Chemical Stability and Suppressing Ion Migration in CH3NH3PbI3Perovskite Solar Cells via Direct Backbone Attachment of Polyesters on Grain Boundaries. *Chem. Mater.* **32**, 5104–5117 (2020).
188. Greczynski, G. & Hultman, L. X-ray photoelectron spectroscopy: Towards reliable binding energy referencing. *Prog. Mater. Sci.* **107**, 100591 (2020).
189. Briggs, D. Handbook of X-ray Photoelectron Spectroscopy C. D. Wanger, W. M. Riggs, L. E. Davis, J. F. Moulder and G. E.Muilenberg Perkin-Elmer Corp., Physical Electronics Division, Eden Prairie, Minnesota, USA, 1979. 190 pp. $195. *Surf. Interface Anal.* **3**, v–v (1981).
190. *NIST X-ray photoelectron spectroscopy database – Pb3O4, in: H. Kanai, M. Yoshiki, M. Hayashi, R. Kuwae, Y. Yamashita (Eds.), J. Am. Ceram. Soc. 77 (1994) 2229.*
191. *NIST X-ray photoelectron spectroscopy database – PbO, in: T.L. Barr, Y. Mengping, S. Varma (Eds.) 10, 1992, p. 2383. J. Vac. Sci. Technol. A.*
192. *NIST X-ray photoelectron spectroscopy database – PbO2, in: G. Gokagac, B. J. Kennedy (Eds.) 353, 1993, p. 71. J. Electroanal. Chem.*
193. *NIST X-ray photoelectron spectroscopy database – Pb(0), in: L. Ley, S. P. Kowalczyk, F.R. McFeely, R.A. Pollak, D.A. Shirley (Eds.) vol. 8, 1973, p. 2392. Phys. Rev. B.*
194. Wincukiewicz, A. *et al.* Enhanced Performance of Camphorsulfonic Acid-Doped Perovskite Solar Cells. *Mol. 2022, Vol. 27, Page 7850* **27**, 7850 (2022).
195. Navickas, E. *et al.* Dislocations Accelerate Oxygen Ion Diffusion in La0.8Sr0.2MnO3 Epitaxial Thin Films. *ACS Nano* **11**, 11475–11487 (2017).
196. Park, J., Yoon, H., Sim, H., Choi, S. Y. & Son, J. Accelerated Hydrogen Diffusion and Surface Exchange by Domain Boundaries in Epitaxial VO2 Thin Films. *ACS Nano* **14**, 2533–2541 (2020).
197. Emami, S., Andrade, L. & Mendes, A. Recent Progress in Long-term Stability of Perovskite Solar

Cells. *U.Porto J. Eng.* **1**, 52–62 (2015).

198. Lee, S. W. *et al.* UV Degradation and Recovery of Perovskite Solar Cells. *Sci. Reports 2016 61* **6**, 1–10 (2016).
199. Fick, A. Ueber Diffusion (On Diffusion). *Ann. der Phys. und Chemie von J. C. Pogendorff* 59–86 (1855).
200. Leguy, A. M. A. *et al.* Reversible hydration of CH3NH3PbI3 in films, single crystals, and solar cells. *Chem. Mater.* **27**, 3397–3407 (2015).
201. Yi, Z. *et al.* Will organic–inorganic hybrid halide lead perovskites be eliminated from optoelectronic applications? *Nanoscale Adv.* **1**, 1276–1289 (2019).
202. Sato, T., Takagi, S., Deledda, S., Hauback, B. C. & Orimo, S. I. Extending the applicability of the Goldschmidt tolerance factor to arbitrary ionic compounds. *Sci. Reports 2016 61* **6**, 1–10 (2016).
203. Pratap, S. *et al.* Out-of-equilibrium processes in crystallization of organic-inorganic perovskites during spin coating. *Nat. Commun.* **12**, (2021).
204. Kim, J., Lee, S. H., Lee, J. H. & Hong, K. H. The role of intrinsic defects in methylammonium lead iodide perovskite. *J. Phys. Chem. Lett.* **5**, 1312–1317 (2014).
205. DeQuilettes, D. W. *et al.* Impact of microstructure on local carrier lifetime in perovskite solar cells. *Science (80-.).* **348**, 683–686 (2015).
206. Segovia, R. *et al.* Evolution of Photoluminescence, Raman, and Structure of CH3NH3PbI3 Perovskite Microwires Under Humidity Exposure. *Nanoscale Res. Lett.* **13**, 0–7 (2018).
207. Yin, W. J., Shi, T. & Yan, Y. Unusual defect physics in CH3NH3PbI3 perovskite solar cell absorber. *Appl. Phys. Lett.* **104**, 063903 (2014).
208. Koutselas, I. B., Ducasse, L. & Papavassiliou, G. C. Electronic properties of three- and low-dimensional semiconducting materials with Pb halide and Sn halide units. *J. Phys. Condens. Matter* **8**, 1217 (1996).
209. Jang, Y. H. *et al.* Plasmonic Solar Cells: From Rational Design to Mechanism Overview. *Chem. Rev.* **116**, 14982–15034 (2016).
210. Qi, J., Dang, X., Hammond, P. T. & Belcher, A. M. Highly efficient plasmon-enhanced dye-sensitized solar cells through metal@oxide core-shell nanostructure. *ACS Nano* **5**, 7108–7116 (2011).
211. Kim, H. Do, Ohkita, H., Benten, H. & Ito, S. Photovoltaic Performance of Perovskite Solar Cells with Different Grain Sizes. *Adv. Mater.* **28**, 917–922 (2016).
212. Wincukiewicz, A. *et al.* The effects of doping and coating on degradation kinetics in perovskites. *Sol. Energy Mater. Sol. Cells* **230**, 111142 (2021).
213. Kim, I. S. *et al.* Amorphous TiO2 Compact Layers via ALD for Planar Halide Perovskite Photovoltaics. *ACS Appl. Mater. Interfaces* **8**, 24310–24314 (2016).
214. Zhou, Y. *et al.* Growth control of compact CH3NH3PbI3 thin films via enhanced solid-state precursor reaction for efficient planar perovskite solar cells. *J. Mater. Chem. A* **3**, 9249–9256 (2015).